Experiments and Modeling of PEM Fuel Cells for Dead-Ended Anode Operation

by

Jason B. Siegel

A dissertation submitted in partial fulfillment
of the requirements for the degree of
Doctor of Philosophy
(Electrical Engineering: Systems)
in The University of Michigan
2010

Doctoral Committee:

Professor James S. Freudenberg, Co-Chair
Professor Anna G. Stefanopoulou, Co-Chair
Professor Jessy W. Grizzle
Professor Jing Sun
Professor Serhat Yesilyurt, Sabanci University

“Non Impediti Ratione Cogitationis”

— Click and Clack, the Tappet Brothers.

To my lovely wife Lauren and my dog Tessa, for helping me find the light in my day.

Acknowledgments

I would like to acknowledge my professors and advisors for giving me the guidance to pursue my research; Anna Stefanopoulou, Serhat Yesilyurt, Jim Freudenberg, Stani Bohac, Jesse Grizzle, and Kurt Metzger. Daniel Hussey, David Jacobson and Eli Baltic at the National Institute for Science and Technology Center for Neutron Research provided the expertise and patience required to collect the data making this thesis possible. My lab-mates bestowed an excellent collaborative research environment; Denise McKay, Buz McCain, Amey Karnik, Toyoaki Matsuura, James Marcicki, Patty Laskowsky, Jixin Chen, and Xinfan Lin. Finally, I would like to thank my family for supporting me, listening to my ranting, and providing inspiration.

Table of Contents

List of Tables

Table

List of Figures

Figure

Abstract

This thesis develops models for the design and control of Dead-Ended Anode (DEA) fuel cell systems. Fuel cell operation with a dead-ended systems anode reduces fuel cell system cost, weight, and volume because the anode external humidification and recirculation hardware can be eliminated. However, DEA operation presents several challenges for water management and anode purge scheduling. Feeding dry hydrogen reduces the membrane water content near the anode inlet. Large spatial distributions of hydrogen, nitrogen, and water develop in the anode, affecting fuel cell durability. The water and nitrogen which cross through the membrane accumulate in the anode during dead-ended operation. Anode channel liquid water plugging and nitrogen blanketing can induce hydrogen starvation and, given the right conditions, trigger cathode carbon oxidation leading to permanent loss of active catalyst area. Additionally, the accumulation of inert gases in the anode leads to a decrease in cell efficiency by blocking the catalyst and reducing the area available to support the reaction. Purging the anode uncovers the catalyst and recovers the available area, but at the expense of wasting hydrogen fuel.

To understand, design, and control DEA fuel cells, various models are developed and experimentally verified with plate-to-plate experiments using neutron radiography and gas chromatography. The measurements are used to parameterize dynamic models of the governing two-phase (water liquid and vapor) spatially distributed transport phenomena. A reduced order model is developed that captures the water front evolution inside the gas diffusion layer and channels. A second model captures the nitrogen blanketing front location along the anode channel. The reduced order models are combined to form a complete description of the system. They require less computational effort, allow efficient parameterization, and provide insight for developing control laws or designing and operating DEA fuel cells.

Chapter 1
Introduction

Advances in the design and control of Polymer Electrolyte Membrane (PEM) Fuel Cells (FC)s are necessary to significantly improve durability and reduce cost for commercial applications. Degradation of the membrane and catalyst support structure has been observed and is associated with undesired reactions which occur during load following [1] and start-up conditions [2]. This degradation is also caused by the local build-up of liquid water [3, 4], nitrogen, and oxygen in the anode channel. Anode channel plugging, for example, can induce hydrogen starvation and, given the right conditions, trigger cathode carbon oxidation and loss of active catalyst area [5, 6, 2]. Apart from the permanent degradation, nitrogen accumulation and blanketing in the anode channel leads to a recoverable decrease in cell efficiency through reduction of the catalyst area available to support the reaction.

To avoid performance loss and degradation, excess water and nitrogen accumulation in the anode channel are minimized by using high hydrogen flow rates, resulting in the Flow-Through Anode (FTA) configuration. To increase the fuel utilization, a Re-Circulated Anode (RCA) architecture is used. In this configuration, water is removed from the gas stream leaving the channel and the reaming hydrogen (which is diluted with nitrogen) is recirculated back into the stack inlet. There, the gas is combined with additional high-purity hydrogen from the storage medium. The hydrogen rich gas is then humidified and fed to the anode inlet. The combined water removal, recirculation, and humidification in the FTA configuration minimizes the spatial variability in the hydrogen distribution along the anode channels, but leads to higher system cost and lower power density due to the external humidification and anode recirculation hardware. To achieve competitive cost and power density for low temperature fuel cells Dead-Ended Anode (DEA) operation is considered in this thesis. DEA systems can operate with dry hydrogen at low flow rates and without external humidification, however, large variations in the spatial distributions of water (dry inlets and flooded outlets) and nitrogen need to be addressed.

Liquid water formation can appear under various conditions leading to stationary, cyclostationary, or erratic patterns [3, 7]. It is therefore difficult to statistically assess or

physically model the impact on degradation due to lack of repeatable data. This thesis develops and shows plate-to-plate experiments with controlled flooding patterns [8], which are used to parameterize models of two-phase (water liquid and vapor), dynamic and spatially distributed transport phenomena inside a low temperature fuel cell. Detailed experiments show that nitrogen crossover and accumulation strongly impacts the distribution of reactants and current density when operating in DEA mode. The model is then reduced in complexity, first by deriving ordinary differential equations that capture the water front evolution inside the FC porous media and channels. The simplification reduces the computational effort and allows for efficient parameterization. Once parameterized, the model can be used to study system behavior [9] and develop control laws [10, 11].

1.1 PEM Fuel Cell Basics

Proton Exchange Membrane, also called Polymer Electrolyte Membrane, Fuel Cells (PEMFC)s are electrochemical energy conversion devices. PEMFCs produce electricity by combining hydrogen and oxygen, typically from the air, to form water and a small amount of heat. The heart of PEMFCs is the polymer electrolyte membrane. Two half reactions half reactions take place at the catalyst layers on either side of the membrane as shown in Fig. 1.1. The splitting of hydrogen into protons and electrons takes place at the anode catalyst layer. Protons crossing the membrane combine with oxygen and electrons at the cathode catalyst layer to generate water. The membrane provides a barrier to keep the hydrogen and oxygen separated. It must conduct protons easily, yet be electronically insulating to force the electrons through an external circuit and provide useful work. One such membrane material is Nafion© manufactured by DuPont, another competing product is provided by Gore. These polymer membranes have low melting temperatures, which limit operating temperature below 100 °C. Typical operating temperatures range from 50 to 70 °C. PEMFCs have several attributes, including low operating temperature and high efficiency (typically 50-70% for the fuel cell stack and 40-60% for the overall system), which make them good candidates for automotive and portable power applications.

The basic structure of the PEM fuel cell is shown in Fig. 1.1. The fuel and oxygen (air) are delivered across the active area through a series of channels. These channels are typically machined into the backplanes which are a conductive material, allowing electron transfer to the current collectors and completion of an electric circuit. The ratio of channel width to rib (contact) width, and the channel flow-field pattern are important design parameters affecting fuel cell performance. The Gas Diffusion Layer (GDL) is a porous material

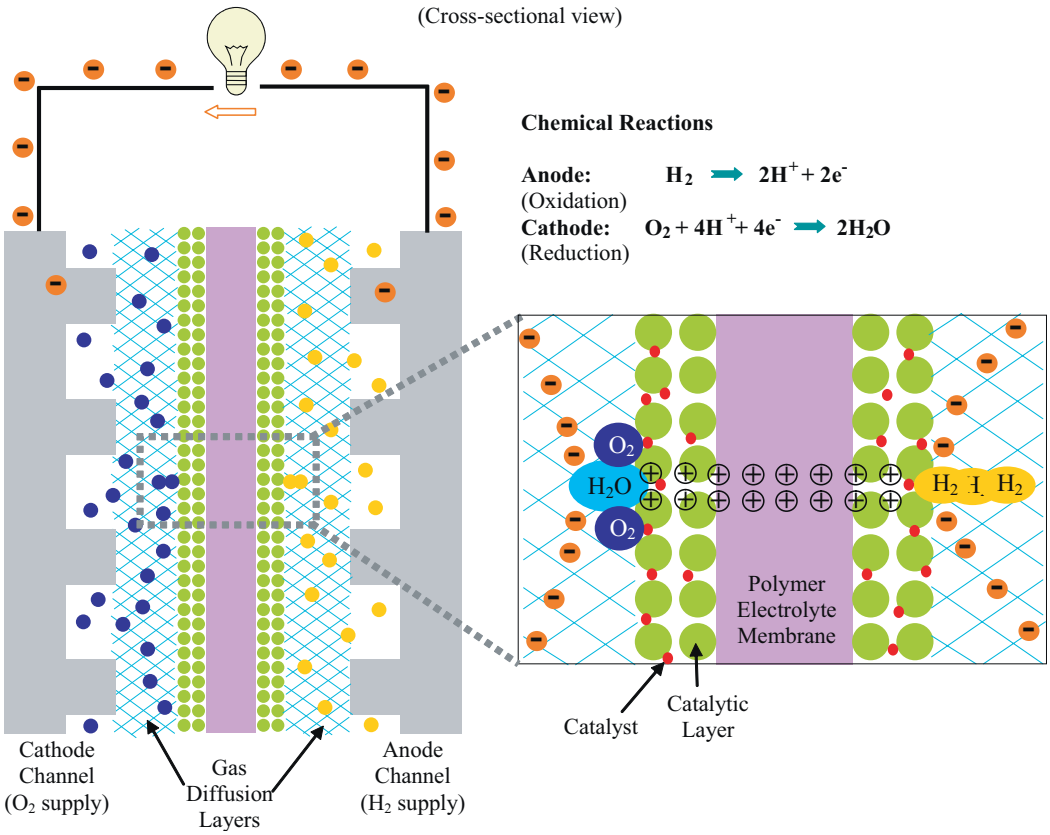

Figure 1.1 Basic Fuel Cell structure (not to scale) [12].

used to evenly distribute the reactant gases from the channel to the catalyst surface in the area under the ribs and channels. The GDL is typically composed of an electrically conductive carbon paper or cloth material. It is also designed to promote the removal of product water from the catalyst area, by treatment of the carbon with a hydrophobic coating such as Teflon. Finally the Catalyst Layer (CL) contains platinum particles supported on a carbon structure. The CL is where the reaction takes place inside the fuel cell. For the reaction to take place at the cathode, all three reactants, protons, oxygen, and electrons, must be able to reach the Platinum (Pt) particle. Protons are conducted through the Nafion© membrane material, electrons through the carbon support structure, and oxygen gas through the pore space. Therefore, each Pt particle must be in contact with all three portions of the cell [13]. A thin Micro-Porous Layer (MPL) can also be inserted between the GDL and CL to increase the electrical contact and aid in water removal from the catalyst or membrane hydration [14].

The membrane is a polymer that absorbs water, and the membrane water content λ_{mb}, defined as the number of moles of water per mole of SO_3H in the membrane, is a critical parameter for describing both proton transport and the permeation of molecular species

through the membrane. As the water content of the membrane increases, both the proton conductivity and the rate of gas permeation through the membrane also increase. Increased proton conductivity is good for fuel cell efficiency. However, increased permeability increases the rate of molecular crossover through the membrane, lowering the fuel cell efficiency, and thereby resulting in excess accumulation of water (plugging) and nitrogen (blanketing) of the anode channels. Hydrogen is thus displaced or blocked from reaching the catalyst sites. Modeling and managing this accumulation is the subject of this thesis.

1.2 Fuel Cell Sub-Systems

The PEMFC systems can be organized into three main categories, each of which evolves on different time-scales, the fastest is reactant gas supply (air or oxygen and hydrogen), followed by thermal management, then water management. Although dynamic behavior of each sub-system is tightly coupled (for example excess reactant supply may be used to carry heat and product water out of the cell, overlapping with the objectives of the thermal management system), these divisions provide a useful modeling framework. This thesis focuses on management of dead-ended anode operation. This topic has not been covered extensively in the literature or studied by the control society. Water management is considered to be one of the main barriers to commercialization of low temperature PEMFC stacks [15]. In this section, the overall stack management system is presented in order to provide adequate perspective and motivate DEA operation.

Figure 1.2a shows a basic fuel cell control architecture with many of the common control actuators for the reactant supply systems, hydrogen on the anode and air on the cathode. Although some small portable fuel cell systems are low-pressure ambient air breathing, which rely on free convection to deliver the oxidant, most automotive applications use forced air. In forced air systems, a scroll or centrifugal compressor is used to increases the oxygen partial pressure in the channels and hence the power density of the system [16]. The actuator u_2 controls the supply rate and back-pressure of the air to the cathode side of the fuel cell. If the compressor is driven by the fuel cell, a limit on the rate of power increase should be used in order to prevent oxygen starvation [17]. Various control techniques have been used to model and handle the constraints of the air compressor and manifold filling dynamics [16, 18], including feedback linearization [19] and a reference governor [20]. In addition to buffering the fuel cell from damaging increases in load current, excess air supplied to the cathode aids the removal of liquid water from the channels [3, 21, 22].

Since excess air is supplied, typically 2 - 3 times the amount required to support the re-

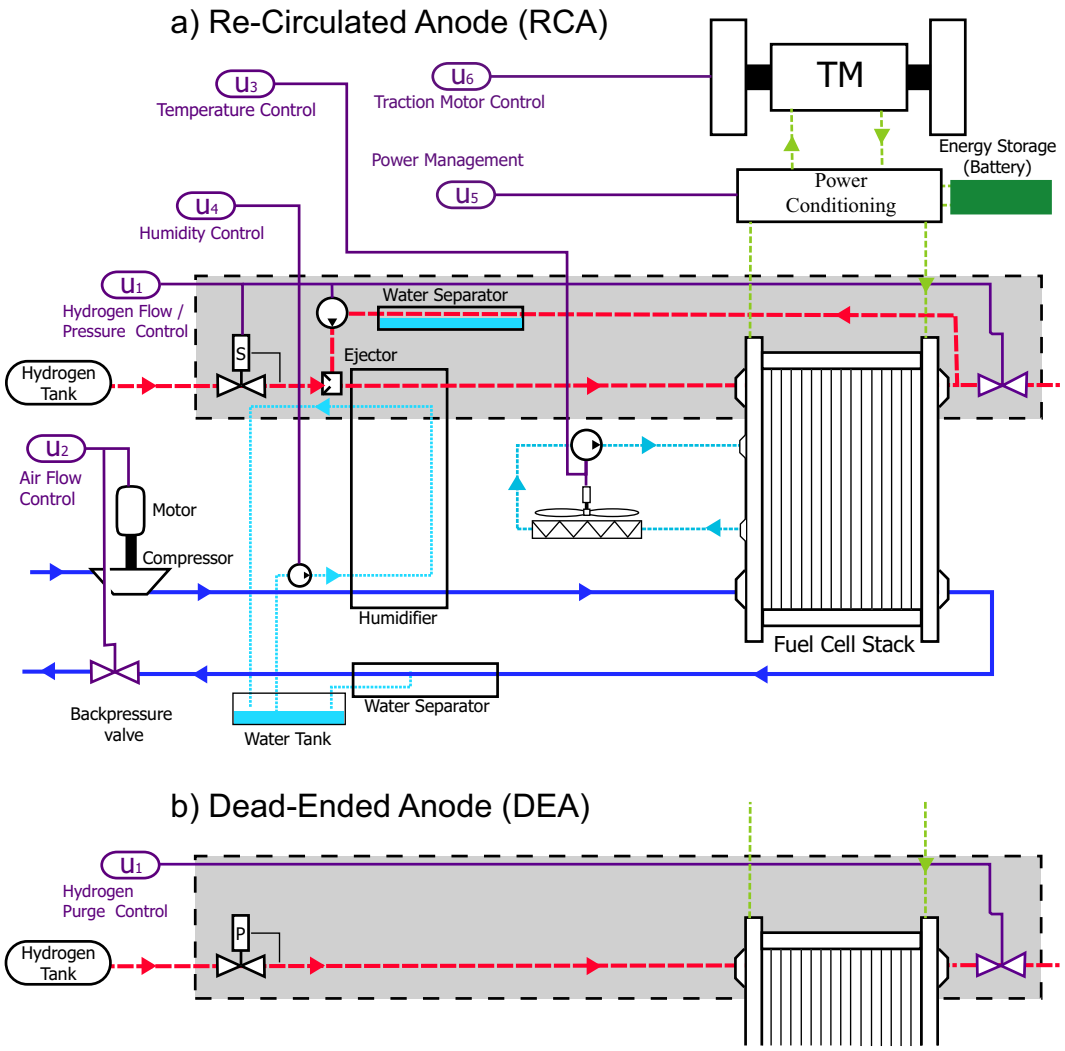

Figure 1.2 Fuel cell control actuators and sub-systems (modified from [16]). a) Dashed gray box shows hardware required for anode re-circulation (RCA). b) Simplified hydrogen delivery system for pressure regulated Dead-Ended Anode (DEA), which reduces or removes the need for inlet humidification, ejector, water separator and recirculation plumbing.

action, there is a very high flow rate of gas through the cathode channels and humidification of the incoming air is required to prevent drying the membrane. Bubblers, hotplate injection, and other novel humidifiers are employed for the inlet air humidification. The water temperature and flow rate (indicated by actuator u_4) through a membrane-type humidifier may be used to control the relative humidity of the incoming air [23, 24]. This sub-system is tightly coupled with the air flow and thermal management sub-systems [25, 26, 27], since the coolant water exiting the stack is then fed into the humidifier. The coolant flow rate and fan speed, u_3, can be used for control of the cooling system.

The overarching difficulty in the subsystem level control paradigm is that the control of air flow rate, cathode pressure, cathode inlet relative humidity, and stack temperature are

all tied to the higher level control objective of water management. Water management is a critical issue for PEMFC operation to ensure long stack life and efficient operation. Two of the limiting factors which prevent the mainstream adoption of PEMFCs are cost and durability or stack lifetime [15]. One of the major culprits affecting PEMFC durability is water, specifically the formation of liquid water inside the cell [3] and the wet-dry cycling of the membrane [28, 29]. The formation of liquid water can block reactants from reaching the catalyst leading to starvation and carbon corrosion [5, 30, 2], a permanent degradation of the cathode support structure. Conversely, drying of the membrane increases protonic resistance which yields lower cell efficiency, as illustrated in section 2.5. There needs to be sufficient water content in the membrane, (high λ_{mb}), so that proton conduction through the membrane is easy, however, too much water results in flooding and channel plugging. The delicate balance between drying and flooding is called management [4, 6, 31]. Modeling can provide the necessary tools to achieve this delicate balance in a cost-effective way.

1.3 Anode Water Management

Flow-through operation is used on both the anode and cathode of most laboratory or experimental hydrogen PEMFC systems. However, the fuel utilization of flow-through anode (FTA) operation is too low for commercial and portable systems. Fuel utilization is the rate of fuel consumption divided by the rate of fuel delivery, $U_{fuel} = (I_{fc}/(nF))/\nu_{fuel}$ [13], where I_{fc} is the fuel cell current in Amperes (A), $n = 2$ is the number of electrons taking part in the reaction, F=96,400 C mol^{-1} is Faraday's constant and ν_{fuel} is the hydrogen delivery rate in mol s^{-1}. The fuel stoichiometry, $\lambda_{H_2} = 1/U_{fuel}$, is the inverse of utilization. The anode reactant sub-system, shown in Fig. 1.2a, uses a re-circulation loop to re-cycle excess hydrogen back through the fuel cell stack increasing the fuel utilization. However the RCA requires hydrogen grade plumbing and hardware such as an ejector/blower [32, 33], water separator, and hydrogen humidification. These components add weight, volume, and expense to the system [34, 35]. Note that the water must be removed from the gas exiting the anode before it goes to the ejector and then the dry fuel supplied to the anode must be re-humidified to prevent over-drying of the membrane due to the higher flow rate.

Although the RCA subsystem can remove water from the gas stream, purging is still required to handle the nitrogen. A small amount of nitrogen crosses through the membrane, driven by the gradient in partial pressure from the air fed in the cathode. Over time this nitrogen accumulates in the anode feed system, which dilutes the hydrogen fuel in the anode [36, 37]. The dilution of H_2 lowers the fuel cell terminal voltage, and hence the efficiency.

Therefore the anode re-circulation system needs to be purged at certain intervals to remove the accumulated inert gas and maximize the system efficiency.

This thesis models a Dead-Ended Anode (DEA) system fed by pure dry hydrogen, shown in Fig. 1.2b, which is regulated to maintain anode pressure and supply exactly the amount of hydrogen needed to support the reaction $\lambda_{H_2} = 1$. DEA operation does not have as stringent requirements as the RCA system on hydrogen inlet humidification due to the lower flow velocity in the channels. The water crossing through the membrane could be enough to humidify the hydrogen fuel. The use of a pressure regulator instead of the RCA hardware (comprised of a mass flow controller, outlet water separator, hydrogen ejectors or blower, and inlet humidification), yield a system with lower cost and volume. In DEA operation, the binary control signal, $u_1 \in \{0, 1\}$, opens the downstream solenoid valve, causing a brief high velocity flow through the anode channel as the pressure regulator opens in attempt to maintain the system pressure. The high velocity flow aids in the removal of liquid water droplets [3, 22], which in the case of RCA could remain stationary due to the lower gas velocity. Several anode configurations, and the practical aspects of purging vs. flow-through, have been considered experimentally in [38, 39, 40].

Similar to the RCA system discussed above, nitrogen and water crossover is a concern. In a DEA system, the nitrogen, pushed toward the end of the channel by the flow of reactants, accumulates. The accumulating N_2 forms a blanket, which completely displaces hydrogen from reaching the catalyst layer, effectively shutting down the power production from the affected region of the cell [41]. Water vapor gradients between the humidified cathode and the dry fed anode also drive excess water into the anode, which can cause significant liquid water accumulation. Unlike water vapor whose maximum partial volume is dictated by temperature, liquid can fill the entire free space in the channels [8]. This liquid water accumulation in the channel water blocks the flow of reactants, which is referred to as channel plugging, and stops the production of power in the affected regions of the cell.

The gas velocity, driven by consumption of hydrogen, pulls nitrogen and water toward the bottom of the channel. Gravity helps stabilize the system as heavier molecules get pushed toward the bottom. As the mass accumulation continues, a stratified pattern develops in the channel with a hydrogen rich area sitting above a hydrogen depleted region, as shown in Fig. 1.4. The boundary between these regions is a time-varying front, which proceeds upwards toward the inlet [41]. The mass accumulation physically blocks hydrogen gas from reaching the anode catalyst sites, which is the mechanism for the experimentally observed and recoverable voltage degradation [8, 36, 42]. Therefore, purges of the anode channel volume are necessary to clear the reaction product and inert gas from the channel. After the purge, the catalyst area contributing to the reaction increases and hence the

measured voltage increases.

To prevent confusion and clarify the observed phenomena, the term *flooding* is used to describe the accumulation of liquid water in the GDL or catalyst layer, and the term *plugging* is used to refer to liquid water in the channels, which blocks or hinders the flow of gas through the channels [43]. The term *blanketing* is used to designate N_2 mass accumulation in the AN CH, which prevents hydrogen from reaching the catalyst layer.

Understanding, modeling and predicting the front evolutions in the anode for DEA operation of PEMFCs would allow a judicious choice of purging interval and duration. It is also possible, as shown in Chapter 6. to find operating conditions with stable behavior without purging. Using the modeling framework outlined in this thesis, one could determine an optimum schedule to reduce the H_2 wasted during purges and avoid over-drying the membrane. The advantage to developing simple models is that they can be used for MPC [10] or observer-based feedback algorithms that provide robustness in the control algorithm.

1.4 Neutron Imaging to Measure Liquid Water

The measurement of both water vapor and water liquid in operating PEMFCs is one of the greatest challenges for controlling FC stack operation due to the lack of availability, and cost, of sensors. Therefore, models which can accurately predict the amount of water inside the FC are important. Relative humidity (RH) sensors are expensive and saturate when exposed to liquid water, thus making them unsuitable for controlling FC operation, except for very dry operating conditions. The measurement of liquid water distribution inside an operating fuel cell, needed for model validation, is often complicated by methods which interfere with the quantity to be measured. Optical imaging of water droplets in the channels using high-speed cameras [44] requires the use of plexiglas end-plates or windows to allow visual inspection. Unfortunately, the materials used in the construction of fuel cells with optical viewing windows tend to have very different thermal conductivity properties, and therefore have been shown to induce condensation and impose non-realistic operating conditions. Magnetic Resonance Imaging (MRI) [45] is another relatively new and interesting tool for investigating water behavior inside PEMFC. However, this technique also requires the use of non-standard materials as metallic end-plates and current collectors are incompatible with the MRI equipment. The clear advantage of neutron imaging is the ability to measure in-situ the liquid water concentration while using realistic or commercial FC designs.

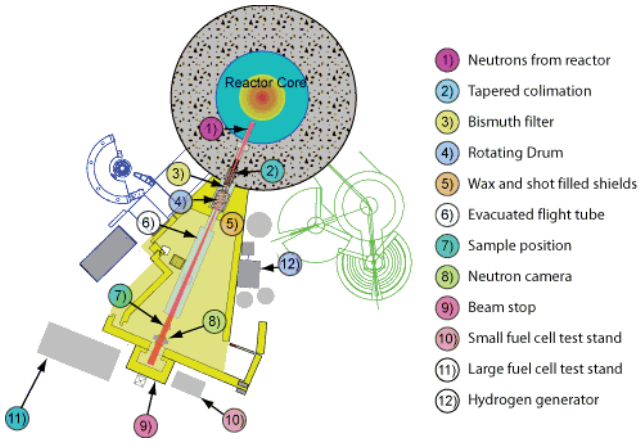

Figure 1.3 NIST Center for Neutron Research: Neutron Imaging facility [46]. `http://physics.nist.gov/MajResFac/Nif/`

The fundamental principle of neutron imaging is based on pinhole optics. Neutrons emitted from the reactor core escape through a small diameter (1 cm) aperture (the pinhole), and travel down the flight tube, as shown in Fig. 1.3. At the end of the 6 m flight tube, the fuel cell is placed in front of a neutron sensitive detector. The intensity of the neutron beam passing through the fuel cell is attenuated by liquid water in the fuel cell, and then the remaining neutrons which pass through are detected by a panel array. This produces a 2-D projection of liquid water distribution in the fuel cell. Dry images of the fuel cell are taken as a reference, which can later be used to calculate the amount (i.e. thickness) of water in the path of the neutron beam, as described in Chapter 3. Some excellent techniques to improve resolution and reduce uncertainty in measurements using neutron imaging can be found in [47, 48].

Beginning with [49] in 1999, many publications have utilized neutron imaging to study the effects of liquid water accumulations and distributions on the operation of PEMFCs [50, 7, 48, 51, 52, 53, 54, 55, 56, 57, 58, 59]. All of these publications deal with imaging the fuel cell during steady state flow through conditions. The research presented in this thesis is the first experimental validation of a dynamic model to predict DEA operation using in-situ measurements of liquid water accumulation.

The capabilities of the National Institute for Standards and Technology (NIST) Neutron Imaging Facility (NIF) for fuel cells are described in [46]. There are only a few other facilities in the world which offer comparable neutron imaging capabilities, including the Paul Scherrer Institute (PSI) [60] in Switzerland, and the International Thermonuclear Experimental Reactor (ITER) in France. There are two imaging setups available at NIST:

1) A low spatial resolution (250 μm) detector with a relatively high time-resolution (for

fuel cell liquid water measurement), on the order of 1 s per frame. This imaging setup was used for in-plane water distribution measurements, as described in chapter 3, where the plane is defined by the membrane.

2) A recently developed high resolution detector (10-20μm) which has poor time resolution (imaging requires long exposure times, $\approx$ 20 mins, and steady state conditions) but can be used for through-plane (i.e. *x*-direction) water distribution measurements. Modeling and measurement results from the high resolution imaging are shown in [61].

1.5 Fuel Cell Modeling

From the simplest model, a static polarization curve, to fully dynamic 3-D multi-phase models [62], the common objective is prediction of the fuel cell terminal voltage as a performance metric. A review of fuel cell modeling approaches can be found in [63] and [64]. Modeling reactant (gas) transport from the channel, through the GDL, to the catalyst layer at surfaces of the membrane, is critical for predicting the performance of the PEMFC, but equally important for high power applications is the description of product water removal from the cathode catalyst surface. Liquid water can block the catalyst surface, reducing the number of active catalyst sites, or fill some of the pore spaces in the GDL inhibiting the flow of reactant gas to the CL. Cathode GDL/CL flooding is the main performance limitation at high current density and therefore most commonly studied in the literature. This is considered to be a materials and design problem, since control actuators have limited authority to impact CCL flooding without over-drying the regions near the inlet [43].

Under DEA operation, product water which diffuses through the membrane (x-direction) back to the anode side will condense and accumulate in the anode channel (along the y-direction), displacing hydrogen, as shown in Fig. 1.4, and preventing it from reaching the anode catalyst layer. The prevention of hydrogen from reaching the catalyst stops the production of power from the affected region of the cell. Observation of water accumulation in DEA operation, and the voltage drop between purges motivates the development of a model to predict the water accumulation in the GDL and channels and its impact on cell voltage [65]. Under galvanostatic, or constant current operation, the remaining "hydrogen rich" regions of the cell must support a larger current density (A cm^{-2}) to account for the area which is no longer active. Hence, the notion of apparent current density can be used to capture this effect [41, 65] and simplify the modeling of distributed current density along the channel (y-direction), as shown in Fig. 1.4.

A simple model for nitrogen accumulation in a dead-ended anode fuel cell stack was first investigated in [41]. This model Assumes single phase, water vapor only, channel conditions and uses the convection equation to describe the accumulation of nitrogen at the end of the anode channel, as shown in Fig. 1.4. This model captured the correlation between Gas Chromatography (GC) measurements, taken from the end of the channel, and the cell voltage, but did not consider the effects of diffusion or liquid water. This previous work motivated the investigation of simultaneous GC measurements and neutron imaging presented in this thesis, since both nitrogen and water accumulations in the DEA contribute to voltage loss. Chapter 4 describes the experiments that were performed and the model developed to study the relative effects of nitrogen and water accumulation. The convection only model is then modified to include diffusion effects using the Stefan-Maxwell modeling framework, which better predicts the nitrogen concentration distribution (at the sampling location) and corresponding voltage measurements. The importance of along the channel modeling for capturing water crossover and cell performance has also been demonstrated in [66, 67]. Although not addressed in this work, the three-dimensional (3-D) effect of local current density distribution between the channels and ribs, resulting from gas transport and liquid water accumulation in the GDL, is addressed in [68] where a quasi-potential transformation was used to reduce a 2-D, GDL modeling domain down to 1-D. This type of method can handle an-isotropic properties of the diffusion medium due to compression of the GDL [69, 70].

The schematic representation of anode channel filling with liquid water and nitrogen is shown in Fig. 1.4. Since water condenses in both the GDL and channels, the water transport between the membrane and GDLs, and from the GDL to channels, determines the rate of water accumulation in the anode. Therefore, a One-Dimensional (1-D) modeling approach is considered, for the GDL, from channel to channel (x-direction). Calculation of the apparent area, shown in Fig. 1.4, from the anode channel masses is shown in Section 5.9. Anode purging directly impacts anode channel water accumulation, and can remove water from the channel which may not be easily removed by conventional flow through operation, as discussed in the previous section.

The water transport models developed in this thesis are based on previous research at the University of Michigan Fuel Cell Control Laboratory (FCCL). A 1-D, isothermal, and dynamic model of liquid water, water vapor, and reactant (H_2 or O_2), and inert (N_2) gas transport through the GDL (x-direction) was developed in [65], and reviewed in chapter 2. Depending on the discretization level, this distributed Partial Differential Equation (PDE) model of GDL transport can be computationally intensive. Using a three section discretization, an ODE model is derived with 24 states, 18 of which come from the discretization of

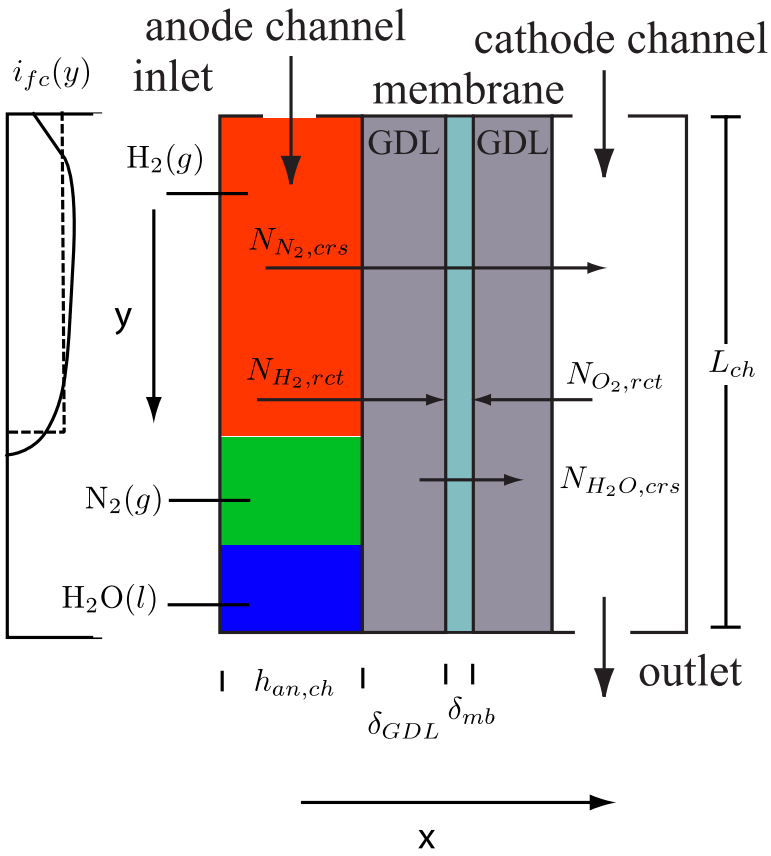

Figure 1.4 The one dimensional fuel cell modeling domain, along the *x*-axis, which denotes the through membrane direction. The *y* axis denotes the distance along the channel from inlet to outlet (not drawn to scale). This caricature shows the stratification of product water, inert nitrogen and the displacement of hydrogen from the bottom portion of the cell. The distributed current density, $i_{fc}(y)$, along the channel is shown to the left of this figure; for a realistic profile (solid line), the modeled apparent current density (dashed line).

the (PDE)s describing gas and liquid water transport in the anode and cathode GDLs. The remaining 6 states correspond to a mass balance for lumped hydrogen or oxygen, nitrogen and water masses in the anode and cathode channels.

The GDL water transport model was derived from the steady state relationship presented in [71], where water transport is driven by the gradient in capillary pressure, described by the Leverett J-function (2.6). The liquid water profile forms a steep front inside the GDL as shown in Fig. 2.4. Several other, more recent, water transport models have been developed in the literature which explain the relationship between liquid water accumulation in the GDL and water flow [72, 73, 74, 75, 76, 77, 78, 79]. These models highlight the dependence of water transport on the material properties; specifically the pore-size distribution of the GDL, and % weight of hydrophobic material such as Teflon. This dissertation focuses on the Leverett approach since there is more information readily available, how-

ever, it is important to note that other capillary pressure models should also exhibit a similar behavior in the formation of a steep liquid water front and propagation mode [80]. Accurate representation of the evolution of this front requires a very fine spatial discretization of the distributed reactants, vapor and liquid water.

The first simplification used to solve the 4 coupled PDEs in the x-direction was developed by McCain et al. [81]. This approach uses a Semi-Analytic Solution (SAS) for the water vapor, and reactant gas transport PDEs in the GDL. Since the reactant gas and vapor diffusion in the GDL evolve with much faster time-constants than the liquid water, due to the difference in density, the SAS uses the steady-state solution of the PDEs for the gas distributions, to propagate the concentration values in the channel through the GDL to the CL. This reduces the number of dynamic states in the GDL model from three per discretization slice down to one, namely liquid water. Further reduction of the number of states in the water transport model in the GDL can be achieved using a moving front approach, which was first introduced by Promislow et al [82, 83]. The PDEs [65, 12] describing liquid water transport require a very fine discretization grid in order to accurately represent the front propagation. Adaptive grids, developed to address the problem of groundwater transport [84], have been used to handle this type of problem, but they are not well suited for a reduced complexity control oriented model. The nature of the sharp transition in the GDL liquid water volume, between the wet and dry regions, can be used to simplify the model. The two-phase front location in the GDL is defined by the point where the reduced water saturation, S, goes to zero along the x direction, in terms of an ordinary differential equation (ODE), similar to [80], greatly reducing the computational complexity of the 1-D 2-phase water model.

The trade-off between model accuracy and computational complexity, 1-D versus 2-D versus 3-D, is a difficult engineering challenge for the control of PEMFC systems. A comparison between 1-D and 2-D models, in terms of voltage accuracy is presented in [85], and a review of CFD modeling for heat and mass transfer in PEMFCs can be found in [86]. In summary, CFD models [87, 88, 62, 89, 90] are great for detailed FC modeling, optimization, and channel design, but are very complicated to setup and require intensive computational resources. Therefore, CFD models are not suitable for control oriented applications. In order to use a fuel cell model for control design, and real-time hardware implementation in an automotive grade microprocessor, development of reduced order models is necessary.

The 1+1-D through the membrane modeling approach, presented in this thesis, is a good compromise between model complexity and accuracy since the apparent current density, shown in Fig. 1.4, captures some of the along the channel effects without increasing

the computational complexity. The reduced order model developed in section 5.2 also has another advantage over CFD models in that the water transport and voltage model can easily be parameterized using analytical tools, as described in sections 5.7 and 2.6.

1.6 Thesis Organization

This thesis follows a chronological progression of hypothesis formulation, testing, and discovery motivated by the desire to understand and model the performance and dynamics of a PEMFC operating under DEA conditions. The second chapter is the result of a joint research effort at the Fuel Cell Control Lab (FCCL) with Denise McKay, and represents the fuel cell model based on the PDEs describing the distribution of water (liquid and vapor) and reactant transport along the x-direction in the GDLs and membrane. A lumped volume approach (also known as a stirred tank reactor or STR [91] in the field of chemical engineering) is used for the channels. The lumped volume model constitutes a mass balance and is described in Sec. 2.4.3. Water accumulation in the GDL and channels can be described simply by a first order integrator ODE model. The parameterization and model tuning using stack data, based on a discretization of the PDEs describing the gas and liquid states in the GDL coupled to a lumped channel model, was published in the Journal of Power Sources [65]. Subsequent work, by Real et al. [92], following this approach using a lumped channel model is shown in [92, 93, 94], where the PDEs describing reactant transport in the GDLs are further simplified and approximated by a single volume each, with the associated ODEs. Their model was tuned to represent the dynamic behavior of a Ballard Nexa PEMFC stack which is auto-humidified and, as a result, also utilized a saturated cathode feed gas supply.

In order to validate the predicted accumulation of water and avoid the issue of cell to cell variability, single cells were built which would allow for neutron imaging. Using neutron imaging, in-situ measurement of the liquid water distribution within the fuel cell was investigated, allowing observation the otherwise immeasurable state of the system. Chapter 3 explains both the neutron imaging data and measurement uncertainty analysis from the first round of testing at NIST. This chapter provides a basic comparison with the (slightly modified) discretized PDE model presented in Chapter 2. The simulation results presented in Chapter 3 include some modeling improvements beyond [65]; specifically, the inclusion of liquid water flow through the outlet orifice. Accounting for liquid water removal during an anode purge is necessary to predict the water balance in the fuel cell because liquid causes plugging of the channel and outlet orifice; hence, gas cannot flow out until the liquid

is pushed out of the way.

Using the 1-D GDL model with lumped channels (STR), the voltage behavior can be captured by liquid water accumulation using a thin film model for the liquid coverage area and the notion of apparent current density. Neutron imaging shows good results with anode channel liquid water mass accumulation, for experimental conditions which match the assumption of uniform channel vapor distribution (i.e. saturated cathode inlets). The observed water accumulation from neutron imaging however, does not corroborate this predicted film thickness. Namely, the experimentally observed water coverage area was insufficient to explain the extent of voltage deviation. The analysis of neutron imaging data is published in the Journal of the Electrochemical Society (JES) [8]. Although the lumped parameter channel model is able to predict the water accumulation in the GDL and anode channel with very good accuracy for operating conditions with fully saturated cathode inlet conditions, it is unable to adequately predict the voltage or sub-saturated (i.e. very dry) cathode inlet conditions. Model inaccuracy for low cathode inlet RH is not surprising, considering that the assumption of uniform/lumped channel conditions would be violated as the vapor concentration increases along the length of the cathode channel due to the production of water.

The inability to predict voltage for some vapor saturated cathode inlet conditions implied that another un-modeled factor could be responsible. Specifically, there is a significant voltage drop even during periods when only a small amount of liquid water build-up in the anode channel is observed. After reviewing the literature [36, 37, 41], it was suspected that nitrogen accumulation in the anode channel is contributing to the voltage drop during DEA, which is recoverable by purging the anode. At first, the effects of nitrogen accumulation were investigated by augmenting the lumped channel model with nitrogen crossover. It was found that a lumped volume (STR) approach can't predict the effect of nitrogen accumulation in the anode channel due to the logarithmic relationship with voltage.

This motivated the development of a new distributed model to predict nitrogen distribution and blanketing effects in the anode channel. Experiments were then proposed to measure the relative effects of nitrogen and water accumulation in the anode channel on fuel cell voltage. Chapter 4 presents the development of a single phase along the channel model with distributed current density to capture the nitrogen crossover and blanketing effects in the anode channel. This chapter also details the August 2008 experiments at NIST with simultaneous gas chromatography measurement of the nitrogen concentration and neutron imaging, recently published in the Journal of the Electrochemical Society (JES) [95]. The single phase nitrogen model is validated against experimental results from NIST. The neutron images confirm that water accumulation in the anode channel is not significant for the

selected operating conditions, hence justifying the validity of the single phase model.

Since the discretized PDE model presented in Chapter 2 requires a very fine spatial discretization to accurately predict the two phase transition between single phase and two phase (liquid) water areas in the GDL. Therefore, an alternative representation of the GDL water distribution and transport was considered. A reduced order method, similar to the slowly moving, two-phase interface model presented in [80], was derived for the model, along with the necessary tools to parameterize the membrane water transport model using measurements from neutron imaging. Based on modeling efforts presented in Chapter 4, a reduced order channel model to capture the N_2 accumulation effect on cell voltage was developed. The model relies on the steady state solution of the PDEs describing reactant concentrations along the channel. Although this reduced order model is better in predicting the voltage drop due to nitrogen accumulation in the anode channel, it has the same limitations as the original lumped channel model for predicting liquid water behavior for low cathode inlet RH. Chapter 5 details the development of a reduced order model to capture liquid water front propagation in the GDL and channel, and the nitrogen front in the channel. This work will also be published in a forthcoming chapter of the CRC Controls Handbook [11].

The existence of equilibrium in the nitrogen blanketing front location is predicted by the single phase anode channel PDE equations. These equilibria, their stability and time-constants to reach equilibrium following an anode purge are evaluated in Chapter 6. Finally, the model predictions are verified by running experiments with DEA for extended periods between purges.

CH2	1-D (through the membrane), 2 phase GDL model with lumped channels (BCs).	Voltage is tuned for 24 cell stack data, and thin film model captures proposed relationship between anode channel water accumulation and voltage.	Spatial discretization of the PDE requires higher computational overhead, which motivates semi-analytic-solution (SAS) of GDL [96] and CH5.
CH3	Neutron Imaging of single cell, and comparison with slightly modified model from CH2.	The model shows good agreement with measured water mass accumulation, however invalidates the thin-film assumption and motivates the investigation of nitrogen effects.	The lumped channel model cannot predict behavior for lower cathode inlet RH due to spatial variation of water content along the channel.
CH4	1-D (along the channel) Single phase model with 0-D GDL and distributed membrane water content, compared with simultaneous GC and NI.	The model describes the effect of nitrogen accumulation and blanketing front evolution on cell voltage.	Single phase model is not valid for flooding conditions.
CH5	1-D (through the membrane) reduced order GDL model based on liquid water front evolution in the GDL with lumped channels. The effect of nitrogen blanketing in anode channel is augmented to the single nitrogen mass accumulation state using an approximation of the steady state nitrogen profile observed from CH4.	This CH demonstrates parameterization of water transport, the model can be tuned to match water accumulation in the anode channel from NI. The combined effects of anode liquid water and nitrogen accumulation on voltage are predicted well for certain operating conditions.	The model has the same limitation as original through membrane model (CH2), lumped channels (and lumped membrane water content) cannot predict the behavior for lower cathode inlet RH due to spatial variation of water content along the channel.
CH6	Equilibrium analysis of 1-D along the channel model.	Used to determine the effects of spatial variations as compared to lumped channel model.	Points to validity and usefulness of lumped channel model. Shows specific operating conditions (i,T,P), and the effect of control inputs, CA inlet SR and RH.

Table 1.1 Chapter-by-Chapter model highlights

1.7 Contributions

The contributions of this dissertation are summarized here:

a) **Voltage tuning algorithm:** In Chapter 2, a reformulation of the voltage model is presented than can be parameterized by minimizing the prediction error using a linear least squares cost function. The solution of the least-squares problem is then related to the parameters K_1-K_4 in (2.40). The discretized GDL model presented in Chapter 2 was programmed and compared with the data.

b) **Neutron imaging, data collection, and analysis:** In preparation for Neutron imaging experiments, the specifications for fuel cell hardware compatible with neutron imaging was determined. The trade-off between measurement uncertainty and image exposure time used to collect data suitable for analyzing transient behavior of the PEMFC, given the constraints of the imaging system, is evaluated. Following the experiments a method for estimating the liquid water mass in the various layers of the fuel cell from the Neutron images was derived and programmed into image processing routines for analysis of the data, as discussed in Chapter 3.

c) **Simultaneous GC and NI measurements:** Experiments were developed and performed at NIST to determine the relative effects of liquid water, and nitrogen accumulation in the DEA, using simultaneous measurement of liquid water accumulation via neutron imaging and nitrogen concentration measurement via gas chromatography. Data processing and analysis were performed to enable comparison with fuel cell models. This research led to the publication of the first experimental results comparing a model with simultaneous measurement of nitrogen and water accumulation.

d) **Development of an along the (anode) channel PDE model:** Based on [41], but modified to include diffusion effects and a distributed current density, a model was developed. This model is needed to explain the two-sloped voltage behavior shown in Fig. 4.8 and the GC measurements taken from the sampling location. A new physics based voltage model was identified from the literature, and incorporated into the modeling framework to account for distributed current density as described in Chapter 4.

e) **Model reduction and water fronts in the GDL:** The fronts based GDL and membrane model presented in Chapter 5 are derived along with a method to parameterize the model using the quasi-steady state measured liquid water accumulation rate in the anode channel derived from neutron imaging.

f) **Improvements to the lumped channel model:** Incorporation of nitrogen crossover into the modeling framework. The channel inlet/outlet flow equations are described

using a model that accounts for liquid water removal from the channels, (stated as important missing feature in A4 of [65] and in B. A. McCain's thesis [96].)

g) **Equilibrium analysis:** The equilibrium that could be achieved during the dead end anode (DEA) operations of PEM fuel cell was investigated. The simulation results indicate that the system pressure and RH of air supply play a critical role in determining the steady state power output during DEA operation. It is shown that the equilibrium is feasible for only small load current. Experimental validation shows the stable voltage output under DEA conditions as predicted by the model. The results suggest that it is possible to coat only the active portion of the membrane, along the channel length, with catalyst, hence reducing the system cost without sacrificing catalyst utilization or durability.

Chapter 2

Modeling PEMFC using distributed PDEs for GDL transport with lumped channels

This chapter describes a simple isothermal dynamic model that predicts the experimentally observed temporal behavior of a PEMFC stack. The DEA operation of PEMFC leads to water accumulation in the anode channel under certain operating conditions. In order to capture the water accumulation in the channel, vapor transport, liquid water transport, and accumulation inside the GDL needs to be considered. A reproducible methodology is presented to experimentally identify six (6) tunable physical parameters. Therefore based on the estimation of the cell voltage, the water vapor transport through the membrane, and the accumulation of liquid water in the gas channels. The model equations allow prediction of the species concentrations through the gas diffusion layers, the vapor transport through the membrane, and the degree of flooding within the cell structure. An apparent current density is related to this flooding phenomenon and cell performance through a reduction in the cell active area as liquid water accumulates. Despite oversimplifying some complex phenomena, this model is a useful tool for predicting the resulting decay in cell voltage over time after it is tuned with experimental data. The calibrated model and tuning procedure is demonstrated with a 1.4 kW (24 cell, 300 cm^2) stack. The stack is operated with pressure regulated pure hydrogen supplied to a dead-ended anode.

2.1 Introduction

The management of water is critical for optimizing performance of a PEMFC stack because the ionic conductivity of the membrane is dependent upon its water content [97]. To maintain membrane water content, a balance must be struck between reactant (hydrogen and oxygen) delivery and water supply and removal. Depending upon the operating con-

ditions of the PEMFC stack, the flow patterns in the anode and cathode channels, and the design of the anode gas delivery system (dead-ended or flow through), this liquid water can accumulate within the gas diffusion layers (GDLs) and channels [56, 98, 7, 51], as shown in Figure 2.1. Whether obstructing reactant flow or reducing the number of active catalyst sites, the impact of flooding is a reduction in the power output of the fuel cell stack, seen by a decrease in cell voltage [99]. Thus, a real-time estimation of the degree of flooding within the cell structure and its impact on the cell electrical output with standard, cheap, and reliable sensors is critical for active water management. Moreover, a low order control-oriented model must be derived to consider such issues as identifiability, observability, and controllability.

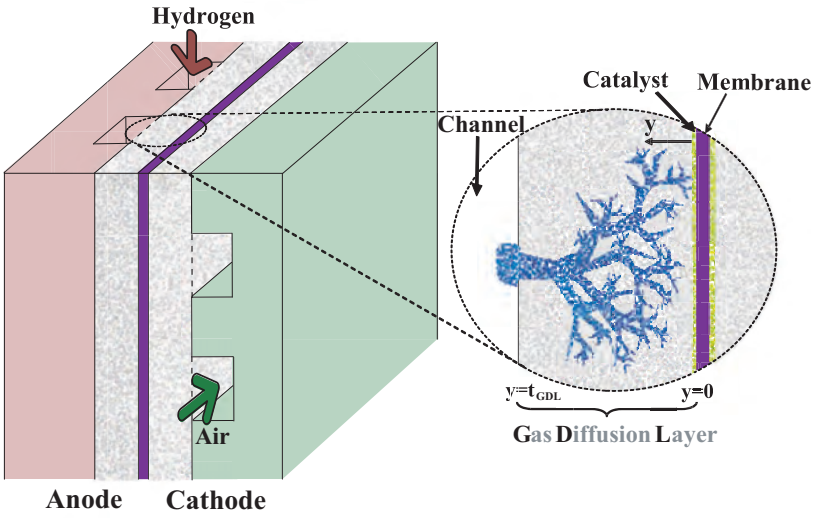

Figure 2.1 Schematic of capillary flow of liquid water through the gas diffusion layers.

To gain a better understanding of reactant and water transport within the GDL and catalyst layers, many CFD models have been developed to approximate the two or three dimensional flow of hydrogen, air, and water at steady-state within the cell structure [100, 101, 102, 103, 104, 87]. Using experimental steady-state polarization (voltage versus current) data for parameter identification, [105] and [106] investigated the sensitivity of the cell performance to the identified parameters. Furthermore, using a model to simulate polarization data with a given set of parameters, constrained quadratic programming was then used to identify these given parameters [107] and address parameter identifiability and uniqueness issues [108].

3-D CFD models are ideal for investigating two phase transport phenomena, spatial gradients, and the influence of material properties on cell performance. Unfortunately parameter sensitivity and experimental validation of these models is still lacking. A few publications address steady-state model validation. They point to a mismatch between model

predictions and the spatially resolved current density data [109] indicating that different spatial distributions can correspond to the same voltage polarization curve [109, 108]. Other work has shown good prediction of steady-state and spatially resolved current density measurements, but their tuned parameters are several orders of magnitude different than the theoretical values [66].

Steady-state polarization measurements do not offer a conclusive data set for model validation, however, the transient response does provide useful data for model validation especially during unsteady operation such as flooding [110, 111]. Several transient models have been reported to capture the relationship between critical material properties and operating conditions on the dynamic fuel cell response [112, 113, 114, 115, 116], however few have been validated against transient experimental data and are of sufficient computational tractability for implementation in real time control applications.

Control-oriented transient models have been developed to account for the formation of liquid water within the gas channels [117] or within both the channels and the GDL [118], however, they do not relate the effect of flooding to decreased cell potential. The voltage response is a key indication of how flooding impacts cell performance. A relationship between flooding and cell performance was introduced in [111], appearing later in [92], using the notion of apparent current density to relate the accumulation of liquid water in the gas channels to a reduction in the cell active area, increase in the cell current density and hence lower cell voltage.

In this chapter, a low order model of the liquid water and gas dynamics within the GDL is presented to simulate both the effects of reactant starvation and flooding. The modeling effort focuses on the one dimensional dynamics through the GDL thickness. It is assumed that the two dimensional properties in the plane parallel to the membrane are invariant, and a lumped volume is used to capture manifold filling dynamics for the gas channels, and lumped parameter characteristics for the membrane. Lumping the GDL and channel into a single volume, Hernandez et al. [119] experimentally validated their model for a flow-through anode with no gas dynamics. Lumped modeling of the GDL volume was also pursued by Real et al. [92] and validated against experimental data for a Ballard® NEXA^{TM} system. In their approach nearly double the number of experimentally identified parameters were used as compared to the work originally presented in [111] and used here.

The validity of the model is tested using a wider range of current densities (0-0.3 A cm^{-2}), temperature (45-65^{o}C) and air stoichiometries (150%-300%). These conditions are tested while the stack operates mostly under full hydrogen utilization with intermittent and short high hydrogen flow conditions associated with dead-ended anode operation. It is shown that the model predicts both the fast voltage dynamics during step changes in cur-

rent (the gas dynamics) and the slow voltage behavior while liquid water is accumulating in the GDL and gas channels (water dynamics), whereas [92] only predicts the slow voltage dynamics well. Hence, the model presented here can be used for estimation and control of fuel cell water and gas dynamics. It is important to note that the fuel cell model presented here is not novel, except in relating cell flooding to performance. The unique contribution lies in applying this simple isothermal model to well approximate the dynamic fuel cell response under a range of operating conditions by leveraging standard off-the-shelf sensors and actuators.

This chapter is organized by first presenting the experimental hardware in Section 2.2 followed by the model of gas and water dynamics in Section 2.3. The applied boundary conditions at the gas channels and membrane surface are then presented in Section 2.4. The impact of the liquid water on cell voltage is modeled in Section 2.5. The parameter identification methodology is presented in Section 2.6. Finally, the model calibration and validation results are shown in Sections 2.7 and 2.8. A list of the model parameters is given in the Appendix.

2.2 Experimental Hardware

Experimental results are collected from a 24-cell PEMFC stack which can deliver 1.4 kW continuous power, capable of peaking to 2.5 kW. The cell membranes are comprised of GORE^{TM} PRIMEA® Series 5620 membrane electrode assemblies (MEAs). The MEAs utilize 35 μm thick membranes with 0.4 mg/cm^2 and 0.6 mg/cm^2 Pt/C on the anode and cathode, respectively, with a surface area of approximately 300 cm^2. The GDL material, which distributes gas from the flow fields to the active area of the membrane, consists of double-sided, hydrophobic, version 3 ETek^{TM} ELATs® with a thickness of 0.43 mm. The flow fields are comprised of machined graphite plates with gas channels that are approximately 1 mm wide and 1 mm deep. The flow pattern consists of semi-serpentine passages on the cathode (30 channels in parallel that are 16.0 cm in length with two 180^o turns) and straight passages on the anode (90 channels in parallel that are 17.1 cm in length).

The experimental hardware, designed in collaboration with the Schatz Energy Research Center at Humboldt State University, is installed at the Fuel Cell Control Laboratory at the University of Michigan. A schematic of the major experimental components along with the measurement locations is depicted in Figure 2.2. A computer controlled system coordinates air, hydrogen, cooling, and electrical subsystems to operate the PEMFC stack. Dry pure hydrogen is pressure regulated at the anode inlet to a desired setpoint. This pressure regula-

tion system replenishes the hydrogen consumed in the chemical reaction. For the majority of the operational time, the hydrogen stream is dead-ended with no flow external to the anode. Using a purge solenoid valve, hydrogen is momentarily purged through the anode to remove water and inert gases. Humidified air (generated using a membrane based internal humidifier) is mass flow controlled to a desired stoichiometric ratio. Deionized water is circulated through the system to remove heat produced due to the exothermic chemical reaction. A fan is used to thermostatically control (on-off) the stack outlet coolant to a desired temperature. Measurements of the dry gas mass flow rates supplied to the PEMFC stack are taken along with the temperature, pressure and relative humidity in the inlet and outlet manifolds.

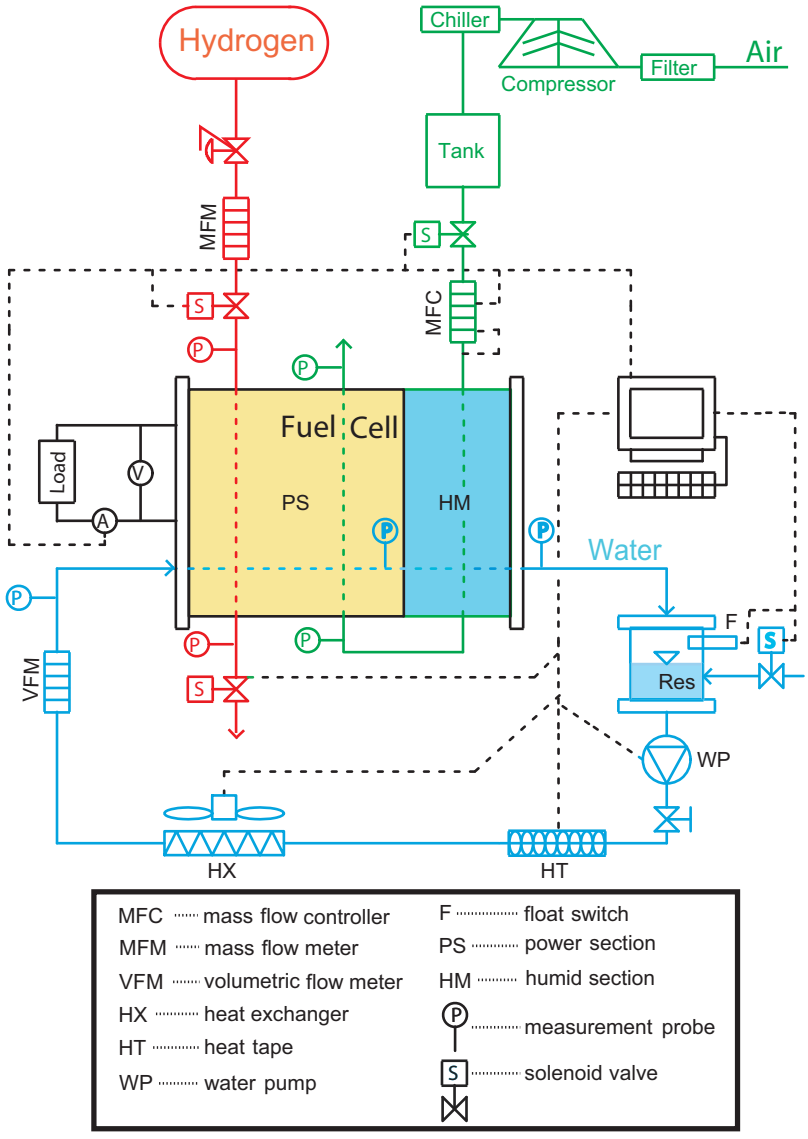

Figure 2.2 Experimental hardware employed and measurement locations. This figure is modified from [120].

Due to the lack of a practical means to directly measure the accumulation of liquid water within a multi-cell stack, consecutive anode purges and cathode surges (momentarily increasing the gas mass flow rates) are used to indicate the presence of liquid water in either the anode or cathode channels, as shown in Figure 2.3. At approximately 240 seconds the cathode is surged, causing an increase in oxygen partial pressure and cell voltage. However, this momentary voltage increase is not sustained following the surge and the general voltage decay due to flooding in the anode persists. Following an anode purge, the voltage quickly improves and then gradually decays until the next anode purge event is initiated. It is important to note that this gradual decay in cell voltage could be attributed to the accumulation of nitrogen in the anode which would also be expelled during and anode purge event. However, during purge events a significant mass of liquid water can be visually detected leaving the anode. Thus, this chapter focuses on the impact of anode flooding on cell voltage and assumes nitrogen is not the culprit.

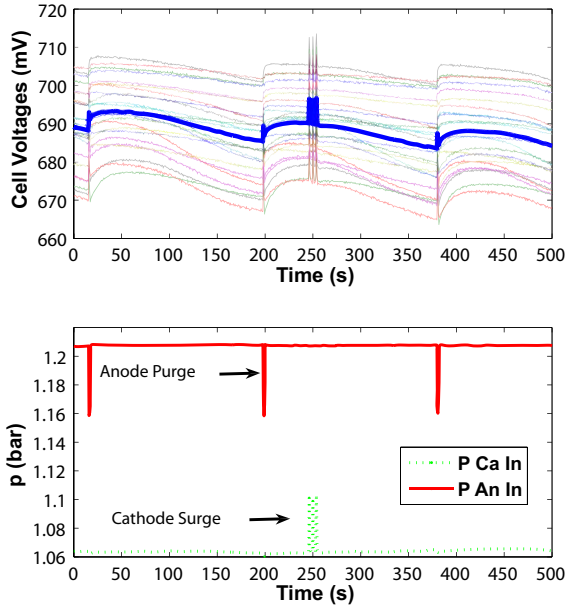

Figure 2.3 Experimental data showing impact of anode purging and cathode surging on cell voltages at a constant nominal current density of 0.3 A cm^{-2}, and an operating temperature of T=65^{o}C. The first subplot shows the 24 individual cell voltages in thin lines along with the average cell voltage with a thick line. The second subplot shows the anode and cathode inlet total pressures.

2.3 Modeling of Gas and Water Dynamics

The model of the reactant and water dynamics is presented in the following sections, describing the capillary transport of liquid water and the diffusion of gases within the GDL,

as well as the time varying boundary conditions at the membrane and gas channel interfaces. To approximate the spatial gradients, the gas diffusion layer is separated into discrete volumes using standard finite difference techniques.

The anode volume contains a mixture of hydrogen and water vapor, whereas the cathode volume contains a mixture of oxygen, nitrogen, and water vapor. The species concentrations in the channel are calculated based on the conservation of mass assuming the channel is homogeneous, lumped-parameter, and isothermal. It is assumed that product water is formed in the vapor phase.

This product water vapor, combined with the water vapor supplied with the cathode gas stream, is exchanged between the anode and the cathode through the hydrophilic membrane. The protons, liberated at the anode, transport water to the cathode through electro-osmotic drag, while back diffusion transfers vapor due to a water vapor concentration gradient across the membrane. The net flux of vapor through the membrane depends on the relative magnitudes of these transport mechanisms. Although there are many efforts to experimentally quantify back diffusion ([121], [122], [123], [124]), conflicting results suggest an empirically data-driven identification of water vapor diffusion might be a practical approach to this elusive subject. Constant parameters have been used to scale back diffusion models for PEMFCs with different membrane materials [118] [125]. Using a similar methodology as [118], in this chapter the membrane water transport algorithm employs a tunable parameter to scale the membrane water diffusion model in [122].

When the production or transport of water vapor overcomes the ability of the vapor to diffuse through the GDL to the channel, the vapor supersaturates and condenses. The condensed liquid water accumulates in the GDL until it has surpassed the immobile saturation limit, at which point capillary flow will carry the liquid water to an area of lower capillary pressure (the GDL-channel interface). Liquid water in the GDL occupies the pore space, reducing the diffusion of the reactant gases. However, the reduction of the reactant concentrations due to the changes in the gas diffusivity alone is not significant enough to degrade the voltage by the magnitude experimentally observed. Similar observations lead to the consideration of the reactant diffusion in the catalyst layer [126].

A different approach is used in this work. Instead of adding the complexity of the catalyst layer to the model, at low current density, channel plugging is hypothesized to impact cell voltage. Water covering the GDL surface reduces the area available for diffusion through the GDL. The water (in liquid and vapor phase) that wicks out of the hydrophobic GDL to the channel ultimately obstructs the area that reactants can diffuse through. This effect is not easily modeled because the GDL surface roughness makes it difficult to predict how much GDL surface area is blocked by a given volume of liquid water. For this

reason, it is assumed the liquid water at the GDL-channel interface forms a layer of uniform thickness. This water layer spreads across the surface of the GDL as the volume of liquid water in the channel increases. The resultant reduction in surface area increases the calculated current density, thereby lowering the cell voltage at a fixed total stack current. In this model, the thickness of the water layer, t_{wl}, is an experimentally tuned parameter.

The estimation of the average cell voltage is a function of the reactant concentrations at the surface of the membrane, the membrane water content, temperature, and the calculated current density based on the reduced active area, which in turn is a function of liquid water present in the gas channel. There are four experimentally tunable voltage parameters, $K_1 - K_4$, which are determined using linear least squares for a given set of membrane diffusion, α_w, and water thickness, t_{wl}, parameters. By comparing the average measured cell voltage to the model prediction, these parameters can be re-adjusted to match the rate of decay and magnitude of the voltage degradation. This iterative process allows all six tunable parameters to be identified.

2.3.1 Summary of Modeling Assumptions

In summary, the following assumptions are used in the model:

A1 The volume of liquid water within the GDL does not restrict the volume occupied by the gases. The authors in [127] indicated that the diffusion of gas through the GDL occurs through a hydrophobic macroporous structure, whereas the liquid water travels through the non-wet proofed pores (a microporous structure), implying that the pore volume occupied by gases is fixed. Examining the time scale decomposition of the reactant and water dynamics [128], this assumption primarily influences the liquid water dynamics and, due to the relatively small change in liquid water volume between the GDL sections, has a negligible impact. However, if different boundary conditions were applied which significantly modified the spatial distribution of liquid water in the GDL sections, this assumption should be revisited.

A2 The internal cell structure (gas channel, GDL and membrane) is isothermal and equal to the time varying coolant outlet temperature. However, the gas inlet temperatures may vary and are used to calculate the water vapor mass flow rates entrained with the supplied reactants. Although it is true that a multi-cell stack with a large active area will undoubtedly have thermal gradients within the cell structure and impact water transport [129], this assumption is adequate for estimating the temporal evolution in cell voltage experimentally observed under both flooding and drying conditions, as will be shown in Section 2.8. Accounting for dynamic thermal states within the gas diffusion layer adds a significant degree of model complexity which, while useful for design, may not be appropriate for control.

A3 The gas channels are treated as homogeneous lumped parameter volumes. Additionally, flow through the GDL is modeled in one dimension which neglects the

difference in transport mechanisms for flow under the ribs versus under the channels. Although models do exist which characterize all these complex phenomena, the inclusion of this additional dimension has a significant impact on the number of internal states in the model.

A4 Liquid water removal from the anode channel during purging is incorporated into the model via (5.31). It has been shown [22] that liquid water droplet instability and the resultant detachment from the GDL to the gas channel can be a significant liquid water removal mechanism at high current density (high gas velocity). Therefore, if this model is to be extended to high current density operation, this assumption should be revisited.

A5 All gases behave ideally. The range of system operating temperatures and pressures permits the assumption of ideal gas behavior for the gas constituents of interest.

A6 Hydrogen and oxygen molecules, which crossover through the membrane, are assumed to react in the opposing CL, contributing to the i_{loss} term in (2.37), and hence do not accumulate in the opposing channels. Crossover of nitrogen molecules is neglected in this work, but will be addressed in chapter 4. Where there is a concentration gradient across the membrane, nitrogen crossover can be modeled using a permeation rate [36]. The nitrogen diffusion in the GDL is not considered, because it is much faster than the permeation rate through the membrane.

A7 Due to the relatively small gas flux within the GDL at the current density range considered, the convective transport of gas due to bulk flow was neglected.

2.3.2 Nomenclature

This section describes the nomenclature used throughout this paper. A list of the parameters is provided in the Appendix, along with values and units. Time derivatives are denoted as $d(\,)/dt$. Spatial derivatives through the GDL thickness in the membrane direction (x) are denoted as $\partial(\,)/\partial x$. In the presented model, all equations have SI units of *Pa*, *N*, *m*, *kg*, *s*, and *J* unless explicitly stated.

The symbol a is used for water activity, c for molar concentration (mol/m^3), $\langle D \rangle$ for effective diffusivity (m^2/s), D_w for water vapor diffusion coefficient (m^2/s), E for the theoretical open circuit voltage (V), i for the nominal current density (A cm^{-2}), i_{app} for the apparent current density (A cm^{-2}), i_o for the exchange current density (A cm^{-2}), I for the total stack current (A), K_{rl} for relative permeability, n_d for electroosmotic drag coefficient (mol H_2O/ mol H$^+$), N for molar flux (mol/s/m^2), p for pressure (Pa), p_{sat} for the water vapor saturation pressure (Pa), R_{evap} for the evaporation rate (mol/s m^3), s for the fraction of liquid water volume to the total volume, S for the reduced liquid water saturation, T for temperature (K), U_{act} for the activation voltage loss (V), U_{ohmic} for the ohmic voltage loss (V), U_{conc} for the concentration voltage loss (V), $\bar{v}$ for the measured terminal cell voltage (V), $\hat{v}$ for the estimated terminal cell voltage (V), W for mass flow rate (kg/s), x for the mass

fraction, and y for the mole ratio. Greek letters are used where ε is for the GDL porosity, λ for membrane water content (mol H_2O/mol SO_3^-), ϕ for relative humidity (0-1), and ω for humidity ratio.

The subscript *amb* is used to represent ambient conditions, *an* for anode, *c* for capillary, *ca* for cathode, *ch* for channel, *ct* for catalyst, *da* for dry air, *dg* for dry gas, *e* for electrode (*an* or *ca*), fc for fuel cell stack, H_2 for hydrogen, *in* for the control volume inlet or input, j as an index for gas constituents, k as an index for discretization (in time or space), l for liquid water, *mb* for membrane, N_2 for nitrogen, O_2 for oxygen, *out* for the control volume outlet or output, p for pore, *rm* for return manifold, v for water vapor, and w for water (gas and/or liquid phase).

2.3.3 Membrane Water Transport

The membrane provides a barrier to keep the hydrogen and oxygen separated. It must conduct protons easily, yet be electronically insulating to force the electrons though an external circuit and provide useful work. The most common membrane material Nafion®, used in this work, is modeled widely in the literature. The membrane water content λ_{mb}, is defined as the number of moles of water per mole of SO_3H in the membrane. λ_{mb}, is a critical parameter for describing both proton transport, diffusion of water, electro-osmotic drag, and the permeation of molecular species though the membrane.

The distribution of membrane water content is described by a PDE, the divergence of the water flux though the membrane;

$$\frac{\partial \lambda_{mb}}{\partial t} = -\frac{EW}{\rho_{mb}} \frac{\partial N_{w,mb}}{\partial x}, \tag{2.1}$$

where $EW = 1100$ g mole^{-1} is the equivalent weight of the membrane and $\rho_{mb} = 1.9685$ g cm^{-3} is the membrane dry density. However, since the membrane is very thin, $\delta_{mb} = 25\ \mu$m, it can be discretized in space and represented by a single ODE.

Membrane water flux, $N_{w,mb}$ (mol cm^{-2}), from cathode to anode is calculated from the diffusion and electro-osmotic drag terms,

$$N_{w,mb} = -D_w(\lambda_{mb}, T) \frac{\partial \lambda_{mb}}{\partial x} - n_d(\lambda_{mb}, T) \frac{i_{fc}}{F}, \tag{2.2}$$

where $D_w(\lambda_{mb}, T)$ is the water diffusion coefficient for water in the membrane (5.14), and $n_d(\lambda_{mb})$ is the coefficient of electro-osmotic drag (5.17) [130]; both of which are λ_{mb} and T dependent and increase with both membrane water content and temperature.

The boundary conditions complete the description of transport in the membrane, coupling it with the GDL. Dirichlet boundary conditions are imposed for λ_{mb}, at the left and right edges of the membrane, assuming the membrane is at equilibrium with the water vapor vapor concentration in the GDL at the membrane surface, $c_{v,an}(0)$ and $c_{v,ca}(0)$. The equilibrium value, λ_{an}, is calculated using the membrane water uptake isotherm, $\lambda_{T,a}$ as shown in (5.10) [65, 130], and the water activity at the GDL-MB interface $a_{an,mb} = c_{v,an}(0)/c_{v,sat}$. The water flux leaving the membrane, $N_{w,mb}$ is the boundary condition for the GDL, as shown in (5.37). Due to the relative thickness of the membrane (i.e. extremely thin), it can be modeled as a resistance, and lumped into the boundary conditions of the GDL as discussed in Sec. 2.4.1

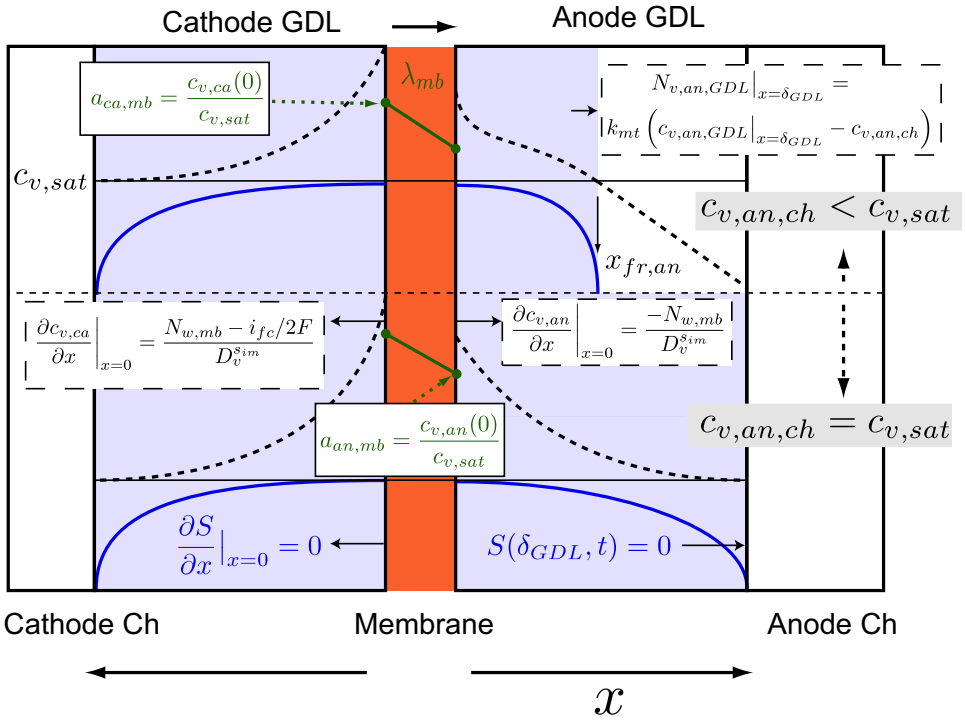

Figure 2.4 Water transport in the GDL and membrane. Dashed lines indicate the vapor distribution in the GDL, c_v, and solid blue lines represent the reduced water saturation, S. The boundary conditions for the PDE models are shown, and arrows indicate positive x-direction in each region. The water distributions are shown for two distinct cases; saturated (bottom half) and sub-saturated (top half) anode channel conditions. In the case of sub-saturated anode channel conditions, the transition between two phase (water liquid and vapor) and single phase (vapor only) is indicated by the front location, $x_{fr,an}$, as the point where $S \to 0$ in the GDL along the x-direction.

2.3.4 Liquid Water Capillary Transport

In hydrophobic GDL material as the GDL pore spaces fill with liquid water the capillary pressure increases causing the water to flow to adjacent pores with less water. This process creates a flow of liquid water through the GDL, resulting in an injection of liquid into the channel. The liquid water dynamics are calculated by applying conservation of mass to the GDL volume,

$$\frac{ds}{dt} = \left(\frac{1}{\rho_l \varepsilon A_{fc}}\right) \frac{\partial W_l}{\partial x} - \frac{r_v(c_{v,an}) M_v}{\rho_l} \,. \tag{2.3}$$

where the mass of liquid water in the GDL is expressed in terms of liquid water saturation, s, which represents the fraction of the liquid volume to the pore volume ($s = V_l/V_p$). W_l is the liquid water mass flow, $r_v(c_{v,an})$ is the molar evaporation rate, ,A_{fc} is the nominal fuel cell active area, ρ_l is the liquid water density, M_v is the molecular weight of water, and ε is the GDL porosity.

The flow of liquid water through the GDL is a function of the capillary pressure gradient ([71, 131]) described by

$$W_l = -\frac{\varepsilon A_{fc} \rho_l K K_{rl}}{\mu_l} \left(\frac{\partial p_c}{\partial S}\right) \left(\frac{\partial S}{\partial x}\right) \,, \tag{2.4}$$

where p_c is the liquid water capillary pressure, K is the absolute permeability, μ_l is the viscosity of liquid water, and $K_{rl} = S^3$ is the relative permeability of liquid water. The relative permeability function suggests more pathways for capillary flow are available as liquid water saturation increases, and is a function of the reduced liquid water saturation, S, shown by

$$S = \begin{cases} \dfrac{s - s_{im}}{1 - s_{im}} & \text{for} \quad s_{im} < s \leq 1 \\ 0 & \text{for} \quad 0 \leq s \leq s_{im} \end{cases} \,, \tag{2.5}$$

where, s_{im} is the value of the immobile saturation describing the point at which the liquid water path becomes discontinuous and interrupts capillary flow. This capillary flow interruption occurs when $s < s_{im}$. The results of capillary flow experiments using glass beads as porous media show that $s_{im} = 0.1$ [71].

Capillary pressure is the surface tension of the water droplet integrated over the surface area. The Leverett J-function describes the relationship between capillary pressure and the reduced water saturation, S,

$$p_c = \frac{\sigma \cos\theta_c}{\sqrt{K/\varepsilon}} \underbrace{\left[1.417S - 2.120S^2 + 1.263S^3\right]}_{J(S)} \,, \tag{2.6}$$

where σ is the surface tension between water and air, and θ_c is the contact angle of the water droplet [71]. Other, more recent, capillary pressure models can be found in [72, 73, 75].

The liquid and vapor PDEs (2.3)-(2.11) are coupled through the molar evaporation rate,

$$r_v(c_{v,an}) = \begin{cases} \gamma(c_{v,sat}(T) - c_{v,an}) & \text{for } s > 0, \\ \min\{0, \gamma(c_{v,sat}(T) - c_{v,an})\} & \text{for } s = 0 \end{cases} \tag{2.7}$$

where γ is the volumetric condensation coefficient[71], $c_{v,sat}(T)$ is the vapor saturation concentration and $c_{v,an} = p_v/RT$ is the vapor concentration in the GDL. R is the ideal gas constant, T is temperature, and p_v is the water vapor partial pressure. When the partial pressure of water vapor is greater than the saturation pressure, r_v is negative, representing the condensation of water. A logical constraint must be included such that if no liquid water is present ($s \leq 0$)) and the saturation pressure is greater than the water vapor pressure, then water can not be evaporated ($r_v = 0$).

2.3.5 Gas Species Diffusion

The diffusion of gas species in the GDL is a function of the concentration gradient, transferring gas from regions of higher concentration to regions of lower concentration. The molar concentration of gas species j is denoted c_j and is a function of the number of moles of gas within the pore volume, V_p, where

$$c_j = \frac{p_j}{RT} \, . \tag{2.8}$$

Diffusion of hydrogen and water vapor occurs in the anode GDL and the diffusion of oxygen and water vapor occurs in the cathode GDL. As a result, both the anode and cathode gas diffusion can be modeled assuming binary diffusion. It is important to note that nitrogen gas is present in the cathode. The nitrogen concentration in the channel is modeled as a dynamic state, however, the concentration of nitrogen in the GDL is assumed to be equal to the channel value. A constant nitrogen profile across the GDL is reasonable since it is not involved in the reaction at the catalyst layer. Ternary diffusion must be assumed at both the anode and the cathode if nitrogen cross-over were to be considered. The total molar flux is related to the concentration gradient, represented by

$$N_j = -\langle D_j \rangle \frac{\partial c_j}{\partial x} \, , \tag{2.9}$$

where $\langle D_j \rangle$ is the effective diffusivity of the gas constituents in the GDL,

$$\langle D_j \rangle = D_j \varepsilon \left(\frac{\varepsilon - 0.11}{1 - 0.11} \right)^{0.785} (1-s)^2 \,, \tag{2.10}$$

for two dimensional bulk diffusion with flow perpendicular to the GDL carbon fibers, where D_j is the gas diffusion coefficient. Porosity, effective diffusivity and liquid water saturation for carbon Toray® paper GDL, are modeled from [71].

Finally, the general temporal derivative of gas concentration as a function of the local molar flux gradient and the local reaction rate, R_j, of the particular gas species forms a partial differential equation (PDE),

$$\frac{dc_j}{dt} = \frac{\partial N_j}{\partial x} + R_j \,. \tag{2.11}$$

where (2.9-2.11) are combined to yield a second order PDE.

2.4 Boundary Conditions

The membrane and gas channels serve as time-varying boundary conditions for the GDL model. This section presents the application of mass conservation in the channel as well as the model for the water vapor exchange between the anode and cathode through the membrane. It is important to remember that the spatial gradients within the GDL are approximated with finite difference equations. A variable taken from a GDL section that is adjacent to the boundary of interest will be denoted by $\psi(1)$ or $\psi(L)$, where $(L = 3)$ indicates the section next to the gas channel and (1) indicates the section next to the membrane.

Each gas diffusion layer is separated into (L=3) discrete volumes, shown in Figure 2.5, to approximate the solution of (2.3) and (2.11) for each of the constituents in the GDL. Spatial discretization of the GDL yields eighteen coupled ordinary differential equations (ODEs), describing the gas constituent concentrations and liquid water saturation, that approximate the solution of the original PDEs.

2.4.1 Membrane Boundary Conditions

The reaction at the catalyst surface of the membrane results in a loss of hydrogen and oxygen at the anode and cathode, respectively. These fluxes, $N_{j,e}(0)$, are used in the calculation

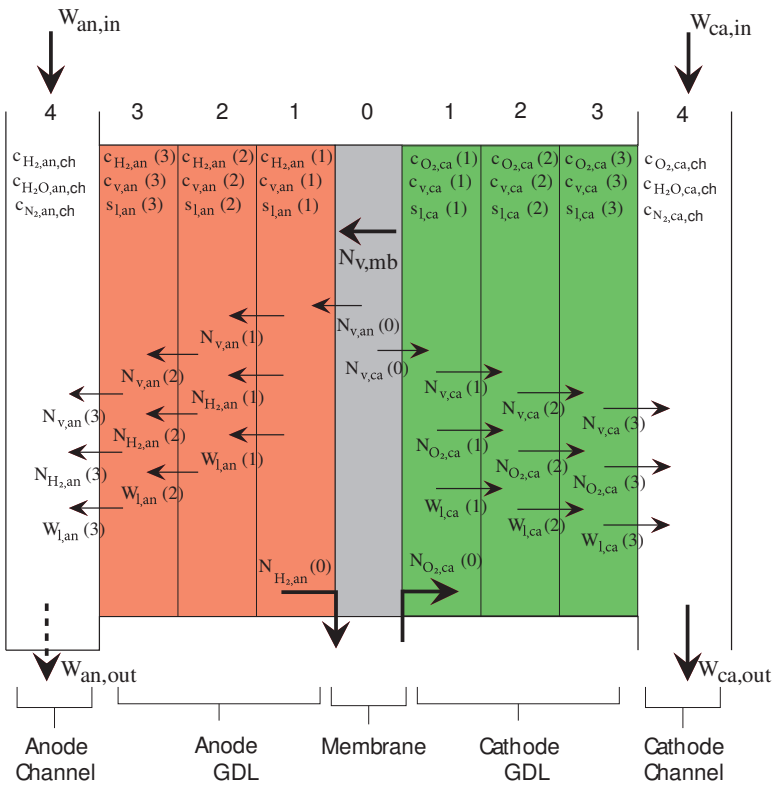

Figure 2.5 Discretization of the gas diffusion layers. The direction of the assumed mass flow rate is indicated with a solid arrow. The dashed arrow is used to indicate periodic mass flow rates. Note the swapped direction of transport for the Anode GDL and membrane from [65], to be consistent with rest of thesis.

of the molar flux spatial gradients, described by:

$$N_{j,e}(0) = \frac{I}{\varepsilon A_{fc} 2\xi F} \text{ with } \begin{cases} \xi = 1 & \text{for } j = H_2 \\ \xi = 2 & \text{for } j = O_2 \end{cases} \tag{2.12}$$

where I is the total current drawn from the stack and F is the Faraday constant. The molar flux of water vapor at the GDL-membrane boundary, $N_{v,e}(0)$, is influenced by the generation of water vapor at the cathode membrane surface as well as the flow of water vapor through the membrane.

$$N_{v,an}(0) = \frac{1}{\varepsilon} N_{v,mb} \tag{2.13a}$$

$$N_{v,ca}(0) = \frac{1}{\varepsilon}\left(\frac{I}{2FA_{fc}} + N_{v,mb}\right) \tag{2.13b}$$

Note, a constant scaling factor of $1/\varepsilon$ is used here to ensure that the water vapor mass flow rate through the membrane is equal to the mass flow rate entering the GDL at the membrane

boundary.

The water content of the membrane influences the membrane vapor transport which establishes a time-varying boundary condition for both the anode and the cathode. These membrane properties, described in [121], are assumed to be invariant across the membrane surface. The spatial variation of water vapor throughout the membrane is neglected due to the significant difference in thickness between the GDL (432 μm) and the membrane (35 μm). It is important to note that the membrane transport properties presented in this section are taken from experimental work conducted at steady-state. Non steady-state phenomena, such as membrane swelling and hysteresis, could be added in the future to improve model fidelity.

As with the other volumes, the membrane is considered to be homogeneous and lumped parameter. The flux of water vapor through the membrane, $N_{v,mb}$, accounts for the effects of both back-diffusion and electro-osmotic drag, suggested by [121],

$$N_{v,mb} = n_d \frac{i}{F} - \alpha_w D_w \frac{(c_{v,ca,mb} - c_{v,an,mb})}{t_{mb}}, \tag{2.14}$$

where i is the nominal fuel cell current density (I/A_{fc}), n_d is the electro-osmotic drag coefficient, D_w is the membrane water vapor diffusion coefficient, and t_{mb} is the membrane thickness. The parameter α_w is a tunable parameter that will be identified using experimental data. The convective water transport mechanisms suggested in [129, 100, 132] are neglected due to the relatively small water pressure gradients at these operating conditions.

The electro-osmotic drag coefficient, described by [121], is calculated using:

$$n_d = \frac{2.5\lambda_{mb}}{22} \quad . \tag{2.15}$$

where the membrane water content, λ_{mb} is defined as the ratio of water molecules to the number of charge sites.

The water vapor concentration in the electrode at the membrane surface is:

$$c_{v,e,mb} = \frac{\rho_{mb,dry}}{M_{mb,dry}} \lambda_e \tag{2.16}$$

where $\rho_{mb,dry}$ is the membrane dry density, $M_{mb,dry}$ is the membrane dry equivalent weight, and λ_e is the membrane water content at the surface of the membrane next to either the anode or cathode GDL.

The water vapor diffusion coefficient for a perflourinated ionomeric membrane, Nafion® 117, was determined at 25^{o}C by [122] by applying a mass balance to determine

the water vapor flux through the membrane, resulting in

$$D_w = 3.5 \times 10^{-6} \left(\frac{\lambda_{mb}}{14} \right) exp \left[\frac{-2436}{T} \right]. \tag{2.17}$$

Two different cubic polynomials were presented by [121] and [133] to relate water activity to membrane water content at 30^{o}C and 80^{o}C, shown as

$$\lambda_j^{30^oC} = 0.043 + 17.81 a_j - 39.85 a_j^2 + 36.0 a_j^3 \tag{2.18a}$$

$$\lambda_j^{80^oC} = 0.300 + 10.8 a_j - 16.0 a_j^2 + 14.1 a_j^3 \tag{2.18b}$$

where a is the water activity and the subscript j is used here to distinguish between the anode or cathode membrane surface and within the membrane itself, $j \in \{an,\ ca,\ mb\}$. To estimate the water content at intermediate temperatures and sub-saturated conditions, [134] suggested a linear interpolation between the two uptake isotherms shown in (2.18), such that

$$\lambda_j = \left(\lambda_j^{80^oC} - \lambda_j^{30^oC} \right) \left(\frac{T - 303}{353 - 303} \right) + \lambda_j^{30^oC} \ . \tag{2.19}$$

It is important to note that these two uptake isotherms are applicable only when water is in the vapor phase ($a_j \leq 1$).

In [121] it was shown that a membrane equilibrated with liquid water has a water content of λ=16.8 at 80^{o}C, which differs from the water content when the membrane is equilibrated with a saturated vapor. It was further indicated that the water content is sensitive to temperature when equilibrated with liquid water, but assumed to be a linear relationship between [λ=14,a=1] and [λ=16.8,a=3] regardless of temperature, due to a lack of data regarding the membrane equilibration for water in both the liquid and vapor phase. Similarly, a linear relationship is assumed between the membrane water content when equilibrated with water vapor, shown in (2.19) for a_j=1, and the value of $\lambda = 16.8$ at a=3 published by [121], such that

$$\lambda_j = \left(\frac{16.8 - \lambda_j^{a=1}}{3 - 1} \right) (a_j - 1) + \lambda_j^{a=1} \tag{2.20}$$

for $1 < a_j < 3$. Further experimental results from [135] and [133] provided data regarding the temperature sensitivity of the membrane water content equilibrated with liquid water. The membrane water activity is assumed to be the average between the anode and cathode water activities (defined by the GDL sections closest to the membrane surface), described

by:

$$a_{mb} = \frac{a_{an}(1) + a_{ca}(1)}{2} \text{ and } a_e(1) = \frac{p_{v,e}(1)}{p_{sat}}. \tag{2.21}$$

where $p_{v,e}(1)$ is the water vapor pressure in the GDL layer next to the membrane, calculated using the water vapor concentrations.

It is assumed that reactant molecules do not transfer through the membrane between the anode and the cathode. Additionally, only water vapor can penetrate the membrane, not liquid water, implying $W_{l,e}(0) = 0$.

In summary, the water vapor partial pressures in the GDL section closest to the membrane surfaces are used to determine the water activity in the first GDL section, which is assumed to be equal to the membrane water activity at the membrane-GDL interface. These two membrane water activities are averaged to calculate the lumped membrane water activity. The lumped membrane water activity is then used to calculate the diffusion and electro-osmotic drag coefficients. Finally, the net water vapor flux is calculated, given diffusion, drag and the water vapor concentrations at the membrane surfaces.

2.4.2 Boundary Conditions at the Cathode Channel

The concentration of oxygen and water vapor in the cathode channels, $c_{O_2,ca}(L+1)$ and $c_{v,ca}(L+1)$, are used for the calculation of the gas concentration gradient for the GDL section next to the channels, $\frac{\partial c_{j,ca}}{\partial x}(L)$. Mass conservation for the gas species in the cathode is applied using the cathode inlet conditions as inputs, requiring measurements of the dry air mass flow rate, $W_{da,ca,in}$, temperature, $T_{ca,in}$, total gas pressure, $p_{ca,in}$, and humidity, $\phi_{ca,in}$, along with the cathode outlet pressure, $p_{ca,out}$. After completing several experiments under a range mass flow rates and temperatures, it was found that the cathode inlet total gas flow was fully humidified and the cathode outlet total pressure was approximately atmospheric, motivating the assumptions that $\phi_{ca,in}$=1 and $p_{ca,out}$=p_{atm}.

The mass flow rates of the individual gas species supplied to the cathode channel are calculated as follows:

$$\begin{aligned} W_{O_2,ca,in} &= x_{O_2,ca,in} W_{da,ca,in}, \\ W_{N_2,ca,in} &= x_{N_2,ca,in} W_{da,ca,in}, \\ W_{v,ca,in} &= \omega_{ca,in} W_{da,ca,in}, \end{aligned} \tag{2.22}$$

where the humidity ratio, ω, is generally defined by

$$\omega = \frac{M_v}{M_{dg}} \frac{\phi p_{sat}}{p - \phi p_{sat}} \tag{2.23}$$

for a gas-water vapor mixture, with the mass fraction of oxygen and nitrogen in the dry air (da) defined as $x_{O_2} = y_{O_2} M_{O_2}/M_{da}$ and $x_{N_2} = (1-y_{O_2})M_{N_2}/M_{da}$, where $M_{da} = y_{O_2} M_{O_2} + (1-y_{O_2})M_{N_2}$ and y_{O_2} is the oxygen mole fraction in dry air.

The gas species masses in the cathode channel are balanced by applying mass continuity:

$$\begin{array}{ll} \frac{dm_{O_2,ca}(L+1)}{dt} & = W_{O_2,ca,in} - W_{O_2,ca,out} + W_{O_2,ca}(L), \\ \frac{dm_{N_2,ca}(L+1)}{dt} & = W_{N_2,ca,in} - W_{N_2,ca,out}, \\ \frac{dm_{w,ca}(L+1)}{dt} & = W_{v,ca,in} - W_{v,ca,out} + W_{w,ca}(L). \end{array} \tag{2.24}$$

The cathode channel pressure is calculated applying Dalton's law such that

$$p_{ca}(L+1) = \underbrace{\frac{RT}{V_{ca}}\left(\frac{m_{O_2,ca}(L+1)}{M_{O_2}} + \frac{m_{N_2,ca}(L+1)}{M_{N_2}}\right)}_{p_{dg,ca}(L+1)} + \underbrace{\min\left[p_{sat}, \frac{RT m_{w,ca}(L+1)}{M_v V_{ca}}\right]}_{p_{v,ca}(L+1)}. \tag{2.25}$$

Although in the physical system the cathode air mass flow rate may be responsible for removing some liquid water from the cathode channel, for modeling purposes it is assumed that all water exiting the cathode is in the form of vapor.

The mass flow rates of the gases exiting the cathode are calculated as:

$$\begin{array}{ll} W_{ca,out} & = k_{ca}(p_{ca}(L+1) - p_{ca,out}), \\ W_{da,ca,out} & = \frac{1}{1+\omega_{ca,out}} W_{ca,out}, \\ W_{O_2,ca,out} & = x_{O_2,ca,ch} W_{da,ca,out}, \\ W_{v,ca,out} & = W_{ca,out} - W_{a,ca,out}, \\ W_{N_2,ca,out} & = (1-x_{O_2,ca}) W_{da,ca,out}, \end{array} \tag{2.26}$$

where k_{ca} is an orifice constant found experimentally. Although the mole fraction of oxygen at the cathode inlet is assumed to be constant, $y_{O_2,ca,in} = 0.21$, the mole fraction of oxygen in the channel (driving the outlet mass flow rates) is dependent upon the oxygen mass (pressure) state in the channel, such that $y_{O_2,ca} = p_{O_2,ca}/p_{ca}$.

Finally, the oxygen and total water mass flow rates between the GDL and the channel, $W_{O_2,ca}(L)$ and $W_{w,ca}(L)$, are calculated to solve the mass conservation equations shown in (2.24). The oxygen mass flow through the GDL-channel interface is a function of the oxygen molar flux, $N_{O_2}(L)$. The total water mass flow rate, $W_{w,ca}(L)$, exchanged between the GDL and channel is a function of the liquid water mass flow, $W_{l,ca}(L)$, and the water vapor

flux, $N_{v,ca}$. Both the oxygen and total water mass flow rates are described by,

$$\begin{aligned} W_{O_2,ca}(L) &= N_{O_2}(L) M_{O_2} \varepsilon A_{fc} n_{cells}, \\ W_{w,ca}(L) &= \left(W_{l,ca}(L) + N_{v,ca}(L) M_v \varepsilon A_{fc}\right) n_{cells}\ , \end{aligned} \tag{2.27}$$

where the assumption $S_{ca}(L+1) = 0$ is employed in the calculation of the reduced water saturation gradient to determine the liquid water mass flow rate between the GDL-channel interface, $W_{l,ca}(L)$. Within the channel, the volume of liquid water is assumed to be negligible compared with the total channel volume, motivating this assumption that $S_{ca}(L+1)$ =0.

2.4.3 Boundary Conditions at the Anode Channel

Similarly to the cathode, the inputs for the anode calculations are the measured anode inlet conditions including the dry hydrogen mass flow rate, $W_{H_2,an,in}$, the supply manifold temperature, $T_{an,in}$, the total pressure, $p_{an,in}$, and the relative humidity, $\phi_{an,in}$. Dry hydrogen is supplied to the anode, as a result $\phi_{an,in}$= 0. The resulting mass balances for hydrogen and water are

$$\begin{aligned} \frac{dm_{H_2,an}(L+1)}{dt} &= W_{H_2,an,in} - W_{H_2,an,out} - W_{H_2,an}(L), \\ \frac{dm_{w,an}(L+1)}{dt} &= W_{v,an,in} - W_{v,an,out} - W_{w,an}(L). \end{aligned} \tag{2.28}$$

The dry hydrogen inlet mass flow rate, $W_{H_2,an,in} = k_{an,in}(p_{an,in} - p_{an}(L+1))$, is controlled with a pressure regulator to maintain a constant anode inlet total pressure. Because the hydrogen supplied to the anode is dry, the vapor mass flow rate is assumed to be zero ($W_{v,an,in}$= 0). In calculating the anode total channel pressure, both the partial pressures of hydrogen and water vapor must be estimated such that,

$$p_{an}(L+1) = \underbrace{\frac{RT}{M_{H_2} V_{an}} m_{H_2}(L+1)}_{p_{H_2,an}(L+1)} + \underbrace{\min\left[p_{sat}, \frac{RT m_{w,an}(L+1)}{M_v V_{an}}\right]}_{p_{v,an}(L+1)}. \tag{2.29}$$

The total mass flow rate leaving the anode channel, $W_{an,out}$, exists only during an anode gas purge to remove both water, and unfortunately, hydrogen. The equations quantifying the hydrogen and water vapor mass flow rates leaving the anode channel are expressed as:

$$\begin{aligned} W_{an,out} &= k_{an,out}(p_{an}(L+1) - p_{an,out}), \\ W_{H_2,an,out} &= \frac{1}{1+\omega_{an,out}} W_{an,out}, \\ W_{v,an,out} &= W_{an,out} - W_{H_2,an,out}. \end{aligned} \tag{2.30}$$

Similarly to the cathode, the gas and liquid water mass flow rates between the GDL and channel are calculated by

$$\begin{aligned} W_{H_2,an}(L) &= N_{H_2}(L) M_{H_2} \varepsilon A_{fc} n_{cells}, \\ W_{w,an}(L) &= \left(W_{l,an}(L) + N_{v,an}(L) M_v \varepsilon A_{fc} \right) n_{cells}. \end{aligned} \tag{2.31}$$

where the assumption $S_{an}(L+1) = 0$ is employed in the calculation of the reduced water saturation gradient to determine the liquid water mass flow rate between the GDL-channel interface, $W_{l,an}(L)$.

The calculation of the mass flow rates leaving the anode channel depends on the measurement of the anode outlet total pressure, $p_{an,out}$, shown in (2.30). The anode outlet pressure can also be estimated using a similar approach as presented for the anode channel and documented in [117], where $W_{an,rm} = k_{an,rm}(p_{an,out} - p_{amb})$, resulting in the addition of two states (hydrogen and water mass in the return manifold).

2.5 Output Voltage Equation

In this section, the voltage equation is presented as a mapping from the apparent current density, reactant concentrations, temperature and membrane humidity conditions. All units for current density used throughout the presentation of the voltage model are given in A cm^{-2} for consistency with other published models.

Once anode flooding occurs, the resulting voltage degradation is associated with the accumulation of liquid water mass in the anode channel,

$$m_{l,an}(L+1) = max\left[0, m_{w,an}(L+1) - \frac{p_{sat} M_v V_{an}}{RT}\right], \tag{2.32}$$

where the mass of water in the anode channel, $m_{w,an}(L+1)$, is taken from (2.28). The accumulated liquid water mass is assumed to form a thin film of thickness, t_{wl}, blocking part of the active fuel cell area, A_{fc}, and consequently increasing the apparent current density [111],

$$i_{app}\left(\frac{A}{cm^2}\right) = \frac{I(A)}{10000 A_{app}(m^2)}, \tag{2.33}$$

where the apparent fuel cell area A_{app} is approximated as

$$A_{app} = A_{fc} - \frac{2\, m_{l,an}(L+1)}{n_{cells}\, \rho_l\, t_{wl}}. \tag{2.34}$$

The scaling factor of 2 in (2.34) was used to account for the fact that one half of the surface area at the GDL-channel interface is occupied by channel ribs, which reduces the area available for the formation of a liquid water film. This methodology for relating the accumulation of the liquid water in the channel to a restricted active area was first proposed in [111] and a similar methodology was employed by [119]. Some models that deal with cathode flooding, however, propose an increased current density due to the water accumulation in the catalyst layer at the GDL-membrane interface [136]. Ongoing experimental work from many researchers has focused on quantifying this accumulation of liquid water using direct visualization [137] or neutron imaging techniques [98, 99, 48].

The thickness of this water layer, t_{wl} is a tunable parameter that impacts the rate at which the active area is reduced and in turn the rate of voltage decay as the liquid water accumulates. Note that the notion of apparent current density, influenced by t_{wl} in the gas channel, is a simplification of the flooding phenomenon that nevertheless captures the experimentally observed dynamic voltage behavior of a multi-cell stack under a range of conditions including both flooding and non-flooding. As shown in Section 2.7, this tuned parameter is similar to that experimentally determined in [99].

Once the apparent current density is calculated it is used, together with the partial pressure of the reactants in the anode and cathode GDL sections next to the membrane, to determine the average cell voltage. The average cell voltage, v, is equal to the theoretical open circuit voltage, E, minus the activation, U_{act}, and ohmic, U_{ohmic}, losses such that

$$v = E - U_{act} - U_{ohmic} \, . \tag{2.35}$$

It is assumed that the concentration voltage loss due to a mass transport limitation at high current density is negligible as a result of operation at relatively low current densities ($i < 0.4$ A cm^{-2}).

The theoretical open circuit voltage, if the chemical reaction were a reversible process, varies with respect to reactant partial pressures and temperature according to the change in Gibbs free energy and the Nernst Equation [13],

$$E = -\left(\frac{\Delta H}{2F} - \frac{T\Delta S}{2F}\right) + \frac{RT}{2F} \ln\left(\frac{p_{H_2,an}(1)\sqrt{p_{O_2,ca}(1)}}{(p_o)^{1.5}}\right) \tag{2.36}$$

where ΔS and ΔH are the differences in entropy and enthalpy from standard state conditions, p_o is the standard pressure, and the oxygen and hydrogen partial pressures, $p_{O_2,ca}(1)$ and $p_{H_2,an}(1)$, are located in GDL Section 1 next to the membrane.

The activation overvoltage accounts for the energy required to drive the chemical reaction (a deviation from equilibrium), as well as the loss current density resulting from the transport of molecular hydrogen from the anode to the cathode through the membrane. The total activation voltage loss was parameterized according to [138], such that

$$U_{act} = K_1 \frac{RT}{F} \ln\left(\frac{i_{app} + i_{loss}}{i_o}\right), \tag{2.37}$$

where K_1 is a tunable parameter representing the reciprocal of the charge transfer coefficient, i_{loss} is the loss current density due to hydrogen crossover, i_{app} is the apparent current density that is a function of the reduced active area due to the accumulation of liquid water at the GDL-channel interface from (2.33), and i_o is the exchange current density which is a function of the reactant partial pressure and temperature [138], expressed as

$$i_0 = K_2 \left(\frac{p_{O_2,ca}(1)}{p_o}\right)^{K_3} \exp\left[-\frac{E_c}{RT}\left(1 - \frac{T}{T_o}\right)\right], \tag{2.38}$$

where K_2 and K_3 are tunable parameters, E_c is the activation energy for oxygen reduction on Pt, and T_o is the reference temperature.

The ohmic voltage loss is dominated by the membrane conductivity as well as the contact and bulk electrical resistance of the conductive materials. This loss was shown experimentally in [121] to have the following functional form,

$$U_{ohmic} = K_4 \left[\frac{t_{mb}}{(b_{11}\lambda_{mb} - b_{12})} e^{-1268\left(\frac{1}{303} - \frac{1}{T}\right)}\right] i_{app}, \tag{2.39}$$

where K_4 is a tunable parameter, t_{mb} is the membrane thickness, b_{11} and b_{12} are experimentally identified parameters from [121], and λ_{mb} is the membrane water content from (2.18-2.20).

2.6 Parameter Identification Approach

Lacking a practical experimental means to measure the spatial distribution of water mass in the anode and cathode of a large multi-cell stack for the use of on-line control, the lumped-parameter two-phase flow model developed here is indirectly calibrated and validated through model prediction of the effects of flooding on cell voltage. A reasonably wide variation in the experimental operating conditions has been examined, including both flooding and non-flooding conditions, to ensure that the model adequately estimates the

relationship between GDL flooding and cell voltage degradation. The range of operating conditions examined is limited due to operation with a stack, not a single cell, and the desire to minimize cell to cell voltage variations [120].

There are two sets of model parameters which must be either calibrated or tuned. The calibrated parameters are based on the fuel cell hardware specifications and are listed in Table 2.1 with values provided in the Appendix. These parameters may require additional experiments to determine, such as the orifice constants describing the back pressure flow characteristics for each gas channel.

Table 2.1 Parameters required based on PEMFC stack specifications.

* Note: values for these parameters are provided in the Appendix.

A_{fc}	Fuel cell nominal active area
K	Absolute permeability
$M_{m,dry}$	Membrane dry equivalent weight
n	Number of cells in the stack
t_{gdl}	GDL thickness
t_{mb}	Membrane thickness
V_{an}	Total anode channel volume
V_{ca}	Total cathode channel volume
ε	GDL porosity
$\rho_{m,dry}$	Membrane dry density
k_{an}	Anode orifice constants
k_{ca}	Cathode orifice constants

The two water related tunable parameters that require experimental identification are the scaled "stack-level" membrane back diffusion, α_w in (2.14) and thickness of liquid water layer accumulating at the GDL-channel interface, t_{wl} in (2.34). Additionally, there are four tunable parameters K_1-K_4 associated with the output voltage in (2.35-2.39). Although the water related parameters do not appear linearly, the voltage equation can be rearranged such that each of the tunable K's is linear in the coefficient,

$$\begin{aligned}\hat{v} =& E - K_1 \frac{R\,T}{F}\left(\ln\left(i_{app}+i_{loss}\right)+\frac{E_c}{R}\left(\frac{1}{T}-\frac{1}{T_0}\right)\right)\\ &+\ln\left(K_2\right)K_1\frac{R\,T}{F}+K_3\,K_1\frac{R\,T}{F}\,\ln\left(\frac{p_{O_2,ca}(1)}{p_0}\right)\\ &-K_4\left[\frac{t_{mb}}{\left(b_{11}\lambda_{mb}-b_{12}\right)}e^{-1268\left(\frac{1}{303}-\frac{1}{T}\right)}\right]\left(i_{app}+i_{loss}\right)\ . \end{aligned} \tag{2.40}$$

Given a set of values for α_w and t_{wl}, the voltage parameters are identified using linear

least squares to minimize the difference between the measured average cell voltage, $\overline{v}$, and the modeled cell voltage, $\hat{v}$,

$$J = \int^{t_{exp}} [\overline{v}(\tau) - \hat{v}(\tau)]^T [\overline{v}(\tau) - \hat{v}(\tau)] \, d\tau \,, \tag{2.41}$$

over the experimental testing time, t_{exp}. The statistics associated with the estimation error are examined over a range of $[\alpha_w, t_{wl}]$ pairs to find the locally optimal $[\alpha_w, t_{wl}]$ combination and the resulting K values.

Note here, there are 24 individual cell voltages being measured. The average and median cell voltages exhibit similar dynamics with a relatively small difference in voltage between them. However, there is a significant difference in the magnitude and deviation between the minimum and maximum cell voltages. As a result, the use of either the minimum or maximum cell voltages for parameter tuning results in an underestimation or overestimation of the degree of flooding. For these reasons, the average cell voltage is used for model tuning.

2.7 Model Calibration

Experimental calibration data are collected for a range of nominal stack current densities from i=0-300 mA cm^{-2}, air stoichiometries of 250% and 300%, and coolant outlet temperatures from 45-63^{o}C, at an anode inlet total pressure of 1.2 bar, as shown in Figure 2.6. A polarization curve (I-V) is conducted at approximately 70 minutes, at which time the purge events are temporarily disabled.

The purge events were scheduled to occur every 180 seconds for a duration of 1 second. During purge events, the purge solenoid valve is momentarily opened, exposing the anode outlet manifold to ambient pressure. As a result of this decreased anode total pressure, the manual pressure regulator, which tries to maintain its downstream pressure, increases the hydrogen mass flow rate through the system. Following the closure of the purge solenoid valve, small spikes in pressure occur as the pressure regulator readjusts its delivery pressure.

As shown in Figure 2.6, the initial coolant outlet temperature setpoint is 50^{o}C and then changes to 60^{o}C at approximately 185 minutes. Thermostatic controllers are used to control the heat exchanger fans to regulate the coolant outlet temperature. As these fans are cycled, oscillations in temperature are induced.

The standard deviation in the cell voltage measurements is greater at high current density (300 mA cm^{-2}) than at low current density [120]. This increased uncertainty at high

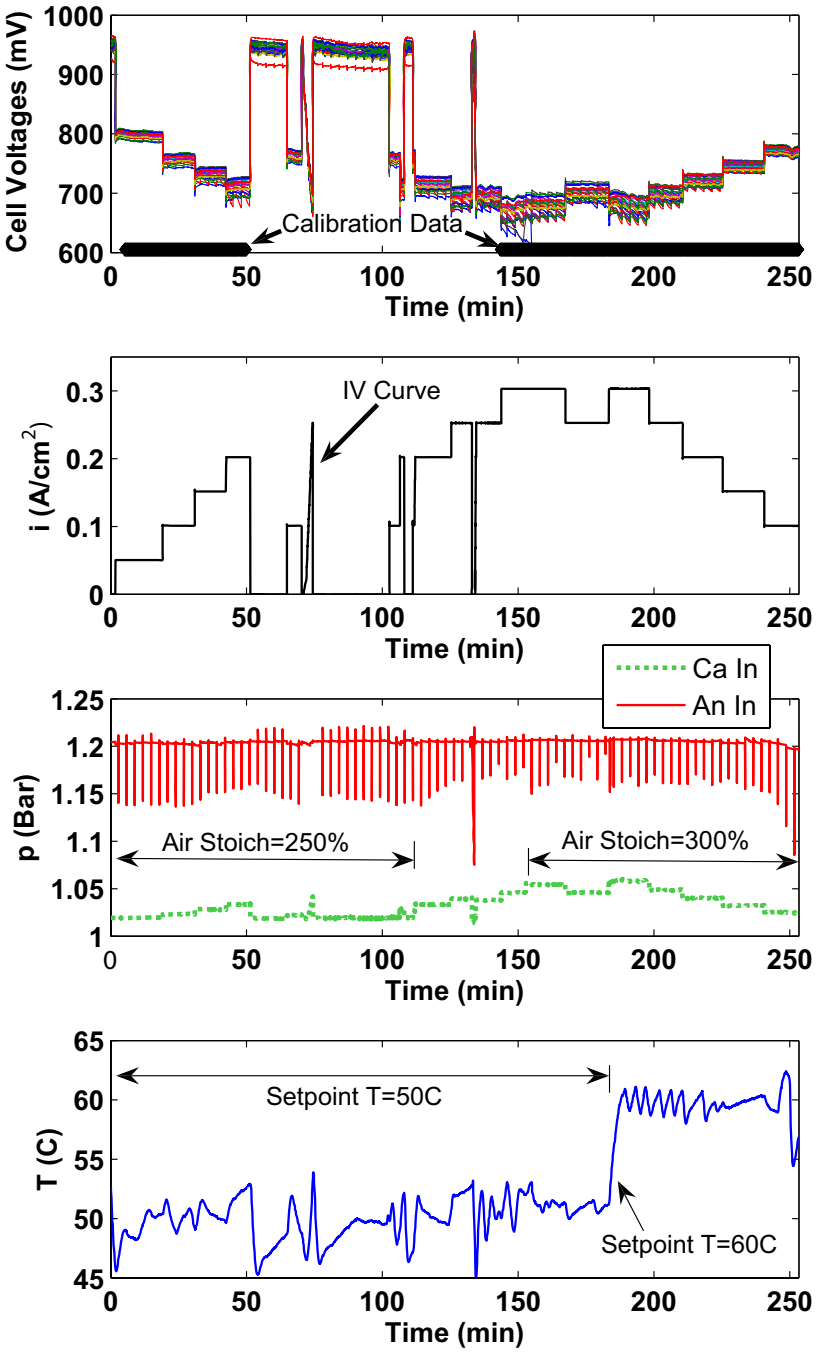

Figure 2.6 Experimental measurements used for model calibration. The first subplot shows the 24 individual cell voltages along with black dots at 600 mV which illustrate the portions of the data set used for calibration. The second subplot shows the nominal current density. The third subplot is the anode and cathode inlet total pressures. The fourth subplot is the temperature of the water coolant leaving the stack.

current density, seen in Figure 2.6, is due to both the increased difference in the cell to cell voltage variation as well as the increased excursions in cell voltage between anode purges.

Moreover, at high current density the cell with the minimum voltage exhibits greater voltage excursions between anode purges than the cell with the maximum voltage. However, the mean and median voltages have similar dynamic and steady-state responses.

For the purposes of model calibration, a portion of the calibration data set is selected to include a range of both transient and "steady-state" operating conditions. This portion of data is indicated with a black *x* in the voltage plot shown in Figure 2.6. Data at open-circuit are avoided due to the high uncertainty associated with operation at open-circuit voltage [120]. The identified parameters resulting in the smallest mean, maximum and standard deviation in the estimation error over the set of $\alpha_w \in$[7,12] and $t_{wl} \in$[0.12mm,0.14mm], while still capturing the voltage response during flooding conditions, are shown in Table 2.2.

Table 2.2 Experimentally identified parameter values for PEMFC stack

Parameter	Tuned Value
K_1	1.00
K_2	1.24 μ A
K_3	2.05
K_4	3.40
α_w	10.0
t_{wl}	0.14 mm

The first tunable voltage parameter, K_1, which scales the total activation overvoltage, has a local minimum whose value is dependent on t_{wl}, near α_w=10.5. The second and third tunable voltage parameters, K_2 and K_3, influence the exchange current density and tend to increase as α_w increases or t_w decreases. The fourth tunable voltage parameter, K_4, scales the ohmic overvoltage and decreases as α_w increases or t_w decreases.

Using the identified parameters, the model is simulated to produce voltage estimations for the entire calibration data set. Figure 2.7 shows the model estimation at 300 mA cm^{-2} between 180-200 minutes. The second subplot compares the nominal current density, $i = I/A_{fc}$, to the apparent current density, i_{app} from (2.33), based on the apparent surface area that is not blocked by the liquid water film at the GDL-channel interface.

As liquid water accumulates in the anode gas channels, the apparent area decreases, causing an increase in the apparent current density. Following a purge, the liquid water is removed and the apparent current density returns to the nominal value. Following some purges, not all of the water is removed from the gas channels, causing the apparent current density to remain greater than the nominal current density. Since the apparent current density is used to calculate the cell voltage, the estimation of cell voltage is then sensitive to the degree of flooding in the anode gas channels and GDL. The values for the identified param-

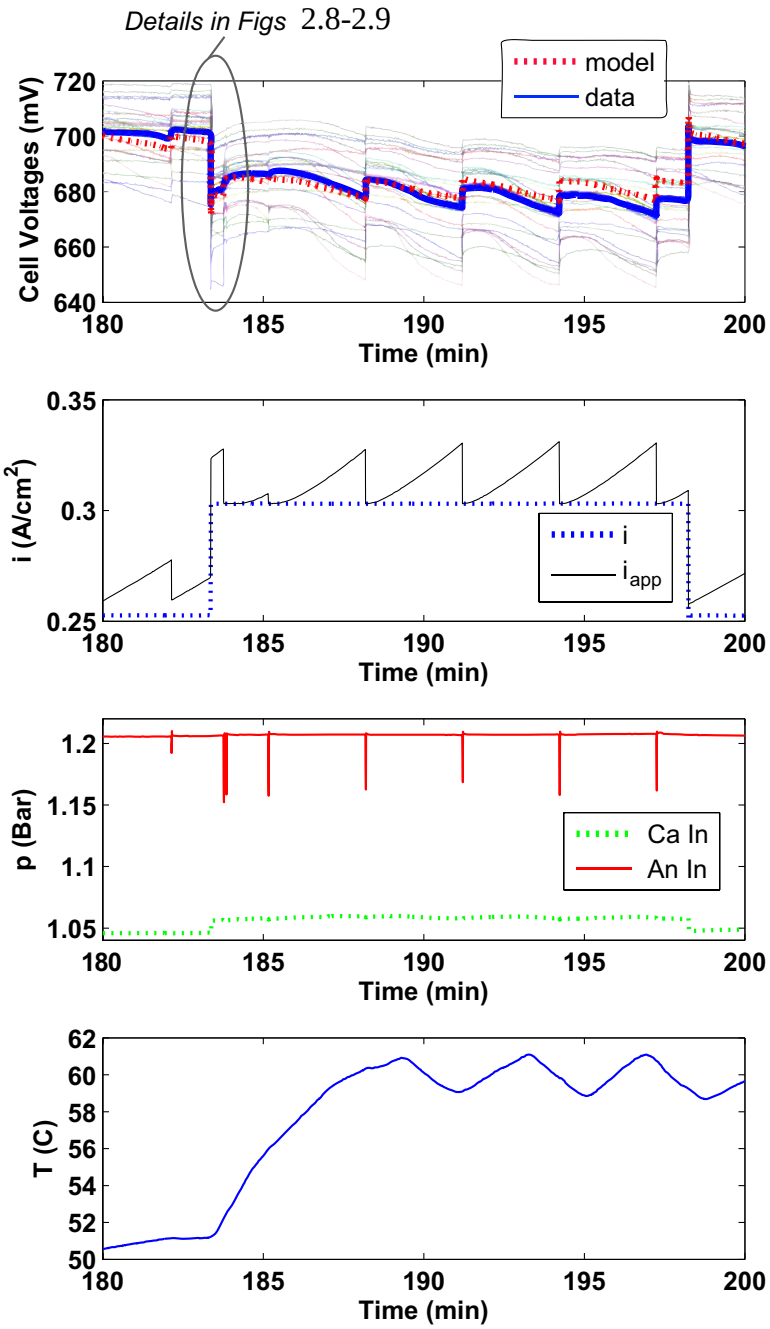

Figure 2.7 Model calibration results. The first subplot shows the 24 individual cell voltages in thin faint colored lines with the average cell voltage in a thick solid blue line and the model estimated average cell voltage in a thick dotted red line. The second subplot shows the nominal and apparent current densities. The third subplot is the anode and cathode inlet total pressures. The fourth subplot is the temperature of the water coolant leaving the stack.

eters, α_w and t_{wl} influence the rate at which liquid water accumulates in the gas channels (impacting the rate of decay in voltage between purges) as well as how much liquid water mass accumulates in the gas channel (how much the voltage recovers following a purge).

When all of the liquid water is removed from the gas channels, the cell voltage returns to approximately the same value following each purge event.

Although the voltage prediction is an indirect means for evaluating the overall predictive ability of our model, voltage is a stack variable that combines the internal states of the stack and provides an accessible, cheap, fast and accurate measurement. The model accurately captures the trend of the voltage decay and subsequent recovery after an anode purging event. Note here, for the entire calibration data set, the average estimation error is 2.9 mV, the maximum estimation error is 42 mV and the standard deviation in the estimation error is 3.6 mV.

In addition to adequately capturing the temporal evolution in voltage during flooding, the model accurately estimates the reactant dynamics during load changes. The overshoot in cell voltage during a step change up in current from 0.25 A cm^{-2} to 0.3 A cm^{-2} at approximately 183.4 minutes is shown in detail in Figure 2.8, along with subsequent purging events near 183.7 minutes. A decrease in the partial pressure of oxygen at the cathode membrane surface occurs due to volume filling dynamics; however, there is very little deviation in the hydrogen partial pressure during the load change. As a result, the reactant starvation occurs predominantly on the cathode and not the anode under these operating conditions. Referring back to Figure 2.7, the overshoot in cell voltage at approximately 198 minutes for a step change down in current from 0.3 A cm^{-2} to 0.25 A cm^{-2} is also well approximated. Note here, for simulations of reactant dynamics during a load change reported in [139] and [114], the model predictions are not compared with experimental data.

Figure 2.9 displays the predicted water vapor partial pressures, the liquid water saturation, and the mass of liquid water accumulating in the anode channel during the same load change and subsequent purging events as described previously for Figure 2.8. The slow rise in the water vapor partial pressure is due to the increase in the cell operating temperature.

Immediately following the purge valve opening, the mass of liquid water in the anode channel evaporates into the bulk gas stream (due to the increased hydrogen mass flow rate during the purge). The volumetric condensation coefficient, γ in (2.7), influences the non-instantaneous rate of evaporation of water vapor in the GDL section allowing the water vapor partial pressure to decrease before all of the liquid water is removed from the GDL sections.

The liquid water saturation in the GDL section closest to the channel, $s_{an}(3)$, decreases most significantly during a purge. Liquid water flows from the GDL towards the channel until the immobile saturation limit is reached, $s_{an}(3) \leq s_{im}$, at which point only water vapor enters the channel from the GDL. Liquid water does not flow from the GDL to the

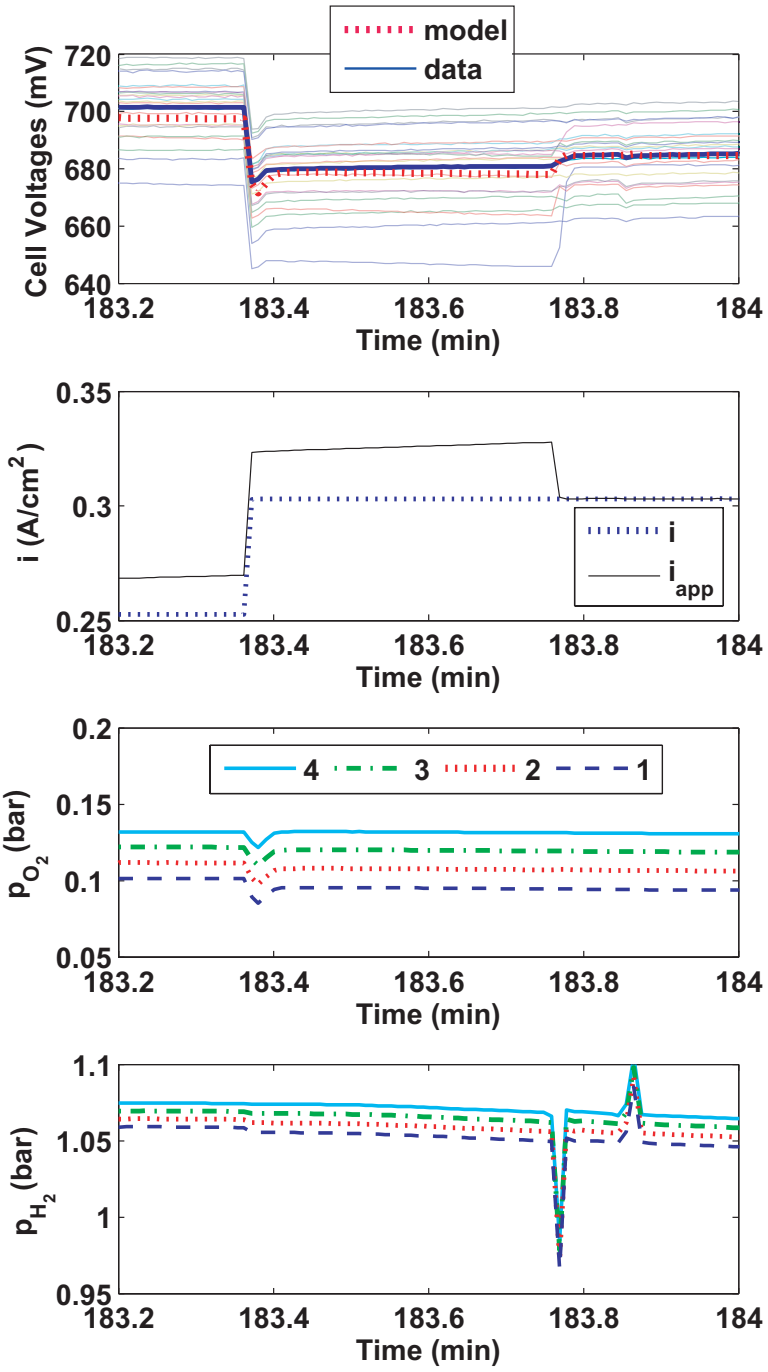

Figure 2.8 Reactant dynamics during a load change and purging event. The first row of subplots shows the cell voltages along with the nominal and apparent current densities. The 24 individual cell voltages are displayed in thin faint colored lines with the average cell voltage based on the measurements in a thick solid blue line and the estimated cell voltage in a thick dotted red line. The second row of subplots shows the oxygen and hydrogen partial pressures in each GDL section (1-3) as well as in the channel (4). A load change from 0.25 A cm^{-2} to 0.3 A cm^{-2} occurs at approximately 183.4 minutes followed by an anode purging event at approximately 183.7 minutes

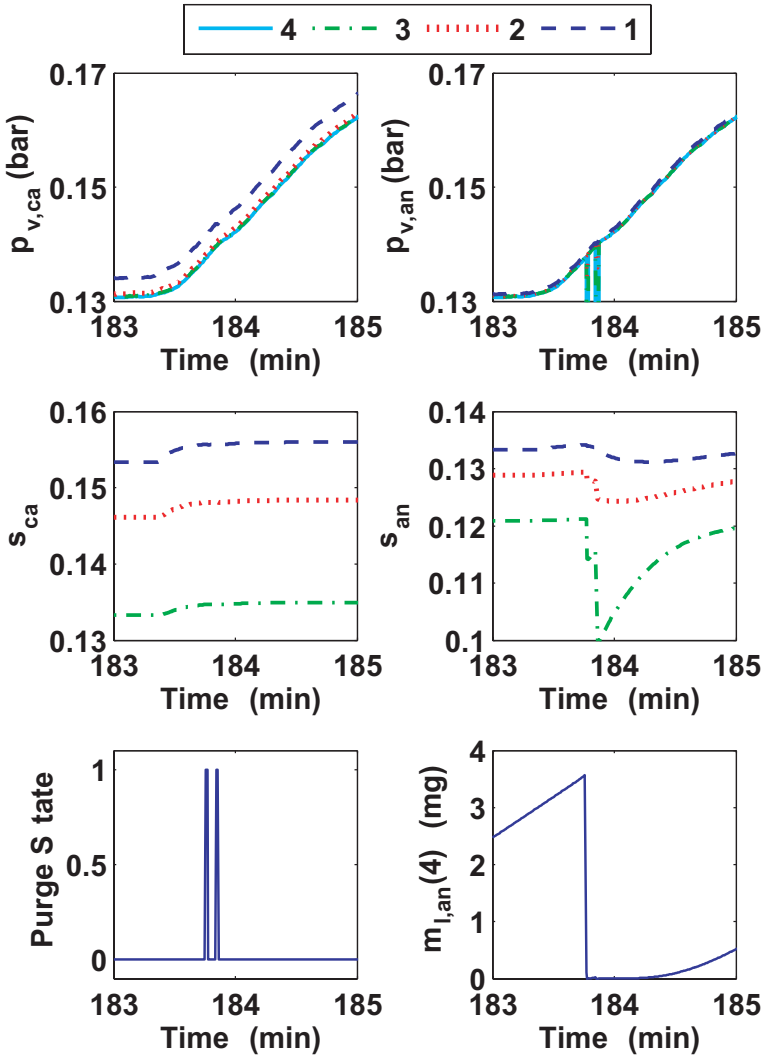

Figure 2.9 Water dynamics during a load change and purging event. The first row of subplots shows the water vapor partial pressures in the GDL and channels. The channel is indicated by a solid line and the three GDL sections are represented by dashed lines. The second row of subplots displays the liquid water saturation in the GDL. Finally, the third row of subplots indicates first the state of the purge solenoid valve (0 indicates the valve is closed and 1 means the valve is open), followed by the mass of liquid water accumulating in the anode channel.

anode channel, following the purge, until the liquid water saturation in the GDL exceeds the immobile saturation limit. If the purge event were to have occurred over a longer time interval, more water vapor in the anode GDL would have been removed, causing a more significant impact on the cathode liquid water saturation due to the water vapor transport through the membrane.

2.8 Model Validation and Discussion

For the purposes of model validation, the calibrated model is simulated with experimental inputs that are different from the ones used in the calibration process. The resulting model predictions are shown in Figure 2.10 and compared with the actual cell voltage measurements at five different load levels. The data shown demonstrate the model predicting capability over a range of current densities and air stoichiometries. At approximately 162 minutes, the air stoichiometry is increased from 200% to 300%, causing a more significant increase in the voltage estimation (through the partial pressure of oxygen at the membrane boundary) than is experimentally observed. Despite the increased error associated with the oxygen partial pressure, the model correctly estimated the degree of anode flooding at various current densities, correctly predicting no significant flooding at low loads. As the load level is reduced, the degree of flooding decreases, which is seen from inspection of the difference between the apparent and nominal current densities at each load level. As a result, the deviation in voltage decreases between purges, which is experimentally confirmed.

For the entire validation data set, the average estimation error is 8.7 mV, the maximum estimation error is 105 mV and the standard deviation in the estimation error is 11.5 mV. Although these validation error statistics are approximately two times greater than the error statistics associated with the calibration data, at all times throughout the experiment the estimated average cell voltage is bounded between the measured minimum and maximum cell voltages, and the measured cell to cell variation is larger than the average estimation error.

Although the model of the reactant and water dynamics results in an accurate estimation of the voltage degradation between purges, it is assumed that this degradation was solely due to the accumulation of liquid water in the gas channels. However, it is conceivable that some of this degradation could be due to the accumulation of nitrogen on the anode as a result of operation with air, rather than pure oxygen, or catalyst flooding. The model has tunable parameters that can compensate for these model assumptions and simplifications, but it is very important to check the tuned parameter values against other published values. As Table 2.2 shows, the tuned α_w and t_{wl}, are reasonable and within the range of published results [118, 99].

2.9 Conclusions

A two-phase isothermal one-dimensional model of reactant and water dynamics has been developed and validated using a multi-cell stack. The lumped parameter model depends

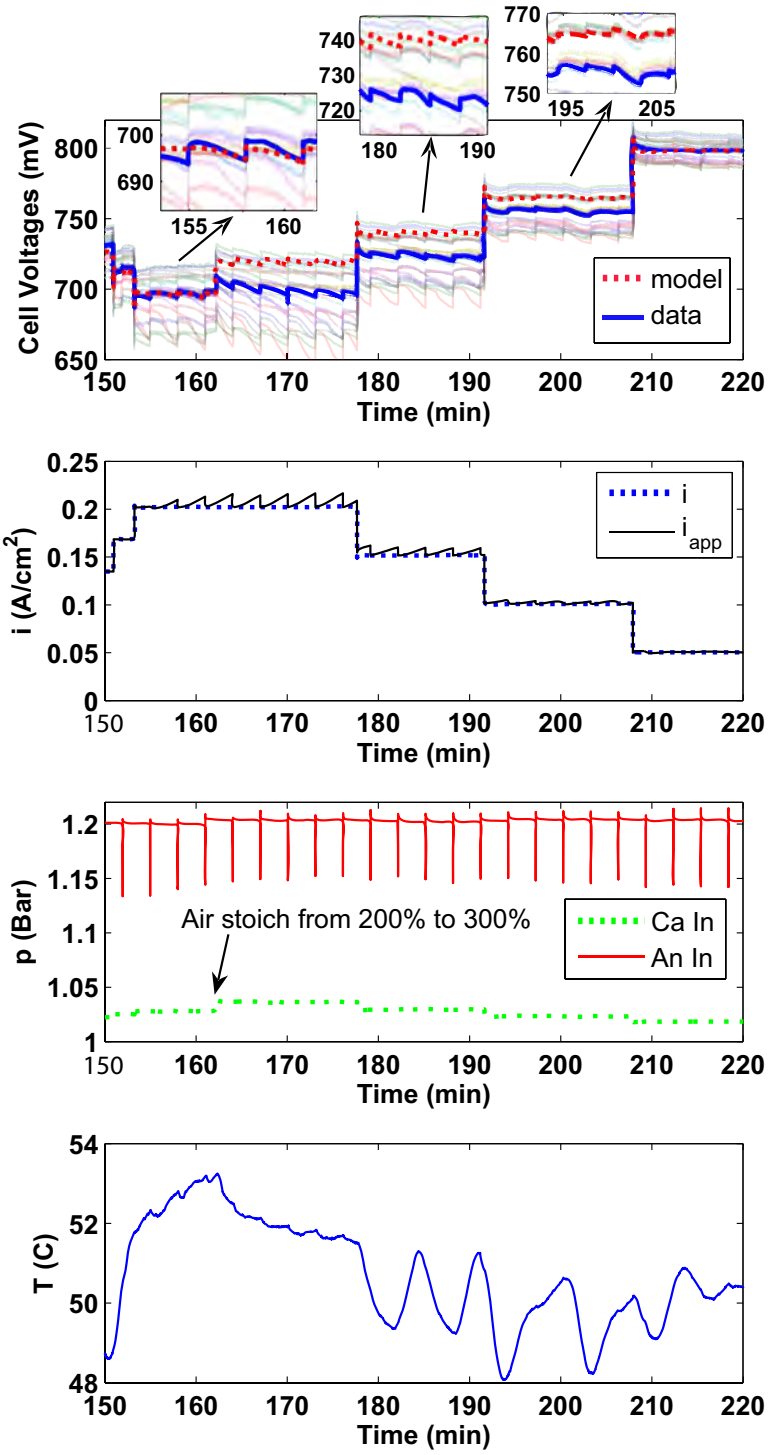

Figure 2.10 Model validation results. The first subplot shows the 24 individual cell voltages in thin faint colored lines with the average cell voltage based on the measurements in a thick solid blue line and the estimated cell voltage in a thick dotted red line. The second subplot shows the nominal and apparent current densities. The third subplot contains the anode and cathode inlet total pressures. The fourth subplot is the temperature of the water coolant leaving the stack.

on six tunable parameters associated with the estimation of voltage, the membrane water vapor transport and the accumulation of liquid water in the gas channels. During step changes in load, a good voltage prediction is achieved by reproducing both the steady-state and dynamic voltage response due to the instantaneous increase in current, as well as the excursions in oxygen partial pressure resulting from the manifold filling dynamics, as demonstrated. Finally, the model predicted the dynamic effect of temperature on voltage as shown during the temperature transient from 50^o to 60^oC. Although simple, this model captures the voltage dynamics observed in a fuel cell stack at low and moderate current densities under the range of conditions tested. However, caution should be used in extending this model to conditions not examined, as this model has significant empirical and tuned functions.

The notion of apparent current density is a means for describing the impact of water accumulation on the dynamic voltage behavior of a PEMFC. The next chapter is focused on extending and validating this simple GDL model at higher current density, and establishing the connection between the liquid water mass accumulation and voltage using neutron imaging techniques [140].

Table 2.3 Parameter symbols, definitions and values.

Symbol	Definition
A_{fc}=0.030 m^2	fuel cell nominal active area
b_{11}=0.005139 [121]	ohmic resistance parameter
b_{12}=0.00326 [121]	ohmic resistance parameter
D_{H_2}=114 mm^2/s [71]	hydrogen diffusion coefficient
D_{O_2}=30.3 mm^2/s [71]	oxygen diffusion coefficient
E_c=66 kJ/mol [138]	activation energy
F=96485 C/mol e^-	Faraday's constant
ΔH=-228,740 J/mol	Enthalpy difference from STP (water in vapor phase)
i_{loss}=1 mA cm^{-2} [138]	loss current density
$k_{ca,in}$=11.3e-7 m s	cathode orifice constant
$k_{ca,out}$=11.3e-7 m s	cathode orifice constant
$k_{an,in}$=9.34e-7 m s	anode orifice constant
$k_{an,out}$=9.34e-7 m s	anode orifice constant
$k_{an,rm}$=11.31e-7 m s	return manifold orifice constant
K=2.55e-13 m^2 [71]	absolute permeability
K_1=1.17	tuned voltage parameter
K_2=4.44 μA	tuned voltage parameter
K_3=1.78	tuned voltage parameter
K_4=3.27	tuned voltage parameter
L=3	number of GDL sections
M_{H_2}=0.002 kg/mole	hydrogen molecular weight
M_{O_2}=0.032 kg/mole	oxygen molecular weight
M_{N_2}=0.028 kg/mole	nitrogen molecular weight
M_{H_2O}=0.018 kg/mole	water molecular weight
n_{cells}=24 cells	number of cells in stack
p_o=1 atm	standard state pressure
R=8.314 J/mol K	universal gas constant
s_{im}=0.1 [71]	immobile saturation
ΔS=-44.43 J/mol K	Entropy difference from STP (water in vapor phase)
t_{gdl}=0.5 mm	total GDL thickness
t_{mb}=0.038 mm	PEMFC membrane thickness (includes catalyst layer)
t_{wl}=0.131 mm	tunable water layer thickness
T_o=298.15 K	standard state temperature
V_p=2.5 cm^3	GDL section pore volume
V_{ca}=380 cm^3	cathode channel volume
V_{an}=430 cm^3	anode channel volume
$V_{an,rm}$=345 cm^3	anode return manifold volume
α_w=11.5	tuned water vapor diffusion parameter
δx=0.167 mm	GDL discretization width
γ=900 s^{-1} [71]	volumetric condensation coeff.
ε=0.5 [71]	material porosity
θ_c=60 degrees [71]	contact angle
μ=0.405 g/m s [71]	liquid water viscosity
ρ=997 kg/m^3	liquid water density
σ=0.0644 N/m [71]	surface tension
$\rho_{mb,dry}$=1900 kg/m^3	mb dry density
$M_{mb,dry}$=1.0 kg/mol	mb dry equivalent weight

Chapter 3

Neutron Imaging of Liquid Water Accumulation In PEMFC

The operation and accumulation of liquid water within the cell structure of a polymer electrolyte membrane fuel cell (PEMFC) with a dead-ended anode is observed using neutron imaging. The measurements are performed on a single cell with 53 cm^2 active area, Nafion 111-IP membrane, and carbon cloth gas diffusion layer. Even though dry hydrogen is supplied to the anode via pressure regulation, accumulation of liquid water in the anode gas distribution channels is observed in most tested conditions. Moreover, the accumulation of liquid water in the anode channels is followed by a significant voltage drop. Anode purges and cathode surges are also used as a diagnostic tool for differentiating between anode and cathode water flooding. The rate of accumulation of liquid water and its impact on the rate of cell voltage drop are shown for a range of temperature, current density, cathode inlet relative humidity, and air stoichiometric conditions. Operating the fuel cell under dead-ended anode conditions offers the opportunity to observe water dynamics and measured cell voltage during large and repeatable transients.

3.1 Introduction

The electrochemical power generation of a popular category of fuel cells depends on the proton-conducting properties of their polymer electrolyte membranes. The ability of the membrane to conduct protons increases with increasing water content. However, polymer electrolyte membrane fuel cells (PEMFCs) operate below the boiling point of water, causing excess water to condense and restrict gas delivery or block the catalyst active area. The buildup of water mass, referred to as flooding, in an operating fuel cell was first observed with neutron imaging in [49]. The impact of this flooding phenomena is a recoverable reduction in the power output of the fuel cell, seen by a decrease in cell voltage [99, 58], but can also lead to irrecoverable material degradation [141, 2].

This chapter presents the neutron imaging of liquid water accumulation in a PEMCF operating with a dead-ended anode. Modeling and testing for anode flooding conditions are rare because most experimental fuel cells operate under flow-through conditions for which anode flooding is highly unlikely. Here, a solenoid valve placed downstream from the cell allows for an occasional purging event with high hydrogen flow rate to remove water from the anode, preventing severe voltage drop and reactant starvation. Optimal scheduling of purge events is necessary to prolong fuel cell life and minimize wasted hydrogen. An adjustable purging schedule applied to a stack with a dead-ended anode can enable high hydrogen utilization and remove the need for costly, heavy, and bulky anode humidification and recirculation hardware. Furthermore, understanding the water removal with anode purging is important for designing shutdown procedures to alleviate damage caused by freeze and thaw cycling.

Therefore, models which accurately predict the accumulation and removal of water are necessary. If, in addition to water accumulation, the model can also predict the resulting cell voltage, it could be used in combination with voltage measurement to allow real-time adaptation of the purging events in response to component aging, environmental changes, and system faults. Specifically, the estimated voltage is compared with the actual voltage, and the error is used to adjust the model-based purge schedule. A similar model-based technique was used for the estimation of hydrogen starvation [142] and control of the hydrogen production rate from a fuel processor [143]. Hence, the experiments and experimental results detailed here sought to confirm that a consistent correlation between water accumulation and voltage degradation exists.

To this end, the experimental results offer the opportunity to observe water dynamics and measured cell voltage during large and repeatable transients and hence, provide useful data for calibrating and validating simple lumped parameter transient models [65, 140] during anode flooding conditions. There are some limitations of the imaging system [55], however, with careful cell design and masking the approximate location of the liquid water within the structure can be inferred. These techniques have been applied in similar work using neutron imaging [99, 58, 48, 98, 50, 53, 144, 57]. Neutron imaging experiments with higher resolution in the membrane through-plane direction could provide more information on the intrinsic mechanism of voltage degradation during anode flooding. However, higher spatial resolution imaging requires longer exposure times [145] and hence, the method is impractical for calibrating or validating transient models with a time resolution less than 1 min. Controlled cathode surging and anode purging events are used to distinguish anode versus cathode channel plugging and flooding. During an anode purge, fed with dry hydrogen, a high gas flow rate through the cell is used to remove the liquid water stored in the

anode. During a cathode surge, the air flow is momentarily and abruptly increased beyond the nominal excess ratio to remove any liquid water stored in the cathode.

It is demonstrated that liquid water accumulates in the anode gas channels, and this buildup of liquid water is well correlated with the dynamic cell voltage response during the majority of the experiments, as originally predicted in [146]. These data also indicate that there is sometimes significant voltage drop, even if the mass of water does not increase in the fuel cell. Hence, water flooding cannot be considered always responsible for the voltage drop and nitrogen accumulation in the anode should also be considered [36, 37]. Conclusions about channel water mass are based on several homogeneity assumptions, which ignore the difference in the stored liquid water mass in the Gas Diffusion Layer (GDL) under the channels as compared to areas under lands [55, 112]. Nevertheless, the data and data analysis provide useful new information regarding PEMFC transient behavior.

3.2 Experimental Hardware

Experiments were conducted at the Neutron Imaging Facility at the National Institute for Standards and Technology (NIST) Center for Neutron Research [145]. The amorphous silicon detector was used for its 1 Hz image acquisition rate to capture the change in mass of liquid water over time. A 1 cm diameter aperture was used for the experiment, with a neutron fluence rate I_0 of 7.2 $\times 10^6$ cm^{-2} s^{-1} and a neutron flight path of 6 m. In this case, the ratio of source-to-detector distance over the source aperture diameter (L/D) is equal to 600. The width of a pixel in the image corresponds to 127 μm, but the resolution of the imaging system is about 250 μm as a result of scintillator blooming [145].

The NIST test stand is used to supply a humidified gas stream to the cathode in flow-through operation. The air is humidified using a bubbler, and it is assumed that the gas leaving the bubbler is saturated at the water temperature. The inlet relative humidity can be calculated at the fuel cell temperature by assuming the air has a dewpoint temperature equal to the bubbler temperature. A portable anode purging system was constructed, which allows dead-ended operation of the fuel cell. This anode purge system consists of a pressure regulator, which supplies dry hydrogen to the anode inlet, and a solenoid valve downstream of the anode outlet. A needle valve placed downstream from the solenoid valve is used to set the desired flow rate during an anode purge event. The pressure drop across the needle valve is used to reduce the gas flow rate leaving the channel during an anode purge event. This valve was adjusted prior to beginning and kept fixed for the duration of the experiments. The anode gas flow rate during a purge is about 5 SLPM. Between purges

the anode is supplied with hydrogen via pressure regulation, at a stoichiometry equal to one, as shown in Fig. 3.1. Voltage, current, pressure, temperature, and cathode flow rate measurements are recorded continuously at 1 Hz resolution. The image data are selectively recorded when repeatable large transients are observed. Due to the large file size, it is not desirable to capture data for all times, creating gaps in the measured liquid water mass data.

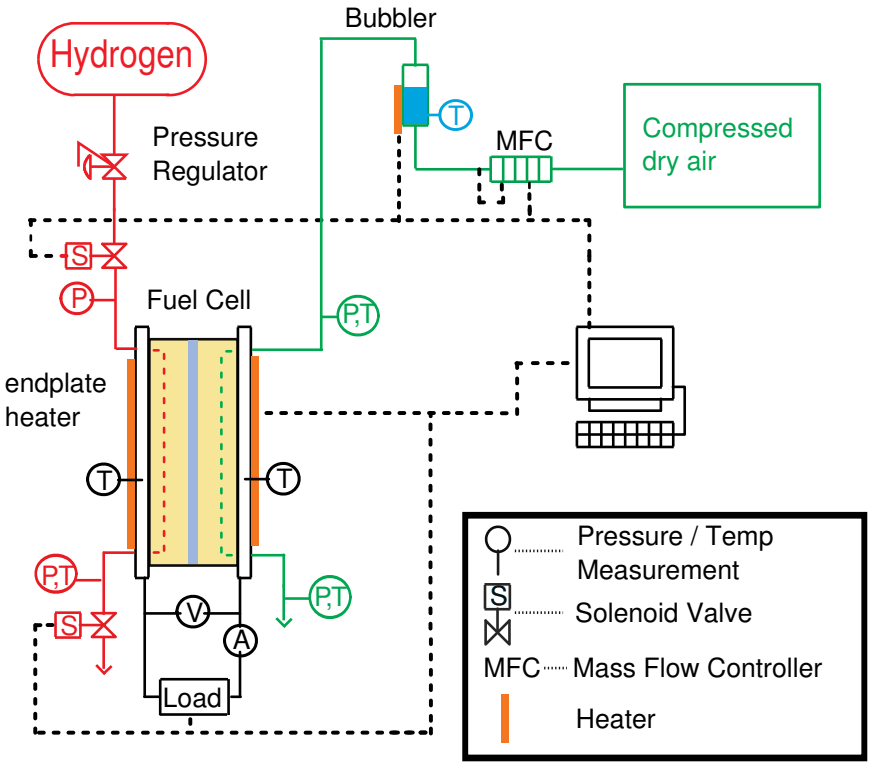

Figure 3.1 Experimental hardware detailing sensor and actuator locations.

The cell is comprised of a single 53 cm^2 Nafion 111-IP membrane which is 25.4 μm thick with anode and cathode catalyst layers containing a Pt areal density of 0.3 mg cm^{-2} purchased from Ion Power. SGL 10BB nonwoven carbon GDLs, were used, which have an uncompressed thickness of 420 μm and a porosity of $\varepsilon = 0.84$. The cell hardware, purchased from Electrochem, consists of aluminum endplates, gold coated aluminum current collectors, and resin-impregnated graphite flow fields. Resin-impregnated graphite is used to prevent liquid water from accumulating inside the pore-structure of the graphite [56]. The graphite plates were thinned to 0.32 cm to reduce neutron attenuation. The anode gas channels are straight with a channel width of 2.08 mm, depth of 1.78 mm, and land width of 0.838 mm. A semiserpentine flow path is used on the cathode with five parallel paths, each having a channel width of 0.686 mm, a channel depth of 0.991 mm, and a land width of 0.762 mm. A square 45 W resistive heater, with a surface area of 58 cm^2, is attached to each end plate to ensure that uniform heating and that the desired temperature at low

current density is maintained.

3.3 Quantification of Liquid Water Mass

The attenuation properties of a neutron beam passing through an object can be used to form a projected image on a detector, similar to X-ray radiography. Neutrons are strongly scattered by hydrogen atoms and only weakly interact with the other materials used in PEMFCs, such as aluminum and carbon. The scattering interaction is also density dependent; therefore, neutron imaging is particularly sensitive to the amount of liquid water present in the cell due to the high density of hydrogen atoms, but is unable to detect to hydrogen gas or water vapor. This technique provides a useful tool for in-situ measurement of liquid water content while employing commercial fuel cell materials with realistic cell designs. The use of these materials reduces the possibility of temperature gradients induced by selection of nonstandard materials, which would otherwise greatly impact the formation of liquid water within the cell.

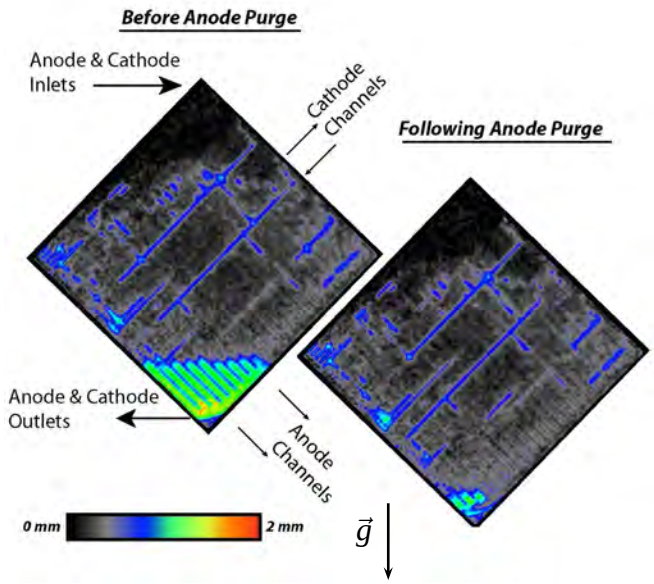

Figure 3.2 Neutron images of the fuel cell active area before and after anode purge events, indicating the actual cell orientation. The cell is operated at 566 mA cm^{-2}, 55 °C, with fully humidified air at a stoichiometry of 200 % for cathode and dry hydrogen supplied to anode.

Figure 3.2 shows two images collected before and after a purge event. The areas with high liquid water accumulation are clearly visible in the top left frame, which corresponds to a condition before an anode purge event. The second frame in Fig. 3.2 shows the drier

neutron image collected after the purge. The downward pointing vector $\vec{g}$ indicates the direction of gravity.

The image, $I(j,k)$, formed by scattering and absorption of neutrons can be modeled by the Beer-Lambert law

$$I(j,k) = I_0(j,k) \exp\left[-\sum_{l=1}^{N} \mu_l t_l(j,k)\right] , \tag{3.1}$$

where $I_0(j,k)$ is the incident flux rate of neutrons, N is the number of material layers in the object, t_l is the thickness of each layer, and μ_l is the linear attenuation coefficient of each layer.

The thickness of liquid water is quantified by determining the amount of attenuation which is caused by water in the image. A section of the image outside the active area, defined by S_p, is used to normalize each image before processing, to account for fluctuations in the nuclear reactor power output and $I_0(j,k)$ over time, according to

$$I^{norm}(j,k) = \frac{I(j,k)}{\sum_{j,k\in S_p} I(j,k)} . \tag{3.2}$$

To reduce systematic error, care is taken to ensure reference images, $I^{norm}_{dry}(j,k)$, are taken with a completely dry cell, and 1500 images are averaged to reduce noise in the image. To account for the effects of thermal expansion, which cause portions of the cell to move within the imaging frame, dry reference images are taken at 5°C increments over the operating temperature range of the fuel cell. The relative neutron transmission, found by dividing an image by the dry reference image of the cell, can be used to calculate water thickness, assuming that the attenuation caused by everything but liquid water remains unchanged since the reference image was captured. A 3×3 median filter is applied to the images to further reduce random noise before calculating the liquid water thickness. The thickness of the water layer is calculated using

$$t_w(j,k) = -\frac{1}{\mu_w} \ln\left[\frac{I^{norm}(j,k)}{I^{norm}_{dry}(j,k)}\right] , \tag{3.3}$$

and the experimentally obtained attenuation coefficient, $\mu_w = 0.3708 \pm 0.0008$ mm^{-1} [145], which is valid for liquid water thickness less than 1 mm.

Liquid water quantification is further complicated by instrument broadening caused by the scintillator screen, scattering of neutrons by objects in the beam and detector noise [48, 47]. The trends in the data will still be evident without correction for these effects.

Quantification of the error introduced by each phenomena is currently under investigation at NIST [145].

3.3.1 Temporal Averaging to Reduce Uncertainty

The measured uncertainty in water volume for a single pixel in the detector system sampled at the 1 Hz rate is 0.32 x 10^{-6} cm^3 using (L/D) = 450 [145], which is different from the experimental setup of (L/D) = 600. The measured uncertainty can be scaled to account for the different neutron flux used in the experiment by multiplying by the ratio of the square root of the fluence rates, which yields a per pixel liquid water volumetric uncertainty of 0.537×10^{-6} cm^3. This relationship can be derived from the equation for the theoretical uncertainty [145],

$$\delta_t = \frac{1}{\mu}\sqrt{\frac{1+e^{\mu t}}{I_o A T \eta}} \approx \frac{1}{\mu}\sqrt{\frac{2}{I_o A T \eta}}\,, \tag{3.4}$$

where t is the water thickness, μ is the attenuation coefficient, I_o is the fluence rate, A is the area, T is the integration time, and η is the detector efficiency. Equation (3.4) also indicates that a reduction in uncertainty of the measured liquid water volume can be achieved at the expense of temporal resolution by averaging several frames. The uncertainty in an averaged frame of 11 s as compared to 1 s is decreased by a factor of $\sqrt{1/T} \approx 0.3$. Since the time constant associated with liquid water is on the order of 100 s [56, 147], the 11 s imaging rate is used. The resulting liquid water volume uncertainty is 0.16×10^{-6} cm^3 $pixel^{-1}$, which corresponds to a water thickness of 10 μm. Unfortunately, the temporal averaging exacerbates the difficulty in tracking movement of water droplets and slugs in the channels; liquid water droplet movement with the gas stream in the channel could be much faster than the 1 s imaging time, and therefore, during a cathode surge or anode purge, liquid water flow in the channels would appear blurred, even without averaging at the fastest exposure rate of the imaging system.

3.3.2 Masking

The processed water thickness image, $t_w(j,k)$, is a two-dimensional (2-D) projection of the liquid water inside the fuel cell. In order to infer the location of liquid water in the third dimension, a knowledge of the physical material structure can be combined with logical arguments. For example, liquid water cannot be located within an impervious solid material. Several masking techniques have been used to analyze neutron images [99, 58, 50, 53]. A

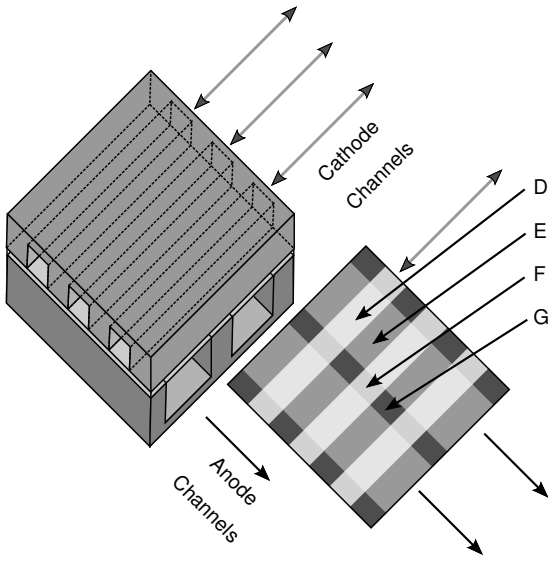

Figure 3.3 Schematic of fuel cell layers used for masking, the beam direction is into the page and perpendicular to the membrane.

similar process is employed to estimate the mass of liquid water in three layers: the anode channel, cathode channel, and combined membrane and GDL layer (which consists of both anode and cathode GDLs). The masks are formed using the drawings of the graphite plates. Mask A defines the active area of the fuel cell, mask B is for the anode channels, and mask C is for the cathode channels. Four mutually disjoint masks, D-G, identify regions of the fuel cell corresponding to the different possible combinations of channels and lands on each side of the membrane as shown in Fig. 3.3. The area of each mask and their logical relationships are shown in Table 3.1. The water thickness in the combined membrane and GDL layer can be directly measured from the images for regions identified by mask G, which contain both anode and cathode lands and therefore water could not be present in either of the other two layers.

Table 3.1 Masks

Mask	Description	#Pixels	Relationship
A	Active Area	313600	$D \cup E \cup F \cup G$
B	Anode Channel Area	234099	
C	Cathode Channel Area	169392	
D	Both Ch +MEMB+GDL	128047	$B \cap C$
E	An Ch + MEMB+GDL	106052	$(B \cap \bar{C}) \cap A$
F	Ca Ch + MEMB+GDL	41345	$(\bar{B} \cap C) \cap A$
G	MEMB+GDL only	38155	$(\bar{B} \cap \bar{C}) \cap A$
H	Subset of G	11239	$H \subset G$

3.3.3 Local Spatial Averaging

Estimation of the distribution of liquid water in the third dimension, using masking over the entire active area, requires consideration of the significant spatial variations in the liquid water thickness along the channels. Therefore, a local 2-D spatial average is constructed. Specifically, the active area is partitioned into a 9×9 grid of 81 segments similar to [58]. A 9×9 grid is chosen corresponding to the nine segments of parallel cathode channels as seen in Fig. 3.4, which is overlaid on mask C. Within each of the 81 segments, the flow of reactant gases is in the same direction. Due to a manufacturing error the cathode inlet and outlet manifolds were incorrectly positioned, rendering the first and last serpentine flow pass ineffective. The cathode inlet should be located in segment 1, for proper operation, but is instead located in segment 9 as shown in Fig. 3.4. As a result, segments 1-8 and 74-81 are not included in the cathode flow path; therefore no excess air is passed though these segments of the cathode during normal operation of the cell. Hence, the cathode channel exhibits an unusual accumulation of liquid water in theses segments. Due to the orientation of the cell, prior to masking, each thickness image is rotated 44.3° to the right using a bi-cubic interpolation method to facilitate registration with the mask. In the rotated orientation, studies can be performed along the channels by traversing the coordinate axis of the image. Note that segment 9, which is highlighted in Fig. 3.4, corresponds to the upper corner of the fuel cell shown in Fig. 3.2. Segment 9 is also the location of the gas inlets where the dry hydrogen and humidified air enter the anode and cathode channels, respectively.

The fuel cell conditions are assumed to be uniform within each of the 81 segments. Five image masks (D-H) are applied to each of the 81 segments individually, and the average liquid water thickness in each of the masked regions is calculated for each segment. A fifth mask H, which is a subset of the points in mask G not adjacent to either channel, is used to get a more accurate estimate of the water content in the combined GDL and membrane layer. This mask reduces the effects of instrument broadening and neutron scattering when there is liquid water present in the neighboring channels [48, 145]. Since only points near the center of the lands are counted, the effect of different gas flow distributions in the GDL in the adjacent regions, underneath the channel as compared to the land, on liquid accumulation may not be accurately represented.

The top subplot in Fig. 3.5 shows a comparison of the average water thickness calculated using masks G and H over the entire active area for the combined membrane and GDL layer. If the entire active area is considered, there is little difference between the average water thicknesses when using mask G as compared to using mask H. However, for individual segments, a more significant difference between the applications of mask G

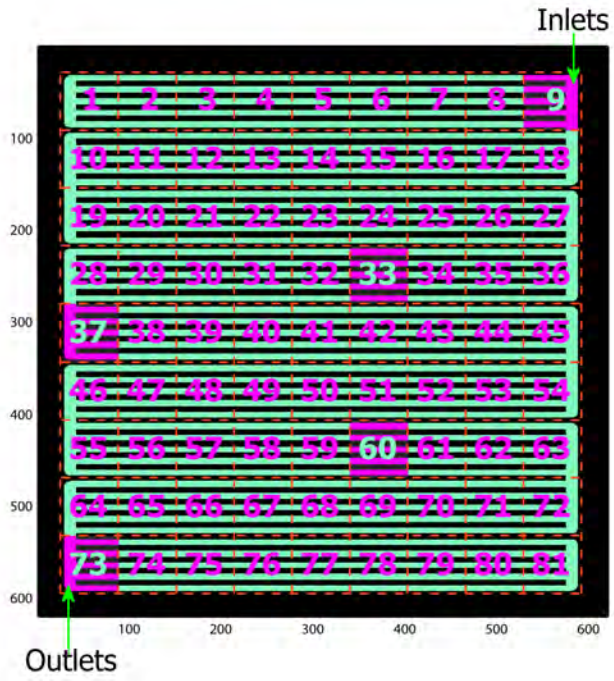

Figure 3.4 The cathode channel, mask C, is partitioned into 81 segments for the evaluation of the spatial distribution in cathode channel liquid water. Five representative segments are highlighted and shown in later analysis.

versus mask H is observed, as indicated in the remaining subplots. The largest difference in average thicknesses is found in segment 73, located at the gas outlet near the bottom of the cell. Due to the orientation of the cell and dead-ended anode, liquid water accumulates in this corner of the anode channel because it is forced by the reactant gas flow and gravity. A detailed description of the testing conditions for this experiment can be found in Fig. 3.6.

The standard deviation in water thickness for points identified by mask G, shown in Fig. 3.5, provides a metric for how uniform the water content in the combined membrane and GDL layer is over that segment. A large standard deviation in thickness may indicate nonuniform conditions in the membrane and/or GDL. Scintillator blurring and/or scattering, where a significant amount of water is present in the channel, reduces the measured standard deviation but creates a systematic uncertainty. In the limiting case, where the water thickness is uniform, the standard deviation in measured thickness should be equal to that of the Poisson counting process given by (3.4), which increases with increasing water thickness. The large standard deviation measured for segment 9 between t=725 and 800 min, shown in Fig. 3.5b, is likely due to condensation and buildup of liquid water near the cathode inlet manifold. A cathode surge conducted at around t=780 min pushes liquid water out of segment 9, reducing the measured standard deviation in that segment. Seg-

ment 73 consistently contained the most water and therefore also has the highest standard deviation.

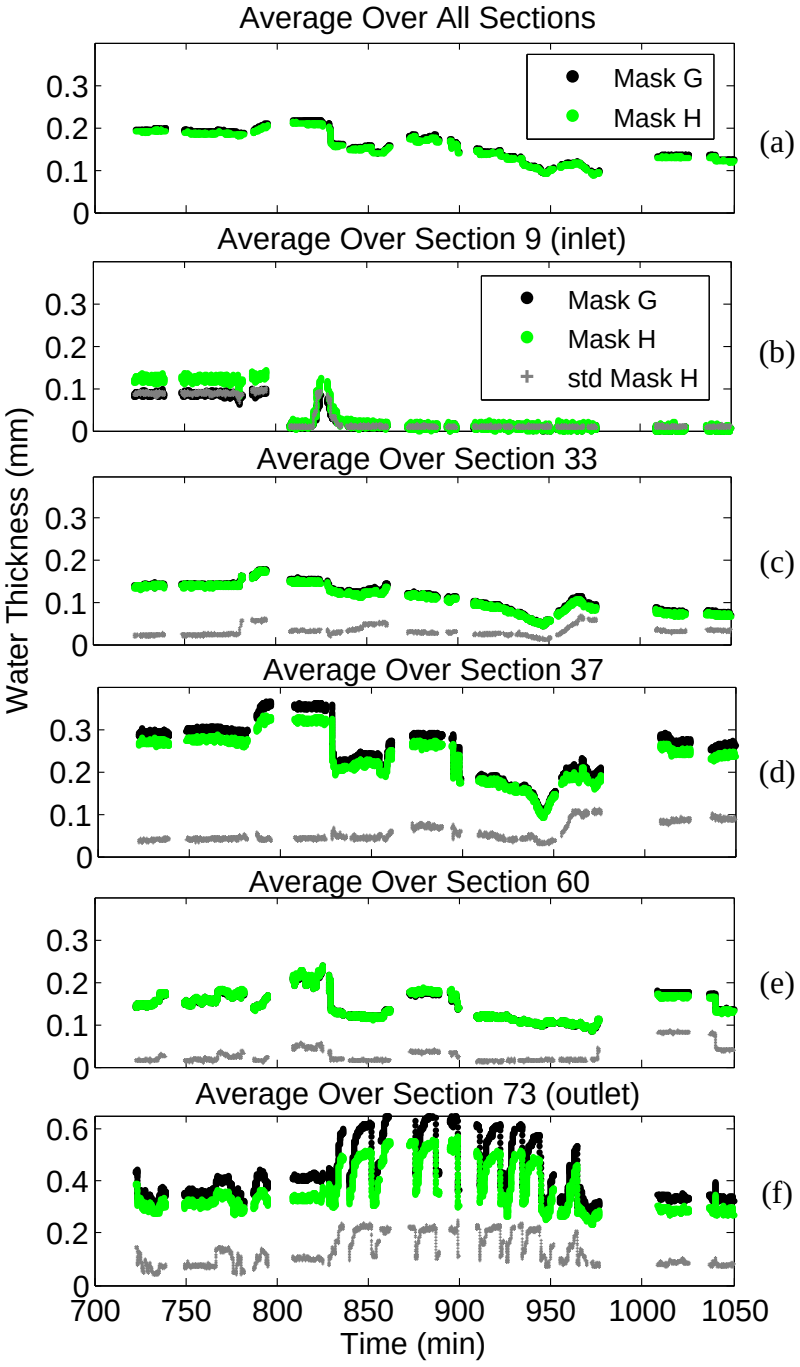

Figure 3.5 Average (spatial) liquid water thickness in the membrane/GDL layer. The average liquid water thickness for the combined membrane/GDL layer over the entire active area is shown in the top subplot and within selected segments in subsequent subplots. Data are taken from the same set shown in Fig 3.6.

3.3.4 Channel Liquid Mass

To calculate the mass of liquid water in the gas channels, assume that the water thickness in the combined membrane and GDL layers is uniform over a segment, and then it is equal to the averaged thickness in the region defined by mask H. In this case, the average liquid water thickness in the anode channel can be estimated by taking the difference between averaged water thickness in masked regions H (MB/GDL) and E (MB/GDL+AnCh) for each segment. Similarly, the average cathode channel liquid water thickness can be estimated by the difference between averaged water thickness in regions H and F. The total estimated liquid water mass in each layer of the cell is found by summing the masses calculated for each of the 81 segments, according to

$$\bar{M}^{W}_{GDLMB} = \rho_l A_P \sum_{i=1}^{81} N_{P,AA}[i] H[i] \ , \tag{3.5}$$

$$\bar{M}^{W}_{AnCh} = \rho_l A_P \sum_{i=1}^{81} N_{P,AnCh}[i] \left(E[i] - H[i]\right) \ , \tag{3.6}$$

$$\bar{M}^{W}_{CaCh} = \rho_l A_P \sum_{i=1}^{81} N_{P,CaCh}[i] \left(F[i] - H[i]\right) \ , \tag{3.7}$$

where ρ_l is the density of water; A_P is the area of the fuel cell corresponding to a single pixel in the detector; $N_{P,AA}[i]$, $N_{P,AnCh}[i]$, and $N_{P,CaCh}[i]$ are the number of pixels defining the active area, anode channel, and cathode channel, respectively, and $H[i]$, $E[i]$, and $F[i]$ are the measured average water thickness in segment i for each of the corresponding masks, where the thickness is given by (3.3). The results of this image processing and data analysis are shown in Fig. 3.6.

Three-dimensional computational models have demonstrated the possibility of a nonuniform liquid water distribution inside the GDL, with a buildup of water in regions underneath channel lands [55, 112]. If the true water distribution in the GDL is concentrated under the lands, then the previous assumptions would lead to an underestimation of the amount of liquid water in the channel, and an overestimation of the GDL water content. Therefore this data analysis method represents a lower bound on the mass of accumulated water in the channels and an upper bound on the mass of water in the GDL.

Local averaging combined with masking yields more accurate results than simply averaging the masked regions over the entire active area due to the nonuniform distribution of water within the cell. The percent difference between the total liquid water mass, and the estimated mass calculated via masked local averages, $\bar{M}^{W}_{AnCh} + \bar{M}^{W}_{CaCh} + \bar{M}^{W}_{GDLMB}$, is less than 2%, indicating that the relative uncertainty introduced by the assumption of a uni-

form water thickness in the combined membrane and GDL layer for each segment is small. Therefore, there is a high level of confidence using the locally averaged and masked data to infer the mass of liquid water in each of the three layers: anode channel, cathode channel, and combined membrane GDL.

3.4 Results and Discussion

The neutron imaging data were collected over 4 continuous days of testing (42 hours) for the range of operating conditions summarized in Table 3.2 and shown in Fig. 3.6 and Figs. 3.8- 3.10. The same cell is used throughout all the experiments, with pressure regulated dry hydrogen feed at various current densities, air stoichiometric ratios, cathode inlet relative humidities (RHs) and cell temperatures. It is assumed that the air supplied to the cathode has a dewpoint equal to the bubbler temperature. Control of the fuel cell endplate temperature and cathode bubbler temperature can therefore be used to achieve the desired cathode inlet RH. Relatively low current densities are used as compared to those typically reported in the literature. These low-to-medium current density conditions are interesting in portable and mobile applications where the system typically idles for a significant time. They are also conditions for which anode flooding is most predominant. However, at higher current density electro-osmotic drag tends to dry out the anode [148].

Parameter	Operating Range
Anode inlet RH	0 %
Cathode inlet RH	40 % - 100 %
Anode Pressure	123.6 kPa absolute
Cathode Pressure	120 kPa-125 kPa absolute
Cell Temperature	40 °C, 50 °C, 60 °C
Cell Current	0 A - 30 A
Cell Current density	0 mA cm^{-2} - 566 mA cm^{-2}

Table 3.2 Cell operating conditions

One can notice that the operating temperature is also lower than typical. Due to the software temperature calibration, the intended operating conditions were not attained and the cell was operated at a temperature colder than desired. The thermocouple was re-calibrated after the experiment, and the corrected temperature is presented in the data. As a result of the mis-calibration, the bubbler temperature is higher than the fuel cell temperature for some of the experiments. Therefore, the dewpoint of the air entering the cathode channel is higher than the cell temperature, which is indicated by a calculated value of RH greater than 1 as shown in Fig. 3.6.

In the two subsections below the results of the neutron image processing are presented. The effects of the anode purge and surge events on the measured voltage is demonstrated. Surges and purges can be used as a diagnostic tool to distinguish between operation with anode channel water flooding (anode plugging) or cathode channel water flooding (cathode plugging) conditions. Snapshots of the liquid water thickness images are shown to verify the purging and surging diagnostic capability. These snapshots also clarify differences in the 2-D flow pattern, which affects the quality or ability of the purge event to remove water accumulated in the anode channels. Finally, note portions of the data where the water visualization indicates no anode plugging; however, repeatable voltage improvement is seen after every purge. These data sets indicate that there is (a) an anode nitrogen blanketing problem, and (b) a GDL water mass value below which there is no liquid water flux to the anode channels and hence, anode water plugging is avoided. This information can be used to tune a value for the immobile saturation of liquid water inside the GDL, which is used in later sections to calibrate a simple model.

3.4.1 Channel Water Plugging

Figure 3.6 shows the data from one full day of testing (6 hr continuous operation), and Fig. 3.8-3.10 shows the rest of the data collected on three other days. A detailed discussion of the data shown in Fig. 3.6 is presented first. These data illustrate how changing the operating conditions can drive the system from a state of cathode channel flooding to anode channel flooding at low-to-medium current density. The first subplot of Fig. 3.6a shows the mass of liquid water in each of the four mutually disjoint masked regions, described in Sec 3.3.2, over the entire active area. The next three subplots show the estimated liquid water mass in each of the three layers (anode channel, cathode channel, and the combined membrane/GDL layer). The last four subplots of this figure display the important operating conditions which are typical model inputs [65]: current density (A cm^{-2}), end plate cell temperature ($^{\circ}$C), cathode inlet RH and cathode stoichiometric ratio.

The cell is initially operated at low current density (Fig. 3.6f) and high cathode stoichiometric ratio (CA SR) (Fig. 3.6i), and heaters are used to maintain the endplate temperature at 50°C (Fig. 3.6g). Fig. 3.6h shows the estimated cathode inlet relative humidity (CA RH) which is the ratio of the saturation pressure at the bubbler temperature over that of the cell temperature. At t=783 min the cathode stoichiometry is decreased and water begins to accumulate in the cell as seen in Fig. 3.6b and c. Cathode channel flooding is evident in the neutron radiographs, which can be seen in Fig. 3.7(a) at t = 820 min, and can be inferred by the rapid but small voltage fluctuations. This fluctuation in voltage occurs as

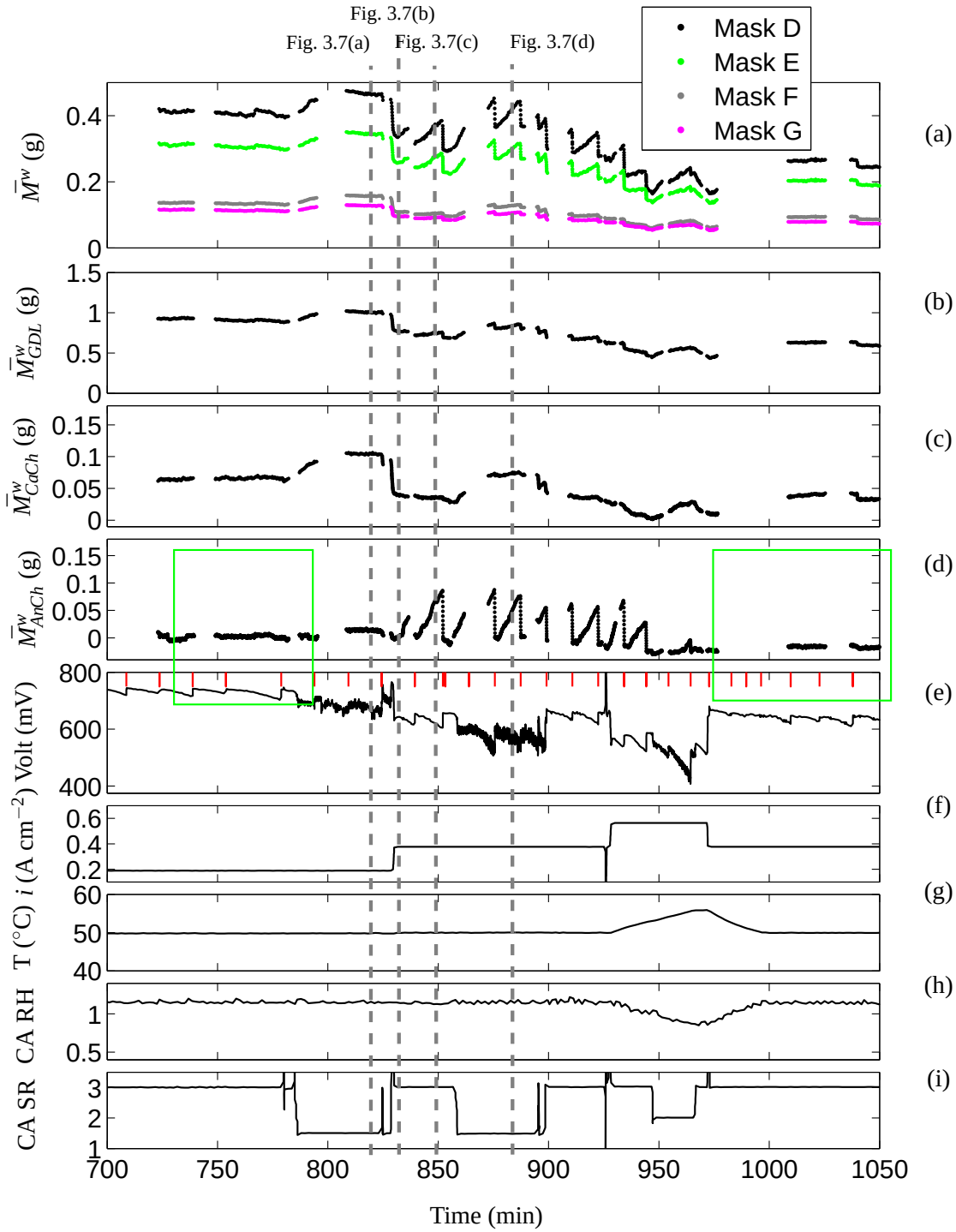

Figure 3.6 Data set 1: Measured total liquid water mass, estimated membrane/GDL and channel liquid water masses, voltage, current density, temperature, cathode inlet relative humidity (CA RH) and cathode stoichiometric ratio (CA SR); fully humidified cathode gas (air) and dry hydrogen inlet. The (red) vertical lines in the voltage subplot indicate an anode purges.

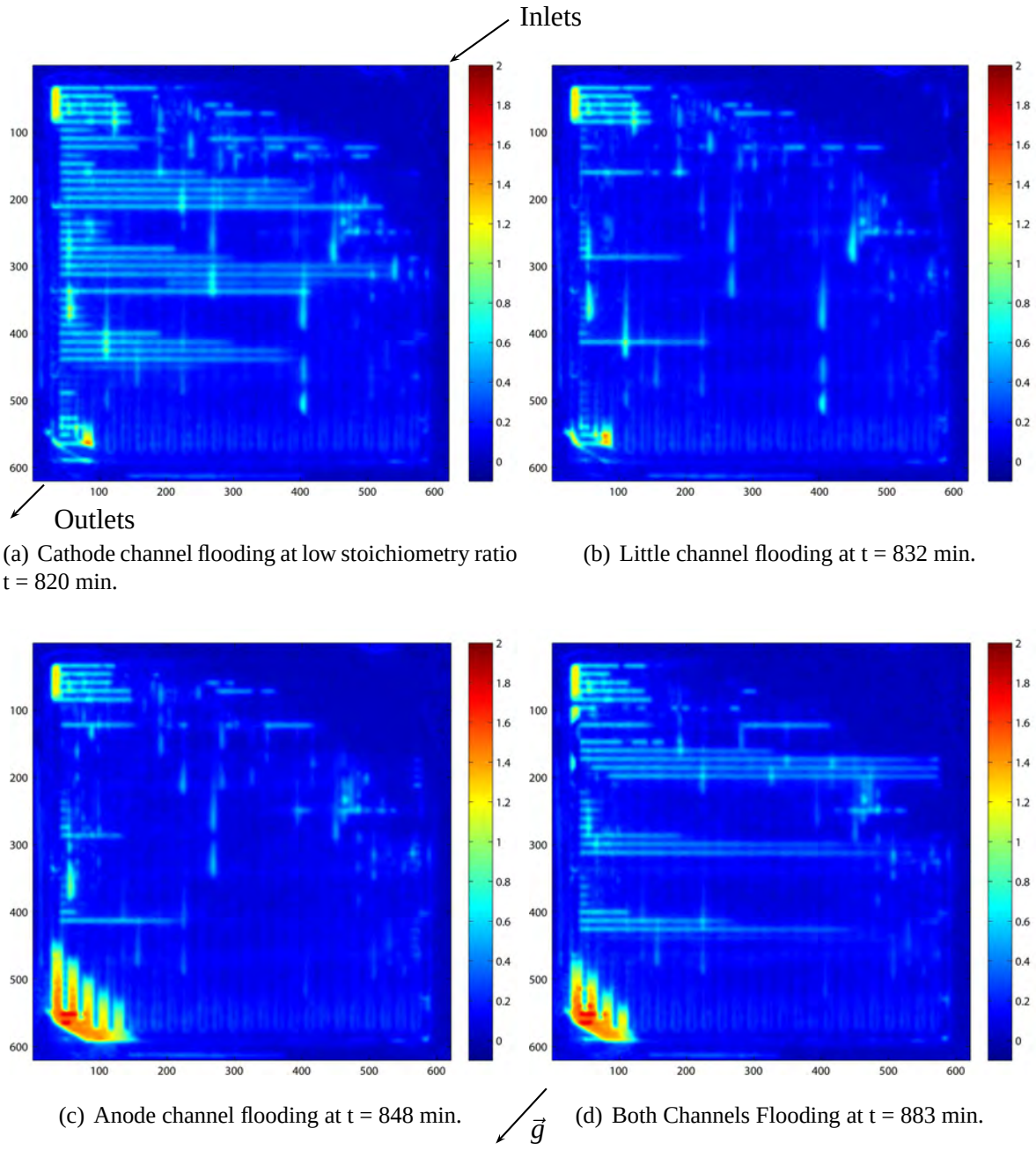

(a) Cathode channel flooding at low stoichiometry ratio t = 820 min.

(b) Little channel flooding at t = 832 min.

(c) Anode channel flooding at t = 848 min.

(d) Both Channels Flooding at t = 883 min.

Figure 3.7 Processed neutron images showing liquid water thickness (mm) under a variety of conditions.

the cathode channels are intermittently plugged with water, and the voltage is insensitive to the anode purges indicating the absence of anode plugging. The the terms flooding and plugging are used to differentiate between the accumulation of water mass in the GDL and channel. Water accumulating in the channels forms slugs which block the flow of reactants along the channel; hence, the adoption of the term plugging.

Figure 3.7(a) also shows the buildup of liquid water after the 180 degree bends in the cathode semi-serpentine flow path as observed by [7]. However, the water in the cathode channel only accumulates after the 180 degree bends on the left side of the image, which corresponds to the "downhill" turnarounds when viewed in the original orientation as shown in Fig. 3.2. The gravity vector, $\vec{g}$, delineates the image rotation relative to the cell orientation. The orientation of the cell and the effects of gravity may have a non-negligible effect on the location of liquid water buildup within the channels [3]. This is different from common modeling assumptions of transport in the GDL, where gravitational effects are negligible [149].

Just before t=825 min the cathode is surged, removing liquid water from the cathode channels, and a sustained voltage recovery of 25 mV is observed. Following the surge, the current density and stoichiometry are both increased. The higher cathode gas velocity more readily removes liquid water from the cathode channel, as seen in Fig. 3.7(b) at t=832 min. This new operating condition eventually leads to anode channel flooding, shown in Fig. 3.7(c) and clearly detected by the large periodic voltage increase following every purge. At t=858 min the cathode stoichiometry is again decreased, leading to a condition in which both anode and cathode channel flooding occurs, as seen in Fig. 3.7(d) and detected by the small voltage fluctuations superimposed by purge-induced voltage improvements.

Data at lower CA RH (70%) also resulted in anode channel flooding, shown in Fig. 3.9 near t = 3700 min. A good example of cathode channel flooding can be seen shortly after startup in Fig. 3.8 at t = 2215 min, where a 25 mV sustained voltage recovery occurs following a cathode surge. Cathode flooding is also present at t = 3554 min in Fig. 3.9, under similar conditions of low CA RH and low current density 189 mA cm^{-2}. At the two higher current densities which were tested, cathode surges do not provide any sustained voltage recovery, indicating that cathode channel flooding is not a problem under these conditions.

3.4.2 Dry Anode Channel Conditions

This section discusses the limitations of the purging and surging methodology used for detecting the approximate location of water in the direction perpendicular to the membrane plane.

The first limitation is apparent where the 2-D distribution of water along the channels is such that a purge or a surge cannot remove a significant amount of water. At lower current density, 189 mA cm^{-2}, the liquid water is more evenly distributed, rather than concentrated at the end of the channel. Due to the low rate of water generation and subsequently small

droplet growth rate, the liquid droplets on the surface of the anode GDL did not grow large enough, during the observed time between purges, to be pulled by the gravity to the end of the channel. It was observed that only liquid water at the end of the anode channel is effectively removed by purging.

This is seen in the buildup of liquid water mass in the anode channel, Fig. 3.8 between t=2200 -2275 min and in Fig. 3.9 between t=3550 -3650 min, which is insensitive to anode purges. At higher current densities, there is a greater liquid production and crossover rate; hence, water collects near the end of the anode channels, as shown in Fig. 3.7(c), and repeatable liquid water transients occur.

The second limitation in using the voltage-purge relation for diagnosing anode water plugging arises from the effects of nitrogen crossover and eventual nitrogen accumulation in the anode. In the event of nitrogen blanketing, an anode purge can also improve the cell voltage. In the collected data, there are cases where the image processing indicates that there is no anode water plugging; however, there is a repeatable voltage improvement after every purge event. Specifically, Fig. 3.10 (t=5400 -5480 min) shows data at higher temperature (60°C) and low CA RH (40 %), where anode channel water is no longer detected in the neutron images. For these conditions, the total water content in the GDL decreases significantly, about half that of the case with a fully humidified cathode inlet, because the water carrying capacity of air increases exponentially with temperature and therefore can remove far more liquid water under these conditions [57, 150]. Dry anode channel conditions with voltage drop between purges are also shown in Fig. 3.8 (t=2475 -2530 min) while operating at relatively low current density (377 mA cm^{-2}), high cathode stoichiometric ratio, high temperature, and sub-saturated cathode inlet flow.

Dry anode channel conditions are also encountered in the first day of testing shown in Fig. 3.6 (t=700-780 min) and (t=965-1045 min) where fully saturated air flow was fed to the fuel cell. Some discussion of these two cases is warranted, as the membrane water dynamics and the thermal dynamics [57] might explain why there is no water anode plugging in these two cases. The period (t=700-780 min) in Fig. 3.6 was after start-up where the membrane might not have been fully hydrated and hence, might have been absorbing water from the surrounding GDLs. At t=925 min, a slow temperature rise of about 5°C is measured at the end plates, following the current density increase to 566 mA cm^{-2}. It is expected that the current increase causes a large spatial gradient in temperature. The thermal history of the membrane impacts the membrane water uptake and conductivity [151, 152]. This thermal history may account for the absence of anode flooding following the return to lower current density and nominal temperature at t=1000 min in Fig. 3.6, conditions which previously (t = 830 min $-$ 850 min) exhibited anode channel water accumulation.

In all the cases where dry anode channel conditions are observed, except the start-up period of Fig. 3.6 (t$\leq$ 780 min), the combined GDL plus membrane water mass, estimated through masking, is less or equal to 0.5 g. This liquid water mass is equivalent to a GDL volume fraction of $s = 0.21$. Because no liquid water is flowing to the anode channel, this value is assumed to be equal to the immobile saturation limit s_{im}. A linear GDL compression of 20% is assumed for this calculation, which yields a compressed porosity of $\varepsilon = 0.67$, and distribution of water evenly between the anode and cathode GDL layers is also assumed.

3.5 Flooding, Plugging and Voltage Response

A consistent correlation between voltage and anode purging is observed at low-to-medium current density under a variety of operating conditions. This relationship can be used to establish a phenomenological model that connects the accumulation of water and nitrogen in the channel with an apparent active area available for the reaction and hence, establish an easily tunable model with low computational complexity for control applications [65, 140].

The hypothesis of a direct effect of anode channel water and nitrogen mass accumulation on voltage is controversial, as most existing models use the decrease of reactant pressure and the effect of liquid water accumulation in the cathode GDL-Catalyst interface on voltage [66, 126] assuming a thin film-model which predicts the blockage of the cathode catalyst interface [99]. A similar argument is used here to formulate an anode channel interfacial blockage which leads to an apparent active area, hence an apparent current density, and consequently a voltage degradation, as shown in Section2.5.

First, test periods are investigated where voltage decay is observed but no channel or GDL water mass accumulation. A simple model using published membrane crossover values for nitrogen [36] confirms the hypothesis that nitrogen crosses over from the air supplied cathode through the membrane, accumulates in the anode, and contributes to the measured voltage degradation. The confirmation of the hypothesis is based on the good match between the predicted and the measured voltage degradation between purges. The exact accumulation of nitrogen in the anode channel has to be confirmed with independent nitrogen concentration measurements, which is the subject Chapter 4.

Second, investigation of data that show anode flooding and voltage decay are used to demonstrate that a simple one-dimensional (1-D) (channel-to-channel through the membrane), isothermal, and lumped parameter model can be used to predict the transient anode water accumulation and voltage behavior well during anode flooding conditions under

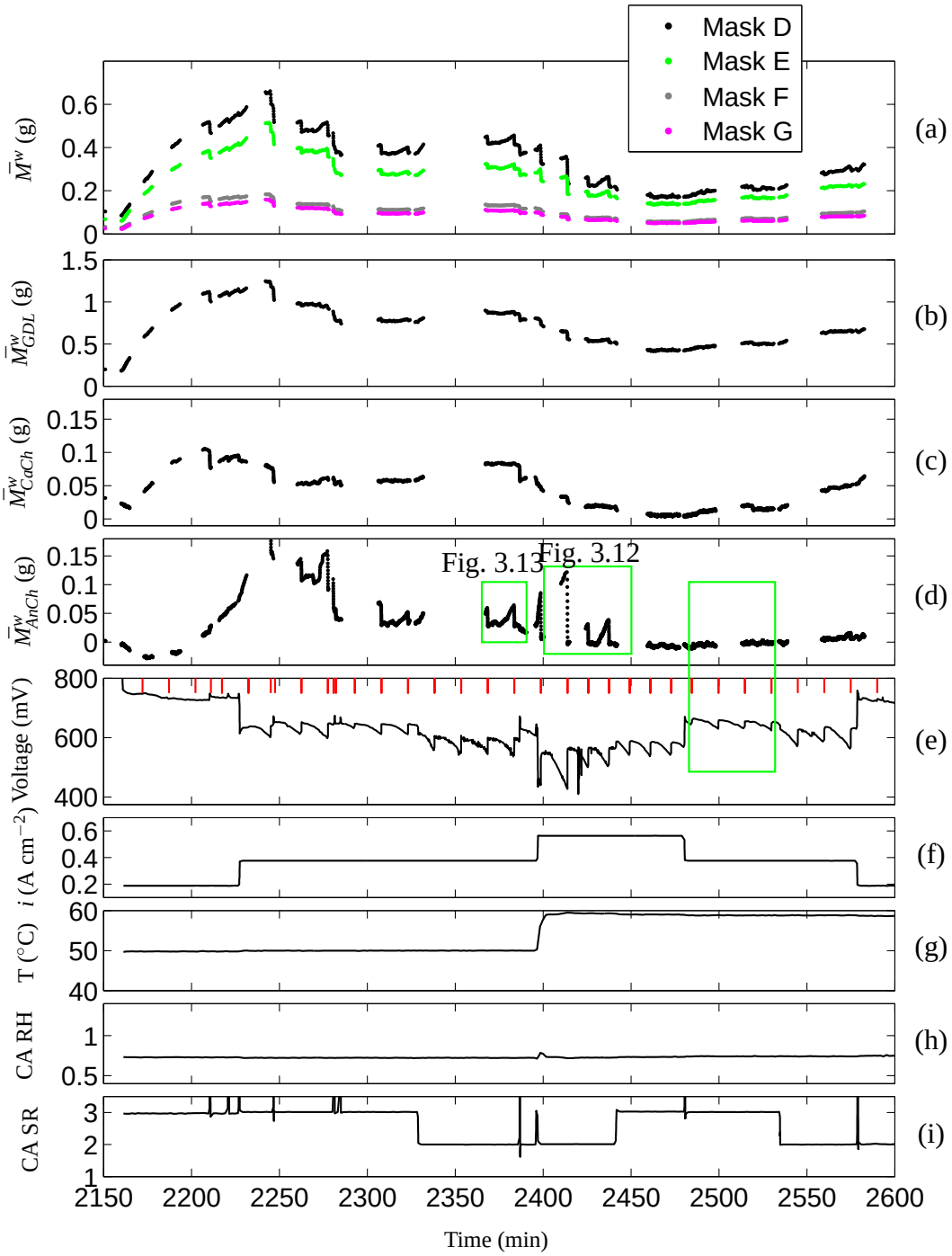

Figure 3.8 Data set 2: Measured total liquid water mass, estimated membrane/GDL and channel liquid water masses, voltage, current density, temperature, cathode inlet relative humidity (CA RH) and cathode stoichiometric ratio (CA SR). Sub-saturated cathode gas (air) and dry hydrogen inlet. The (red) vertical lines in the voltage subplot indicate an anode purges.

dead-ended operation [65, 146, 138].

For the model validation, test periods with anode flooding and without cathode flooding

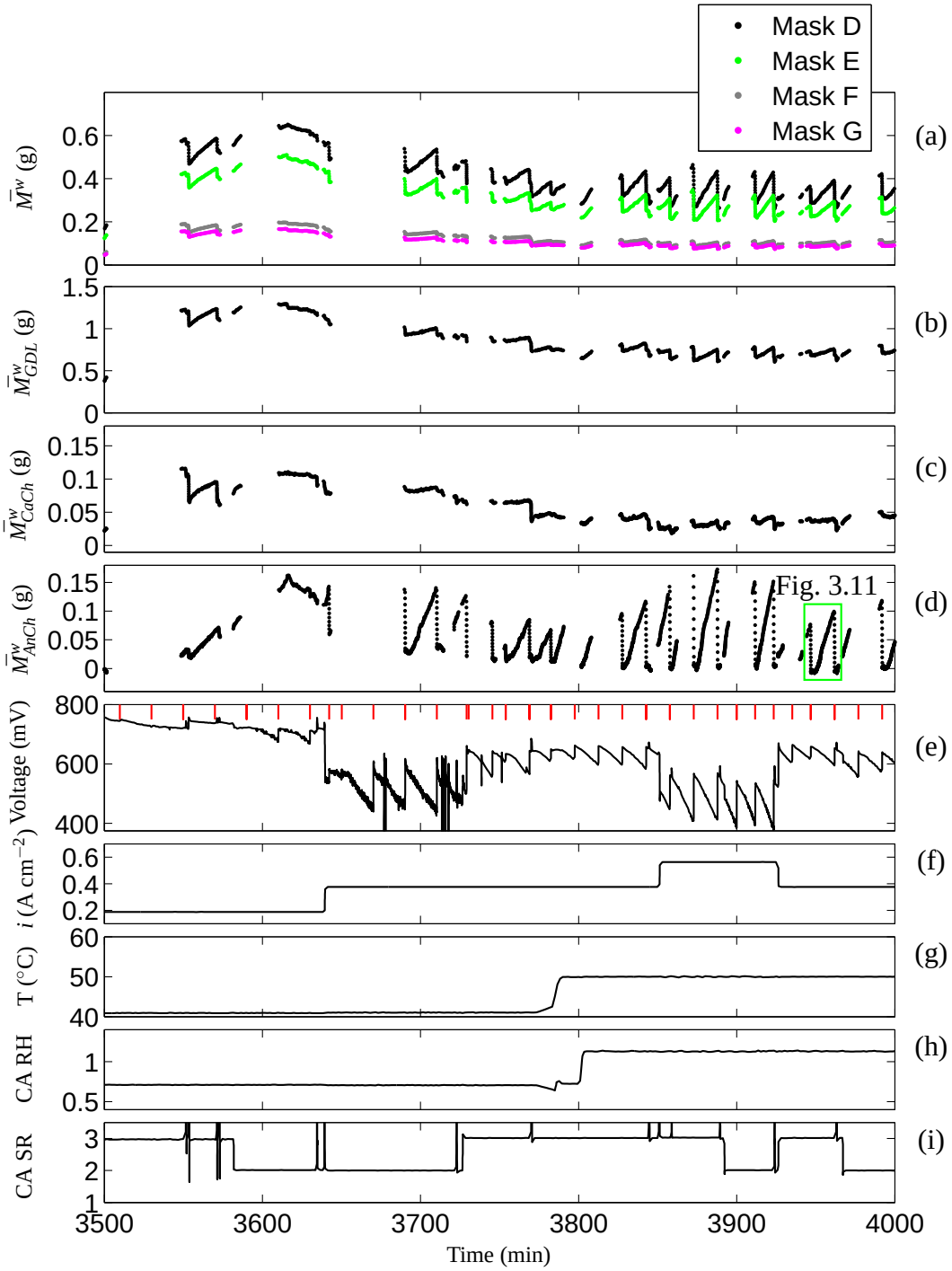

Figure 3.9 Data set 3: Measured total liquid water mass, estimated membrane/GDL and channel liquid water masses, voltage, current density, temperature, cathode inlet relative humidity (CA RH) and cathode stoichiometric ratio (CA SR). Sub-saturated cathode gas (air), switching to fully humidified at t = 3800 min and dry hydrogen inlet. The (red) vertical lines in the voltage subplot indicates anode purge events.

are used. Another detailed graph shows a period where anode flooding and voltage decay exhibit a characteristic two-slope behavior, corroborating the hypothesis of voltage decay

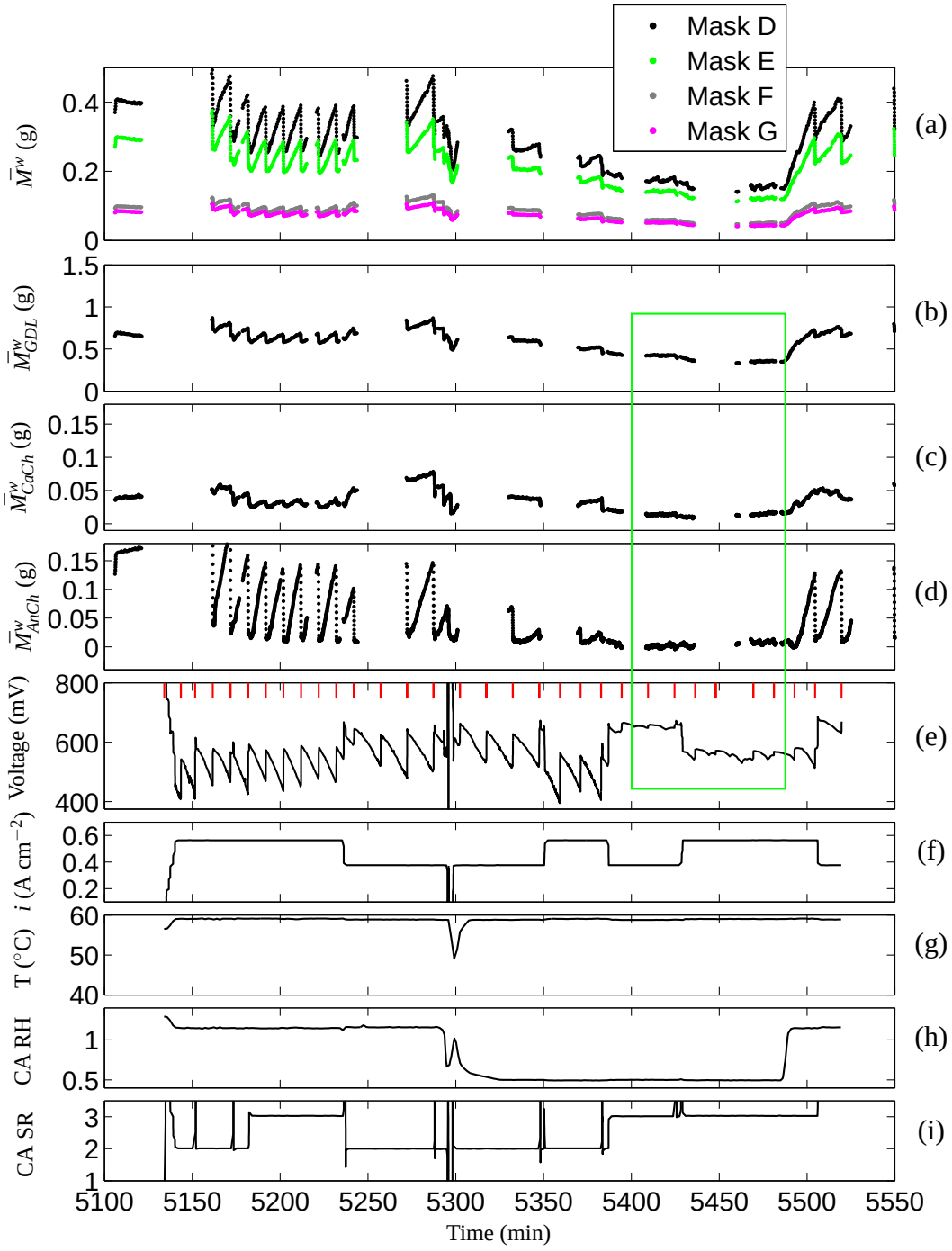

Figure 3.10 Data set 4: Measured total liquid water mass, estimated membrane/GDL and channel liquid water masses, voltage, current density, temperature, cathode inlet relative humidity (CA RH) and cathode stoichiometric ratio (CA SR). Both saturated and sub-saturated cathode gas (air) conditions with dry hydrogen. At t = 3800 min the bubbler is filled with colder water causing a drop in inlet CA RH. The (red) vertical lines in the voltage subplot indicates anode purge events.

due to anode plugging instead of cathode catalyst flooding. Finally, a detailed view of a testing period with concurrent anode and cathode flooding is used for the model validation.

3.5.1 Anode Nitrogen Blanketing and Voltage Response

Figures 3.6, 3.8, and 3.10 contain boxes which highlight a portion of the experiments where a small voltage degradation, 2 mV min^{-1}, is not correlated to any liquid water accumulation. As one can see, the voltage pattern is repeatable between purges despite the lack of any similar pattern in the water observed. Portions of the experimental data indicate that nitrogen accumulation in the anode channels should be responsible for the relatively small (2 mV min^{-1}) versus the larger (5 - 8 mV min^{-1}) voltage drop that is typically observed during anode water plugging conditions.

To investigate the effects of nitrogen, a channel-to-channel lumped parameter mass balance can be used to calculate the rate of nitrogen accumulation using the permeation coefficient $k_{N_2} = 10^{-14}$ mol m^{-1} s^{-1} Pa^{-1} [36]. At the pressure conditions highlighted in Fig. 3.6 between t=960-1045 min, a predicted nitrogen accumulation of 0.15 mg min^{-1} in the anode leads to a drop of hydrogen partial pressure of 2 kPa min^{-1}. Assuming homogeneous channel conditions, the reduction in hydrogen partial pressure affects the cell voltage through the Nernst equation (2.36), and this leads to a voltage drop of only 0.6 mV min^{-1} instead of 2 mV min^{-1} observed here. Because a large change in hydrogen partial pressure alone cannot account for the significant voltage drop observed in the data, an effective active area is modeled to represents the nonblocked (or nonblanketed) area. The effective area can be used to calculate the apparent current density. The reduced area is caused by displacement of hydrogen in the anode channel. Specifically, in a pressure-regulated cell with dead-ended anode, nitrogen will be pushed by the feed gas and accumulate at the end of the channel [36]. So if complete anode channel plugging is assumed to occur when 100% of the anode cross-sectional area has been filled with nitrogen, then the predicted nitrogen accumulation of 0.15 mg min^{-1} will result in a voltage decay of 2.2 mV min^{-1} using A_{app} from Eqn. (2.34), by replacing t_* with the channel depth, $m_{*,an,ch}$ with the anode channel accumulated nitrogen mass, and ρ_* with nitrogen density, using the tuned voltage model presented n Section 2.5.

In the model, the resulting voltage degradation is related to the accumulation of liquid water mass in the anode channel, $m_{l,an,ch}$, which is assumed to form a thin film of thickness, t_{wl}, blocking part of the active fuel cell area, A_{fc}, to give an effective active area, A_{app} in m^2,

$$A_{app} = A_{fc} - \frac{1.3\, m_{l,an,ch}}{n_{cells}\, \rho_l\, t_{wl}} - \frac{1.3\, m_{N_2,an,ch}}{n_{cells}\, \rho_{N_2}\, t_{ch}}. \tag{3.8}$$

The scaling factor of 1.3 is the ratio of the total active area to the anode channel area, since only that surface area at the channel interface can be covered with liquid. In the case of water plugging the thickness of the water layer, t_{wl}, is a tunable parameter that impacts the

rate of voltage decay as liquid water accumulates. A similar notion of reduced area is used in [153] to account for the reduction in fuel cell output power when the anode is filled with liquid water. In the case where nitrogen plugging is considered, Eq. (3.8) can also be used to calculate effective area, but the actual channel depth is used for t_* instead of a tunable parameter. It is most likely that accounting for the diffusion and mixing between hydrogen and nitrogen in the channel using an along-the-channel model will correct for the estimated higher voltage drop. Nevertheless, the simplicity of the model provides a remarkable match with the experimental observations of nitrogen plugging effects on voltage response.

3.5.2 Anode Water Plugging and Voltage Response

A summary of the imaging data indicates that for the majority of the tested conditions, anode water plugging should be considered in order to model the cell performance. Nitrogen should clearly also be considered, but the accelerated rate of voltage decay where water plugging is observed requires a more rapid control action and better modeling to prevent potential damage to the cell. A model which includes the effect of both nitrogen and liquid water on voltage requires a more detailed channel model to determine the reduction in active area. Standard diffusion and density values for the hydrogen and nitrogen gases and a simple along-the-channel model, detailed in chapter 4, indicate that the anode constituents form stratified layers with liquid water on the bottom, followed by a nitrogen-rich and then a hydrogen-rich area moving toward the channel inlet. The resulting fuel cell area, which is unavailable to support the reaction, is given by the sum of the nitrogen-blanketed and water-covered areas. The mass of liquid water accumulated in the anode channel is calculated using well-known equations for the membrane water transport [65, 121, 133, 134] and the one-dimensional (channel-to-channel through-membrane plane), isothermal, two-phase (liquid and vapor) flow of water through the GDL. A detailed description of the water crossover through the membrane, the two-phase flow-through the GDL, and the accumulation of liquid in the channel, is presented in chapters 2 and 5, and in [65].

The neutron imaging data, with the applied masking techniques, confirm the presence of liquid water in the anode channel, as shown in Fig. 3.11. This figure represents a typical purge cycle and is taken from the third day of testing shown in Fig. 3.9. The red vertical lines shown in the voltage subplot indicate anode purge events. Following an anode purge, all of the liquid water in the anode channel is removed and then slowly accumulates until the next purge event. Note that there is little change in the cathode channel water mass between or during purges.

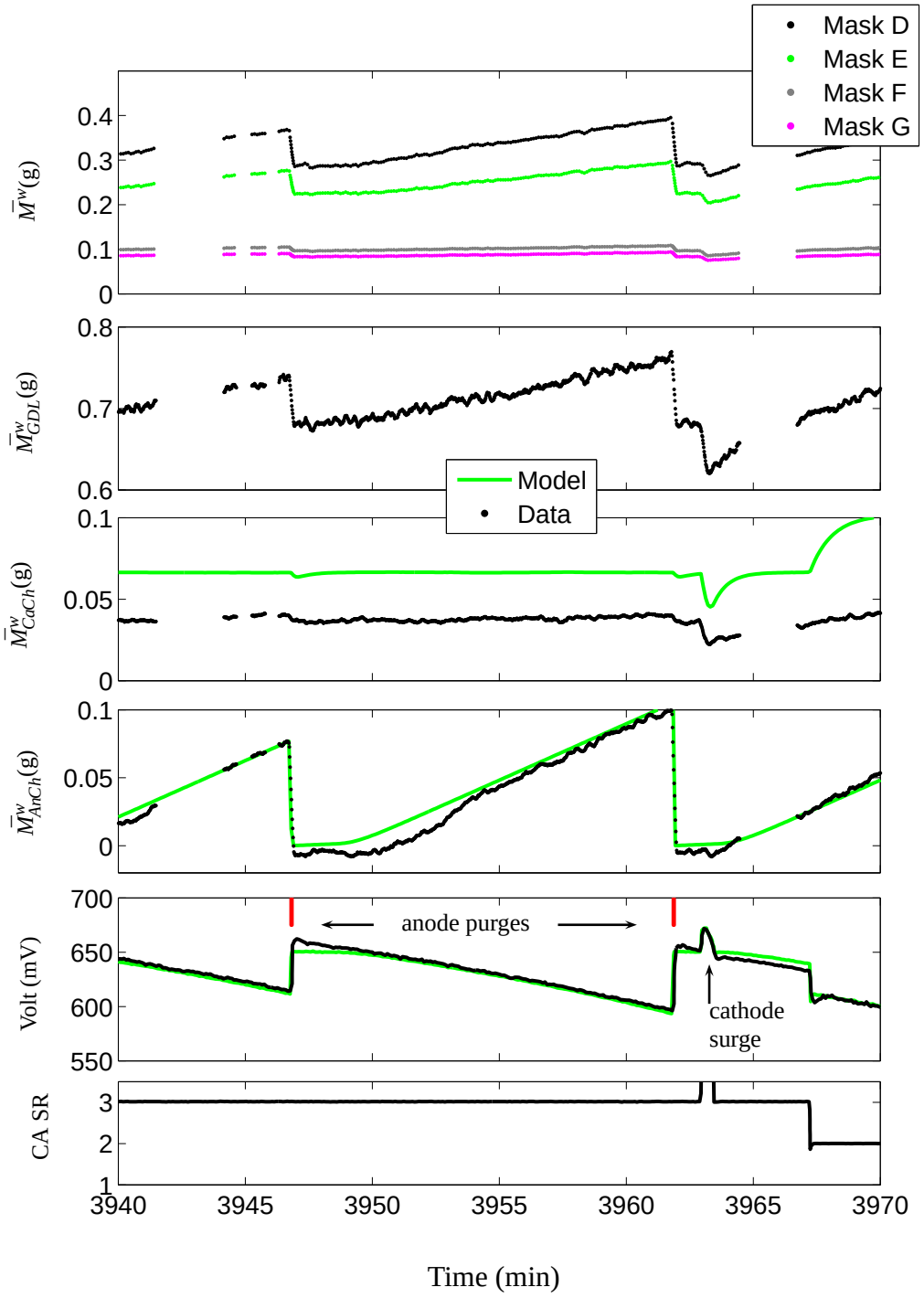

Figure 3.11 Measured cell voltage degradation and liquid water mass accumulation between anode purges, taken from the third data set. These experiments were conducted with fully humidified air at a current density of 378 mA cm^{-2}, a cell operating temperature of 50 °C, and an air stoichiometry of 300 %.

Following the anode purge, a cathode surge is conducted at approximately 3963 min. During the surge, the cell voltage increases due to the higher oxygen partial pressure. However, after the cathode flow rate is restored, the voltage returns to its previous value. The mass of liquid water in the cathode channel decreases as a result of the increased water removal rate with higher gas flow rate during the surge. In some experiments, even where the cathode surge event occurs just preceding the anode purge event, the voltage continues to degrade at the same rate as experienced before the cathode surge. These results indicate that liquid water in cathode channel has little effect on voltage under these conditions. In contrast, following the two anode purges at 3947 and 3962 min, the voltage recovery is significant and sustained until liquid water begins to accumulate in the anode channel again. There exist other operating conditions, where accumulation of water in the cathode is detected and a sustained voltage recovery occurs following a cathode surge.

Figure 3.12, shows no liquid water accumulation in the cathode channel, with anode channel water accumulation between purges. Following the anode purge at t=2425 min, the imaging data shows a period with no water accumulation in the channel followed by a linear increase with time. This distinct, two-slope behavior of liquid water accumulation can be explained by a "strong" anode purge which removes liquid water from the GDL. In this case, water accumulation in the channel has two modes. The first is a slow mode which represents vapor transport through the GDL; with condensation in the GDL occurring primarily near the GDL/CL interface. Once the accumulation of water in the GDL has surpassed the immobile saturation limit [65, 146, 71] the second mode evolves, both capillary liquid and vapor flow into the channel are present, yielding a faster rate of liquid water accumulation in the channel. Hence, following an anode purge which removes water from the GDL, it takes time before water begins to accumulate in the channel again. The observed voltage degradation under this condition is very well correlated with the two-slope liquid water accumulation in the anode channels and has excellent repeatability. The simulated response using the channel-based apparent current density shows an excellent match despite the two-slope behavior. It would be interesting to investigate whether voltage models that depend on catalyst flooding (water accumulation at the membrane catalyst interface) alone can capture the observed behavior.

Figure 3.13 shows the voltage during a substantial change in liquid water mass for both the anode and cathode channels. Specifically, the slow decay in voltage, shown in Fig. 3.13, can be attributed to the stored anode channel water accumulation. Here the observed voltage clearly depends on both cathode catalyst layer and channel water mass. A cathode surge at t=2387 min removes liquid water from the GDL and cathode channel, resulting in voltage recovery attributed to cathode flooding, which could be caused by blockage of

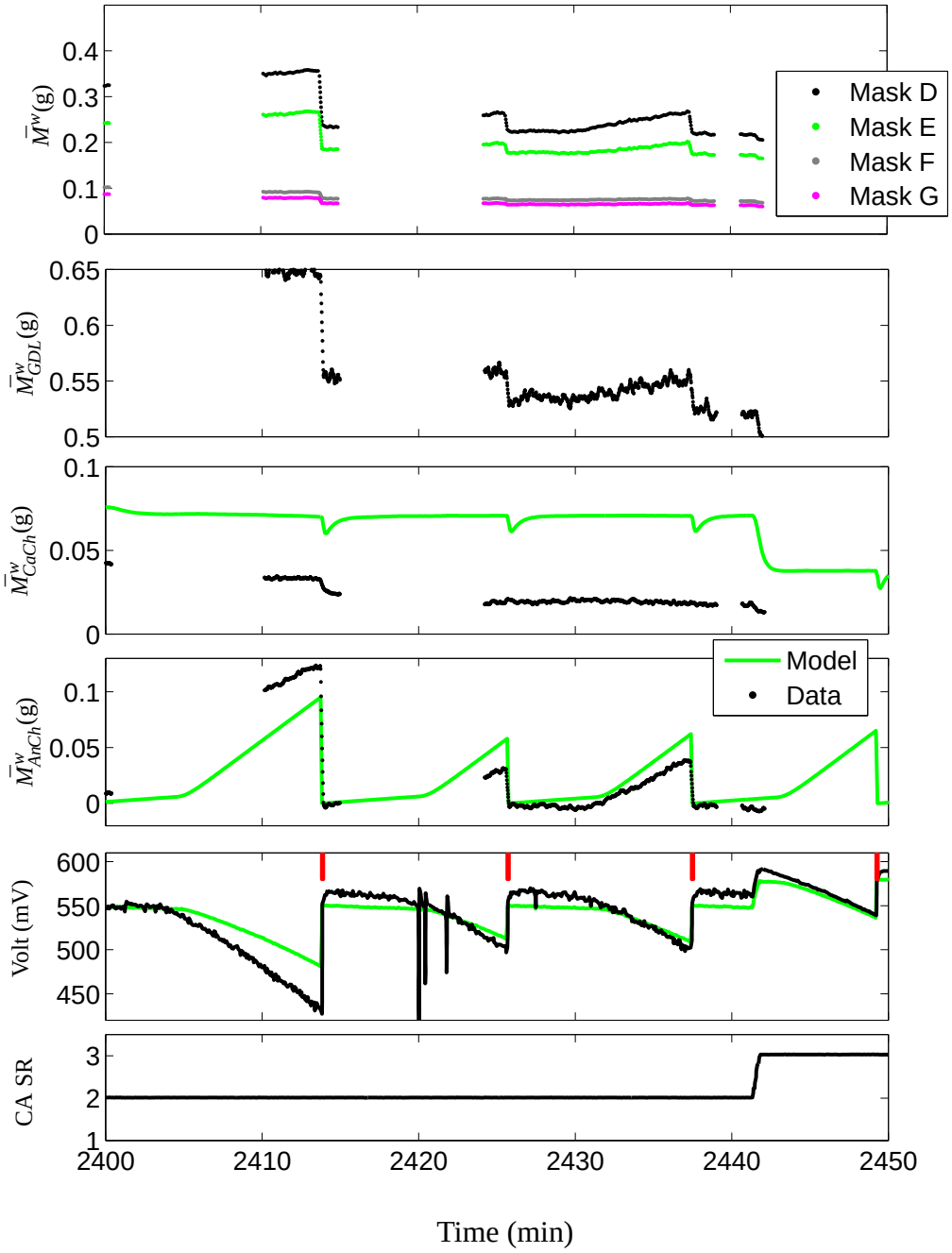

Figure 3.12 Voltage is well correlated with anode liquid water two slope behavior at 60 °C, 566 mA cm^{-2} and with a 75 % relative humidity for cathode gas stream at 200 % stoichiometry.

the catalyst or a reduction in oxygen partial pressure due to channel plugging. The simulation results show that the model prediction is reasonable during these testing conditions. Better prediction accuracy could be expected by including the membrane catalyst domain in the modeling approach, the model employed here is simple enough to allow real-time predictions, even in automotive microcontroller hardware [154].

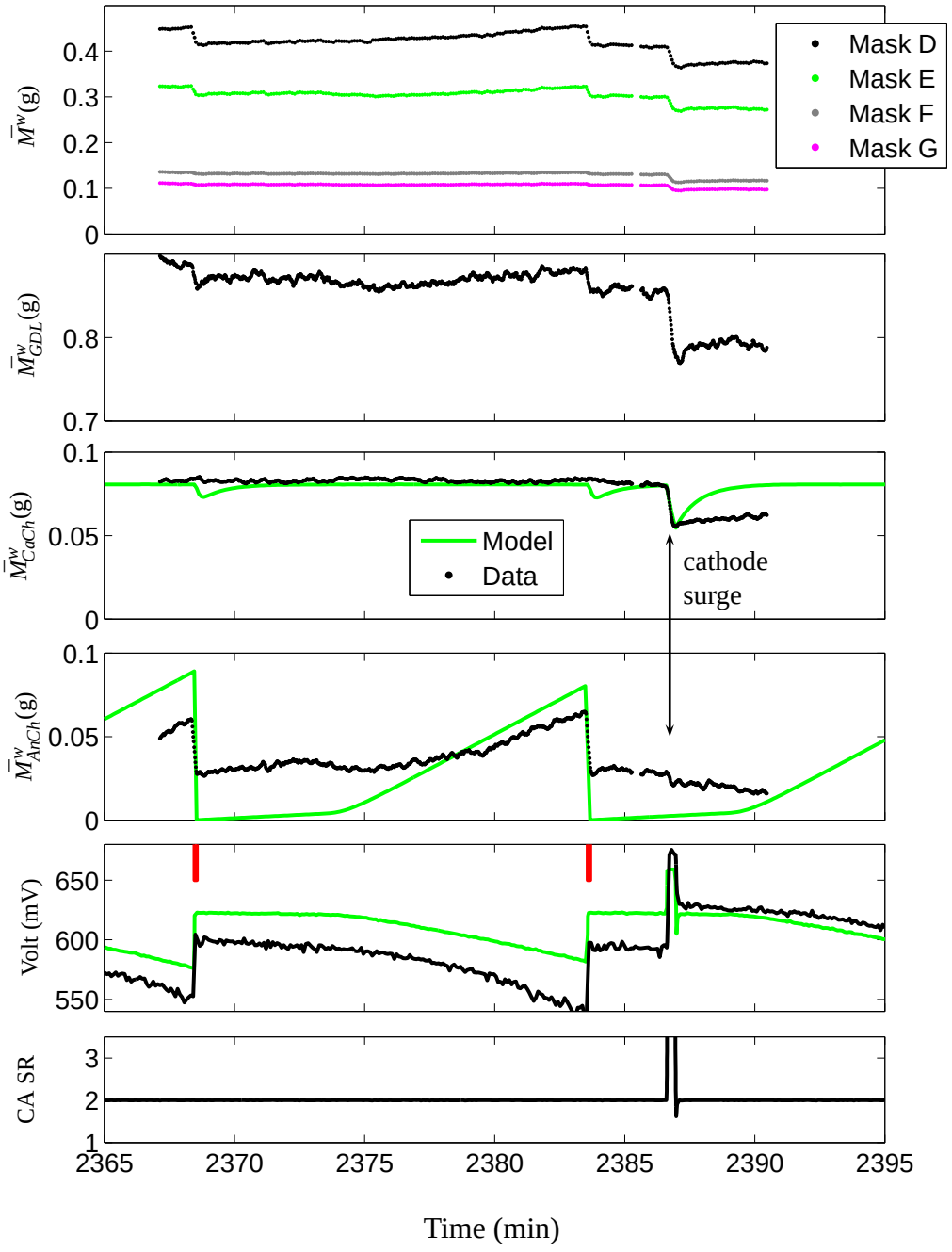

Figure 3.13 Voltage is well correlated with anode liquid water at 50 °C, 377 mA cm^{-2} and with a 75 % relative humidity for cathode gas stream at 200 % stoichiometry.

The data analysis and Fig.s 3.8-3.10 demonstrate that for the majority (80%) of the tested conditions (Table 3.1) the notion of apparent current density, which relates the accumulated mass of liquid water in the anode channel to voltage degradation, can be used to

estimate the cell voltage. This estimate agrees well with the measured value, both between purges as well as during purging and surging events where anode water plugging conditions are observed. Fast voltage responses due to the increase in oxygen partial pressure during surges are also estimated well due to the inclusion of the fast reactant dynamics associated with gas concentrations. For the range of current densities tested, a fully humidified cathode gas stream was sufficient to ensure anode flooding conditions, although at higher current density this may not hold [148]. In the case where the cathode inlet gas is fully humidified, the cathode channel always contains a saturated gas stream; therefore, it can be assumed that there is no vapor pressure gradient along the channel, which implies a uniform boundary condition along the cathode channel and consequently allows us to neglect the variation along the channel and employ a 1-D (through-the-membrane) modeling approach for the water dynamics. A similar argument is used in [155] to show how uniform boundary conditions in a 2-D fuel cell model can be treated as a 1-D partial differential equation system. The model currently is not able to predict anode drying conditions when the cathode inlet RH $< 80\%$, because the assumption of uniform channel conditions in the lumped model may be violated. When a sub-saturated gas stream is supplied to the cathode, there will be a gradient in vapor concentration along the cathode channel, leading to a time-varying and spatially varying boundary condition along the cathode channel. As current density and air flow rate change, the point along the channel at which the gas stream becomes fully saturated will move [57], which effects the net membrane water transport.

3.6 Conclusion

The mass of liquid water in an operating single-cell fuel cell is measured at the NIST neutron imaging facility under dead-ended anode operation. Image masks, based on the cell design, were employed to calculate liquid water mass in the anode versus cathode gas channels and the combined membrane and anode-cathode GDLs. Anode purges and cathode surges were conducted to remove liquid water, correlate the water removal to voltage improvement, and visually confirm the approximate location of the accumulated liquid water inside the fuel cell. The observed voltage recovery during these purges and surges can be employed as a diagnostic tool indicating anode or cathode plugging and flooding.

Anode channel water plugging followed by a significant (5-8 mV min^{-1}) voltage decrease was observed even without cathode channel water plugging, indicating the importance of anode flooding to cell performance. Further understanding the fuel cell performance limitations associated with anode operating conditions is needed. The observed

voltage and liquid water accumulation in the anode channel exhibit a distinct and repeatable two-slope transient behavior after an anode purge. This points to a direct phenomenological relationship between the mass accumulated in the anode channel and the cell voltage. Such a relation can be explained using the notion of apparent current density and a simple 1-D (through the membrane) model can capture the observed dynamic fuel cell behavior under a wide range of operating conditions.

Chapter 4

Nitrogen Front Evolution in Purged PEMFC with Dead-Ended Anode

This chapter details our August 2008 experiments[1] at NIST with simultaneous GC measurement and neutron imaging.

4.1 Introduction

The dynamic behavior of Fuel Cell (FC) operation under Dead-Ended Anode (DEA) conditions is modeled and measured in this chapter. Although a flow-through operation is used on both the anode and cathode of most laboratory/experimental hydrogen Proton Exchange Membrane Fuel Cell (PEMFC) systems, the fuel utilization of the anode flow-through operation is too low for commercial and portable systems. To increase the flow-through utilization, anode recirculation is employed but the required hydrogen grade plumbing and hardware (ejector/blower) adds weight, volume, and expense to the system [34, 35]. Additional complexity is also added to the balance of plant with the use of external humidification to prevent over-drying of the membrane. However, a DEA can be fed with dry hydrogen which is regulated to maintain anode pressure. In this configuration hydrogen is supplied at exactly the rate needed to support the reaction. FC operation with dry hydrogen using a dead-ended system architecture is possible because water crossing through the membrane is enough to humidify the fuel. The use of a pressure regulator instead of a mass flow controller and lack of anode inlet humidification can yield a system with lower cost and weight.

The only problem with this architecture is that nitrogen, from air fed into the cathode, can also cross the membrane, driven by the gradient in partial pressure, creating a blanket

[1] Note the cathode channel end-plates have been re-machined to resolve the manufacturing defect which was present in the previous data set. Also a defect in the ASi detector mounting plate which caused decreased spatial resolution was corrected since the previous data were collected.

of N_2. The humidified cathode and the dry fed anode cause a large water vapor gradient across the membrane. This gradient drives excess water into the anode, which can cause significant liquid water accumulation. Unlike water vapor whose maximum partial volume is dictated by temperature, liquid can fill the entire free space and block the flow of reactants, also known as channel plugging. The accumulation of liquid water and nitrogen in the anode channel (AN CH) is first observed near the outlet of the channel. Both gravity and gas velocity driven by consumption of hydrogen pull these heavier molecules toward the bottom of the channel. As the mass accumulation continues, a stratified pattern, which is stabilized by the effect of gravity, develops in the channel with a hydrogen-rich area sitting above a hydrogen depleted region. The boundary between these regions is a time-varying front, which proceeds upward toward the inlet [41]. The mass accumulation physically blocks hydrogen gas from reaching the anode catalyst sites, which is the mechanism for the experimentally observed and recoverable voltage degradation [36, 42, 8]. The accumulation of N_2 and H_2O initially leads to larger concentration losses due to decreasing hydrogen concentration near the bottom of the AN CH. When a critical amount of N_2 accumulates in the channel, it completely blocks H_2 from reaching the catalyst, effectively shrinking the active area of the cell, causing larger activation potential in the cathode. This two-stage mechanism is clearly visible in all experimental conditions and scales with operating conditions such as load current density, relative humidity (RH), and stoichiometric ratio (SR) in the cathode.

Purges of the AN CH volume are necessary to clear the reaction product and inert gas from the channel. An anode purge event consists of opening a downstream solenoid valve, which creates a brief, high velocity flow through the anode, removing liquid water and nitrogen. After the purge, the catalyst area contributing to the reaction increases and, hence, the measured voltage increases. Understanding, modeling, and predicting the front evolution and overall dynamics in DEA FC would allow judicious choice of purging interval and duration. Better purging strategy can reduce the H_2 wasted during purges and avoid over drying the membrane. The operation of a PEMFC with hydrogen starved areas can also lead to carbon corrosion [30, 2, 156]; therefore, the study of these operating conditions and the derivation of controllers to schedule anode purges are critical for DEA operation and prolonging stack life.

For a fixed purge period and duration, the FC reaches a stable cyclic behavior, typically within a few purge periods, with both consistently repeatable voltage degradation rates between purges and voltage recovery with each purge. Repeatability of the front evolution is verified with in-situ neutron imaging, measuring the liquid water front. Gas Chromatography (GC) is also used to measure the hydrogen and nitrogen concentrations at a specific

location in the AN CH (see Fig. 4.1) which is discussed later. Gravity, buoyancy, and channel orientation help establish these statistically repeatable and large spatiotemporal variations with hydrogen starvation fronts. Figure 4.2 shows typical spatial and temporal patterns of liquid water thickness and associated measurements during DEA operation with infrequent anode purging events. The stratification of the hydrogen/nitrogen fronts and the gravity-driven liquid water in the channels also provide a unique modeling paradigm and distinct conditions augmenting earlier work [3, 153, 8, 22, 21, 157] that has not been studied extensively before despite several strictly experimental results [40, 5, 39].

This chapter elucidates the DEA hydrogen PEMFC behavior, specifically by first introducing the experimental setup, examining the data, and then proposing a simple along-the-channel model. The model is then used to explain the observed voltage behavior during DEA operation. Because accumulation of both liquid water and nitrogen in the AN CH of a PEMFC operating under dead ended conditions contributes to the recoverable voltage degradation, experiments are devised to characterize the relative effects of both constituents using simultaneous in-situ measurements of both nitrogen and liquid water. Anode purges and cathode surges, when coupled with voltage measurement, can be used as a diagnostic tool for determining the location of water flooding and the impact of nitrogen blanketing in the AN CH. An anode purge, which is a short duration, high flow rate of gas though the anode initiated by opening a downstream valve, removes both liquid water and nitrogen gas from the AN CH and recovers the voltage drop caused by a reduced active area on the anode side. A cathode surge is a momentary increase in the air flow rate supplied to the cathode. The excess air increases the partial pressure of oxygen in the channel, which leads to increased voltage for the duration of the surge. The excess air flow rate can also remove water from the cathode channel (CA CH) and cathode GDL, which leads to an improvement of the FC voltage after the surge relative to the value before initiating the surge.

Finally, the data are compared with a model that captures the relative impact of each process on the measured cell voltage. In [41], the effects of nitrogen accumulation driven by convection are investigated. This model improves upon previous work by including diffusive terms in the AN CH and a physics based voltage model, which accounts for membrane water content with a distributed current density. The correlation of measurements of voltage, liquid water mass, and AN CH gas concentration are used to develop and validate a model of PEMFC under DEA operating conditions. Once properly calibrated, this model can be used for anode purge scheduling and stack health monitoring. Snapshots of the data are presented to demonstrate the repeatability of the observed phenomena and to provide comparisons with the model. To prevent confusion and clarify the observed phenomena,

the term *flooding* is used to describe the accumulation of liquid water in the GDL or catalyst layer, and the term *plugging* is used to refer to liquid water in the channels, which blocks or hinders the flow of gas through the channels [43]. The term *blanketing* is used to designate N_2 mass accumulation in the AN CH, which prevents hydrogen from reaching the catalyst layer.

4.2 Experimental Setup

A Shimadzu GC-17A gas chromatograph was used to measure the hydrogen, nitrogen, and oxygen content of gas samples taken from the AN CH of a PEMFC during dead-ended operation. Simultaneous measurement of the liquid water distribution inside the FC was acquired via neutron imaging at the National Institute for Standards and Technology (NIST), in Gaithersburg, MD [145, 8].

4.2.1 Configuration and Operating Conditions

The tested fuel cell has an active area of 50 cm^2. The anode gas flow path consists of 25 parallel straight channels with a depth of 1.78 mm and a width of 2.08 mm. The anode land width is 0.838 mm and the channel length is 7.3 cm. The anode channels are oriented on a 45° angle and connected at the top and bottom of each channel by a manifold, as shown in Fig. 4.1. A supply of dry pressure regulated hydrogen, at 4.5 psig is fed to the dead-ended anode. As hydrogen is consumed in the reaction, the pressure regulator maintains constant pressure in the anode channel, effectively maintaining operation at hydrogen utilization of one. A solenoid valve located downstream of the fuel cell anode can be periodically opened to purge the anode volume, as shown in Fig. 4.1. This valve is referred to as the Purge Valve (PV). An adjustable valve is located downstream from the anode PV to reduce the pressure drop and flow during a purge. The valve is adjusted before starting the experiment and remains fixed. The steady-state flow rate during purging is measured to be 1 SLPM of hydrogen. The value N_{purge} listed in Table 4.3, is used to model this outlet flow. Due to the small diameter passageway between the anode channels and the outlet manifold of the FC, liquid water may impede the flow of gases during the initial portion of a purge. Another solenoid valve is located downstream, connected by capillary tubing, to allow gas sampling from the anode channel. This solenoid valve is referred to as the Sampling Valve (SV) and is described in section 4.2.2. A micro-controller is used to actuate the solenoid valves precisely in time and control the purge event period and duration.

A traditional flow-through architecture with air is used on the cathode side with a bubbler-type humidifier. A backpressure regulator downstream from the cathode maintains the pressure between 3.5 and 4.5 psig, depending on the flow rate. The cathode channels have a nine-pass semi-serpentine flow path consisting of five parallel channels. Typical cathode flow rates range from SR 1.5-3 (oxygen supplied / oxygen consumed). Due to the use of air on the cathode, the gas velocities in the channel are much higher than a system running on pure oxygen at the same SR. The Relative Humidity (RH) of the gas stream is varied between 50 and 100%. Cathode surges, which are short duration (1-2 s) increases in the air flow rate (up to SR 10), are used during the experiment to remove liquid water from the cathode channels and to diagnose the extent of cathode channel plugging. The cathode flow field is aligned perpendicular to the anode channels, but the inlets and outlets are co-located at the upper and lower corners of the cell, respectively. As a result, the system behavior can be approximated by an equivalent co-flow model, as discussed in Sec. 4.4.

4.2.2 Gas Chromatography Setup

The setup shown in Fig. 4.1 illustrates the interconnection of the GC equipment and fuel cell. A heated capillary tube is inserted into the last anode channel (near the edge of the cell), 3 cm from the bottom corner, as shown in Fig. 4.1. The 0.005 in. diameter capillary tube is connected to an electrically actuated six-port rotational valve. A sampling valve (SV) is placed downstream from the six-port valve which, when opened, allows for filling of the sample loop (SL) from the fuel cell anode channel when the six-port valve is in position A. After a sample is collected in the SL and the SV is closed, the six-port valve is rotated to position B, and the high pressure carrier gas (helium) pushes the sample into the GC for analysis.

Ultrahigh purity helium is used as the carrier gas and supplied at a pressure of 200 kPa gauge. This produces a steady flow of 12 ml min^{-1} to the GC. A Thermal Conductivity Detector (TCD) is used for gas detection. As a result of the choice of column (Heyesep D column Restek, 100/120 mesh, 3 m length, 1 mm inner diameter), the measurement of water vapor is not possible due to the very long elution time for water in the column. The difference in retention times of the GC for hydrogen and nitrogen measurement constrains the maximum sampling rate at one sample every 40 s. The SV is opened for 1 s, during which ≈ 300 μl of gas is removed from the anode channel (hence, the sample volume is less than 5% of the total anode volume). The total anode volume is 6500 μl. Only the last 5 μl of the sample are trapped in the sample loop and then pushed into the GC when the six port valve is rotated. The capillary tubing, six-port rotating valve, and SL are maintained

at a constant temperature of 110 °C to ensure that a consistent sample concentration is delivered to the GC and to prevent condensation in the tubing. Details on the GC calibration can be found in the Appendix.

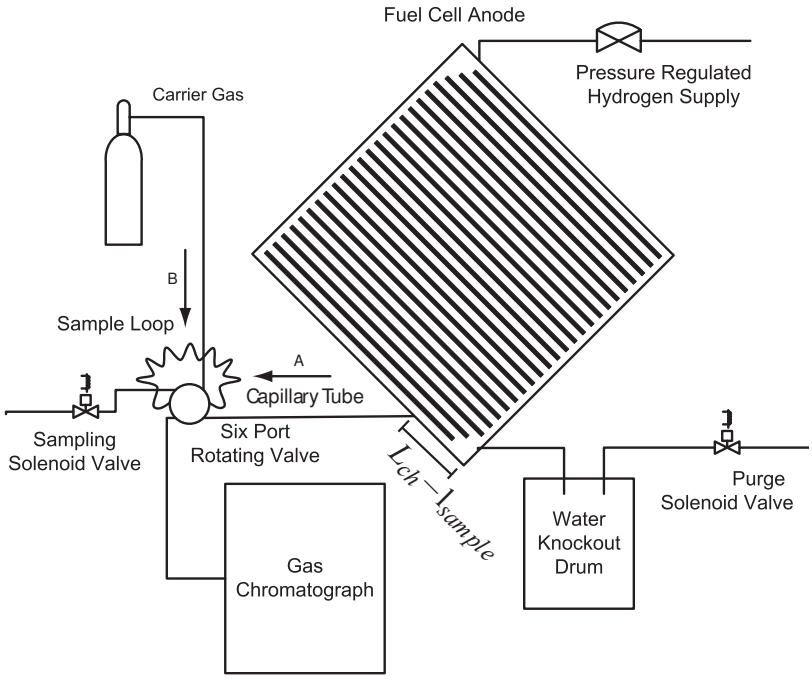

Figure 4.1 Illustration of anode flow-field orientation and GC setup. Flow through the six-port rotating valve changes based on actuator position. In position A, the flow-through of the SL is from right to left, the FC is connected to the SL and SV, whereas the carrier gas flows to the GC. In position B, the flow through of the SL is from top to bottom, the carrier gas is connected to the SL and GC, whereas the FC is connected to the SV.

4.2.3 Neutron Radiography

Neutron radiography is an in situ, nondestructive test that involves placing the fuel cell in a beam of neutrons and measuring the change in beam intensity as it passes through the fuel cell. The decrease in beam intensity is caused primarily by neutron interaction with liquid water in the fuel cell. By comparing the image intensity with that of a known dry fuel cell, the two-Dimensional (2-D) distribution of liquid water thickness values in the plane perpendicular to the beam can be calculated [8, 48]. Six of these processed images, showing water thickness values in millimeters, are presented in Fig. 4.2, where the images are selected from the data set shown in Fig. 4.3. Fig. 4.2(a) and Fig. 4.2(b) clearly shows anode channel water accumulation and the effectiveness of the anode purge in removing water from the channel. Fig. 4.2(e) and Fig. 4.2(f) shows the effect of cathode surge at re-

moving water from plugged cathode channels. Fig. 4.2(c) and Fig. 4.2(d) shows the small reduction of the anode channel water plugging, which occurs during repeated anode sampling. During this period, the voltage continuously improves, as shown in Fig. 4.3, which is the combined effect of nitrogen and liquid water removal from the channel. Nitrogen is removed with the gas sample and liquid water droplets are dislodged by the pressure variations in the channel due to the sampling and fall to the bottom of the channel via gravity.

The time-series sequence of neutron images is further processed in two ways so that the amount of data is reduced and the relevant features are easier to visualize over time. The first method of data reduction is to estimate the total liquid water mass in each of the three layers; the Cathode Channel (CA CH), Anode Channel (AN CH), and the combined membrane/GDL sandwich layer, by comparing the local water distributions corresponding to the different combinations of channels and lands, as described in [8]. These values are shown in the fifth and sixth subplots of Fig. 4.3 and Fig. 4.4, and help identify the presence of GDL water flooding or channel water plugging. To make an inference about the channel water mass from the 2-D projection of water distribution in the FC, it is assumed that locally, the GDL water content is uniform in the rib and channel areas. If this assumption is not valid, this algorithm overestimates the GDL water content (attributing too much of the measured water mass to the GDL) and underestimates the channel water content. Computational fluid dynamic models have demonstrated water accumulation to be greater under the ribs [158] for single serpentine co-flow channels under certain operating conditions. Another plausible scenario is that the high gas flow rate in the cathode channel could have a Venturi effect, drawing liquid from the GDL, when the water saturation is above the immobile limit, which could explain the correlation in water removal. It is not possible to determine if the correlation (a decrease in total water masses) between the GDL and cathode channel during a surge, as shown in Fig. 4.3 at t=3400 s, is physical or an artifact, given the present set of measurements. Future work, using neutron imaging with the beam-direction parallel to the membrane, will be used to investigate the relationship between GDL and channel liquid water removal. This uncertainty in the location of water accumulation does not impact the nitrogen accumulation or voltage degradation rates measured or modeled in this chapter, and conditions with less channel water accumulation are chosen for model validation.

The second method of analysis quantifies the fractional area coverage by liquid water and is shown in the seventh subplot of Fig. 4.3 and Fig. 4.4. Hence, the image processing provides information for (a) the total liquid water mass, which is a volume average along the path of the beam at a specific time and (b) information about the distribution of

water within the FC, specifically the membrane area that is exposed to liquid water. This additional information is important for modeling because of the difference in membrane properties, proton conductivity and permeation rate, as a function of membrane water content. The fractional area coverage is calculated for two different water thickness values: Water thickness values greater than 0.3 mm indicate the presence of water in the channels, and values greater than 0.05 mm are chosen to indicate the start of GDL hydration, which also indicates an area with higher membrane water content.

4.3 Experimental Results

The data listed in Fig. 4.3 and 4.4 represent the dynamic responses of a PEMFC; there are changes in air flow, current density, cathode inlet RH, and temperature, as indicated in the upper subplots of these figures. In the time period before what is shown in Fig. 4.3, the FC was operated for several hours at 55°C, with a low current density (0.2 and 0.4 A cm^{-2}) and a fully humidified cathode inlet. The data in Fig. 4.4 follow Fig. 4.3 after the cell was dried at 50% cathode inlet RH for 1 h.

The repeatable and recoverable voltage decay, which is caused by mass accumulation in the anode, can be seen in the voltage plot, with the solid line type in the fifth subplot of Fig. 4.3 and Fig. 4.4. The anode purge events indicated by the black vertical lines in the fourth subplot precede each of the largest voltage improvements. Cathode surges are also correlated with voltage improvement, as discussed in the following section.

An important feature of the observed voltage dynamic is the two-sloped decay. A slow initial decay, which can be attributed to the dilution of hydrogen in the anode, is followed by a steeper linear decay, which marks the development of a hydrogen depleted region that is covered by a blanketing N_2 front moving upward toward the inlet. Various operating conditions are selected to demonstrate the complex phenomena occurring during the DEA operation.

Table 4.1 summarizes the operating conditions depicted in the following figures and discussion. The operating conditions are described using the following notation: (*i*#_T#_SR#_RH#), where the number following *i* denotes the current density in A cm^{-2}, *T* represents temperature (°C), SR is the cathode stoichiometry, and RH is the cathode inlet RH. The data sets are available on-line at `http://orion.engin.umich.edu`.

Both N_2 blanketing and liquid water plugging could displace H_2, preventing it from reaching the catalyst sites. To study the relative effects of both constituents, portions of the data set corresponding to conditions with and without anode water accumulation are

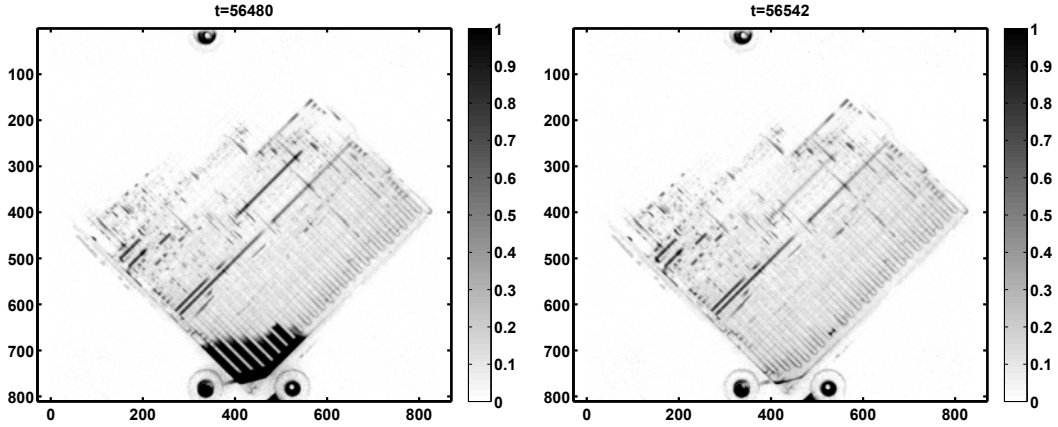

(a) Before Purge (b) After Purge

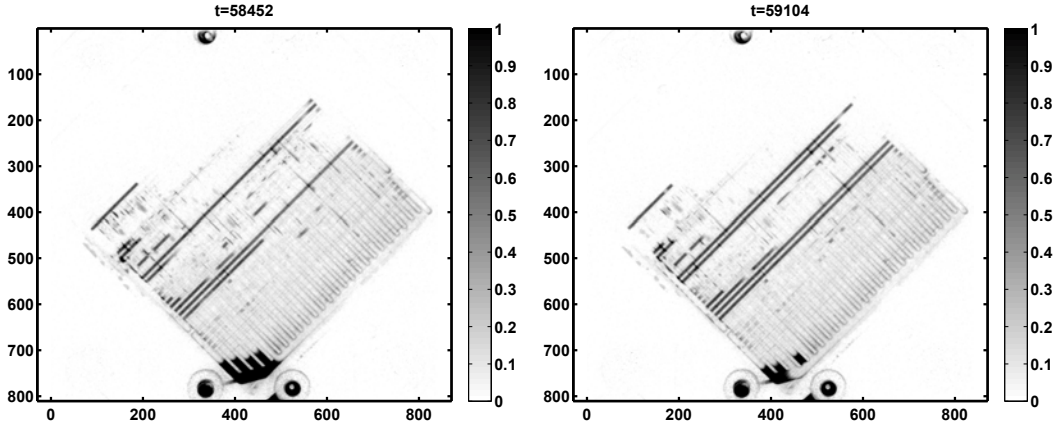

(c) Low Voltage (d) Before Purge

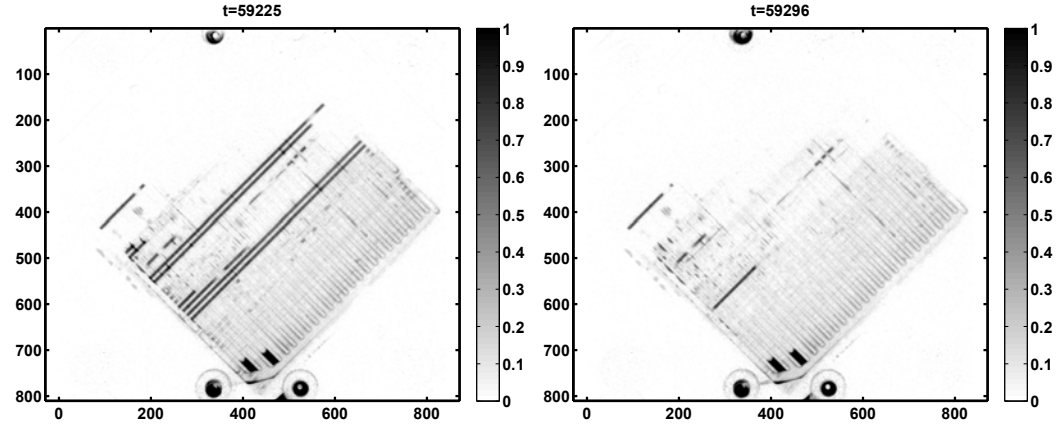

(e) After Purge / Before Surge (f) After Surge

Figure 4.2 Neutron images corresponding to the events shown in Fig. 4.3, from sequential purge cycles. Image intensity represents liquid water thickness in mm.

identified. In this work, lower cathode inlet RH (60%) cases are used for the investigation of a single phase channel model; hence, the influence of N_2 accumulation on voltage can be separately identified. The lack of anode channel plugging is verified from the neutron radiography data.

The operating conditions for case 5 are (*i*0.4_T60_SR3_RH60), as shown in Table 4.1, which are medium current density, 60° C, and high flow rate of sub-saturated air supplied to the cathode. This case is shown in Fig. 4.4, and is chosen to represent a single phase condition for model comparison in section 4.5.

Table 4.1 Select Cases From Data Set for Model Comparison

T=50 C

RH \ SR	Low (2)	High (3)
Full	[1], 8	[6], (7)
Mid		

T=60 C

RH \ SR	Low (2)	High (3)
Full	11	[2], (9), [10]
Mid		

OPC x Current Density
(x) 0.2 A cm^{-2}
[x] 0.4 A cm^{-2}
x 0.6 A cm^{-2}

T=65 C

RH \ SR	Low (2)	High (3)
Full		
Mid	3, [4]	[5]

4.3.1 Cathode Surges versus Anode Purges

In the DEA operation of PEMFCs, anode purges and cathode surges, when coupled with voltage measurement, can be used as a diagnostic tool for determining the location of water flooding and the impact of nitrogen blanketing in the anode channel. An anode purge, which is a short duration, high flow rate of gas through the anode initiated by opening the PV, removes both liquid water and nitrogen gas from the anode channel and recovers the voltage drop caused by the reduced active area on the anode side. A representative section of the experiments is shown in Fig. 4.3. The first anode purge at t=680 s removes 0.19 g of liquid water from the anode channel and the voltage improves by 130 mV following the anode purge, as shown in the fifth subplot of Fig. 4.3. Neutron images, from before (Fig. 4.2(a)), and after (Fig. 4.2(b)) the purge, confirm the removal of liquid water from the anode channel.

A cathode surge is a momentary increase in the air flow rate supplied to the cathode. The excess air increases the partial pressure of oxygen in the channel, which leads to an increase in the measured cell voltage for the duration of the surge. The excess air flow rate also removes water from the cathode channel and cathode GDL, which leads to an improvement of the fuel cell voltage after the surge relative to the value before initiating the surge. This change in voltage should be related to the amount of water removed from the cathode channel, GDL, or catalyst layer. Also, the resistance to O_2 transport between

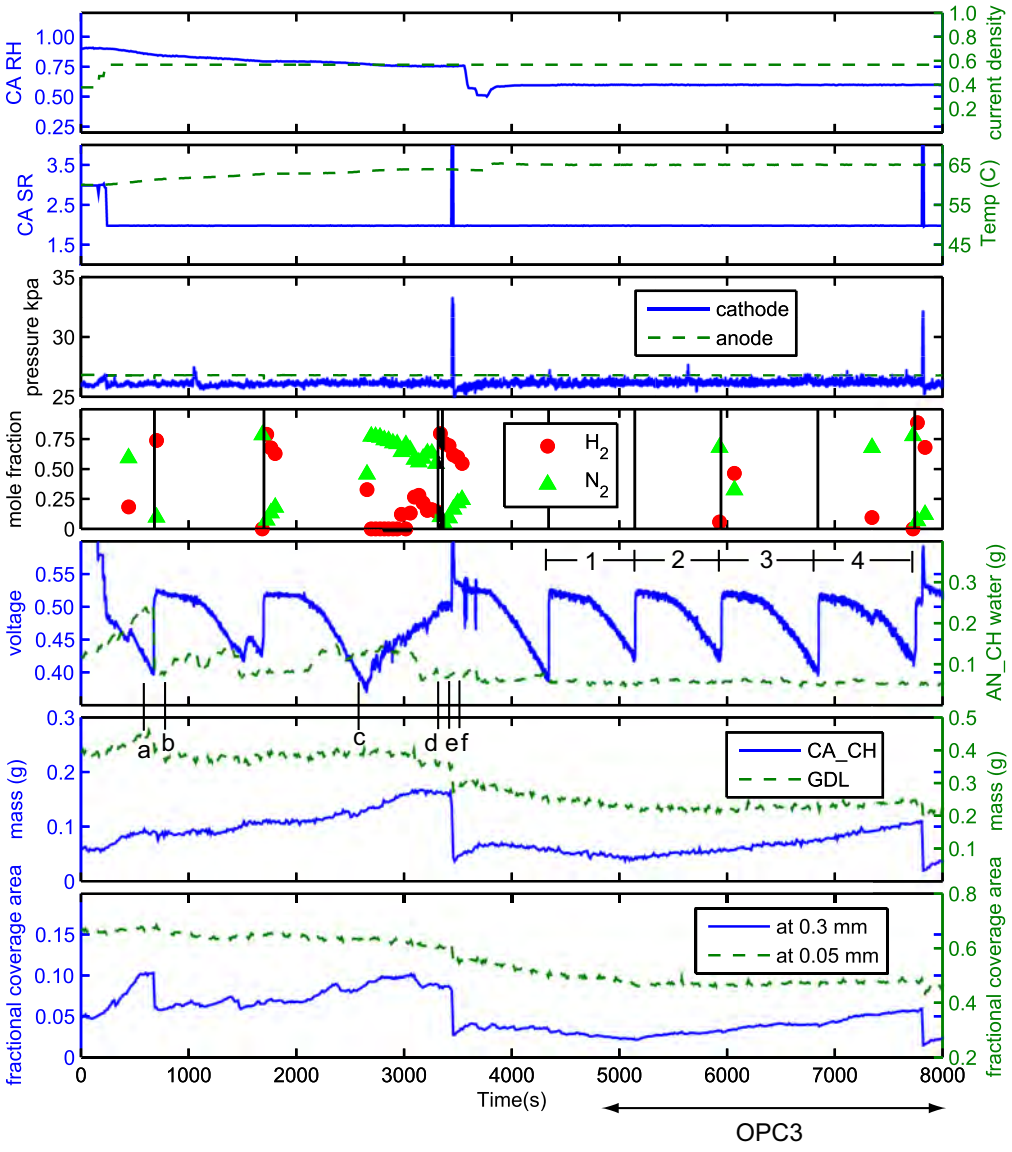

Figure 4.3 Operating conditions and processed liquid water data from neutron images. The data correspond to initial experiment time t_0=55800s. The dashed (green) lines correspond to the axis on the right, and solid (blue) lines use the left axis. The top subplot shows CA RH as a fraction (0-1) (solid lines) and current density (A cm^{-2}) (dashed lines). The second subplot shows CA SR (solid lines) and cell temperature ($^{\circ}$C) (dashed lines). The third subplot shows cathode (solid lines) and anode channel pressure (kPa gauge) (dashed lines). The fourth subplot shows the mole fraction of hydrogen and nitrogen that was measured from GC sampling, and the vertical lines indicate anode purge events. The fifth subplot shows the cell voltage (solid lines) and the estimated mass of liquid water in the anode channel (dashed lines). (a)-(f) indicate the times at which neutron images (a)-(f) in Fig. 4.2 were acquired. The sixth subplot shows the estimated CA CH liquid water mass (solid lines) and GDL mass (g) (dashed lines). Finally, the seventh subplot shows the fractional FC area from neutron imaging, with a measured liquid water thickness greater than 0.3 or 0.05 mm.

the channel and the cathode catalyst layer is reported to be large, especially for carbon cloth GDLs [70], and cathode purges effectively enhance the O_2 transport to those areas, especially under the rib. Cathode surges at $t = 3400$ s and $t = 7800$ s, indicated by the short duration spikes in the Cathode Stoichiometric Ratio (CA SR) in the second subplot of Fig. 4.3, cause a temporary increase in cathode back-pressure and voltage during the duration of the surge, as shown in the third and fifth subplots of Fig. 4.3, respectively.

The surge at $t = 3700$ s recovers 36 mV of voltage, and the removal of liquid water from the cathode channel can be clearly seen by comparing Fig. 4.2(e) from before the surge to Fig. 4.2(f) after. A larger voltage recovery from both surges and purges is expected at a high current density (0.6 A cm^{-2}) for two reasons. A higher amount of cathode flooding is expected and any water accumulation has a greater effect on voltage because the higher local current density leads to lower overall electrochemical efficiency. The fractional coverage area at 0.3 mm, shown as the solid lines in the last subplot of Fig. 4.3, decreases with both anode purges and cathode surges that remove water from the channels because water thickness values above this threshold are attributed to channel accumulation. The estimates of channel water mass shown in the above subplots are well correlated with the surges, purges, and voltage recoveries.

4.3.2 Temperature Effects

The overall effect of temperature on fuel cell voltage is difficult to quantify because temperature influences several competing factors. For example, an increased temperature leads to faster reaction kinetics and increased proton conductivity, which both increase voltage. However, the increase in vapor pressure also decreases the oxygen partial pressure, which decreases voltage. So, the overall effect may be a decrease in voltage. Temperature also impacts the nitrogen crossover rate though the membrane. The nitrogen permeation rate, K_{N_2} in (4.30), increases exponentially with temperature. Saturation pressure also increases exponentially with temperature, so the partial pressure of water vapor is small at lower temperatures.

The slow decrease in cathode inlet RH, shown in Fig. 4.3, from t=200 s to t=3200 s following the increase in current density, can be attributed to the increased heat generation that leads to a higher cell temperature than the set point value (60° C), whereas the dew point of the inlet air stream remains constant. This sub-saturated cathode air feed leads to a slight recession of the two-phase front location, as shown in the seventh subplot by the fractional coverage area. Note that the decrease in CA SR keeps the gas velocity in the channel close to the previous value after considering the increase in current density.

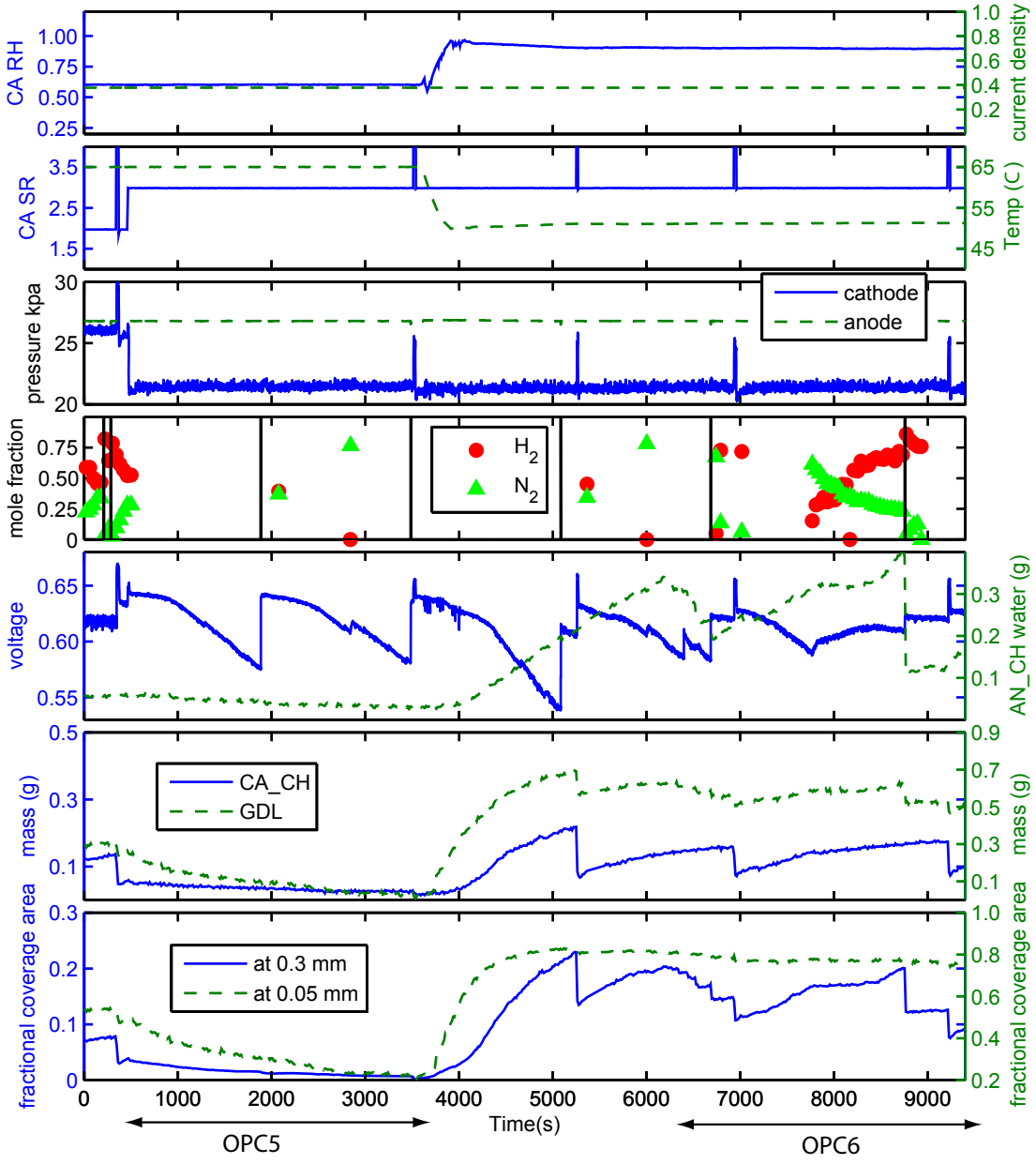

Figure 4.4 Selected data set 2. Beginning at t_0=67800s, these data show the transition from sub-saturated cathode inlet conditions to fully humidified conditions and the onset of channel plugging.

Finally, the decrease in CA RH and increased cell temperature at the beginning at t=3800 s lead to a more rapid drying of the fuel cell.

The high temperature and low cathode inlet RH conditions shown in the first half of Fig. 4.4 lead to a dry condition within the fuel cell. The total water mass is very low and the fractional water coverage is also low, indicating that the transition from sub-saturated

to saturated conditions along the length of the co-flow channels is near the outlet. After the transition to lower cell temperature at t=3700 s, which increases the cathode inlet RH from 60 to 100%, the two-phase front moves back toward the inlet, as indicated by the increase in the fractional area coverage (> 0.05 mm). This leads to the onset of both AN CH plugging and CA CH plugging. When the channels are not plugged, the cathode surge at t=3500 s has no sustained effect on voltage, but the surges following the increase to fully humidified cathode inlet conditions at t=5100 s and t=7000 s see voltage improvement that is well correlated with the water removal from the cathode channel. Data indicate that GDL water accumulation (data points taken from under the lands) precedes the accumulation of water in the channels, hence liquid condensation in the GDL occurs prior to channel flooding.

4.3.3 GC Sampling Effects

The intent of GC sampling is to measure nitrogen accumulation in the anode channel. The measurement, however, modifies the system behavior. Specifically, the effect of GC sampling, that is, the removal of gas from the AN CH, can improve the FC voltage. When a sample removes accumulated nitrogen or water from near the end of the anode channel, it is replaced by a pure hydrogen flow from the inlet.

GC samples are initiated typically right before and after each purge event and sometimes in the middle of a purge period, as shown in the fourth subplot of Fig. 4.3. Individual GC sampling events are correlated with the small voltage increases shown in the fifth subplot of Fig. 4.3. A series of samples, between $t = 2700$ and 3500 s, is taken at the fastest sampling rate of the GC detector.

The effect of sampling has more impact on voltage with increasing time since the last anode purge event. This can be explained by the nitrogen accumulation model presented in Sec. 4.4. Samples taken from later in the cycle allow more nitrogen to accumulate in the anode channel; see, for example, the sample taken at t=350 s in Fig. 4.3. If nitrogen does not have sufficient time to accumulate, the sample is removes primarily hydrogen from the channel and no voltage improvement is observed; see, for example, the sample taken at t=700 s immediately following an anode purge.

The continuous sampling, at one sample every 40 s, between $t = 2700$ and 3500 s in Fig. 4.3, is responsible for the voltage recovery observed over that time interval. If the sampling rate is fast enough to remove more volume than the amount of nitrogen that crosses over through the membrane in that time, then the measured voltage increases with each subsequent sample. The fluctuations in anode pressure, due to the repeated sampling, also enhance liquid water removal from the anode channel by allowing liquid water to escape

from the channel into the outlet manifold. During normal operation, the outlet manifold is at the same pressure at the channel, so there is no flow between these volumes. This explains the drop in AN CH liquid water mass observed between Fig. 4.2(c) and Fig. 4.2(d).

4.3.4 Voltage Repeatability

The repeatability of several purge cycles, from the end of the larger data set shown in Fig. 4.3, can be seen by plotting each cycle vs the time since the previous purge, as show in Fig. 4.5, creating an overlay of the voltage decays with time. The repeatability of the voltage decay characteristics between cycles is remarkable, given the fact that some purge cycles contain surge events. Similarly, the repeatability and consistency of the measured mole fractions every purge cycle is very important for modeling and understanding the underlying phenomena. This analysis is useful, considering the impact of GC sampling on voltage and nitrogen distribution in the anode channel. The composition of several samples from different points in time during the purge cycle and from different cycles allows an accurate representation of nitrogen accumulation and voltage decay. Notice that the nitrogen mole fraction, shown in the bottom subplot of Fig. 4.5, saturates at around 0.8; the remaining 20% of the gas is saturated water vapor in the AN CH.

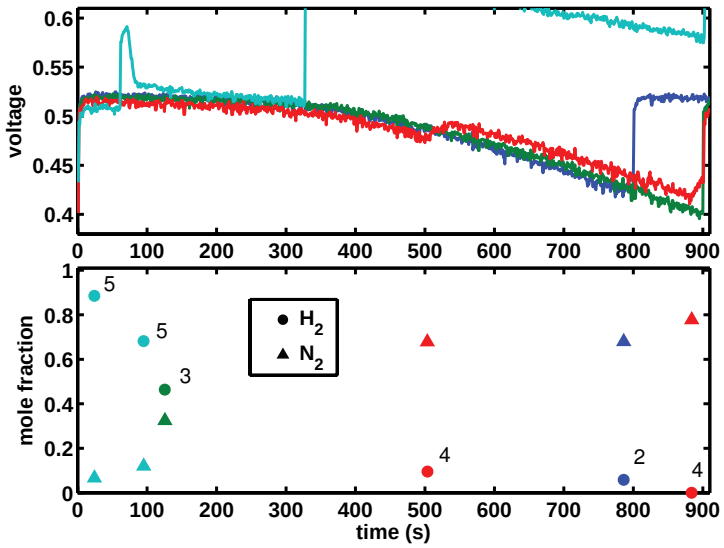

Figure 4.5 Sequential purge cycles plotted vs. time since the previous purge. The data correspond to operating condition 3 from the larger data set shown in Fig. 4.3. The numbers 1-5 on the bottom subplot indicate during which purge cycle each GC sample was taken.

4.4 Modeling

In this section, a one-dimensional model of nitrogen crossover and accumulation in the AN CH of a DEA PEMFC is presented. The modeling domains for this work are the anode channel and membrane. Nitrogen crossing though the membrane, into the AN CH, is pushed to the end of the channel by the convective velocity [41]. The convective velocity is the result of hydrogen consumption and, therefore, the velocity is greatest near the anode inlet, decreasing along the length of the channel. Due to the high diffusivity of hydrogen in the AN CH, the Stefan-Maxwell equation is uesd to describe the nitrogen distribution along the channel. Modeling the influence of both convection and diffusion, is needed to compare with the measured mole fractions from GC sampling. A physics-based voltage model is used to account for the distributed current density and hydrogen consumption rate. The voltage model includes the effect of membrane water content and proton concentration. An isothermal modeling approach is used, where the measured cell end plate temperature is used for T.

The important dimensions for channel modeling are x, the through membrane direction, and y, the along-the-channel direction, as shown in Fig. 4.6. For the anode, the spatial variation of gas concentrations in the x-direction is considered, but the steady-state gas diffusion profiles are calculated and used to propagate the channel values (which are modeled as dynamic states) across the GDL to the surface of the membrane. A similar decoupling between the x and y distributions is proposed in [83], to address the computational complexity and to take advantage of the very different length scales. On the cathode, only the steady state profiles are considered for modeling both the x- and y-dimensions. The approximation of steady-state distributions is appropriate for the cathode gas channel due to the high gas flow rate and the large time scales over which the anode dynamics evolve.

The constants, listed in Table 4.3, and equations describing the gas constituents in the channels are written using SI units. The exceptions are the related parameters in the voltage model, Table 4.2 , which use A cm^{-2} consistent with the FC literature. In the along-the-channel model, the fluxes N have units (mol m^{-2} s^{-1}), reaction rates r_i (mol m^{-3} s^{-1}), and fluxes per unit length n (mol m^{-1} s^{-1}).

4.4.1 Nitrogen Accumulation (single phase along the channel model).

To consider both water and nitrogen transport though the membrane, the modeling effort requires consideration of a ternary system for the anode. The Stefan-Maxwell model

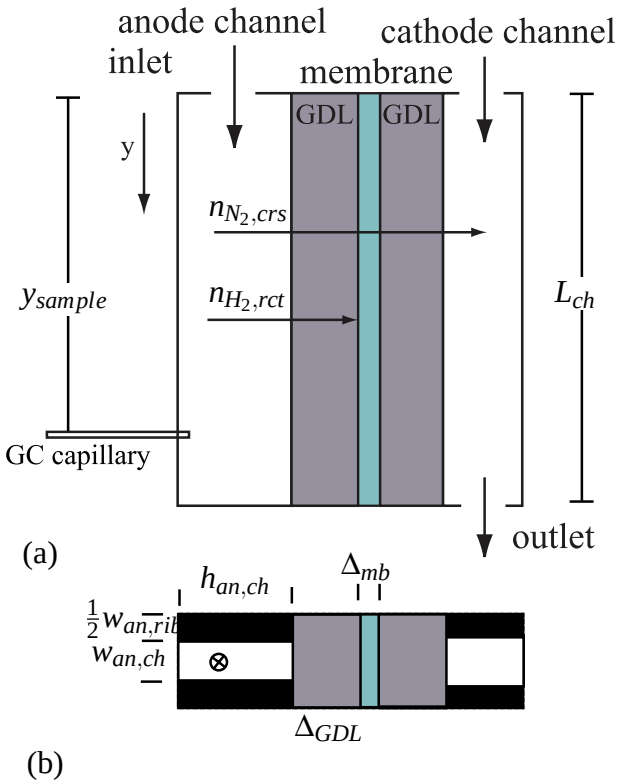

Figure 4.6 One-dimensional FC modeling domain, along the channel. In subfigure (a), y denotes the distance along the channel from inlet to outlet (not drawn to scale). Subfigure (b) shows a view from the top, indicating the FC channel dimensions.

describes convection, diffusion, and reactions in the gas-channel,

$$\frac{P_{an}}{RT}\frac{\partial X_i}{\partial t} = -\frac{\partial}{\partial y}\left(J_i + X_i N_t\right) + r_i, \tag{4.1}$$

for $i = [1,2]$, where N_t is the total gas flux, J_i is the diffusive flux, and r_i denotes the reaction terms. Only two of the three components are independent in this modeling framework. The mole fractions of nitrogen, $X_{N_2} = X_1$, and water vapor, $X_{H_2O} = X_2$, are chosen as dynamics states. Because the mole fractions must sum to one,

$$\sum X_i = 1, \tag{4.2}$$

the hydrogen fraction can be calculated from the other gases $X_{H_2}(y) = 1 - X_{N_2}(y) - X_{H_2O}(y)$. $X_{H_2O} = \min(X_2, P_{sat}(T)/P_{an,in})$ is used for all the following calculations, including J_i. The remaining water is assumed to be liquid water and is tracked separately, assuming instant condensation/evaporation.

The convective flux, N_t, is driven by the consumption of hydrogen Eq. (4.7). In Eq. (4.1), a constant pressure is used as an approximation because the anode volume is

fed via pressure regulation and the straight channel geometry introduces minimal pressure drop along the length of the channel. Although a pressure gradient, corresponding to the convective flux, develops along the length of the channel, the pressure drop is less than 1 Pa at 1 A cm^{-2}, so a constant pressure is valid for calculating the concentrations. The ideal gas law, $PV = nRT$ or $P = cRT$, is used to relate pressure and mole fraction of gas species in the channel.

A causal formulation for the diffusive fluxes is used [159]

$$\begin{bmatrix} J_1 \\ J_2 \end{bmatrix} = -\frac{P_{an}}{RT\phi(X)} \begin{bmatrix} D_1(X_1), & D_2(X_1) \\ D_3(X_2), & D_4(X_2) \end{bmatrix} \begin{bmatrix} \frac{\partial X_1}{\partial y} \\ \frac{\partial X_2}{\partial y} \end{bmatrix}, \tag{4.3}$$

where

$$\begin{aligned} D_1(X_1) &= (1-X_1)D_{13}D_{12} + X_1 D_{23}D_{13}\ , \\ D_2(X_1) &= -X_1(D_{23}D_{12} - D_{23}D_{13})\ , \\ D_3(X_2) &= -X_2(D_{13}D_{12} - D_{23}D_{13})\ , \\ D_4(X_2) &= (1-X_2)D_{23}D_{12} + X_2 D_{23}D_{13}\ , \end{aligned} \tag{4.4}$$

and D_{ij} are the temperature-dependent binary diffusion coefficients from [87]. $\phi(X)$ is given by

$$\phi(X) = (D_{23} - D_{12})X_1 + (D_{13} - D_{12})X_2. \tag{4.5}$$

Conservation of mass allows solving of Eq. (4.1) for $N_t(y)$, assuming the outlet flow is known $N_t(L) = N_{out}$. The equation for conservation of mass can be written as,

$$\frac{\partial N_t}{\partial y} = \sum r_i, \tag{4.6}$$

because $\sum J_i = 0$ by definition. Then the convective flux along the channel can be found from Eq. (4.6) by integrating backward in space along the channel,

$$N_t(y) = N_t(L) + \int_y^L \left(\frac{n_{H_2,rct}(\tilde{y}) + n_{N_2,crs}(\tilde{y}) + n_{H_2O,crs}(\tilde{y})}{w_{an,ch} h_{an,ch}} \right) \mathrm{d}\tilde{y}. \tag{4.7}$$

Because the anode is dead-ended, $N_{out} = 0$ unless the downstream solenoid valve is open and the anode is purging, in which case $N_{out} = N_{purge}$, a constant.

The source term for nitrogen in the AN CH is membrane crossover, which is calculated from the difference in nitrogen partial pressure across the membrane of thickness Δ_{mb},

$$n_{N_2,crs}(y) = -K_{N_2}(T, \lambda_{mb})(w_{an,ch} + w_{an,rib}) \frac{(P_{N_2,ca,mb}(y) - P_{N_2,an,mb}(y))}{\Delta_{mb}}. \tag{4.8}$$

It is assumed that the permeation takes place both over the ribs and channels $(w_{an,ch} + w_{an,rib})$, where w_* indicates the width of each. The partial pressure of nitrogen at each membrane surface is calculated using the following expressions, $P_{N_2,an,mb}(y) = X_{N_2}(y)\, P_{an,in}$ and $P_{N_2,ca,mb}(y) = P_{ca,in} - P_v(T) - P_{O_2,ca,mb}(y)$, assuming uniform pressure and saturated water vapor everywhere. This is reasonable, considering the water generation rate, especially when humidified inlets are used at low to mid temperatures. The oxygen concentration at the cathode surface of the membrane, $P_{O_2,ca,mb}(y)$, is calculated using Eq. (4.26). The nitrogen permeation rate, $K_{N_2}(T,\lambda_{mb})$, is given by Eq. (4.30), and depends both on temperature and membrane water content.

The hydrogen reaction rate is calculated from the local current density

$$n_{H_2,rct}(y) = \frac{i_{fc}(y)}{2F}(w_{an,ch} + w_{an,rib}), \tag{4.9}$$

where F is Faraday's constant.

The source term for water vapor in the AN CH is also membrane crossover, which is calculated from the diffusion and electro-osmotic drag

$$n_{H_2O,crs} = -\left(\frac{\lambda_{ca} - \lambda_{an}}{R_{w,mb}} - n_d(\lambda_{mb})\frac{i_{fc}}{F}\right)(w_{an,ch} + w_{an,rib}) \tag{4.10}$$

where $R_{w,mb}$ is the resistance to membrane transport,

$$R_{w,mb} = \frac{\Delta_{mb}}{D_w(\lambda_{mb},T)} + \frac{1}{k_{ads}} + \frac{1}{k_{des}}, \tag{4.11}$$

arising from diffusion, where $D_w(\lambda_{mb},T)$ is the water diffusion coefficient for water in the membrane [130] and interfacial mass transfer attributed to membrane adsorption k_{ads} and desorption k_{des} [130, 160, 161]. The coefficient of electro-osmotic drag, $n_d(\lambda_{mb})$, can also be found in Rer. [130]. Both D_w and n_d are λ_{mb} dependent and increase with membrane water content.

The membrane water content is the final dynamic state in the model and is calculated from the difference between the anode and cathode equilibrium lambda values

$$\frac{\partial \lambda_{mb}(y)}{\partial t} = K_{mb}(\lambda_{an}(y) + \lambda_{ca}(y) - 2\lambda_{mb}(y)) \tag{4.12}$$

where $K_{mb} = k_{ads}/\Delta_{mb} = 0.25$ is the membrane water uptake rate. Other, more recent models for membrane water uptake [160, 161], will be investigated in a future work but should not impact the results for nitrogen accumulation presented here.

The equilibrium membrane water content is calculated from the water activity using the uptake isotherm [130]

$$\lambda_{an}(y) = c_0(T) + c_1(T)a_{H_2O,an} + c_2(T)a^2_{H_2O,an} + c_3(T)a^3_{H_2O,an} \tag{4.13}$$

where $a_{H_2O,an}(y) = X_{H_2O}(y)\, P_{an,in}/P_{sat}(T)$.

There exists a coupling between membrane water content, $\lambda_{mb}(y)$, the current density distribution, $i_{fc}(y)$, and nitrogen crossover rate, $K_{N_2}(T,\lambda_{mb})$. The nitrogen permeation rate depends on membrane water content, and the nitrogen accumulation rate depends on both the permeation rate and current density distribution (convective vs diffusive flow). The current density distribution depends on nitrogen accumulation (through blanketing of H_2) and the membrane water content for proton transport losses in the membrane. Finally, the membrane water content depends on the local current density and channel / GDL conditions.

4.4.2 Modeling the GC Sample Location

The flow of gas removed from the AN CH during sampling is modeled by modifying Eq. (4.7) to include the sample flow

$$N_t(y) = N_t(L) + \int_y^L \left(\frac{n_{H_2,rct}(\tilde{y}) + n_{N_2,crs}(\tilde{y}) + n_{H_2O,crs}(\tilde{y})}{w_{an,ch} h_{an,ch}} \right) \mathrm{d}\tilde{y} + \begin{cases} N_{sample} & \text{for } (y \le y_{sample}) \\ 0 & \text{for } (y > y_{sample}) \end{cases} \tag{4.14}$$

where y_{sample} is the location of the sampling port along the equivalent channel.

Because the FC is on a 45 $^\circ$ angle and each of the AN CHs is connected at the top and bottom, as shown in Fig. 4.1, the N_2 blanketing front propagation needs to be transformed for comparison with an equivalent straight single channel. The nitrogen coverage area, however, can be directly related to the coverage area in the single channel equivalent model. Hence, we use the following relationship for the virtual single channel fuel cell sampling location y_{sample},

$$\frac{(L_{ch} - y_{sample})}{L_{ch}} = \frac{(L_{ch} - l_{sample})^2}{2A_{fc}} \,. \tag{4.15}$$

This equation relates the fractional area below the sampling location for the fuel cell placed in the diagonal orientation (right), as shown in Fig. 4.7, to the fractional area below the sampling location in the equivalent model (left), as shown in Fig. 4.6. The physical nitrogen sampling location is 3 cm from the bottom edge of the FC along the last channel,

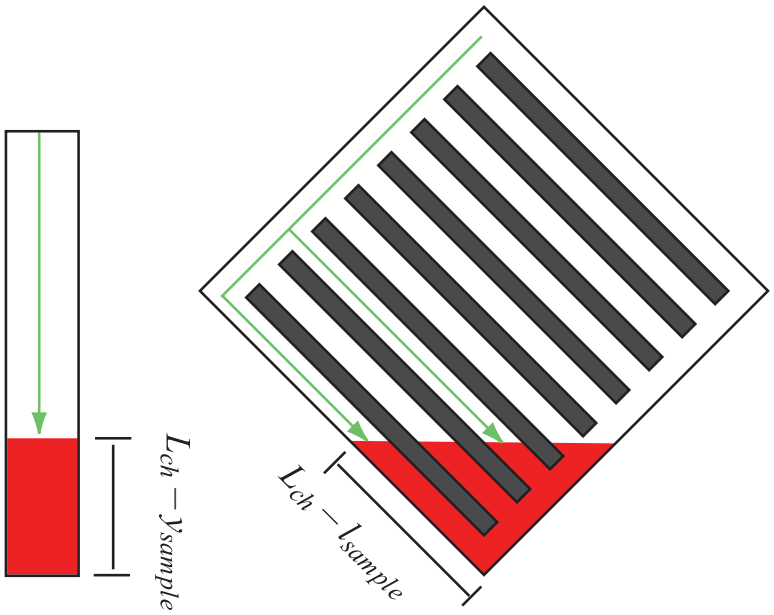

Figure 4.7 Mapping AN CHs to an equivalent single channel. The path length, in the 45° orientation, to nitrogen front location is the same for all channels.

$L_{ch} - l_{sample} = 0.03$, as shown in Fig. 4.7.

4.4.3 Distributed Current Density

In a previous work, the voltage was calculated based on a uniform apparent current density [65], which is related to the catalyst area with sufficient reactants to support the reaction, i.e., the channel length not covered by nitrogen [41] or water [65]. In this work, the distributed current density is considered, which is calculated directly from the reactant concentrations. Although the apparent area modeling technique captures the correct voltage output behavior of the system, the full distributed current density approach is chosen for this work to match internal model states and the measurement of nitrogen molar fraction during sampling from the AN CH at the fixed sampling location, l_{sample}. The diffusion of hydrogen and nitrogen in the AN CH affects both the current density distribution and GC measurement.

The inputs to the voltage model are: total current $I_{fc}(A)$, temperature T (K), membrane water content distribution $\lambda_{mb}(y)$, hydrogen partial pressure at the membrane surface $P_{H_2,an,mb}(y) = RTc_{H_2,an,mb}(y)$ (Pa), and oxygen partial pressure at the cathode membrane surface $P_{O_2,ca,mb}(y)$ (Pa), which is calculated in Eq. (4.26). The cell terminal voltage is calculated from the open-circuit potential minus the concentration, over-potential, and ohmic

losses

$$E_{cell} = E_{rev}(y) - \eta_{mb}(y) - \eta_{GDL}(y) - \eta_{act,ca}(y) - \eta_{act,an}(y). \tag{4.16}$$

The calculation of the FC terminal voltage and current density distribution requires the additional computation effort to solve $N+1$ simultaneous non-linear algebraic constraint equations, where N is the number of discretized sections used to solve the partial differential equation (PDE) system. The distributed current density is resolved by solving the set of N equations, shown in Eq. (4.16), for a uniform potential E_{cell} and one equation for the conservation of current

$$\frac{I_{fc}}{A_{fc}} = \frac{1}{L_{ch}} \int_0^{L_{ch}} i_{fc}(y) \mathrm{d}y. \tag{4.17}$$

The reversible voltage is given by

$$E_{rev}(y) = E_0 - \frac{RT}{nF} \log \left(\frac{aH_2O(y)}{aH_2(y)\ \sqrt{(aO_2(y))}} \right). \tag{4.18}$$

where $E_0 = 1.229 - (T - T_0) \cdot 2.304 \times 10^{-4}$ [13]. The reactant and product activities are calculated from the concentrations $aH_2(y) = c_{H_2,an,mb}(y)/C_{ref,H_2}$, $aO_2(y) = c_{O_2,ca,mb}(y)/C_{ref,O_2}$ and $aH_2O = 1$ because the liquid water product is assumed. The subscript ref refers to the reference quantity, and subscript ca,mb refers to the cathode membrane surface.

To simplify the calculation of cell voltage, a hyperbolic sine function is used for the calculation of over-potentials, $\eta_{act,ca}$ and $\eta_{act,an}$, from the exchange current density, $i_{o,ca}(y)$ and $i_{o,an}(y)$

$$\eta_{act,ca}(y) = \frac{RT}{\alpha_{c,a} nF} \mathrm{asinh} \left(\frac{k_{units}\, i_{fc}(y) + i_{loss}}{2 i_{o,ca}(y)} \right), \tag{4.19}$$

where, $k_{units} = 100^{-2} \frac{m^2}{cm^2}$ is for units conversion, $i_{fc}(y)$ is the distributed current density from Eq. (4.17) and i_{loss} is the lost current density due to hydrogen crossover, a tuned parameter which is listed in Table 4.2. The hyperbolic sine is equivalent to the Butler-Volmer equation when the forward and reverse reaction coefficients ($\alpha_{c,a} = \alpha_{c,c}$) are equal [162].

Although the cathode reaction depends on the oxygen concentration as well as the activity of protons in the membrane [163], the proton activity term is typically neglected because there are sufficiently many protons under the FC normal operation. A low hydrogen concentration in the anode near the end of the channel is expected, therefore, the proton effect on the exchange current density is included

$$i_{o,ca}(y) = i_{o,ref,ca} \left(\frac{c_{O_2,ca,mb}(y)}{C_{ref,O_2}} \right)^{\gamma_{O_2}} \left(\frac{c_{H^+_{ca,mb}}(y)}{C_{ref,H^+}} \right)^{\gamma_{H^+}} \exp \left(\frac{-E_c}{R} \left(\frac{1}{T} - \frac{1}{T_0} \right) \right), \tag{4.20}$$

where $i_{o,ref,ca}$ is the reference current density, c is the reactant concentration, γ is the concentration parameter, and E_c in the Arrhenius term is the activation energy for hydrogen oxidation on platinum [138]. The cathode concentration parameter for the local proton activity ($\gamma_{H^+} = 0.5$) is given by [164]. The inclusion of proton concentration is required to capture the effect of nitrogen blanketing in the AN CH, which prevents hydrogen from reaching the catalyst layer to supply protons for the reaction. The cathode exchange current density is proportional to the square-root of the local proton activity at the cathode catalyst layer. The proton activity in the cathode catalyst layer depends on the concentration of protons dissolved in the aqueous phase in the membrane, which is proportional to the square root of the hydrogen pressure at the anode membrane surface, for low P_{H_2}, [165]. This relationship is approximated with a hyperbolic tangent function

$$\left(\frac{c_{H^+_{ca,mb}}}{C_{ref,H^+}}\right)^{\gamma_{H^+}} = K_{H_2}\tanh\left(100\frac{c_{H_2,an,mb}}{C_{ref,H_2}}\right). \tag{4.21}$$

The constant K_{H_2} is absorbed into the reference current density $i_{o,ref,ca}$. At the limit, where the hydrogen concentration is zero, the proton activity at the anode drops to zero. Thus, where the anode is subjected to local fuel starvation, the hydrogen partial pressure drops; hence, the proton concentration in the cathode decreases. Furthermore, the membrane electrolyte conductivity also decreases due to lower contribution from the proton conduction in the bulk phase akin to increasing electrolyte resistance due to decreasing ionic concentration [163].The overall reduction of proton activity at the cathode ultimately leads to a drop in the local current density near the dead-ended exit of the anode. For constant load current (galvanostatic) conditions, as the power production near the outlet shuts down, the current density increases near the anode inlet, where the membrane is relatively dry, which may lead to higher losses and increased temperature.

Similarly, for the anode side

$$\eta_{act,an}(y) = \frac{RT}{\alpha_{a,a}nF}\text{asinh}\left(\frac{k_{units}\, i_{fc}(y) + i_{loss}}{2i_{o,an}(y)}\right), \tag{4.22}$$

where the anode exchange current density is

$$i_{o,an} = i_{o,ref,an}\left(\frac{c_{H_2,an,mb}}{C_{ref,H_2}}\right)^{\gamma_{H_2}}\exp\left(\frac{-E_c}{R}\left(\frac{1}{T}-\frac{1}{T_0}\right)\right). \tag{4.23}$$

The membrane resistance is calculated as follows

$$\eta_{mb}(y) = \frac{k_{units}\, i_{fc}(y)\, \Delta_{mb}}{\sigma_{mb}(\lambda_{mb},T)\tanh\left(100c_{H_2,an,mb}/C_{ref,H_2}\right)} \tag{4.24}$$

Again, the hyperbolic tangent is used to approximate the relationship between conductivity and proton concentration [165], and to reflect the effect of increasing electrolyte resistance due to decreasing ion concentration [163]. The membrane conductivity $\sigma_{mb}(\lambda_{mb}, T)$ is a function of water content using the standard relationship from Springer et al. [121].

Finally, the GDL and contact resistances are lumped into R_{GDL} for the ohmic loss term

$$\eta_{GDL}(y) = k_{units}\, i_{fc}(y) R_{GDL} \tag{4.25}$$

The voltage model was tuned using flow-through data from the FC, then compared with the experimental voltage degradation rates under dead-ended operating conditions. For model tuning with flow through data, it is assumed that the membrane is fully humidified $\lambda(y) = \lambda(T, a = 1)$, where $\lambda(T, a = 1)$ can be found in [166], and the effects of GDL and cathode catalyst layer flooding are ignored due to the low current density operation.

Along the Channel Distributions

The oxygen partial pressure in the cathode channel is not presently considered as one of the dynamic states in the model, it is calculated simultaneously with the current density distribution $i_{fc}(y)$ (A cm^{-2}) from the cathode inlet pressure and SR using

$$P_{O_2,ca,mb}(y) = P_{O_2,ca,in} - \frac{RT}{4F}\left(\frac{i_{fc}(y)}{h_m} + \frac{i_{fc}(y)\Delta_{GDL}}{D_{O_2,eff}} + \int_0^y \frac{i_{fc}(\tilde{y})}{u_{ca,in} h_{ca,ch}} \mathrm{d}\tilde{y}\right) \frac{(w_{ca,ch} + w_{ca,rib})}{(w_{ca,ch})} \tag{4.26}$$

where $h_{ca,ch}$ is the CA CH height, $w_{ca,ch}$ is the CA CH width, and $w_{ca,rib}$ is the cathode rib width. h_m is the interfacial mass-transfer coefficient [162], and $u_{ca,in}$ is the cathode inlet gas velocity (assumed constant along the length of the cathode channel for simplicity)

$$u_{ca,in} = \frac{SR_{ca}\, I_{fc}\, (w_{ca,ch} + w_{ca,rib})\, L_{ca,ch}(RT)}{(4F) A_{fc}\, P_{O_2,ca,in}\, (h_{ca,ch} w_{ca,ch})} \tag{4.27}$$

where the partial pressure of oxygen at the cathode inlet is given by $P_{O_2,ca,in} = OMF_{ca,in}(P_{ca,in} - P_{v,ca,in})$. $P_{ca,in}$ is the cathode inlet pressure, and $P_{v,ca,in}$ is the cathode inlet vapor pressure, and $OMF_{ca,in} = 0.21$ is the oxygen molar fraction. SR_{ca} is the cathode stoichiometry.

The cathode vapor pressure along the length of the channel is calculated similarly,

$$P_{H_2O,ca}(y) \approx \min\left(P_{sat}(T), P_{H_2O,ca,in} + \frac{RT}{2F} \int_0^y \frac{i_{fc}(\tilde{y})}{u_{ca,in} h_{ca,ch}} \mathrm{d}\tilde{y} \frac{(w_{ca,ch} + w_{ca,rib})}{(w_{ca,ch})}\right). \tag{4.28}$$

This equation actually needs $+\int n_{H_2O,crs}(\tilde{y})\, \mathrm{d}\tilde{y}$ to be correct, but then it becomes difficult

to solve for the steady-state cathode vapor distribution analytically. At high cathode SR, this should not be a problem, but it may affect the O_2 distribution in low SR; however, this still should be a second order effect compared to variations in the anode.

The anode channel hydrogen concentration is propagated to the membrane surface assuming a simple diffusion model,

$$c_{H_2,an,mb}(y) = \frac{X_{H_2}(y)P_{an,ch}}{(RT)} - \frac{i_{fc}(y)}{2F}\frac{\Delta_{GDL}}{D_{H_2,eff}}\frac{(w_{an,ch}+w_{an,rib})}{w_{an,ch}} \tag{4.29}$$

based on the effective diffusivity $D_{H_2,eff} = D_{eff}D_{H_2,N_2}$ [71].

4.4.4 Nitrogen Crossover Rate

Kocha et al. [36] reported a large range of nitrogen permeability, over 1 order of magnitude. The permeation increases with both membrane water content and temperature. Temperature has a larger effect on permeability, when the membrane is well hydrated. In this case, the permeability can change by a factor of 2-5 over the normal range of operating temperatures 30-60 °C. The nitrogen permeation model includes the effects of membrane water content and temperature [37]

$$K_{N_2}(T,\lambda_{mb}) = \alpha_{N_2}(0.0295 + 1.21\,f_v - 1.93\,f_v^2) \times 10^{-14} \exp\left[\frac{E_{N_2}}{R}\left(\frac{1}{T_{ref}} - \frac{1}{T}\right)\right], \tag{4.30}$$

where $E_{N_2} = 24000$ J mol^{-1}, $T_{ref} = 303$, R is the universal gas constant, and f_v is the volume fraction of water in the membrane, given by;

$$f_v = \frac{\lambda_{mb}V_w}{V_{mb} + \lambda_{mb}V_w} \tag{4.31}$$

where $V_{mb} = EW/\rho_{mb,dry}$ is the dry membrane volume, equivalent weight divided by density, and V_w is the molar volume of water. λ_{mb} is the membrane water content.

A change in permeability could account for the different nitrogen accumulation rates observed via different voltage drop rates, assuming the voltage degradation is caused by nitrogen accumulation. The current density would tend to shift toward the inlet, where the membrane is dry and has lower proton conductivity; hence, there would be increased resistive losses when N_2 accumulates in the end of the channel.

4.5 Modeling Results

The PDE Eq. (4.1) is discretized using a central difference in space into $N = 50$ sections and solved using an ode solver. The AN CH model is solved using MATLAB "ode15s", which supports Differential Algebraic Equations (DAEs), of the form

$$M\dot{z} = f(z). \tag{4.32}$$

where $z = [X_{N_2,an}, X_{H_2O,an}, \lambda_{mb}, i_{fc}, E_{cell}]^T$, and $M = \text{diag}(I^N, I^N, I^N, 0^N, 0)$, and I^N is the $N \times N$ identity matrix.

Three simulation plots are shown in Fig. 4.8, 4.10, and 4.11, corresponding to operating conditions 3, 5, and 6, respectively. These portions of data are contained within the large data sets shown in Fig. 4.3 and 4.4. The first two data sets are chosen to match the model assumptions of humidified channel conditions but no channel liquid water plugging. The third condition shows some flooding and hence error in the model prediction of voltage, but the overall dynamic voltage behavior is captured quite well by the model, ignoring the offset. The first plot in Fig. 4.8 corresponding to condition 3 shows the measured and predicted voltage in the top subplot, and the GC measurement and simulated mole fraction at the sampling location in the bottom subplot. The model agrees very well with the data at this operating condition because no AN CH liquid water accumulation was observed during this period. Figure 4.9 shows the time evolution of the hydrogen mole fraction distribution and membrane water content over a purge cycle. Three snapshots of the distributions, corresponding to t=1700 s, t=2000 s, and t=2400 s, from the third cycle in Fig. 4.8 are shown. The "corner" in the voltage trace at t=2000 s, where the rate of voltage degradation increases, indicates that a sufficient amount of nitrogen has accumulated in the channel to create a stratified front and a hydrogen starved region develops at the outlet. Finally, at t=2400 s, the nitrogen front has evolved to cover nearly 20% of the anode channel. At this time, the effect of nitrogen blanketing is clear as the current density (the dashed-dotted line in the third subplot) is shifted.

Operating condition 5, shown in Fig. 4.10, corresponds to higher cathode stoichiometry and lower current density; therefore, we see slightly drier conditions along the channel but very similar membrane water content behavior to the previous case. The corner in the voltage model occurs too late, which indicates that either the diffusion coefficient is too large or the nitrogen accumulation rate is too low. The membrane resistance is too high because the voltage degradation rate after the corner point is too steep. Notice the effect of GC sampling on voltage for the samples that occur early in the purge cycle compared to those that occur later (larger voltage recovery), which the model accurately predicts.

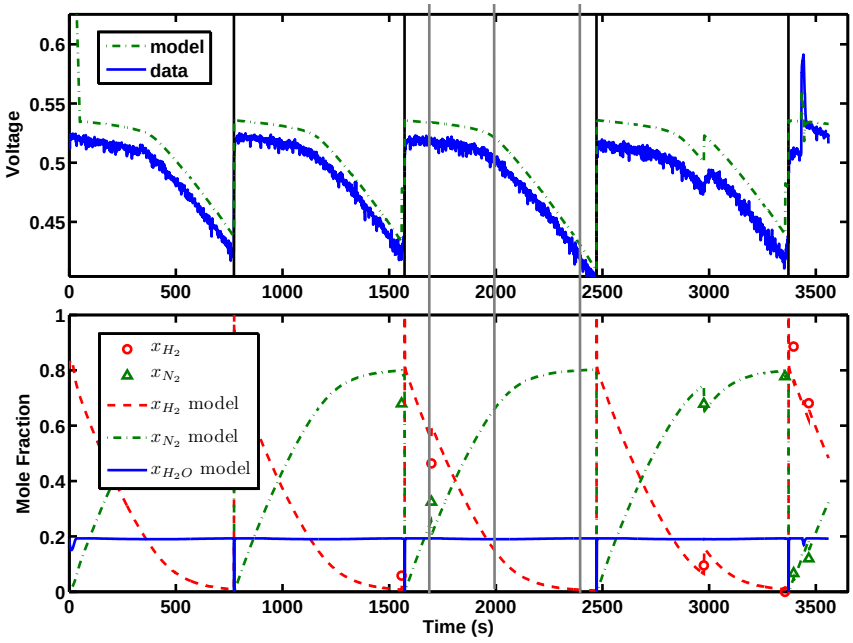

Figure 4.8 Simulation of operating condition 3 (*i*0.6_T65_SR2_RH60). This experiment shows very good results with model matching because the assumption of no liquid water plugging conditions in the channels is satisfied.

Figure 4.11 shows a good match with the GC measurement for repeated sampling. This data set corresponds to lower operating temperature and fully humidified cathode inlet conditions, which exhibit both anode and cathode channel plugging, hence the discrepancy between the modeled and measured voltage. The voltage matching is not very good because the effects of flooding or plugging are not represented in the voltage model. Cathode flooding and plugging are responsible for almost 20 mV of voltage loss, which can be recovered by the cathode surges at t=1000s and t=3400s. The membrane water content distribution, shown in Fig. 4.12, is much more uniform due to the humidified cathode inlet conditions and does not change over the purge cycle as in the previous cases.

The parameters α_{N_2} and D_{H_2,N_2} affect the rate of nitrogen front propagation and the delay before the voltage decay changes slope, as seen in Fig. 4.8. Nitrogen front propagation is also weakly dependent on the current density distribution $i_{fc}(y)$, because the consumption of hydrogen drives convection in the channel. The slope of voltage drop depends on membrane/GDL resistance, the nitrogen diffusion rate, and the nitrogen front propagation speed.

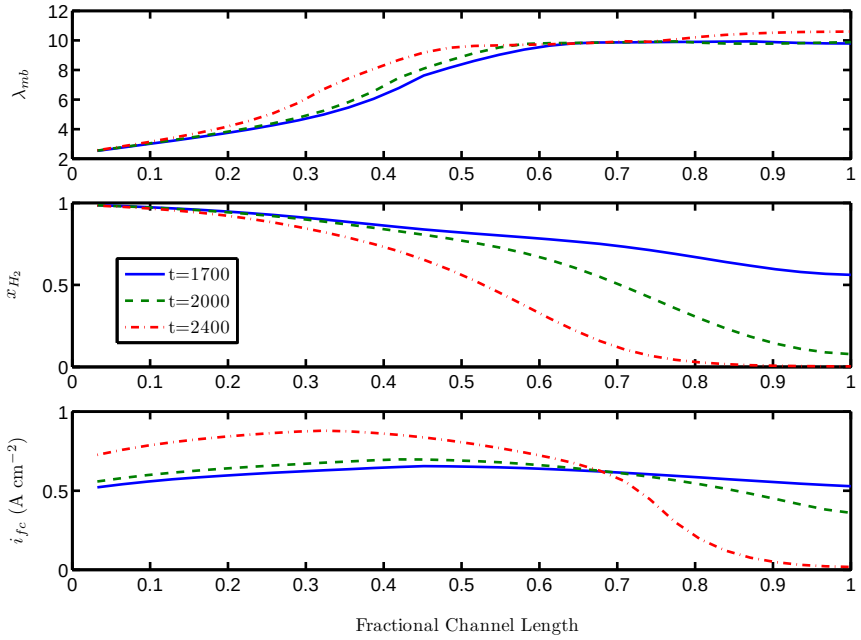

Figure 4.9 Along the channel distributions for operating condition 3. The first subplot shows a snapshot of the membrane water content along the length of the channel for three times, as shown in Fig. 4.8; after a purge, midcycle, and before the next purge. The second subplot shows the hydrogen mole fraction along the length of the channel. The final subplot shows the current density distributions. The front is fully developed at t=2400 s, leading to hydrogen starved region covering nearly 20% of the channel.

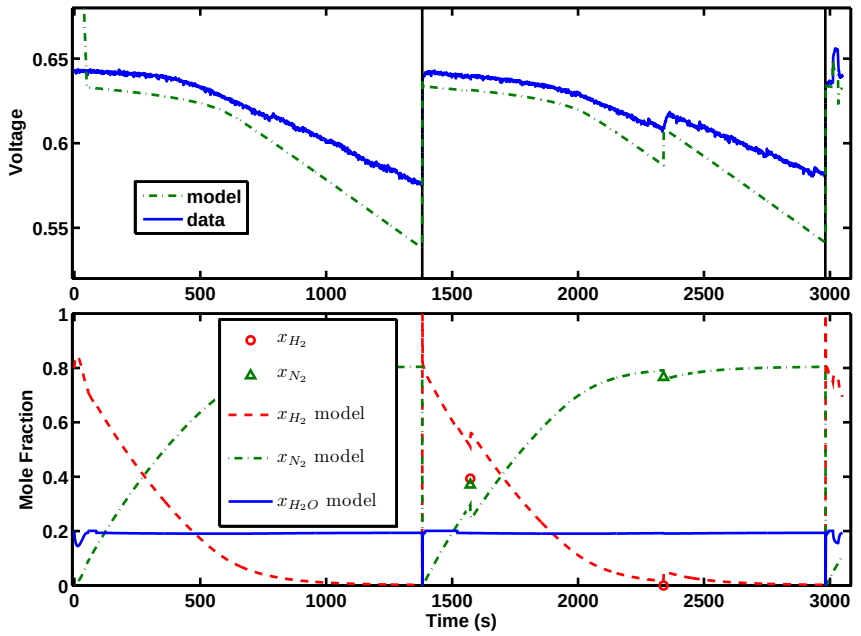

Figure 4.10 Simulation results for operating condition 5 (*i*0.4_T60_SR3_RH60).

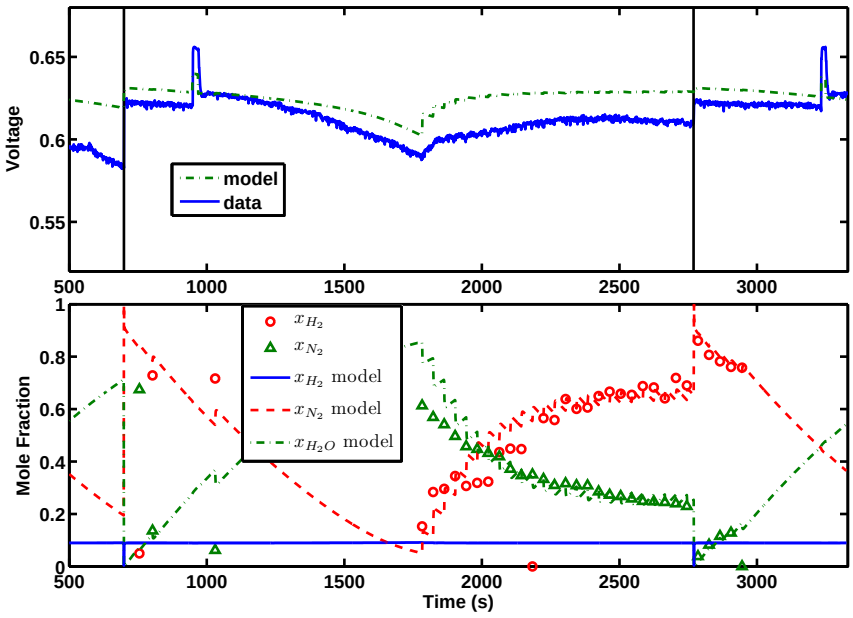

Figure 4.11 Simulation results for operating condition 6 (*i*0.4_T50_SR3_RH90). The model has good agreement with nitrogen measurement during continuous sampling, but poor voltage matching since flooding effects are not included.

4.5.1 Effect of Operating Conditions

Figures 4.13 and 4.14 show the effects of increasing temperature and current density, respectively. Increasing temperature increases both permeation through the membrane and, to a small extent, diffusion. The increased nitrogen permeation rate leads to both a quicker formation of the nitrogen blanket, the time at which the voltage slope changes, and the faster propagation of the blanketing front, which can be seen in the steeper second slope of the voltage plot. The effect of current density is more difficult to visualize because the voltages are very different; therefore, the deviation from the nominal voltage for each given current density is plotted in the first subplot of Fig.4.14. The second subplot shows the hydrogen and nitrogen mole fraction at the sampling location. Because the convective term in Eq. (4.1) is proportional to the current density, nitrogen is pushed toward the end of the channel more quickly with increasing current density. As a result, the blanketing front forms much more quickly at a high current density but the propagation rate of the front does not increase very much because the permeation rate is constant. This can be seen in the third subplot which shows the average mole fraction of nitrogen in the anode channel, which is nearly identical for all four cases.

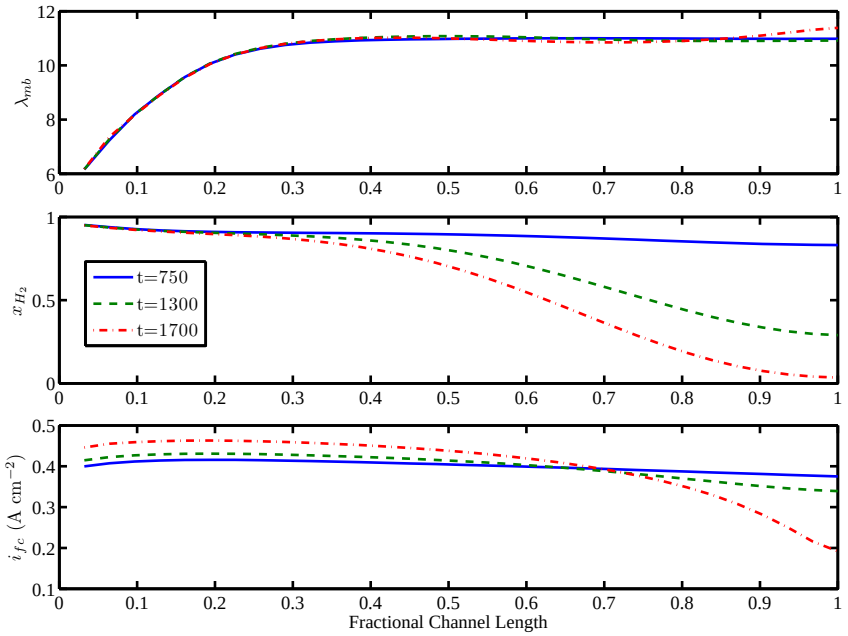

Figure 4.12 Along the channel distributions for operating condition 6. The first subplot shows a snapshot of the membrane water content along the length of the channel for three times shown in Fig. 4.11; after a purge (before surge), midcycle and before the next purge. The second subplot shows the hydrogen mole fraction along the length of the channel. The final subplot shows the current density distributions. Notice the different membrane profiles due to higher cathode inlet RH, and less developed nitrogen front.

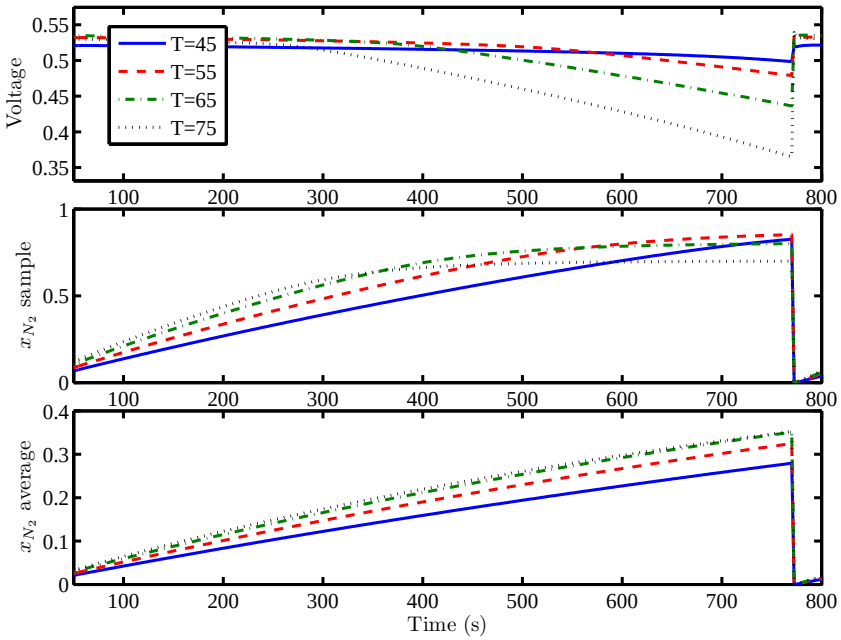

Figure 4.13 Increasing temperature increases nitrogen permeation rate exponentially which leads to much faster voltage decay. The conditions for simulation are (*i*0.6_Tx_S2_RH60).

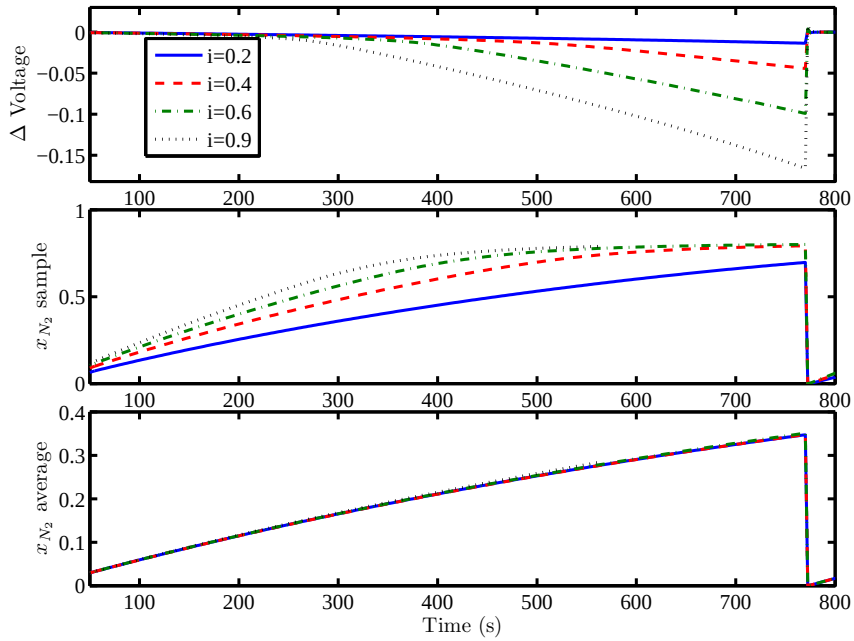

Figure 4.14 Increasing current density increases nitrogen blanket formation rate, but not the accumulation rate. The conditions for simulation are (*i*x_T65_S2_RH60).

4.6 Conclusions

The one-dimensional AN CH model presented in this chapter is able to capture and explain the observed two-sloped voltage drop between purges in a PEMFC with DEA. The model shows very good results when the assumption of dry conditions are met in the channels. The evolution of a nitrogen blanketing front, which leads to a hydrogen depleted region in the AN CH, explains the voltage loss. Although distributed current density measurements [109, 167] were not acquired, the effect of mass accumulation on current density distribution can be observed through the cell potential by measuring the terminal voltage. Specifically, the mass accumulation affects both the rate of voltage drop and the time at which the steeper slope begins.

The ability of the model to predict voltage is limited because the accumulation of liquid water in the anode channel (plugging) and cathode catalyst layer (flooding) are not included in the model, but the voltage degradation and nitrogen accumulation rates match well when the assumption of non-flooding and non-plugging conditions are valid. Future plans include incorporating these effects into the model. The effects of nitrogen and liquid water accumulation can be parameterized by utilizing the measurement of liquid water from neutron imaging along with the GC measurements for combinations of wet and dry channel conditions. The data set corresponding to operating condition 6, shown Fig. 4.11, could be used for parameterizing the liquid water effect using the model of nitrogen accumulation,

which is calibrated for drier (non-flooding/plugging) conditions.

Appendix: Nomenclature and Constants

Table 4.2 Tuned Parameters

$i_{o,ref,ca}$	7E-8 (A cm^{-2})	Cathode exchange current
$i_{o,ref,an}$	0.05 (A cm^{-2})	Anode exchange current
i_{loss}	1E-3 (A cm^{-2})	Crossover current
D_{eff}	0.35	Effective Diffusivity in GDL
R_{GDL}	0.275 (Ω cm^2)	Contract resistance
α_{N_2}	2	N_2 perm scale factor

Table 4.3 Constants

E_{N_2}	24000 (J mol^{-1})	[37]
T_{ref}	303 (K)	[37]
R	8.314	Universal gas constant
V_w	1.81×10^{-5}	Water Volume [130]
V_{mb}	5.59×10^{-4}	Membrane Volume [130]
K_{mb}	0.25	Membrane water uptake
n	2	Electron transfer #
F	96485 (C mol^{-1})	Faraday's Constant
C_{ref,O_2}	40.87 (mol m^{-3})	
C_{ref,H_2}	40.87 (mol m^{-3})	
E_c	66000 (J mol^{-1})	[13]
T_0	298.15 (K)	ref Temperature
$\alpha_{a,a}$	0.5	
$\alpha_{c,a}$	0.5	
D_{12}	2.56 E-6 (m^2 s^{-1})	D_{H_2O,N_2} [87]
D_{13}	8.33 E-6 (m^2 s^{-1})	D_{H_2,N_2} [168]
D_{23}	9.15 E-6 (m^2 s^{-1})	D_{H_2O,H_2} [87]
$w_{an,ch}$	0.0021 (m)	An Ch width
$w_{an,rib}$	8.38E-4 (m)	An rib width
Δ_{mb}	25 (μm)	Membrane thickness
$h_{an,ch}$	0.0018 (m)	An Ch height
L_{ch}	0.0727 (m)	Channel length
Δ_{GDL}	3.36E-4 (m)	Compressed GDL thickness
N_{sample}	9.2e-7 (mol s^{-1})	Sample flow rate
N_{purge}	5e-3 (mol s^{-1})	Purge flow rate

Appendix: GC Calibration

The injection port inside the GC is maintained at 100 °C and the column at 30 °C. A Thermal Conductivity Detector (TCD) is used for gas detection. The TCD is operated at 100 °C and 90 mA current.

Two mass flow controllers are used to create dry gas mixtures of a known (H_2/N_2) concentration in the anode channel for the calibration of the GC detector. Calibration data are collected with the anode channel at 4.5 psig operating pressure and a nominal temperature of t=60 °C. A six point calibration is used, with five samples repeated for each point. Figure 4.15 demonstrates the linearity of the GC measurement. The detector is much more sensitive to nitrogen, due to the choice of carrier gas. The average N_2 response is 1,163,897 (area units / X_{N_2}), and the average hydrogen response is 24,416 (area units/X_{H_2}). Because the measurement of H_20 is not possible during FC operation, the concentration of vapor in the anode is assumed equal to the saturation value and hence only temperature-dependent.

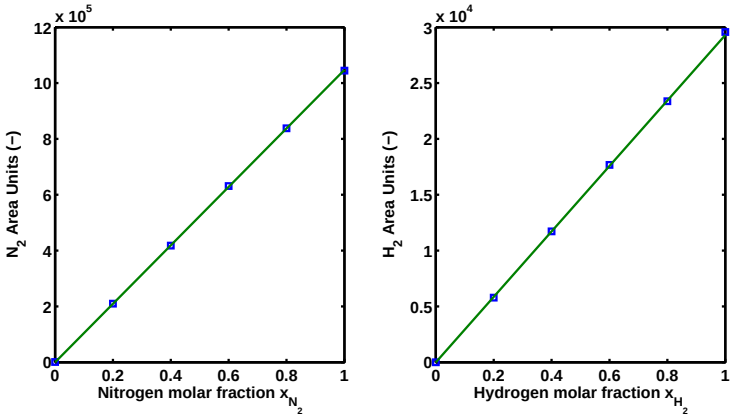

Figure 4.15 GC linear response, with variation in nitrogen concentration

Chapter 5

Reduced Order Modeling of Liquid Water Fronts and Nitrogen Blanketing

This chapter details the derivation of a fronts based, reduced order model for GDL and anode channel water accumulation and anode channel nitrogen accumulation. The model is parameterized using measurements of liquid water accumulation from neutron imaging and GC sampling to characterize nitrogen crossover and the resulting voltage drop under DEA conditions.

5.1 Overview of Modeling Domains

To capture the relevant dynamics, the fuel cell model is divided into five modeling domains corresponding to the five separate regions of the fuel cell in the through membrane direction (x): the anode channel, the cathode channel, the membrane, and the anode and cathode GDLs. Each channel domain contains three dynamic states (the mass in the cathode channel, $\{m_{O_2,ca,ch}, m_{N_2,ca,ch}, m_{w,ca,ch}\}$, and in the anode channel, $\{m_{H_2,an,ch}, m_{N_2,an,ch}, m_{w,an,ch}\}$), and the remaining domains have one state each (cathode GDL liquid water front location $x_{fr,ca}$, anode GDL front location $x_{fr,an}$, and membrane water content λ_{mb}), for a total of nine modeled states. Water states in the GDL and membrane are initially defined as PDE equations in Sections 5.6.3 and 2.3.3, and further simplified to derive the states $x_{fr,ca}$, $x_{fr,an}$, and λ_{mb} in Section 5.4. Since the time constants for gas diffusion are much faster than the liquid states in the GDL, the spatial distribution of the gas species in the GDL can be approximated with the steady state profiles [81]. The modeling domains and the interactions between each domain are shown schematically in Fig. 5.1. The fuel cell stack load current I_{fc} is considered as a measured disturbance to the plant $D1$.

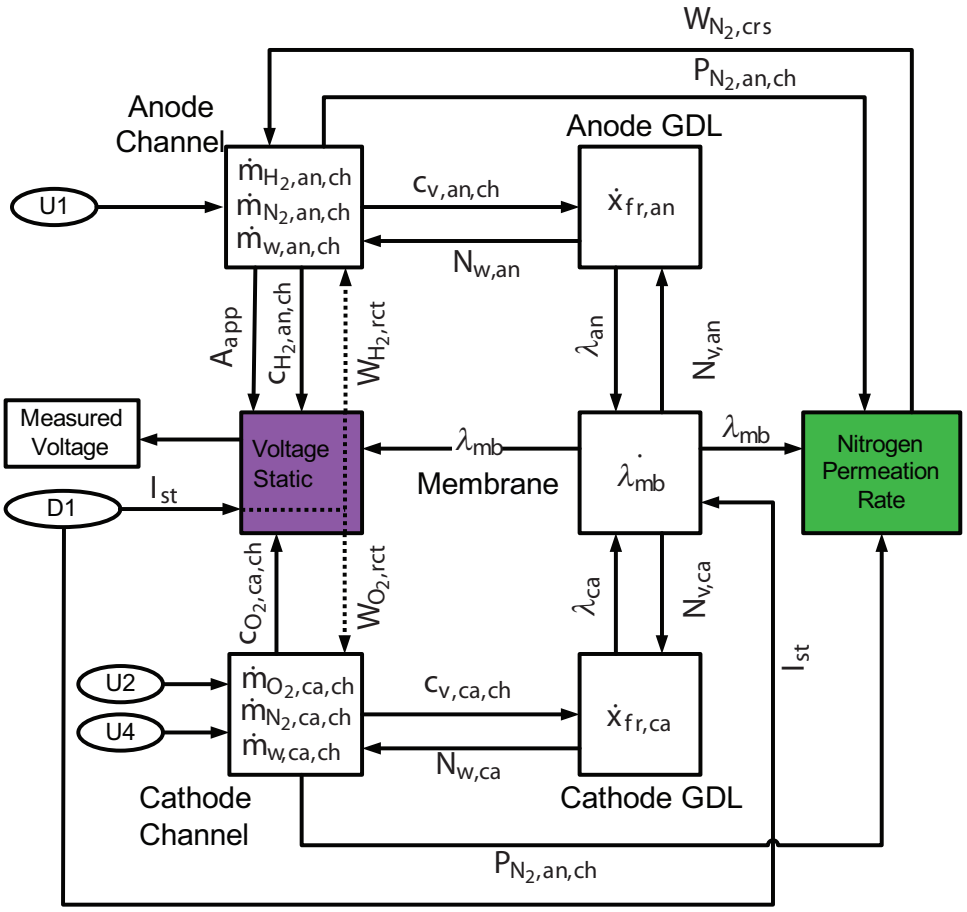

Figure 5.1 Schematic diagram showing the subsystem interconnections and modeled states. The anode channel has three states and the cathode channel has three states: for the anode GDL front location $x_{fr,an}$, for the cathode GDL front location $x_{fr,ca}$, and for membrane water content λ_{mb}.

5.2 GDL Fronts Simplification

The liquid water profile forms a steep front inside the GDL. The steep drop in s at the transition between the two-phase and single-phase water areas in the GDL is the result of the sigmoidal function of the capillary pressure [71]. Other capillary pressure models [72], [73], [75] should also exhibit a similar behavior in the formation of a steep liquid water front and propagation mode [80]. The PDEs [65, 12] describing water transport require a very fine discretization grid to represent the front propagation accurately. Adaptive grids developed to address the problem of groundwater transport [84] have been used to handle this type of problem, but they are not well suited for a reduced complexity control oriented model. The nature of the sharp transition in the GDL liquid water volume is used to reduce to complexity of the model. The two-phase front location in the GDL along the x direction is defined in terms of an ordinary differential equation (ODE), similar to [80], thus greatly

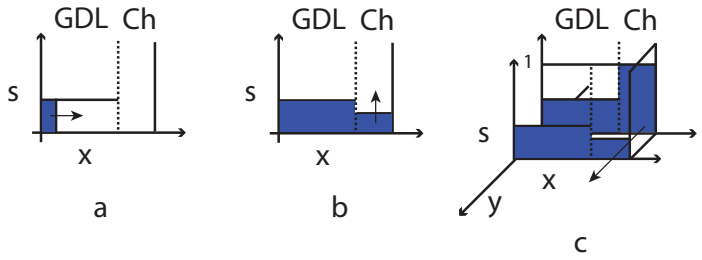

Figure 5.2 Evolution of liquid water fronts in the GDL and channel. In frame (a), liquid water fills the GDL up to $s = s_*$, then the two-phase front propagates toward the channel. Next in (b), the liquid begins to accumulate in the channel. Finally, in (c), once the channel section fills completely, water begins to spread back up along the channel.

reducing the computational complexity of the 1-D, two-phase water model.

It is assumed that the liquid water propagates at a constant, tunable, volume fraction, s_*, which is slightly larger than the immobile limit s_{im}. In [166], the s_{im} value is estimated using neutron imaging data of the water accumulation. The caricature is shown in Fig. 5.2, where a square-shape, two-phase front highlights the steep transition and the front propagation. Using the numerical solution of the physically-derived PDEs in [65, 12] and the experimental observations in [8], we infer that locally, liquid water first begins to accumulate in the GDL as shown in frame (a). In frame (b), the liquid water front has reached the GDL-channel boundary. Since there is little resistance to water entering the channel, it begins to spill out of the GDL and into the channel, where it accumulates. Finally, in frame (c), liquid water fills the anode channel section completely and begins spreading along the y-direction, up the channel, and against gravity.

The following section introduces the ordinary differential equations that describe the water dynamics in the membrane and the water front propagation in the GDLs. The proposed GDL model uses three nonlinear states (the anode GDL liquid front location, $x_{fr,an}$; cathode, $x_{fr,ca}$, GDL liquid front location; and the membrane water content, λ_{mb}) and three inputs (the anode and cathode channel vapor concentrations, which are the states of the channel model, and the current density which is measured) to predict the dynamically evolving front locations in both anode and cathode side GDLs during flooding and drying, as along with the dynamic changes in membrane water content. Detailed equations are presented only for the anode and the membrane. The modifications to these equation necessary to describe the cathode are highlighted.

5.3 Modification to the GDL model for Steady State Gas Transport

The steady state value can be used for the distribution of water vapor in the GDL [81],

$$0 = \frac{\partial c_{v,an}}{\partial t} = \frac{\partial}{\partial x}\left(D_v^{s_{im}} \frac{\partial c_{v,an}}{\partial x} \right) + r_v(c_{v,an}), \tag{5.1}$$

where $D_v^{s_{im}} = D_V D_{eff}(s = s_{im}; \varepsilon)$ is the diffusivity of vapor inside the GDL porous medium when s is near s_{im} [81]; D_V is the diffusivity of vapor in free space; and $D_{eff}(s, \varepsilon)$ is the effective diffusivity [71] correction term.

Assuming steady state conditions for the gases in the GDL [81], the hydrogen consumption at the catalyst surface accounts for the flux of hydrogen leaving the anode channel into the GDL, which is

$$W_{H_2,an,GDL} = -W_{H_2,rct} = -\frac{i_{fc}}{2F} M_{H_2} A_{fc}. \tag{5.2}$$

The combined liquid and vapor flux entering the GDL from the channel $W_{w,an,GDL}$ is found using Eq. (5.22).

Oxygen consumption at the catalyst surface accounts for the flux of oxygen leaving the cathode channel into the GDL,

$$W_{O_2,ca,GDL} = -W_{O_2,rct} = -\frac{i_{fc}}{4F} M_{O_2} A_{fc}. \tag{5.3}$$

and the nitrogen crossover rate is given by (5.27).

5.4 Liquid Water Front Propagation in the GDL

The water dynamics in the GDL-MB-GDL unit model are governed by the membrane water content and the location of a liquid water front in the GDLs as follows. A single state can be used to model water uptake into the membrane. Diffusion within the membrane is fast with respect to water uptake; therefore the diffusion and osmotic drag in each half of the membrane can be solved using (5.8) and (5.21). This approach yields a piece-wise linear water content profile, as indicated in Fig 5.3. The average membrane water content, λ_{mb}, is calculated from the water flux into the membrane from the cathode side, $N_{v,ca,mb}$, and out of the membrane from the anode side, $N_{v,an,mb}$,

$$\frac{d\lambda_{mb}}{dt} = K_{mb}(N_{v,ca,mb} - N_{v,an,mb}) \,, \tag{5.4}$$

where $K_{mb} = EW/(\rho_{mb}\,\delta_{mb})$ is the membrane water uptake rate.

The location of the two-phase (liquid-vapor) water front in the anode GDL, $x_{fr,an}$, is governed by the rate of water accumulation in the GDL condensing into the liquid phase, $N_{l,an}$. Hence, the front propagation is given by,

$$\frac{\mathrm{d}x_{fr,an}}{\mathrm{d}t} = K_L \begin{cases} N_{l,an} & x_{fr,an} < \delta_{GDL} \\ \min(0, N_{l,an}) & x_{fr,an} = \delta_{GDL}\ , \end{cases} \tag{5.5}$$

where $K_L = M_v/(\rho_l\ s_*\ \varepsilon\ \delta_{GDL})$ is a constant that accounts for the geometry and density of liquid water in the two-phase region, assuming the front propagates with constant liquid saturation ($s = s_*$), as shown in Fig. 5.3. The right hand side (RHS) of (5.5) depends on $N_{l,an}$, which is equal to the difference between the flux of water entering the GDL from the membrane, $N_{v,an,mb}$, and the flux of vapor leaving the GDL and entering the channel $N_{v,an}$,

$$N_{l,an} = N_{v,an,mb} - N_{v,an}\ . \tag{5.6}$$

These fluxes are diffusive and hence, depend on the water vapor concentration profile in the GDL, $c_{v,an}(x)$, which in turn, depends on the liquid phase front location, $x_{fr,an}$.

This spatially and temporally dependent coupling between the liquid and vapor phase through the condensation and evaporation is simplified by employing two assumptions. First, the liquid water dynamics are much slower than the gas dynamics, due to the difference in density, which is 1000 times greater. Therefore, for the purpose of tracking the liquid front propagation in the fuel cell, the gas states are taken to be in steady state [12, 80, 158]. Second, it is assumed that all the condensation and evaporation occurs at the membrane-GDL interface (MB-GDL) $x = 0$ [158] and liquid phase front location $x_{fr,an}$. With these assumptions, the steady-state solution of the vapor diffusion equation is a piecewise linear profile for the water vapor concentration, which follows the liquid water front location, as seen in Fig. 5.3,

$$c_{v,an}(x) = \begin{cases} \min(b_v, c_{v,sat}(T)) & x \le x_{fr,an} \\ m_v\,x + b_v & x > x_{fr,an}\ . \end{cases} \tag{5.7}$$

The vapor profile, $c_{v,an}(x)$, behind the front in the two-phase region $x \le x_{fr,an}$ is equal to the concentration at saturation $c_{v,sat}(T)$. In the vapor phase region, between the front location and the channel $x > x_{fr,an}$, the linear profile is the result of Fickian diffusion.

The propagation of the front location in the cathode GDL, $\dot{x}_{fr,ca}$, is defined similarly, where $N_{l,ca}$ is given by (5.20). For brevity, only the equations detailing the anode side will

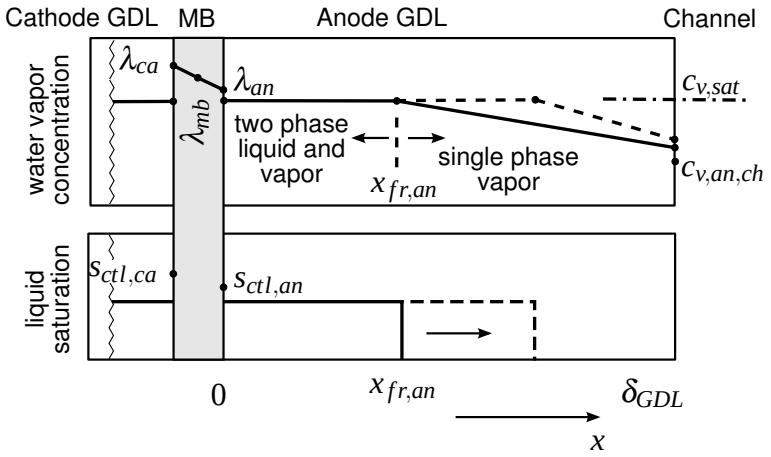

(a) Mode 2: advancing two-phase front on the anode side GDL.

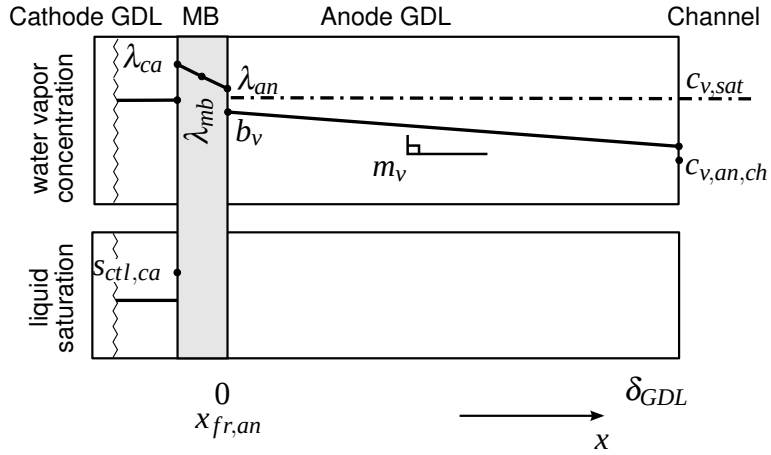

(b) Mode 1: only vapor phase in the GDL when $x_{fr,an} = 0$.

Figure 5.3 Two-phase water front evolution in the anode GDL for the unit fuel cell model, which represents a 1-D slice from Fig. 1. The figures show the assumed profiles in membrane water content (grey region), GDL water vapor concentration (upper plots), and GDL liquid water saturation (lower plots).

be presented; the cathode side equations are similar except where noted. The system can be described using an isothermal model or a slowly evolving temperature profile, where the measured end-plate temperature is imposed as the boundary condition at the GDL-channel (GDL-ch) interface and is a few degrees higher (load dependent) at the membrane-GDL (MB-GDL) interface since the reaction generates heat. A spatially invariant temperature distribution is assumed and the equations are presented with explicit temperature dependencies only where variables are first introduced.

5.5 Membrane Water Transport

Diffusion and osmotic drag govern the water flux out of the membrane and into the anode GDL,

$$N_{v,an,mb} = 2\,\frac{D_w(\lambda_{mb},T)\cdot(\lambda_{mb}-\lambda_{an})}{\delta_{mb}} - \frac{n_d\,i_{fc}}{F}\,. \tag{5.8}$$

The first term in (5.8) describes diffusion in the membrane, which is driven by the anode side gradient of the membrane water concentration, as shown in Fig. 5.3. The anode water gradient is defined by the state, λ_{mb}, and the water content at the membrane interface with the anode GDL, λ_{an}. Since the catalyst layer is very thin, its effect can be lumped into λ_{an}. Therefore, λ_{an} is expressed as a function of the catalyst flooding level, $s_{ctl,an}$, and the vapor concentration in the GDL, $c_{v,an}(0)$,

$$\lambda_{an} = (1-s_{ctl,an})\;\lambda_{T,a} + s_{ctl,an}\;\lambda_{max}, \tag{5.9}$$

where $\lambda_{max} = 22$ [151] is the water content of a liquid equilibrated membrane and $\lambda_{T,a}$ is the membrane water uptake isotherm [65, 130],

$$\lambda_{T,a} = c_0(T) + c_1(T)\;a + c_2(T)\;a^2 + c_3(T)\;a^3, \tag{5.10}$$

which is a function of the water activity, a, at the GDL-MB interface. The water activity in the GDL-MB interface is equal to the ratio of vapor concentration to the saturation value, $a_{an,mb} = c_{v,an}(0)/c_{v,sat}$. The $c_i(T),\ i \in \{0,1,2,3\}$, values are calculated by a linear interpolation of uptake isotherms [130], which were measured at 30 °C and 80 °C,

$$c_i(T) = \frac{(c_{i,353} - c_{i,303})}{50}(T-303) + c_{i,303}, \tag{5.11}$$

using the values in Table 5.1.

Table 5.1 Fuel cell water transport constants.

$\{\, c_{0,303},\, c_{1,303},\, c_{2,303},\, c_{3,303} \,\}$	{ 0.043, 17.81, -39.85, 36 } [121]
$\{\, c_{0,353},\, c_{1,353},\, c_{2,353},\, c_{3,353} \,\}$	{ 0.3, 10.8, -16, 14.1 } [133]
$\{\, D_{w,303},\, D_{w,353} \,\}$	{ 0.00333, 0.00259 } [169]
a_w ($\mathrm{cm}^2\ \mathrm{s}^{-1}$)	2.72E-5 [130]
c_f ($\mathrm{mol\ cm}^{-3}$)	0.0012 [130]
Sherwood number	$Sh = 2.693$ [149]

The dependence of membrane water content on catalyst liquid saturation is introduced to capture the observed anode flooding behavior. $s_{ctl,an}$ is a function of the liquid flux $N_{l,an}$

as follows,

$$s_{ctl,an} = \frac{\max(N_{l,an}, 0)}{N_{L,max}}, \tag{5.12}$$

where $N_{L,max}$ is the maximum liquid water flux the catalyst layer can handle before becoming completely saturated. $N_{L,max}$ should be inversely proportional to liquid water viscosity. The following functional form, with an exponential temperature dependence, is used to describe the relationship,

$$N_{L,max}(T) = N_{L0}\left(\exp\left[N_{L1}\left(\frac{1}{303} - \frac{1}{T}\right)\right]\right), \tag{5.13}$$

where N_{L1} and N_{L0} are tunable parameters.

$$D_w(\lambda, T) = \begin{cases} a_w\, c_f\, \exp[2416(1/303 - 1/T)]\, \frac{M_v\, \lambda_{mb}\, \rho_{mb}}{(\rho_l\, EW + M_v\, \lambda_{mb}\, \rho_{mb})}\, \frac{\mathrm{d}\log a_{mb}}{\mathrm{d}\log \lambda_{mb}} & , \lambda < \lambda_{a=1}(T) \\ D_{w0}(T) + D_{w1}(T)\cdot\lambda & , \lambda \geq \lambda_{a=1}(T) \end{cases} \tag{5.14}$$

$$D_{w0}(T) = \frac{a_w\, c_f\, \exp[2416(1/303 - 1/T)]}{(\rho_l\, EW + M_v\, \lambda_{a=1}(T)\, \rho_{mb})}\, \frac{M_v\, \lambda_{a=1}(T)^2\, \rho_{mb}}{c_1(T) + 2\, c_2(T) + 3\, c_3(T)} - \lambda_{a=1}(T)\, D_{w1}(T) \tag{5.15}$$

$$D_{w1}(T) = \left(D_{w,303} + \frac{D_{w,353} - D_{w,303}}{50}(T - 303)\right)\, a_w\, c_f\, \exp[2416(1/303 - 1/T)] \tag{5.16}$$

Note 1: The liquid volume fraction in the catalyst, $s_{ctl,an}$, represents the fraction of the membrane in contact with liquid water. Therefore, $s_{ctl,an}$ in (5.9) linearly interpolates between the water content of a vapor equilibrated membrane, $\lambda_{T,a=1}$, and the liquid equilibrated value $\lambda_{max} = 22$.

Note 2: There is no vapor gradient across the membrane when liquid is present in both GDLs, since the vapor concentration on both sides of the membrane is equal to $c_{v,sat}$. As a result, the difference between the catalyst flooding levels $s_{ctl,an}$ and $s_{ctl,ca}$ drives water transport through the membrane.

Note 3: The membrane water diffusion coefficient, $D_w(\lambda_{mb}, T)$ in (5.14), has an exponential dependence on temperature, but only a linear dependence on membrane water content for values of λ_{mb} greater than 6 [130, 169]. Typical membrane water content, when the cell is near flooding conditions, is in the range 9 to 14.

The second term in (5.8) describes electro-osmotic drag, which pulls water from the anode to the cathode with the conduction of protons through the membrane, and therefore,

is dependent on the current density, i_{fc}. The drag coefficient is given by,

$$n_d = \begin{cases} \lambda_{mb}/\lambda_{T,a=1} & \lambda_{mb} < \lambda_{T,a=1} \\ K_{\lambda,T}(\lambda_{mb} - \lambda_{T,a=1}) + 1 & \lambda_{mb} \geq \lambda_{T,a=1} \end{cases}, \tag{5.17}$$

which depends on the membrane water content and temperature with,

$$K_{\lambda,T} = \frac{(-1.834 + 0.0126\,T - 1)}{(\lambda_{max} - \lambda_{T,a=1})}, \tag{5.18}$$

a linear interpolation between $n_d = 1$ for the vapor equilibrated membrane and $n_d = -1.834 + 0.0126\,T$, for the liquid equilibrated membrane [169]. The volume fraction of water in the membrane, f_v, is calculated using the following equation,

$$f_v = \frac{\lambda_{mb} V_w}{V_{mb} + \lambda_{mb} V_w}, \tag{5.19}$$

where $V_{mb} = EW/\rho_{mb}$ is the dry membrane volume (equivalent weight divided by density) and V_w is the molar volume of water.

5.5.1 Cathode Side Equations

The same set of equations are used on the cathode, with the inclusion of generated water and a change of sign, which accounts for the use of a different coordinate axis,

$$\frac{1}{2}\frac{i_{fc}}{F} - N_{v,ca,mb} = N_{v,ca} + N_{l,ca}, \tag{5.20}$$

$$N_{v,ca,mb} = 2\,\frac{D_w(\lambda_{mb}, T) \cdot (\lambda_{ca} - \lambda_{mb})}{\delta_{mb}} - \frac{n_d\, i_{fc}}{F}. \tag{5.21}$$

5.6 Water Exchange With the Channel

The two-phase front location inside the GDL also determines the rate of vapor and liquid water exchange with the channel. When the front location is inside the GDL, $x_{fr,an} < \delta_{GDL}$, the water exchange with the channel is in the vapor phase only. When the front reaches the channel, $x_{fr,an} = \delta_{GDL}$, the mass flow of water from the GDL into the channel is the sum

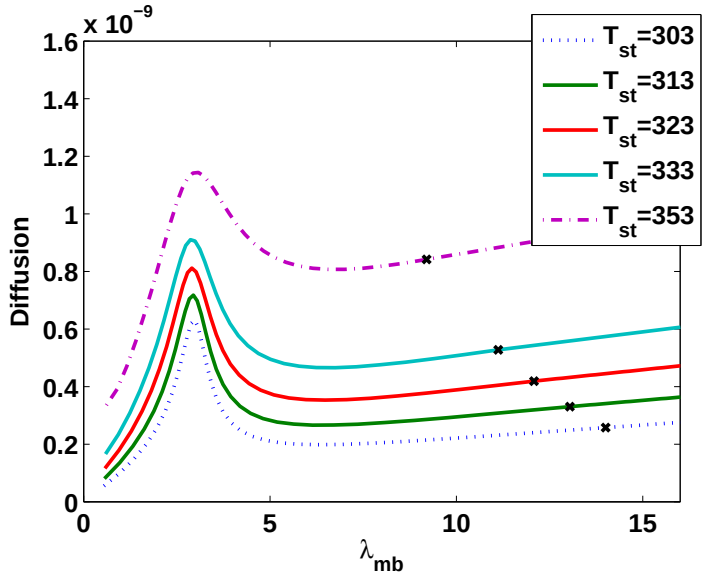

Figure 5.4 Diffusivity vs. membrane liquid water content at various temperatures. *x*s indicate the value of the vapor equilibrated membrane, i.e., $a_{mb} = 1$.

of the liquid and vapor flux,

$$W_{w,an,GDL} = A_{fc} M_v \left(N_{v,an} + \max(N_{l,an}, 0) \text{ if } x_{fr,an} = \delta_{GDL} \right) \tag{5.22}$$

The $\max(\cdot)$ function prevents liquid water in the channel from entering the GDL, since in the model formulation, $N_{l,an} < 0$ represents a receding two-phase front inside the GDL.

5.6.1 Anode Channel Model

The lumped volume equations constitute a mass balance for each of the three constituent gases in the channel (H_2/O_2, N_2, and H_2O) similar to [65]. Three dynamic states are used for the channel,

$$\frac{\mathrm{d}m_{i,an,ch}}{\mathrm{d}t} = W_{i,an,in} + W_{i,an,GDL} - W_{i,an,out}, \tag{5.23}$$

where $i \in \{H_2, N_2, w\}$ correspond to hydrogen, nitrogen, and water.

Liquid and vapor are combined into one state in the channel, and it is assumed that they are at a phase transition equilibrium, therefore,

$$m_{v,an,ch} = \min \left(m_{w,an,ch}, \frac{P_{sat}(T)\, V_{an,ch}\, M_v}{R\, T} \right) \tag{5.24}$$

where M_v is the molar mass of water, and $P_{sat}(T)$ is the temperature dependent saturated

vapor pressure [162]. The remaining water is considered to be in the liquid phase,

$$m_{l,an,ch} = m_{w,an,ch} - m_{v,an,ch}. \tag{5.25}$$

The anode inlet gas flow rate is assumed to be a dry hydrogen supply, therefore, $W_{N_2,an,in} = W_{w,an,in} = 0$ and,

$$W_{H_2,an,in} = W_{tot,an,in}. \tag{5.26}$$

The total flow into the anode, $W_{tot,an,in}$, is calculated using Eq. (5.31), and the anode inlet pressure $P_{an,in}$ is a constant, since it is set via a pressure regulator.

Nitrogen permeation across the membrane is a function of the channel partial pressures of nitrogen,

$$\begin{aligned} W_{N_2,an,GDL} &= -W_{N_2,ca,GDL} \\ &= \frac{k_{N_2,perm}\, M_{N_2}\, A_{fc}}{\delta_{mb}} \left(P_{N_2,ca,ch} - P_{N_2,an,ch}\right). \end{aligned} \tag{5.27}$$

The nitrogen permeation rate, $k_{N_2,perm}(T, \lambda_{mb})$, is a function of temperature and membrane water content as shown in (4.30) from [36].

The partial pressures of each gas are calculated from the mass using the ideal gas law,

$$P_{N_2,an,ch} = \frac{m_{N_2,an,ch}\, R\, T}{M_{N_2}\, V_{an,ch}}, \tag{5.28}$$

where $V_{an,ch}$ is the anode channel volume, and the total channel pressure is given by the sum of the partial pressures: $P_{an,ch} = P_{H_2,an,ch} + P_{N_2,an,ch} + P_{v,an,ch}$.

The gas flow leaving the anode channel is zero during normal operation. During an anode purge, the gas velocity is larger, but still within the laminar flow regime.

The individual gas species flows leaving the channel are calculated from the total flow though the outlet orifice by multiplying with the vector of mass fractions, w_j,

$$\begin{bmatrix} W_{H_2,an,out} \\ W_{N_2,an,out} \\ W_{w,an,out} \end{bmatrix} = w_j\, W_{tot,an,out} \tag{5.29}$$

where $W_{tot,an,out}$ is given by Eq. (5.31) if $u_1 = 1$, and zero otherwise. The subscript $j = 1$ corresponds to the anode channel when $P_1 = P_{an,ch} \geq P_2 = P_{an,outlet}$, and is $j = 2$ otherwise, which indicates back-flow from the outlet manifold. When liquid water is present in the anode channel, it is assumed that it can cover the outlet orifice, and the gas mixture pa-

rameters are replaced with those corresponding to liquid water in equation (5.31), until the liquid is cleared. i.e.,

$$w_1 = \begin{cases} \left[w_{H_2,an,ch},\ w_{N_2,an,ch},\ w_{v,an,ch}\right]^T & , \quad m_{l,an,ch} = 0 \\ \left[0,\ 0,\ 1\right]^T & , \quad m_{l,an,ch} > 0 \end{cases} \tag{5.30}$$

The density of the gas mixture is given by, $\rho_{an,ch} = m_{tot,an,ch}/V_{an,ch}$.

The total mass flow into and out of the fuel cell channel volumes is given by (5.31), where $C_{turb} = 0.61$ is the dimensionless discharge coefficient under turbulent conditions; D_h is the hydraulic diameter in m; A is the area of the orifice in m^2; R_t=9.33 is the critical value from [170]; ρ is the density of the gas in kg m^{-3}; $\nu = \mu/\rho$ is the kinematic viscosity in m^{2}s^{-1}; and P_1 and P_2 are the orifice upstream and downstream pressures in Pa. The dynamic viscosity of the gas mixture μ is calculated from the mole fraction X of gas species in the channel [13].

$$W_{tot} = \begin{cases} A\rho_1 \left(C_{turb} \sqrt{\frac{2}{\rho_1}|P_1 - P_2| + \left(\frac{\nu_1 R_t}{2 C_{turb} D_h}\right)^2} - \frac{\nu_1 R_t}{2 D_h} \right), & \text{if } P_1 \geq P_2 \\ -A\rho_2 \left(C_{turb} \sqrt{\frac{2}{\rho_2}|P_1 - P_2| + \left(\frac{\nu_2 R_t}{2 C_{turb} D_h}\right)^2} - \frac{\nu_2 R_t}{2 D_h} \right), & \text{if } P_1 < P_2 \end{cases} \tag{5.31}$$

5.6.2 Cathode Channel Model

The control inputs u_2 and u_4 shown in Fig. 1.2 affect the amount of air entering the cathode channel, the channel pressure, and the relative humidity of the supplied air. For simplicity, these control inputs are mapped to the parameters: $\lambda_{O_2,ca}$; the oxygen stoichiometry at the cathode inlet, $P_{tot,ca,in}$; the cathode inlet pressure; and $RH_{ca,in}$, the relative humidity air supplied to the cathode. In a physical system, these values would be the dynamic outputs of the blower [16] and humidifier [23].

Three dynamic states are used for the cathode channel, corresponding to a mass balance,

$$\frac{\mathrm{d}m_{i,ca,ch}}{\mathrm{d}t} = W_{i,ca,in} + W_{i,ca,GDL} - W_{i,ca,out}, \tag{5.32}$$

where $i \in \{O_2, N_2, w\}$ correspond to oxygen, nitrogen, and water.

The oxygen flow into the cathode is calculated from the stoichiometric ratio,

$$W_{O_2,ca,in} = \lambda_{O_2,ca} \frac{i_{fc}}{4F} A_{fc} M_{O_2}. \tag{5.33}$$

The nitrogen flow into the cathode channel,

$$W_{N_2,ca,in} = \frac{M_{N_2}}{OMF_{ca,in}\, M_{O_2}}\, W_{O_2,ca,in}, \tag{5.34}$$

can be calculated using the mole fraction of dry air, $OMF_{ca,in} = 0.21$. Finally, using the vapor pressure at the cathode inlet, $P_{v,ca,in} = RH_{ca,in}\, P_{sat}(T)$, the flow of water vapor into the cathode is calculated by

$$W_{v,ca,in} = \frac{P_{v,ca,in}\, M_v}{OMF_{ca,in}\, (P_{tot,ca,in} - P_{v,ca,in})\, M_{O_2}} W_{O_2,ca,in}. \tag{5.35}$$

The cathode channel outlet equations are similar to the anode outlet equation and are skipped for brevity. A fixed cathode outlet pressure is assumed.

5.6.3 Water Transport Through the Gas Diffusion Layer (GDL)

The Boundary Conditions (BCs) complete the model of GDL water accumulation and transport. For $c_{v,an}(x,t)$, Neumann type BCs are imposed at both sides. The channel (ch) boundary condition is,

$$N_{v,an,GDL}\big|_{x=\delta_{GDL}} = k_{mt}\left(c_{v,an,GDL}\big|_{x=\delta_{GDL}} - c_{v,an,ch}\right). \tag{5.36}$$

where $c_{v,an,ch}$ is the vapor concentration in the channel, and $k_{mt} = Sh\, D_V / H_{ch}$ is the mass transfer coefficient [149] related to the Sherwood number Sh, the free space diffusion coefficient for vapor in hydrogen, D_V, and the channel height, h_{ch}, which is the characteristic diffusion length. The water vapor flux across the membrane determines the slope of the water vapor distribution at the membrane,

$$\left.\frac{\partial c_{v,an}}{\partial x}\right|_{x=0} = \frac{-N_{w,mb}}{D_v^{s_{im}}}, \tag{5.37}$$

where electro-osmotic drag and back diffusion govern the membrane water molar flux $N_{w,mb}$ [65], as shown in (2.2).

For the liquid water PDE, mixed BCs are again imposed. Specifically, water passing into the GDL from the membrane is assumed to be in vapor form due to the presence of a micro-porous layer; therefore, $\frac{\partial S}{\partial x}\big|_{x=0} = 0$. The liquid water flux from the GDL into the channel depends on the boundary condition at the GDL-channel interface. Liquid flows

readily when there is sufficient water to form connected pathways. The boundary condition

$$S(\delta_{GDL},t)=0, \tag{5.38}$$

is used to represent this behavior, similar to [80]. Other possible models include using the liquid pressure in the channel [171] and could be considered in the future.

5.7 Fitting Water Transport Parameters

The tunable parameters N_{L0} and N_{L1} in (5.13) can be experimentally determined from the neutron imaging data by observing the rate of liquid water accumulation in the anode channel during operation of the PEMFC under DEA conditions [8].The quasi steady state accumulation rate is calculated from the time evolution of the system and is plotted as a function of current density, i_{fc}, and cell temperature, T, in Figure 5.5. The fuel cell operating conditions are chosen to maintain as close to uniform channel conditions as possible, such that the lumped channel approximation remains valid. Therefore, experimental data with fully humidified cathode inlet gas feeds are used for the parameter identification. Under these operating conditions, it is assumed that both the anode and cathode GDLs are saturated, $x_{fr,an}=\delta_{GDL}$, when liquid water accumulation in the anode channel is observed, and the rate of liquid water accumulation in the anode channel can be attributed to the rate of water flux though the membrane. With these assumptions, $c_{v,an,ch}=c_{v,ca,ch}=c_{v,sat}(T)$ and $x_{fr,an}=x_{fr,ca}=\delta_{GDL}$, the equilibrium value of membrane water content, $\lambda=\lambda_{eq}$ in (5.39), and the resulting membrane flux into the anode $N_{v,an,mb,eq}$ can be found analytically. The function $N_{v,an,mb,eq}(T,i_{fc},\lambda=\lambda_{eq},N_{L0},N_{L1})$, as shown in (5.40), is fit to the measured liquid water accumulation data using the non-linear least squares fitting routine in MATLAB© for the parameters N_{L0} and N_{L1}. An analytic expression for Jacobian matrix is easily calculated, which speeds up the convergence of the parameter fitting. The specific functional form of $N_{L,max}$ given in (5.13) is independent of the tuning procedure, and therefore the model could easily be parameterized using another functional relationship.

Table 5.2 Tuned parameters for the liquid water transport model.

s_*	0.37
N_{L0}	2.3434
N_{L1}	3991

$$\lambda_{eq}=\frac{4F\ \lambda_{a=1}(T)N_{L,max}(T)-\lambda_{a=1}i_{fc}+\lambda_{\max}i_{fc}}{4F\,N_{L,max}(T)} \tag{5.39}$$

$$N_{v,an,mb,eq} = \frac{2\,F N_{L,max}(T)\,D_{ve} D_w(\lambda_{eq},T)\,(\lambda_{eq} - \lambda_{a=1}(T)) - i_{fc}\,\delta_{mb}\,n_d(\lambda_{eq},T)}{F\left(N_{L,max}(T)\,D_{ve}\,\delta_{mb} + 2\,D_{ve}\,D_w(\lambda_{eq},T)(\lambda_{\max} - \lambda_{a=1}(T))\right)} \tag{5.40}$$

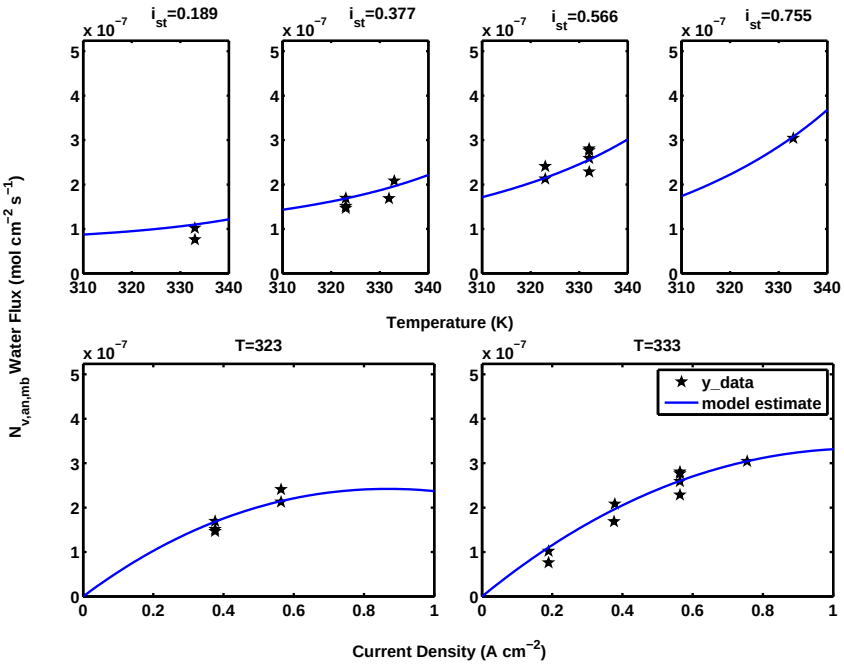

Figure 5.5 Water transport as a function of temperature and current density for saturated channels. The fit parameters yield a model with a convex temperature relationship that is concave with current density.

The tuned model shows an exponential increase in the rate of water crossover and liquid accumulation in the anode channel with increasing temperature due to the exponential term in the diffusion coefficient (5.14). The water crossover rate increases with current density, as the rate of water production increases, until the osmotic drag term begins to dominate (5.8). At this point, the water crossover rate begins to decrease with a further increase of current density.

5.8 Fuel Cell Terminal Voltage

Fuel cell terminal voltage is the main measurable output of the system, and represents a static, non-linear output mapping of the states and operating conditions (temperature and load current). The electrochemical dynamics are very fast [16, 172], and can represented by static relationships. The mass transport of reactants into the cell and the removal of product water are responsible for the dynamic behavior observed in the measured voltage.

The inputs to the voltage model are: total current $I_{fc}(A)$; temperature T (K); membrane water content λ_{mb}; hydrogen partial pressure at the membrane surface $P_{H_2,an,mb}$ (Pa); and oxygen partial pressure at the cathode membrane surface $P_{O_2,ca,mb}$ (Pa), which is calculated in (5.54). The pressure and concentration are related by the ideal gas law $P_{H_2,an,mb} = RTc_{H_2,an,mb}$, where R is the universal gas constant. The cell terminal voltage is calculated from the open circuit potential minus the concentration, over-potential, and ohmic losses.

$$V_{cell} = E_{rev} - \eta_{act,ca} - \eta_{act,an} - \eta_{mb} - \eta_{ohmic}. \tag{5.41}$$

The reversible voltage is given by,

$$E_{rev} = E_0 - \frac{RT}{nF}\log\left(\frac{aH_2O}{aH_2\sqrt{(aO_2)}}\right). \tag{5.42}$$

where $E_0 = 1.229 - (T - T_0)\cdot 2.304\times 10^{-4}$ [13]. The reactant and product activities are calculated from the concentrations, $aH_2 = c_{H_2,an,mb}/C_{ref,H_2}$, $aO_2 = c_{O_2,ca,mb}/C_{ref,O_2}$, and $aH_2O = 1$ since liquid water product assumed. The subscript ref refers to the reference quantity, and the subscript ca,mb refers to the cathode membrane surface.

To simplify the calculation of cell voltage, a hyperbolic sine function is used for the calculation of over-potentials, $\eta_{act,ca}$ and $\eta_{act,an}$, from the exchange current density, $i_{o,ca}$ and $i_{o,an}$,

$$\eta_{act,ca} = \frac{RT}{\alpha_{c,a}nF}\text{asinh}\left(\frac{i_{fc}+i_{loss}}{2i_{o,ca}}\right), \tag{5.43}$$

where $i_{fc} = \frac{I_{fc}}{A_{fc}}$ is the current density and i_{loss} is the lost current density due to hydrogen crossover, a tuned parameter listed in Table 5.3. $n = 2$ is the electron transport number, and $F = 96485$ C per mol of electrons is Faraday's constant. The hyperbolic sine is equivalent to the Butler-Volmer equation when the forward and reverse reaction coefficients ($\alpha_{c,a} = \alpha_{c,c}$) are equal [162]. The following equation gives the exchange current density,

$$i_{o,ca}{=}i_{o,ref,ca}\left(\frac{c_{O_2,ca,mb}}{C_{ref,O_2}}\right)^{\gamma_{O_2}}\left(\frac{c_{H^+_{ca,mb}}}{C_{ref,H^+}}\right)^{\gamma_{H^+}}\exp\left(\frac{-E_c}{R}\left(\frac{1}{T}-\frac{1}{T_0}\right)\right), \tag{5.44}$$

where $i_{o,ref,ca}$ is the reference current density, c_* is the reactant concentration, γ is the concentration parameter, and E_c in the Arrhenius term is the activation energy for hydrogen oxidation on platinum [138]. The cathode concentration parameter for the local proton activity, $\gamma_{H^+} = 0.5$, is given by [164]. Although the cathode reaction depends on the oxygen concentration, as well as the activity of protons in the membrane [163], the proton

activity term is typically neglected since there are sufficient protons under normal fuel cell operation, i.e., $\left(c_{H^+_{ca,mb}}/C_{ref,H^+}\right)^{\gamma_{H^+}} \approx 1$.

Similarly for the anode side,

$$\eta_{act,an} = \frac{RT}{\alpha_{a,a}nF}\text{asinh}\left(\frac{i_{fc}+i_{loss}}{2i_{o,an}}\right), \tag{5.45}$$

where the anode exchange current density is,

$$i_{o,an} = i_{o,ref,an}\left(\frac{c_{H_2,an,mb}}{C_{ref,H_2}}\right)^{\gamma_{H_2}}\exp\left(\frac{-E_c}{R}\left(\frac{1}{T}-\frac{1}{T_0}\right)\right). \tag{5.46}$$

The following equation represents the potential drop due to proton conductivity losses in the membrane,

$$\eta_{mb} = i_{fc}R_{mb}(T,\lambda_{mb}) \tag{5.47}$$

where the membrane resistance is calculated as follows,

$$R_{mb}(T,\lambda_{mb}) = \frac{\exp\left[1268\left(\frac{1}{T}-\frac{1}{303}\right)\right]}{-0.00326+0.005193\lambda_{mb}}\delta_{mb}, \tag{5.48}$$

Where δ_{mb} is the membrane thickness, and the membrane conductivity is a function of water content and temperature using the standard relationship from Springer et al. [121].

Finally, the GDL and contact resistances are lumped into R_{ohmic} for the ohmic loss term,

$$\eta_{ohmic} = i_{fc}R_{ohmic}. \tag{5.49}$$

The typical graph associated with fuel cell operation is the polarization curve shown in Fig. 5.6, which is a plot of the terminal voltage V_{cell} versus the applied current density i_{fc}. The initial drop in cell voltage for small current density is due to the activation losses, $\eta_{act,an}$ and $\eta_{act,ca}$. The middle region of the polarization curve is referred to as the ohmic region, which has a fairly linear *i-v* relationship. The losses for this range of current density are primarily attributed to the ohmic terms η_{mb} and η_{ohmic}.

The steep drop in cell voltage, shown in Fig. 5.6 at high current density, is attributed to concentration loss at the membrane surface. This concentration loss comes from the diffusion of reactants, specifically oxygen from the channel though the GDL to the CL. The concentration value, $c_{O_2,ca,mb}$, represents the amount of oxygen available in the catalyst layer, which decreases at high current density due to the finite resistance to gas transport through the GDL. Since the diffusion is a fast process, the 1-D steady state profile can be

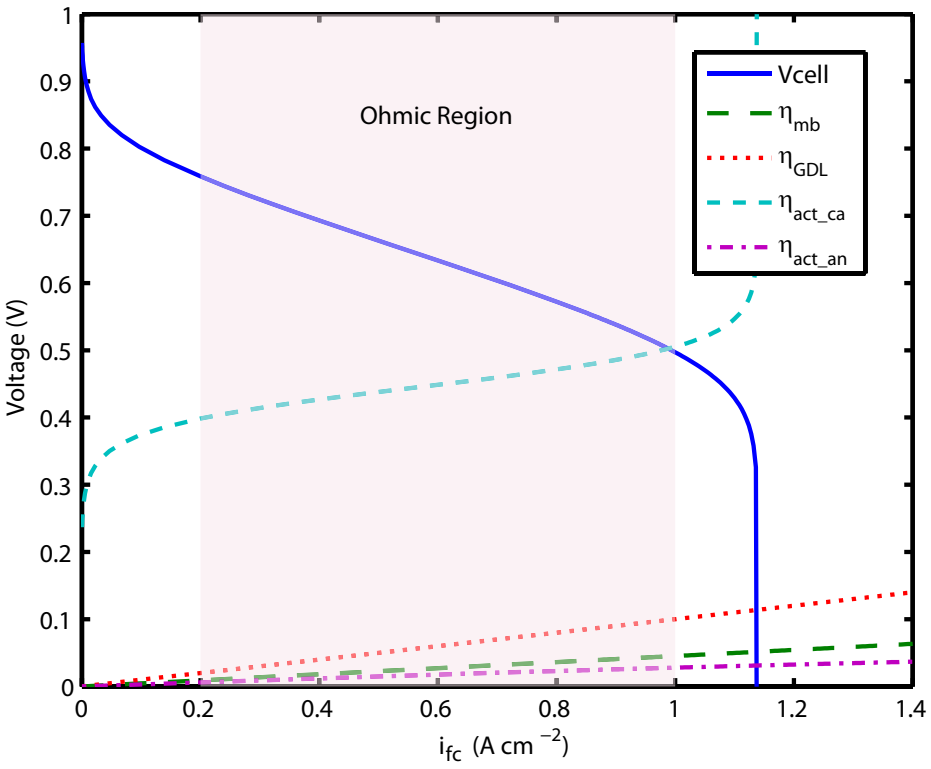

Figure 5.6 Fuel Cell Polarization Curve.

considered assuming Fick's Law in the GDL,

$$N_{O_2,ca,GDL} = -D_{eff}(s,\varepsilon) D_{O_2} \frac{\partial c_{O_2,ca,GDL}}{\partial x} \tag{5.50}$$

with a Neumann boundary condition at the membrane surface where the flux is equal to the consumption of oxygen,

$$N_{O_2,ca,GDL}\big|_{x=0} = -N_{O_2,rct}, \tag{5.51}$$

and a Neumann boundary condition at the channel, which is given by the mass transfer coefficient, k_{mt} [149],

$$N_{O_2,ca,GDL}\big|_{x=\delta_{GDL}} = k_{mt}\left(c_{O_2,ca,GDL}\big|_{x=\delta_{GDL}} - c_{O_2,ca,ch}\right). \tag{5.52}$$

where $c_{O_2,ca,ch}$ is the oxygen concentration in the channel. The consumption rate of oxygen, (mol cm^{-2} s^{-1}), is given by,

$$N_{O_2,rct} = \frac{i_{fc}}{4F}. \tag{5.53}$$

The free space diffusion coefficient D_{O_2} m^{2}s^{-1} is multiplied by an effective diffusivity coefficient, $D_{eff}(s,\varepsilon)$, to account for the porous structure of the GDL and the reduced vol-

ume due to liquid water accumulation in the diffusion medium [71]. In the case of constant diffusivity, $D_{O_2}^{s_{im}} = D_{O_2} D_{eff}(s_{im}, \varepsilon)$, and this reduces to,

$$c_{O_2,ca,mb} = c_{O_2,ca,GDL}\big|_{x=0} = c_{O_2,ca,ch} - \left(\frac{1}{k_{mt}} + \frac{\delta_{GDL}}{D_{O_2}^{s_{im}}} \right) N_{O_2,rct}, \tag{5.54}$$

The same equation holds true for the anode, where,

$$N_{H_2,rct} = \frac{i_{fc}}{2F}. \tag{5.55}$$

For a derivation of the reactant profiles with non-constant $D_{eff}(s(x))$, see [12].

Table 5.3 Tuned Parameters in the Voltage Equation.

$i_{o,ref,ca}$	7E-8 (A cm^{-2})	Cathode exchange current
$i_{o,ref,an}$	0.05 (A cm^{-2})	Anode exchange current
i_{loss}	1E-3 (A cm^{-2})	Crossover current
D_{eff}	0.35	Diffusivity in GDL
R_{GDL}	0.275 (Ω cm^2)	Contract resistance

5.9 Apparent Current Density and Reduced Cell Area

The effect of liquid water and nitrogen accumulation on the measured terminal voltage can be captured by an apparent current density, corresponding to the area of the hydrogen rich portion of the cell. The use of apparent current density, i_{app}, in place of the nominal current density, i_{fc}, in the above voltage model describes the resulting voltage drop from mass accumulation in the channel.

$$i_{app} = \frac{I_{fc}}{A_{app}}, \tag{5.56}$$

where the apparent area is calculated from the nitrogen and water mass in the channel using the following equation,

$$A_{app} = A_{fc} \frac{y_{fr}}{L_{ch}}. \tag{5.57}$$

where L_{ch} is the channel length and y_{fr} is the front location. A simple model, which considers the nominal current density, channel pressure, and temperature, can be used to translate the mass of liquid water, and nitrogen in the dead-ended anode channel into a front location,

$$m_{l,an,ch}, m_{N_2,an,ch} \mapsto y_{fr}, \tag{5.58}$$

based on the assumptions of saturated vapor conditions and uniform apparent current density in the region above of the front, as shown in Fig. 5.7.

$$y_{fr} = \begin{cases} L_w & m_{N_2} \leq m_{N_2,critical} \\ y_{frN_2} & m_{N_2} > m_{N_2,critical} \end{cases}, \tag{5.59}$$

where the liquid water front location, L_w, is defined by the channel dimensions, liquid water density ρ_l, and the mass of liquid water in the anode channel (5.25), using the following equation:

$$L_w = \left(1 - \frac{m_{l,an,ch}}{\rho_l V_{an,ch}}\right) L_{ch}. \tag{5.60}$$

The nitrogen front location y_{frN_2} is found by solving (5.68) and the critical nitrogen mass at which the nitrogen front develops is given by,

$$m_{N_2,critical} = M_{N_2} \frac{V_{ch}}{L_{ch}} \frac{(P_{an} - P_{v,sat}(T))}{(RT)} \left(\frac{\sqrt{2L_w D_{N_2,H_2}} \left(1 - \exp\left(-\frac{K_v i_{fc} L_w}{2D_{N_2,H_2}}\right)\right)}{\operatorname{erf}\left(\frac{\sqrt{K_v i_{fc} L_w}}{\sqrt{2D_{N_2,H_2}}}\right) \sqrt{K_v i_{fc} \pi}} \right). \tag{5.61}$$

This relationship is derived from steady state convection and Fickian diffusion in the anode channel,

$$0 = \frac{\partial c_{N_2}}{\partial t} = \frac{\partial}{\partial y}\left(D_{N_2,H_2} \frac{\partial c_{N_2}}{\partial y}\right) - V(y) \frac{\partial c_{N_2}}{\partial y}. \tag{5.62}$$

The convective velocity, $V(y)$, (m s^{-1}) can be calculated from the consumption of hydrogen, assuming the flux of N_2 crossover is small relative to the reaction rate of H_2. The convective velocity is zero after the front location because no reaction occurs in this region.

$$V(y) = \begin{cases} K_v \frac{i_{fc}}{y_{fr}} (y_{fr} - y) & y \leq y_{fr} \\ 0 & y > y_{fr} \end{cases} \tag{5.63}$$

where K_v is given by the following equation,

$$K_v = L_{ch} \frac{(w_{ch} + w_{rib})}{2F} \frac{RT}{P_{an}(w_{ch} h_{ch})}, \tag{5.64}$$

where P_{an} is the anode channel pressure, and w_{ch}, h_{ch}, and w_{rib} denote the channel width, height, and rib width, respectively.

The steady state solution of (5.62), is of the form,

$$c_{N_2}(y) = \begin{cases} c_1 + c_2 \operatorname{erf}\left(\frac{\sqrt{K_v i_{fc}}(y - y_{frN_2})}{\sqrt{2 y_{frN_2} D_{N_2,H_2}}}\right) & y \le y_{frN_2} \\ (P_{an} - P_{v,sat}(T))/(RT) & y > y_{frN_2} \end{cases} \tag{5.65}$$

c_1 and c_2 can be solved using the boundary conditions $c_{N_2}(0) = 0$ (the system is fed with dry hydrogen) and $c_{H_2}(y_{frN_2}) = 0$, which implies $c_{N_2}(y_{frN_2}) = (P_{an} - P_{v,sat}(T))/(RT)$

Hence, for $y \le y_{frN_2}$, the distributed nitrogen concentration is

$$c_{N_2}(y) = \frac{(P_{an} - P_{v,sat}(T))}{(RT)} \left(1 + \frac{\operatorname{erf}\left(\frac{\sqrt{K_v i_{fc}}(y - y_{frN_2})}{\sqrt{2 y_{frN_2} D_{N_2,H_2}}}\right)}{\operatorname{erf}\left(\frac{\sqrt{K_v i_{fc} y_{frN_2}}}{\sqrt{2 D_{N_2,H_2}}}\right)}\right) \tag{5.66}$$

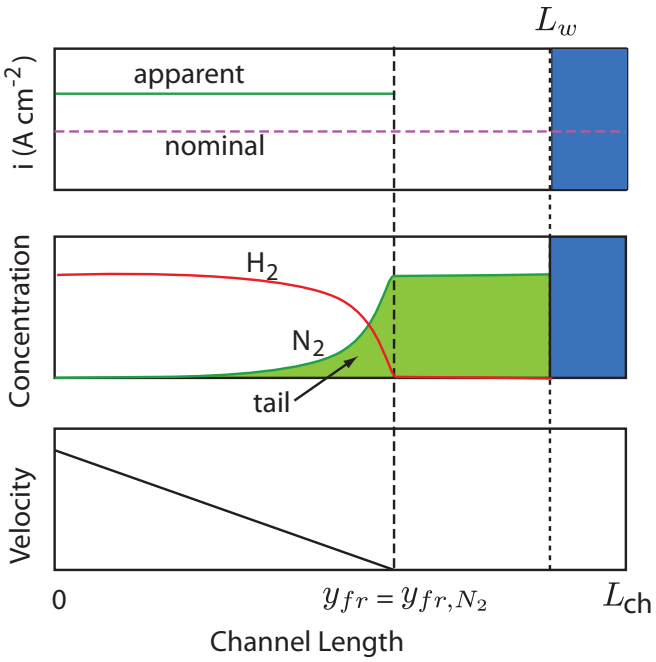

Figure 5.7 Nitrogen front propagation schematic (not to scale).

The nitrogen front location, y_{frN_2} and the mass of nitrogen, which does not contribute to the apparent current density, $m_{N_2,\text{tail}}$, can be found from the system state m_{N_2} using the following equation,

$$m_{N_2} = m_{N_2,\text{tail}} + m_{N_2,\text{blanket}}, \tag{5.67}$$

where the mass of nitrogen in the blanketed region $m_{N_2,\text{blanket}}$ and in the tail can be found

by integrating (5.65) and (5.66) along the channel to get

$$m_{N_2} = M_{N_2} \frac{V_{ch}}{L_{ch}} \frac{(P_{an} - P_{v,sat}(T))}{(RT)} \left((L_w - y_{frN_2}) + \frac{\sqrt{2 y_{frN_2} D_{N_2,H_2}} \left(1 - \exp\left(-\frac{K_v i_{fc} y_{frN_2}}{2 D_{N_2,H_2}}\right)\right)}{\operatorname{erf}\left(\frac{\sqrt{K_v i_{fc} y_{frN_2}}}{\sqrt{2 D_{N_2,H_2}}}\right) \sqrt{K_v i_{fc} \pi}} \right), \tag{5.68}$$

which can be solved for the nitrogen blanketing front location numerically.

5.10 Simulation Results

Current density i_{fc}, stack temperature T, cathode stoichiometric ratio, and cathode inlet relative humidity (dew point temperature) are measured from the experiment and used as the inputs for the model. Fig. 5.8 shows a simulation of the experiment at NIST [8] with a humidified cathode inlet feed. The anode channel water vapor concentration remains near the saturation value, decreasing only slightly during an anode purge. The membrane water content λ_{mb}, shown in the second subplot of Fig. 5.8, is strongly dependent on current density and temperature, increasing with current density at t=3850 (min) and decreasing with temperature at t=3785 (min). The normalized front location is shown in the third subplot of Fig. 5.8, and the liquid water mass in the anode channel is shown in the last subplot.

The anode purges shown in Fig. 5.9 capture the removal of liquid water from the GDL. This can clearly be seen by the flat sections in the plot of anode channel liquid water mass. Liquid water must re-fill the GDL before accumulation of liquid water in the anode channel begins again following an anode purge. The duration of the flat region in the channel liquid water trace depends on the “strength” of the anode purge, its flow rate and duration, and the amount of liquid water present in the channel preceding the purge. The dry hydrogen flowing through the fuel cell must first remove all of the liquid water from the channel before causing the two-phase liquid water front location to recede in the GDL. Our model predicts roughly a 5% change in the anode front location due to the 1 s purge, and matches the time period before water accumulation in the channel resumes.

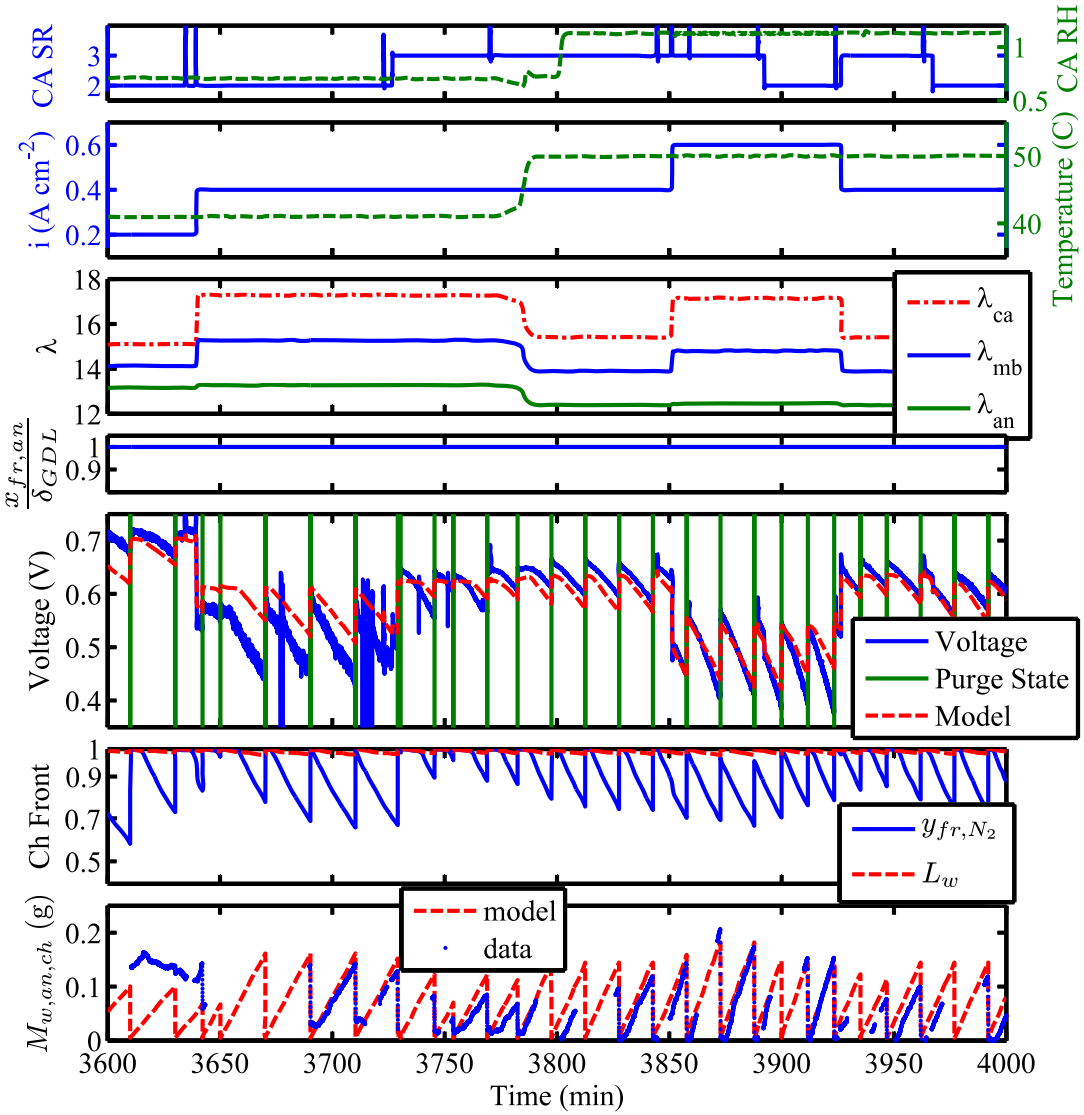

Figure 5.8 Comparison of simulation versus Aug 7, 2007 Experiment at NIST [8]. Cell temperature increased from 314 (K) to 323 (K) at t=3785 (min). The model shows good agreement over the range of temperature and current density, but slightly underpredicts water transport to the anode at higher current density.

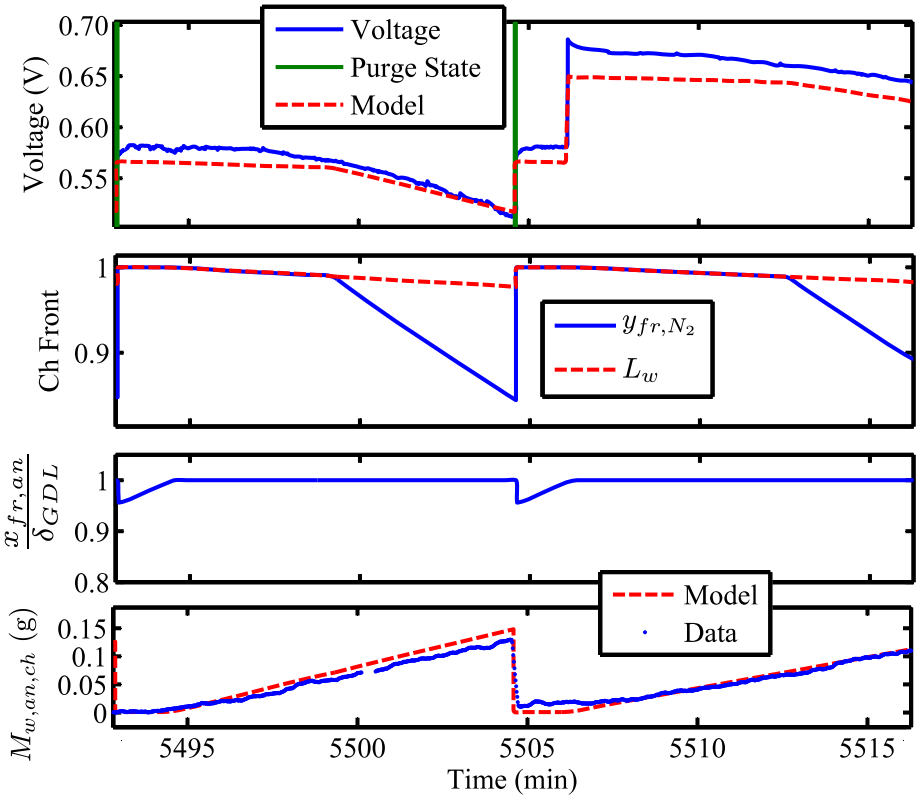

Figure 5.9 Zoomed plot showing model predictions vs. measured data. After an anode purge, which removes liquid water from the GDL, liquid water accumulation in the anode channel resumes only after the liquid front reaches the channel. Experimental conditions are a fully humidified cathode inlet at a cell temperature of 60 °C. There is a change in current density, from 0.6 $\rightarrow$ 0.4 (A cm^{-2}) and cathode stoichimetric ratio, from 3 to 4 at $t = 5506$ min.

Table 5.4 Nomenclature and Constants

Catalyst layer	CTL
Membrane	MB
Gas Diffusion Layer	GDL
Maximum liquid water flux (mol cm^{-2} s^{-1})	$N_{L,max}$
Anode water vapor concentration	$c_{v,an}$
Slope of $c_{v,an}$ in single-phase region	m_v
Y-intercept of $c_{v,an}$ in single-phase region	b_v
Water content of liquid equilibrated membrane	$\lambda_{max} = 22$ [151]
GDL thickness (μm)	$\delta_{GDL} = 420$
Membrane thickness (μm)	$\delta_{mb} = 25$
Mass transfer coefficient	k_{mt}
Channel height (mm)	$H_{ch} = 1$
Vapor flux in the anode GDL	$N_{v,an}$
Liquid saturation in the two-phase region	s_*
Catalyst layer liquid water saturation	$s_{ctl,j}$
Temperature (K)	T
Water activity	$a = c_v/c_{v,sat}$
GDL porosity	ε=0.8
Vapor diffusivity (cm^2 s^{-1})	$D_V = 0.345$
Porosity corrected vapor diffusivity (cm^2 s^{-1})	$D_{v,e}$ [71]
Sherwood number	$Sh = 2.693$ [149]

Chapter 6

Equilibrium of Nitrogen Front with DEA

This chapter investigates the equilibrium behavior during the dead-ended anode (DEA) operation of a polymer electrolyte membrane fuel cell. It is shown that although nitrogen crossover continues in the upper portion of the FC, a balancing mechanism, namely nitrogen back-diffusion in the lower half of the channel, brings the blanketing front to a stop. The reduced order model was developed in Chapter 4, and 5 predicts the species molar fraction of gases in the anode channel and the two-phase front locations both in the GDLs and anode channel. Since nitrogen was shown to be the primary cause of voltage degradation [95], the single-phase anode channel model is sufficient to investigate this phenomenon. Although the membrane hydration model could be improved (see future work in Chap. 7), the model predictions match reasonably well with the experiments, providing a valuable design tool. Analysis and simulations are used to study the influence of certain controllable inputs and system parameters in determining a stable steady-state power output in the DEA operation. It is shown that the equilibrium is feasible only for small load current. Experimental validation shows the stable voltage output under DEA conditions predicted by the model. The results suggest that it is possible to coat only the active portion of the membrane along the channel length with a catalyst; hence, reducing the system cost without sacrificing catalyst utilization or durability. Further device design based on the system equilibria will be performed in subsequent work.

6.1 Introduction

The objective of this work is to explore the equilibrium in DEA operation and to study the key operating parameters controlling the equilibria and outputs (fuel cell terminal voltage). Simulations of the dynamic models [95, 41] have indicated that such equilibria exist. Hikita et al. [39] also showed sustained operation without purging the anode for several

hours. Using the previous model, it is established here that equilibria exist and the effect of various operating conditions on the equilibrium are shown. A straightforward improvement of the fuel cell design can be proposed based upon the reactant distributions in the anode channel. The local catalyst loading could be applied non-uniformly, based on the local hydrogen distribution in steady state, so that the catalyst could be utilized much more efficiently in PEM fuel cells with DEAs. The partial catalyst coating can also be used to avoid the carbon corrosion caused by the hydrogen starvation problem when operating in DEA mode.

The dynamic model presented in Chapter 4 captures the time-evolution of gas species concentrations, membrane water content, local current density along the channel, and cell voltage. The model predicts anode nitrogen blanketing, a unique feature of DEA operation. The model shows that N_2 blanketing is the most significant mechanism and the primary cause of the gradual, yet recoverable, voltage drop. The co-flow and vertical orientation of the fuel cell channels result in the nitrogen/water accumulation at the bottom of the anode channel with the front moving towards the inlet. The simplicity and predictability (no stochastic channel water plugging causing randomly distributed phenomena) of the water front pattern allow for model simplicity. The dynamic model has been verified by in-situ gas chromatography measurement and neutron imaging [95]. The local difference between anode and cathode species partial pressures drive transport through the membrane. The rate constant for permeation depends on the membrane water content. Although the gas phase crossover proceeds at a fairly low rate due to the low membrane permeability, the accumulation effects over time have an integrator type behavior. Therefore, periodic purging of the accumulated inert gas is required for high power operation.

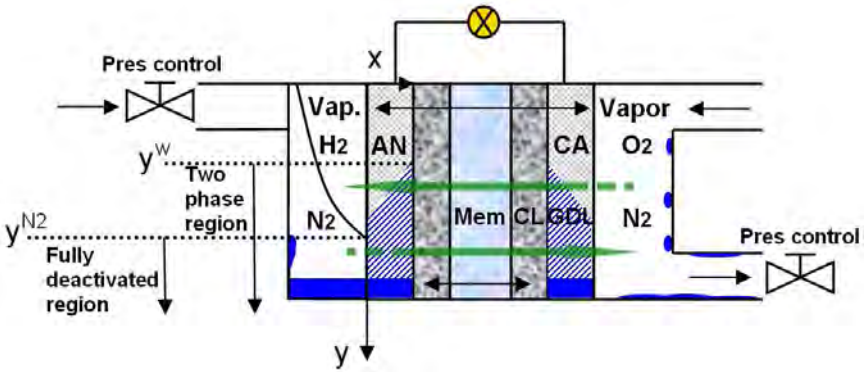

Figure 6.1 Equilibrium scenario in DEA operation. (Not to scale)

6.2 Equilibrium Mechanism

The concept of equilibrium for nitrogen accumulation based on a single volume lumped parameter model is easy to visualize. In the simplest form, when the purge valve is closed, no nitrogen can enter or leave the system except to cross through the membrane; therefore, the nitrogen accumulation is governed by the following ODE,

$$\frac{\mathrm{d}P_{N_2,an}}{\mathrm{d}t} = K_{N_2}\frac{A_{fc}}{RTV_{an}\Delta_{mb}}(P_{N_2,ca} - P_{N_2,an}), \tag{6.1}$$

where A_{fc}, is the membrane area, V_{an} is the anode volume, Δ_{mb} is the membrane thickness, and K_{N_2} is the nitrogen permeation rate through the membrane, which depends on membrane water content and temperature. The accumulation continues until the averaged partial pressure of N_2 in the anode channel is equal to that of air in the cathode volume, assuming uniform membrane water content, and hence uniform K_{N_2}, along the length of the channel.

Departing from the simple lumped-volume model, the effects of convection are shown in [41] and [173]. Convection pushes and packs the nitrogen to the bottom of the channel and prevents hydrogen from reaching that portion of the channel. In this case, the local nitrogen partial pressure may easily exceed the cathode. However, if the nitrogen permeation rate is constant along the y-direction, the average nitrogen partial pressure in the anode will not exceed the cathode's average (for small pressure differentials between the anode and cathode volume). Therefore, convection driven dynamics also predict that dynamically stable equilibrium (with positive cell terminal voltage) exists at low current density, where the active area of the fuel cell is reduced by an amount equal to the mole fraction of nitrogen in the cathode channel (the effective area is reduced by 60 to 80%). In steady state, the nitrogen crossover is from cathode to anode at the upper portion of the channel (negative x-direction) and from anode to cathode in the lower region (positive **x**-direction), as shown in Fig. 6.1 with the arrows of N_2 flux through the membrane. In Chapter 4 and summarized in (6.2), the inclusion of diffusive terms moderates the effect of nitrogen in the anode channel by slowing the rate of formation of the nitrogen blanketing region, which is driven by convection. Alternatively stated, the same averaged molar fraction of nitrogen in the anode channel will blanket a smaller region of the fuel cell active area if diffusive effects are included in the model. The detailed and validated model in [95] is used to investigate the possible equilibria behavior, when the membrane water content is non-uniform. Note that the non-uniform (along the channel) membrane water content can affect the N_2 equilibrium front location. The existence of equilibrium is established and the feasibility of operating

at equilibrium with respect to a reasonable power producing device is investigated, i.e., can the equilibrium result in an acceptable voltage output.

As important prior work, Benziger and co-works [91, 174] reported the experimentally observed equilibrium in (flow-through mode) their stirred-tank-reactor (STR) fuel cells using low humidification (RH 0.3-0.5) supplies for both fuel and air. They identify multiple equilibria of the system using the inlet RH as a parameter and only consider the effect of water. The STR design creates uniformity along the channel length, and hence, only the spatial dimension considered in their model was the through-membrane (or **x**-direction). In DEA operation with very long straight channels, however, the extreme spatial variations of water and nitrogen along the anode (**y**-direction) require additional modeling complexity and a PDE based model to describe the equilibrium.

6.3 Along the Channel Model

The model of Chapter 4 reported in [95] is succinctly summarized here. The major assumptions in the present model are: 1) the catalyst layer is treated as an interface; 2) the temperature is isothermal in both **x** and **y** directions; 3) the oxygen crossover is neglected since it may be completely and quickly reduced at the anode catalyst layer [175]; 4) in-plane current re-distribution is neglected (due to large membrane aspect ratio) [2] and therefore the local current density of the H_2 reaction is exactly the same as the cathode oxidization. The 1-D modeling domain (along the **y**-direction) includes the anode channel, membrane, and cathode channel.

The model inputs are the nominal current I (A), the cathode inlet relative humidity (RH), and the cathode inlet Stoichiometric Ratio (SR). The temperature T and anode/cathode inlet pressures P_{ca} / P_{an} are fixed parameters in the model (due to the modeling assumptions), but may be adjusted prior to simulation to capture the experimental conditions. The physically measurable model output is cell voltage, but the nitrogen blanketing front location, y^{N_2}, and the two-phase water front location, y^{H_2O}, along the length of the anode channel are also calculated and shown as important metrics. The nitrogen blanketing front location, y^{N_2}, is defined as the location along the anode channel at which the local hydrogen concentration drops below a critical value, halting the local reaction. The two-phase front location, y^{H_2O}, is defined similarly as the point at which the vapor pressure reaches saturation; the effects of liquid water are not considered. Due to the difference in density of liquid water, liquid accumulation in significant quantities to block the anode channel completely occurs on a much longer time scale than with the nitrogen front evolution. However,

liquid water accumulation will eventually necessitate purging of the anode volume.

A brief discussion of the dynamic states follows. The state variables of interest are the anode channel partial pressures of nitrogen and water vapor and the membrane water content λ. The anode nitrogen and water vapor partial pressures satisfy the following convection-diffusion reaction PDE. To consider both water and nitrogen transport through the membrane modeling of a ternary system for the anode is required. The Stefan-Maxwell model describes convection, diffusion, and reactions in the gas-channel,

$$\frac{P_{an}}{RT}\frac{\partial X_i}{\partial t} = -\frac{\partial}{\partial y}\left(J_i + X_i N_t\right) + r_i, \tag{6.2}$$

for $i = [1,2] = [N_2, H_2O]$, where N_t is the total gas flux, J_i is the diffusive flux, and r_i denotes the reaction terms. Only two of the three components are independent in this modeling framework. We chose to model the mole fractions of nitrogen, X_{N_2}, and water vapor, X_{H_2O}, as our dynamics states.

The third and final dynamic state in the model is membrane water content, λ, which is governed by diffusion, and electro-osmotic (E-O) drag.

$$\frac{\partial \lambda}{\partial t} = \frac{\partial}{\partial x} D_w \frac{\partial \lambda}{\partial x}. \tag{6.3}$$

where D_w is the diffusion coefficient for water in the membrane and the E-O drag term enters the model through the boundary conditions (BCs). Due to the use of a very thin membrane, the concentration gradient in the membrane can be approximated by a quadratic relationship, and the membrane water-content distribution represented by a single ODE [80]. This ODE for membrane water content is applied at each distributed y location, a 1+1-D modeling framework.

The complete description of the model includes the BCs for the above three PDEs and the coupled algebraic equations described in Chapter 4. The algebraic equations describe the stable and fast dynamic reaction kinetics using the Butler-Volmer equation.

6.4 Simulation Results and Discussion

Simulation of the model is performed to determine equilibrium points, where the right hand sides of (6.2) and (6.3) are equal to zero subject to the algebraic constraints for several controllable system inputs (CA RH and CA SR) and operating conditions (system pressure and load current).

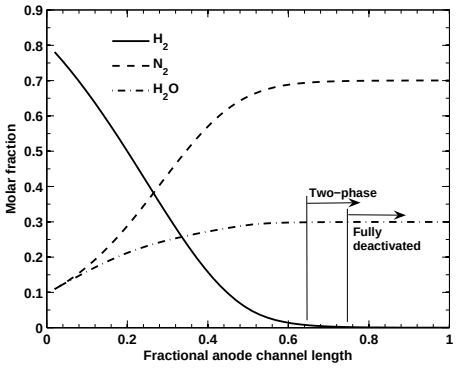

(a) P_{CA}=1.18 bar, CA_RH=0.6, i=0.2,CA_SR=2

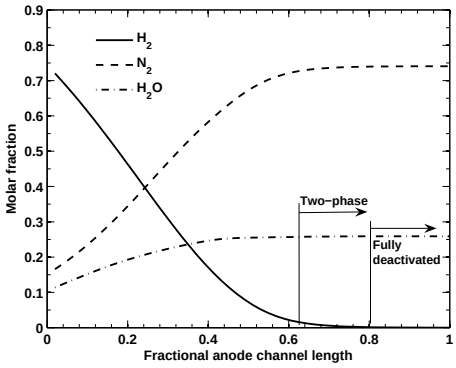

(b) P_{CA}=1.38 bar, CA_RH=0.6, $i = 0.2$,CA_SR=2

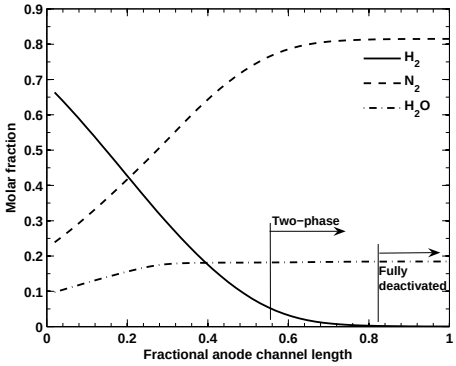

(c) P_{CA}=1.58 bar, CA_RH=0.6, i=0.2,CA_SR=2

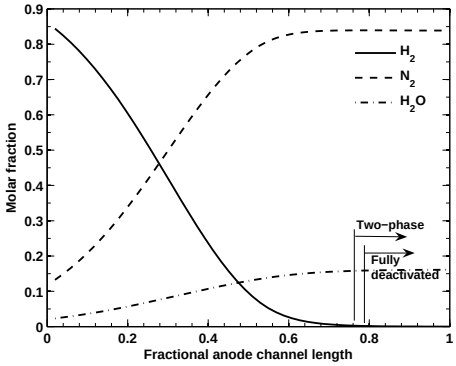

(d) Species molar fractions (X) under equilibrium with low RH ($i_{ave} = 0.2$ A cm^{-2}, RH$_{CA,in} = 0.1$,$P_{CA} = 1.18$ bar)

Figure 6.2 Species molar fractions at equilibrium with different system pressures. The system pressures are (a) P_{CA}=1.18 bar, (b) P_{CA}=1.38 bar, (c) P_{CA}=1.58 bar, and (d) P_{CA}=1.18 bar with low RH.

6.4.1 Influence of System Pressure

To reduce membrane stress and to prevent oxygen from passing into the hydrogen rich anode, for all the results shown below, the anode pressure is set 5% higher than the cathode pressure. Since the two pressures are constrained in the system, the cathode pressure is defined as the system pressure. The simulation conditions are $i = 0.2$ A cm^{-2} and cathode RH=0.6, CA_SR=2, and $T = 65°$C. A distinct trend observed in Fig. 6.2 is that increasing system pressure pushes the nitrogen blanketing front towards the channel outlet. The fully deactivated area is only 17% of the channel if the pressure can be maintained at 1.6 bar as opposed to 27% at 1.2 bar. The location of the two-phase front along the channel at equilibrium moves in the opposite direction (toward the channel inlet) as the system pressure increases. This pattern can be attributed to the cathode channel vapor distribution, which is coupled with the anode through membrane water transport. The increased system pressure

allows more water to be carried into the fuel cell with the humidified air at the same RH, as pressure increases. Note that the influence of the additional cathode water on cell voltage is not significant at low current density, and the elevated oxygen partial pressure dominates the increased voltage performance. Fig. 6.3 shows that increasing pressure results in a more uniform local current distribution, as the blanketing effects are also reduced.

Although beneficial, the increased system pressure in DEA operation has other system-level issues; in particular, the anode sealing may be more likely to fail under higher pressure. Hydrogen itself can readily diffuse into the sealing material and gradually damage its original structure. In addition, simply increasing the pressure for better outputs may not be economic overall due to the cost of pressurization in a real system and the efficiency loss [139].

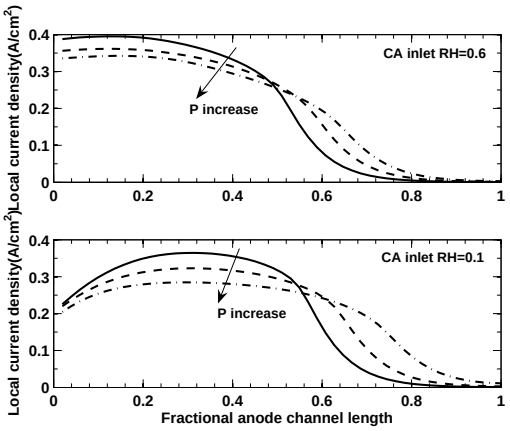

Figure 6.3 Local current densities under equilibrium with different pressures. The operating conditions are P_{CA}=$\{1.18, 1.38, 1.58\}$ bar, RH=0.6 and 0.1, and $i_{ave} = 0.2$ A cm^{-2}.

6.4.2 Influences of Cathode Inlet RH

The influence of cathode inlet RH can be observed by comparing Fig. 6.2(d) and Fig. 6.2(a). As expected, the lower inlet RH pushes the two-phase front toward the end of the channel. In the case of CA RH=0.1, the channel two-phase front is very close to the fully blanketing front, indicating the presence of single-phase water along most of the active channel region. A higher cathode inlet RH causes an increase in water in the anode channel at equilibrium, but only if the water generation at the cathode is insufficient to humidify the incoming air near the inlet. Once the water generation is sufficient to humidify the air near the inlet of the cathode channel, any further increase in inlet RH has very little effect on system performance and may lead to increased flooding at higher current. From the local current profile (Fig. 6.3), it is shown that for RH=0.1, the current density distribution along

the channel exhibits non-monotonic behavior. Low current occurs near the inlet due to dry cathode inlet conditions (higher protonic resistance in the dry membrane and lower nitrogen permeation). Self-humidification is achieved near the mid-channel region, which has the highest current density. The end of the channel again has lower current density due to nitrogen blanketing. The drier membrane conditions near the inlet could also explain the shift in nitrogen front location at equilibrium toward the end of the anode channel; since the nitrogen permeation decreases with membrane water content, the nitrogen flux from cathode to anode in the upper region of the fuel cell is decreased. However, the nitrogen crossover rate in the lower half of the cell remains unchanged as the membrane is still fully humidified due to sufficient water generation.

6.4.3 Influences of Cathode Stoichiometry

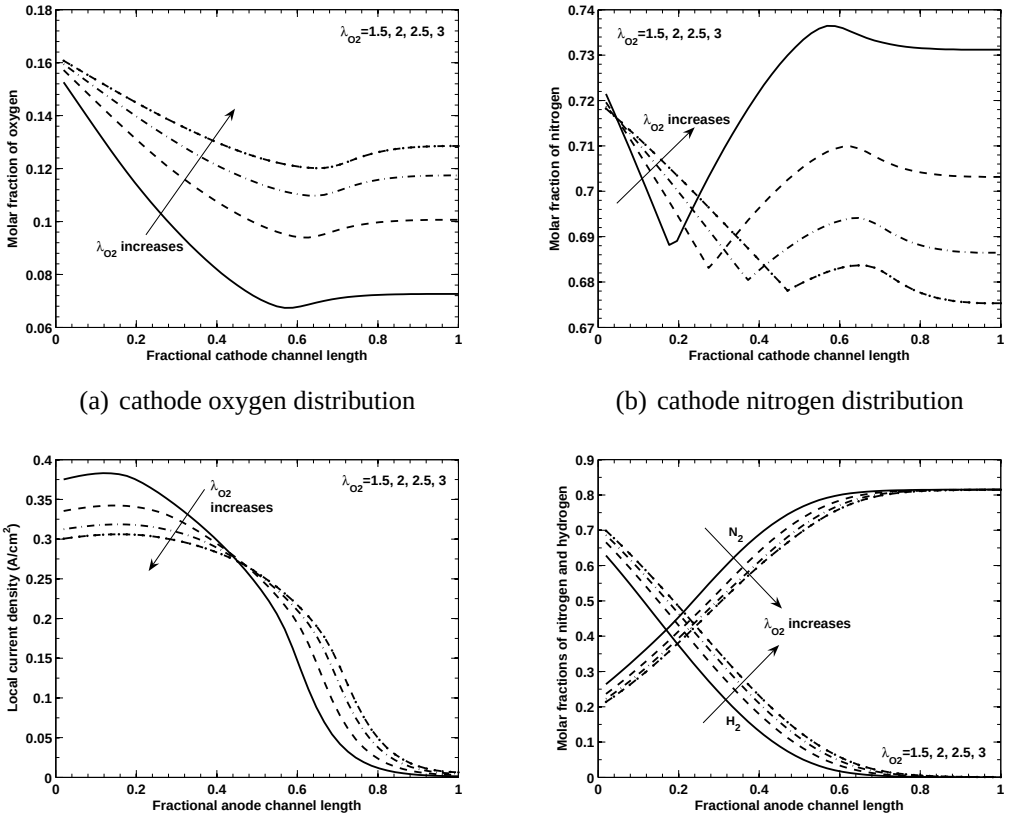

(a) cathode oxygen distribution (b) cathode nitrogen distribution

(c) current density distribution (d) anode nitrogen and hydrogen distributions

Figure 6.4 Nitrogen and oxygen distribution along the cathode channel. Note the effect of cathode SR: low SR near 1 produces the highest nitrogen concentration at the end of the channel. Cathode inlet RH and temperature also affect the nitrogen distribution along the length of the cathode channel.

Cathode stoichiometry plays a very limited role in determining the anode N_2 distribution and front location within the range of 2-3 (normal selection for PEM fuel cell operation), as the cathode nitrogen distribution does not change significantly from the inlet condition. If the cathode stoichiometry is further reduced near 1, the consumption of oxygen leads to a significant increase in the partial pressure of the nitrogen at the end of the cathode channel, as shown in Fig. 6.4(b), decreasing the flow of nitrogen from anode to cathode in the lower half of the cell (at the end of the anode channel).

6.4.4 Evolution Toward Equilibrium

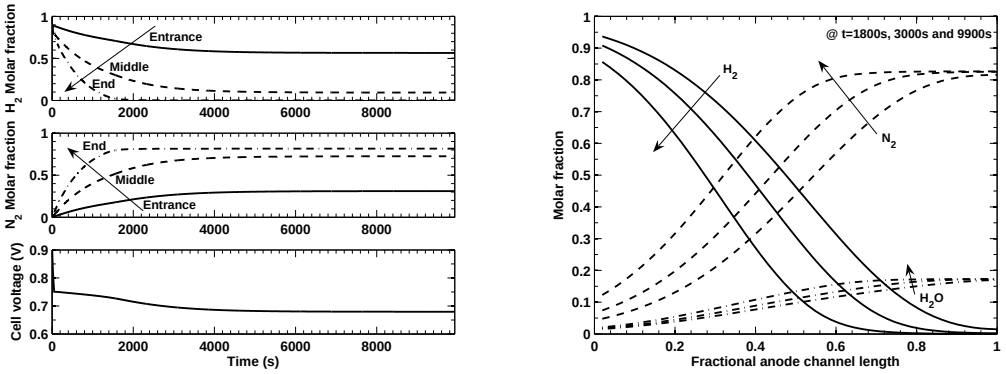

(a) Time evolution cell voltage and mole fractions of H_2 and N_2 at three representative points along the channel length.

(b) Dynamic evolution of species molar fraction distribution along the channel, shown at selected times of 1800 s, 3000 s, and 9900 s.

Figure 6.5 Cell voltage and species molar fractions approaching the equilibrium. The simulated operating conditions are ($P_{CA} = 1.58$ bar, RH=0.6 , CA_SR=2, $i_{ave} = 0.2$ A cm^{-2}).

The evolution of the molar fractions along the channel is shown in Fig. 6.5(a) and Fig. 6.5(b). The molar fractions at 10%, 50%, and 98% of the channel length are selected to represent the conditions of the entrance, middle, and end regions of the anode channel. Note that the cell voltage equilibrates after the species concentrations of the whole channel have stabilized; thus, the molar fractions at the end region actually reach equilibrium much earlier than overall equilibrium due to the slow propagation of the front.

Table 6.1 presents four important parameters under equilibrium obtained at different average current densities and RHs but at the same pressure and temperature. The time constant for cell voltage τ_V is defined as the time from 10% to 90% of the full voltage step. $P_{N_2}^{eq}$ is the channel-averaged nitrogen partial pressure under equilibrium, and y^{N_2} the normalized nitrogen blanketing front location as indicated in Fig. 6.1.

Overall, high load current increases the deviation in equilibrium voltage from the ini-

(a) **RH=0.1**

i_{ave} A cm^{-2}	V_{cell}^{eq} V	τ_V s	$P_{N_2}^{eq}$ bar	y^{N_2}	i_{max} A cm^{-2}
0.1	0.78	3944	1.10	0.80	0.123
0.2	0.68	4304	1.06	0.75	0.285
0.3	0.57	4935	1.05	0.67	0.500
0.4	0.45	5858	1.03	0.63	0.761

(b) **RH=0.6**

i_{ave} A cm^{-2}	V_{cell}^{eq} V	τ_V s	$P_{N_2}^{eq}$ bar	y^{N_2}	i_{max} A cm^{-2}
0.1	0.79	4150	1.08	0.86	0.159
0.2	0.69	4746	1.06	0.75	0.342
0.3	0.57	5023	1.04	0.63	0.599
0.4	0.45	6089	1.03	0.59	0.902

Table 6.1 Selected parameter values under equilibrium. Cell operating conditions for simulation are T_{st}=70°C and $P_{CA} = 1.58$ bar.

tial/maximum value following an anode purge, and results in a longer time to reach the equilibrium voltage. Increasing RH from 0.1 to 0.6 may only give a very small performance improvement ($\sim 0.01V$) under equilibrium; thus, the stable equilibrium output may be more dependent on the system pressure and temperature, rather than the inlet RH of the air supply, supporting the idea of a self-humidified high utilization fuel cell. The average N_2 partial pressure shows only a slight variation at the selected current level.

6.5 Experimental Results

Experiments were performed with the single cell to validate the calculated equilibria. Although the fuel cell used for the experiment has slightly different operating conditions, the experiment confirms the predicted results with reasonable accuracy. In Fig. 6.6, the time is zero-referenced from each anode purge and plotted for three subsequent purge cycles. The current density was increased after the first purge from $i = 0.2$ to $i = 0.3$ A cm^{-2}. The experiment shows a convergence to the equilibrium voltage by 10000 s after the anode purge, with $\tau_v = 6300$ s. The erratic voltage behavior after the nitrogen front develops can be attributed to liquid water condensation in the channel, which forms droplets that randomly block the channel before falling to the bottom of the channel.

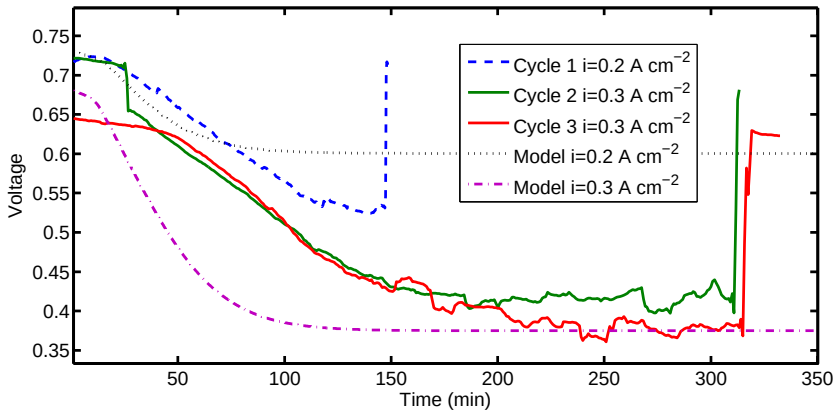

Figure 6.6 (Preliminary) Experimental results showing time evolution and convergence to voltage equilibrium for two different current set-points. ($P_{CA} = 1.18$ bar,T=65°C, CA_RH=0.6, CA_SR=2.5, and $i_{ave} = 0.2, 0.3$ A cm^{-2}).

6.6 Implications for Fuel Cell Design and Operation

The simulation results indicate that equilibrium DEA operation has reasonable performance even at low RH and relatively low pressure. The equilibrium is achieved with part of the electrode region fully deactivated. Therefore, the fuel cell may be manufactured with the MEA non-catalyzed in that deactivated region. Also, catalyst loading may be adjusted based on the uneven local hydrogen distributions found in the simulation. The benefits of DEA operation are the high utilization of anode fuel and the reduced requirement of humidification. However, questions may arise as to whether the expected equilibrium is stable or can be reached under certain operating conditions, such as high load current. At high current, the cell may shutdown quickly even before the membrane becomes humidified. As a result, low current (0.2 A cm^{-2}) was chosen for experimental testing and parametric studies.

6.7 Conclusions

In this work, a 1-D along-channel, isothermal, and dynamic model [95] is used to investigate the existence and associated power output of equilibrium operation in a PEM fuel cell with a DEA. The existence of stable equilibria suggests feasible operating conditions with 100% hydrogen utilization and without anode humidification. Surprisingly, low cathode RH was found to have a weak influence on the equilibrium cell voltage, suggesting that dead-ended operation can truly function as a self-humidifying fuel cell system. Cathode (system) pressure influences the equilibrium voltage significantly, not only affecting the

kinetic but also the formation rate of the nitrogen blanketing and the two-phase fronts. Current drawn from the cell was the most important parameter in determining the blanketing front and the time constant for reaching an equilibrium voltage. The present model could not examine cases with high current load, indicating cell shutdown at elevated load (higher than 0.5 A cm^{-2}). As expected, the DEA FC system could not support high power density, but could target low-cost / portable applications. The large variation of local current density suggests that a spatially varying catalyst loading based on a local hydrogen profile in equilibrium may be preferred and could improve the system power density. Future work includes experiments to validate the stability of equilibrium and to examine the transition between equilibria.

Chapter 7
Conclusions

The dead-ended anode operation of a PEMFC has several attractive qualities, such as reduced weight, cost, and system complexity, which make it an attractive candidate for portable power applications. However, controlling the anode purge period and duration, along with the cathode air supply rate and humidification level are necessary to obtain good system performance. The possibility of running for long periods without purging ultimately will result in very high hydrogen utilization and self-humidification. This thesis shows the important modeling domains and associated states for capturing the dynamic behavior of PEMFCs operating with DEA. These models are important for active (automated and robust) control of purging. More importantly, the DEA conditions allow a unique perspective in operating fuel cells under extremely varying spatiotemporal patterns of reactants and current density.

This dissertation starts by showing how a simple voltage model using a thin film model of the water flooding can be tuned using experimental data to predict the average voltage of a 24-cell stack. Initial modeling attempts utilized a 1-D (through the membrane), two-phase GDL model of the PEMFC to predict the water crossover rate and hence, anode channel liquid water accumulation. The boundary conditions of the GDL PDE model are calculated using a lumped channel approximation and modeled as ODEs. Spatial discretization of the PDEs requires a high computational overhead, which motivated a semi-analytic-solution (SAS) of GDL [96] and the work pursued in Chapter 5. In this chapter a low order, three-state, dynamic model that captures water crossover is derived.

In order to validate the water models, a set of experiments was performed. The experiments conducted at the Neutron Imaging Facility at the National Institute for Standards and Technology (NIST) Center for Neutron Research [46] allowed the measurement of the distribution of liquid water within an operating fuel cell. The attenuation of a neutron beam passing through the FC can be related to the water thickness along the beam path. This technique provided a useful tool for in-situ measurement of liquid water content while employing commercial fuel cell materials with realistic cell designs and DEA operation.

The parameterization of the water transport model was analyzed and it was shown that the model could be tuned to match water accumulation in the anode channel measured by neutron imaging. The low-order model shows good agreement with measured water mass accumulation for most operating conditions. However, the lumped channel model cannot predict behavior for low cathode inlet RH due to the spatial variation of water content along the channel. These experiments also clarified that although the thin film model could be tuned to predict the voltage behavior, the liquid water accumulation could not possibly cause the observed voltage response. This is turn, motivated the investigation of the relationship between nitrogen accumulation and voltage, shaping and focusing the research pursued in this thesis.

To investigate nitrogen effects, another set of experiments was proposed and executed. These experiments utilized simultaneous gas chromatography and neutron imaging to determine the relative effects of nitrogen and water accumulation in the anode channel. The distributions along the channel are important for modeling the accumulation of nitrogen and resulting impact on cell voltage. Therefore a new 1-D (along the channel) single-phase model with 0-D GDL and a distributed membrane water content was developed. This model shows very good results when compared with the experiments. The model describes the effect of nitrogen accumulation and the blanketing front evolution on cell voltage. The 1-D, AN CH model presented in this thesis is able to capture and explain the observed two-sloped voltage drop between purges in a PEMFC with DEA. The model shows very good results when there is no significant water plugging of the channels. Unfortunately, the single-phase model is not valid for flooding conditions.

Motivated by the good predictability of the distributed (1-D) channel model under non-flooding conditions, the effect of nitrogen blanketing in the anode channel is modeled by a dynamic (evolving) nitrogen front. Using an approximation of the steady state nitrogen profile, the front location is calculated from the nitrogen mass accumulation. This static relationship between nitrogen mass and voltage, when added to the low order model, enabled much better prediction of the output voltage.

Finally, a 1-D along-channel, isothermal, dynamic model [95] was used to investigate the existence and associated power output of equilibrium operation in a PEM fuel cell with a DEA. The existence of stable equilibria suggests feasible operating conditions with 100% hydrogen utilization and without anode humidification. The model was used to determine the effects of spatial variations as compared to the lumped channel model and points to the validity and usefulness of the lumped channel model. Simulations show specific operating conditions (i,T,P), and the effect of control inputs, CA inlet SR, and RH. Surprisingly, low cathode RH was found to have a weak influence on the equilibrium cell voltage, suggesting

that dead-ended operation can truly function as a self-humidifying fuel cell system. Cathode (system) pressure influences the equilibrium voltage significantly, not only affecting the kinetic, but also the formation rate of the nitrogen blanketing and two-phase fronts. The load current was the most important parameter in determining the blanketing front and the time constant for reaching an equilibrium voltage. The large variation of local current density suggests that spatially varying catalyst loading based on a local hydrogen profile in equilibrium may be preferred and could improve the system power density.

7.1 Future Work

The current political administration announced a need for three miracles to realize fuel cells: (a) durability, (b) cost, and (c) hydrogen supply infrastructure [15]. This work addresses (a) and (b); thus, pointing to very promising directions.

7.1.1 DEA Operation and Degradation Phenomena

Advancing the design and control of PEMFCs is critical for commercial automotive applications seeking to improve fuel cell durability and costs. Undesired reactions occurring during load following and start-up conditions have been linked to degradation of both the membrane and catalyst support structures. Degradation can affect performance and stack life, and is accelerated when the local build-up of liquid water and nitrogen in the anode channel causes varying spatiotemporal profiles. Anode channel plugging can induce hydrogen starvation and given the right conditions, trigger cathode carbon oxidation, leading to a permanent loss of active catalyst area. Additionally, nitrogen accumulation and blanketing in the anode channel lead to a decrease in cell efficiency by blocking the catalyst and by reducing the area available to support the reaction. Purging the nitrogen uncovers the catalyst and recovers the available area but at the expense of wasting hydrogen fuel.

7.1.2 DEA Modeling

The main problem with the lumped model arises from the vapor concentration boundary condition, which the lumped channels impose on the MEA/GDL model. Whenever liquid water is present in either channel volume, the vapor concentration in that volume is fixed at $c_{v,sat}$, and hence, the net water transport across the membrane is insensitive to changes in the cathode inlet relative humidity and stoichiometry. The only way the cathode inlet RH

can influence water transport with the lumped channel model is when there is no liquid; i.e., the cathode is very dry at high temperature or very low RH$<$ 40%. To address this issue, a 1+1-D model needs to be developed, which combines the models of water fronts in the GDL (Chapter 5) along the channel model (or channel fronts model) to capture the low cathode inlet relative humidity conditions in the experiments. The model reduction of the 1-D, *x*-distributed, GDL, and membrane water dynamics has been investigated, so that the model could be coupled with a 1-D along the channel model, forming a 1+1-D complete two-phase description of the fuel cell. The use of current density measurements [109, 167], in addition to neutron imaging could provide an authoritative validation tool for the channel distributions.

Another important topic recently proposed in the literature is the effect of thermal gradients across the cell. Future work is needed to to address thermal modeling within the current simulation framework. The "Heat-pipe effect" [61] is argued to be the main mechanism for water transport in the GDL, which an isothermal model cannot predict. Finally, it would be prudent to investigate the possibility of using impedance measurements, in addition to voltage, for estimating the internal states; specifically, the membrane humidity [176].

7.1.3 DEA Control of Purging

Understanding, modeling, and predicting the front evolutions in the anode for DEA operation of PEMFCs would allow judicious choice of purging interval and duration. Using the modeling framework outline in this thesis, one could determine an optimum schedule to reduce the H_2 wasted during purges and to avoid over-drying the membrane. The advantage to developing simple models is that simulation of the system can be performed in real time, enabling MPC [10] or observer-based feedback algorithms that provide robustness in the control algorithm. The model can also be used to help identify and account for changes in the FC materials over time, such as corrosion of the carbon catalyst support or deterioration of the GDL Teflon coating, which may cause changes in the system dynamics.

7.1.4 Neutron Imaging

High-resolution, through-plane neutron imaging studies can be performed using the recently developed micro-channel plate detector at NIST. This higher resolution detector enables measurement of the water content across the membrane [177]. Through careful design of the fuel cell and experiments, utilizing stroboscopic imaging techniques to

overcome the temporal resolution limitations of the imaging setup, the liquid water front propagation in the GDL can now be measured. The application of neutron radiography to other electrochemical power devices, such as batteries, is also an important avenue for future research. Initial experiments have shown the principle and potential of applying radiographic techniques for measurement of the change in lithium ion concentration distribution in a pouch cell battery during charge and discharge cycling [178]. This is an important first step in the development of this tool for validation of battery models.

Bibliography

[1] J. H. Ohs, U. Sauter, S. Maass, and D. Stolten, "Modeling hydrogen starvation conditions in proton-exchange membrane fuel cells," *J. Power Sources*, vol. 196, no. 1, pp. 255 – 263, 2011.

[2] J. P. Meyers and R. M. Darling, "Model of carbon corrosion in pem fuel cells," *J. Electrochem. Soc.*, vol. 153, no. 8, pp. A1432–A1442, Aug. 2006.

[3] E. Kimball, T. Whitaker, Y. G. Kevrekidis, and J. B. Benziger, "Drops, slugs, and flooding in polymer electrolyte membrane fuel cells," *AIChE J.*, vol. 54, no. 5, pp. 1313–1332, 2008.

[4] N. Yousfi-Steiner, P. Mocoteguy, D. Candusso, D. Hissel, A. Hernandez, and A. Aslanides, "A review on PEM voltage degradation associated with water management: Impacts, influent factors and characterization," *J. Power Sources*, vol. 183, pp. 260–274, 2008.

[5] W. Baumgartner, P. Parz, S. Fraser, E. Wallnfer, and V. Hacker, "Polarization study of a PEMFC with four reference electrodes at hydrogen starvation conditions," *J. Power Sources*, vol. 182, no. 2, pp. 413–421, Aug. 2008.

[6] W. Schmittinger and A. Vahidi, "A review of the main parameters influencing performance and durability of PEM fuel cells," *J. Power Sources*, vol. 180, pp. 1–14, 2008.

[7] N. Pekula, K. Heller, P. A. Chuang, A. Turhan, M. M. Mench, J. S. Brenizer, and K. nl, "Study of water distribution and transport in a polymer electrolyte fuel cell using neutron imaging." *Nucl. Instrum. Methods Phys. Res., Sect. A*, vol. 542, pp. 134–141, 2005.

[8] J. B. Siegel, D. A. McKay, A. G. Stefanopoulou, D. S. Hussey, and D. L. Jacobson, "Measurement of Liquid Water Accumulation in a PEMFC with Dead-Ended Anode," *J. Electrochem. Soc.*, vol. 155, no. 11, pp. B1168–B1178, 2008.

[9] J. Chen, J. B. Siegel, and A. G. Stefanopoulou, "Nitrogen blanketing front equilibria in dead end anode fuel cell operation," in *Submitted to: the 2011 American Control Conference*, 2011.

[10] G. Ripaccioli, J. B. Siegel, A. G. Stefanopoulou, and S. Di Cairano, "Derivation and simulation results of a hybrid model predictive control for water purge scheduling in a fuel cell," in *2nd Annual Dynamic Systems and Control Conference*, Hollywood, CA, USA, October 12-14 2009.

[11] J. B. Siegel, A. G. Stefanopoulou, G. Ripaccioli, and S. Di Cairano, "Purge Scheduling for Dead-Ended Anode Operation of PEM Fuel Cells," to appear in *The Control Handbook, Second Edition: Control System Applications, Second Edition* , W. S. Levine, Ed. CRC Press, 2010.

[12] B. A. McCain, A. G. Stefanopoulou, and I. V. Kolmanovsky, "On the dynamics and control of through-plane water distributions in PEM fuel cells," *Chem. Eng. Sci.*, vol. 63, no. 17, pp. 4418 – 4432, 2008.

[13] R. P. O'Hayre, S.-W. Cha, W. Colella, and F. B. Prinz, *Fuel Cell Fundamentals*. Hoboken, NJ: Wiley, 2006.

[14] A. Shah, G.-S. Kim, W. Gervais, A. Young, K. Promislow, J. Li, and S. Ye, "The effects of water and microstructure on the performance of polymer electrolyte fuel cells," *J. Power Sources*, vol. 160, no. 2, pp. 1251–1268, Oct. 2006.

[15] DOE, "Hydrogen and fuel cell activities, progress, and plans," DOE, Tech. Rep., 2009. [Online]. Available: http://www.hydrogen.energy.gov/pdfs/epact_report_sec811.pdf

[16] J. T. Pukrushpan, A. G. Stefanopoulou, and H. Peng, *Control of Fuel Cell Power Systems: Principles, Modeling, Analysis and Feedback Design*. New York: Springer, 2000.

[17] K.-W. Suh and A. G. Stefanopoulou, "Performance limitations of air flow control in power-autonomous fuel cell systems," *IEEE T. Contr. Syst. T.*, vol. 15, no. 3, pp. 465–473, May 2007.

[18] A. Vahidi, A. Stefanopoulou, and H. Peng, "Current management in a hybrid fuel cell power system: A model-predictive control approach," *IEEE T. Contr. Syst. T.*, vol. 14, no. 6, pp. 1047–1057, Nov. 2006.

[19] W. K. Na and B. Gou, "Feedback-linearization-based nonlinear control for pem fuel cells," *IEEE T. Energy. Conver.*, vol. 23, no. 1, pp. 179 –190, March 2008.

[20] A. Vahidi, I. Kolmanovsky, and A. Stefanopoulou, "Constraint handling in a fuel cell system: A fast reference governor approach," *IEEE T. Contr. Syst. T.*, vol. 15, no. 1, pp. 86 –98, Jan. 2007.

[21] F. Y. Zhang, X. G. Yang, and C. Y. Wang, "Liquid Water Removal from a Polymer Electrolyte Fuel Cell," *J. Electrochem. Soc.*, vol. 153, no. 2, pp. A225–A232, 2006.

[22] E. Kumbur, K. Sharp, and M. Mench, "Liquid droplet behavior and instability in a polymer electrolyte fuel cell flow channel," *J. Power Sources*, vol. 161, no. 1, pp. 333–345, Oct. 2006.

[23] D. A. McKay, A. G. Stefanopoulou, and J. Cook, "A membrane-type humidifier for fuel cell applications: Controller design, analysis and implementation," *ASME Conference Proceedings*, vol. 2008, no. 43181, pp. 841–850, 2008.

[24] H. P. Dongmei Chen, "Analysis of non-minimum phase behavior of pem fuel cell membrane humidification systems," in *Proceedings of the 2005 American Control Conference*, June 2005, pp. 3853 – 3858 vol. 6.

[25] K. Promislow and B. Wetton, "A simple, mathematical model of thermal coupling in fuel cell stacks," *J. Power Sources*, vol. 150, pp. 129–135, Oct. 2005.

[26] E. A. Ḿuller and A. G. Stefanopoulou, "Analysis, modeling, and validation for the thermal dynamics of a polymer electrolyte membrane fuel cell system," *Journal of Fuel Cell Science and Technology*, vol. 3, no. 2, pp. 99–110, 2006.

[27] G. Vasu and A. Tangirala, "Control-orientated thermal model for proton-exchange membrane fuel cell systems," *J. Power Sources*, vol. 183, no. 1, pp. 98 – 108, 2008.

[28] X. Huang, R. Solasi, Y. Zou, M. Feshler, K. Reifsnider, D. Condit, S. Burlatsky, and T. Madden, "Mechanical endurance of polymer electrolyte membrane and PEM fuel cell durability," *Journal of Polymer Science Part B: Polymer Physics*, vol. 44, no. 16, pp. 2346–2357, 2006.

[29] F. A. d. Bruijn, V. A. T. Dam, and G. J. M. Janssen, "Review: Durability and Degradation Issues of PEM Fuel Cell Components," *Fuel Cells*, vol. 8, pp. 3 – 22, 2008.

[30] C. A. Reiser, L. Bregoli, T. W. Patterson, J. S. Yi, J. D. Yang, M. L. Perry, and T. D. Jarvi, "A Reverse-Current Decay Mechanism for Fuel Cells," *Electrochem. Solid-State Lett.*, vol. 8-6, pp. A273–A276, 2005.

[31] M. Schulze, N. Wagner, T. Kaz, and K. Friedrich, "Combined electrochemical and surface analysis investigation of degradation processes in polymer electrolyte membrane fuel cells," *Electrochim. Acta*, vol. 52, no. 6, pp. 2328–2336, Jan. 2007.

[32] A. Y. Karnik and J. Sun, "Modeling and control of an ejector based anode recirculation system for fuel cells," in *In: Proceedings of the third international conference on fuel cell science, engineering, and technology*, Ypsilanti, MI., 2005, pp. FUELCELL2005–74 102.

[33] A. Y. Karnik, J. Sun, A. G. Stefanopoulou, and J. H. Buckland, "Humidity and pressure regulation in a pem fuel cell using a gain-scheduled static feedback controller," *IEEE T. Contr. Syst. T.*, vol. 17, no. 2, pp. 283–297, March 2009.

[34] A. Karnik, J. Sun, and J. Buckland, "Control analysis of an ejector based fuel cell anode recirculation system," in *American Control Conference, 2006*, June 2006, pp. 6 pp.–.

[35] R. K. Ahluwalia and X. Wang, "Fuel cell systems for transportation: Status and trends," *J. Power Sources*, vol. 177, no. 1, pp. 167 – 176, 2008.

[36] S. S. Kocha, J. D. Yang, and J. S. Yi, "Characterization of gas crossover and its implications in PEM fuel cells," *AIChE J.*, vol. 52, no. 5, pp. 1916–1925, 2006.

[37] R. Ahluwalia and X. Wang, "Buildup of nitrogen in direct hydrogen polymer-electrolyte fuel cell stacks," *J. Power Sources*, vol. 171, no. 1, pp. 63–71, Sep. 2007.

[38] P. Rodatz, A. Tsukada, M. Mladek, and L. Guzzella, "Efficiency Improvements by Pulsed Hydrogen Supply in PEM Fuel Cell Systems," in *Proceedings of IFAC 15th World Congress*, 2002.

[39] S. Hikita, F. Nakatani, K. Yamane, and Y. Takagi, "Power-generation characteristics of hydrogen fuel cell with dead-end system," *JSAE Review*, vol. 23, pp. 177–182, 2002.

[40] L. Dumercy, M.-C. Pra, R. Glises, D. Hissel, S. Hamandi, F. Badin, and J.-M. Kauffmann, "PEFC Stack Operating in Anodic Dead End Mode," *Fuel Cells*, vol. 4, pp. 352 – 357, 2004.

[41] E. A. Müller, F. Kolb, L. Guzzella, A. G. Stefanopoulou, and D. A. McKay, "Correlating nitrogen accumulation with temporal fuel cell performance," *Journal of Fuel Cell Science and Technology*, vol. 7, no. 2, p. 021013, 2010.

[42] A. Z. Weber, "Gas-crossover and membrane-pinhole effects in polymer-electrolyte fuel cells," *J. Electrochem. Soc.*, vol. 155, no. 6, pp. B521–B531, 2008.

[43] H. Li, Y. Tang, Z. Wang, Z. Shi, S. Wu, D. Song, J. Zhang, K. Fatih, J. Zhang, H. Wang, Z. Liu, R. Abouatallah, and A. Mazza, "A review of water flooding issues in the proton exchange membrane fuel cell," *J. Power Sources*, vol. 178, no. 1, pp. 103 – 117, 2008.

[44] S. Ge and C.-Y. Wang, "Liquid Water Formation and Transport in the PEFC Anode," *J. Electrochem. Soc.*, vol. 154, no. 10, pp. B998–B1005, 2007.

[45] Z. Dunbar and R. I. Masel, "Quantitative MRI study of water distribution during operation of a PEM fuel cell using Teflon(R) flow fields," *J. Power Sources*, vol. 171, no. 2, pp. 678–687, Sep. 2007.

[46] D. S. Hussey, D. L. Jacobson, M. Arif, K. J. Coakley, and D. F. Vecchia, "In situ fuel cell water metrology at the nist neutron imaging facility," *Journal of Fuel Cell Science and Technology*, vol. 7, no. 2, p. 021024, 2010.

[47] R. Hassanein, E. Lehmann, and P. Vontobel, "Methods of scattering corrections for quantitative neutron radiography," *Nucl. Instrum. Methods Phys. Res., Sect. A*, vol. 542, no. 1-3, pp. 353–360, Apr. 2005.

[48] D. Kramer, J. Zhang, R. Shimoi, E. Lehmann, A. Wokaun, K. Shinohara, and G. G. Scherer, "In situ diagnostic of two-phase flow phenomena in polymer electrolyte fuel cells by neutron imaging: Part A. Experimental, data treatment, and quantification," *Electrochim. Acta*, vol. 50, no. 13, pp. 2603–2614, Apr. 2005.

[49] R. J. Bellows, M. Y. Lin, M. Arif, A. K. Thompson, and D. Jacobson, "Neutron Imaging Technique for In Situ Measurement of Water Transport Gradients within Nafion in Polymer Electrolyte Fuel Cells," *J. Electrochem. Soc.*, vol. 146, no. 3, pp. 1099–1103, 1999.

[50] R. Satija, D. L. Jacobson, M. Arif, and S. A. Werner, "In situ neutron imaging technique for evaluation of water management systems in operating PEM fuel cells," *J. Power Sources*, vol. 129, no. 2, pp. 238–245, Apr. 2004.

[51] J. Zhang, D. Kramer, R. Shimoi, Y. Ono, E. Lehmann, A. Wokaun, K. Shinohara, and G. Scherer, "In situ diagnostic of two-phase flow phenomena in polymer electrolyte fuel cells by neutron imaging: Part B. Material Variations," *Electrochim. Acta*, vol. 51, pp. 2715–2727, 2006.

[52] D. Ludlow, C. Calebrese, S. Yu, C. Dannehy, D. Jacobson, D. Hussey, M. Arif, M. Jensen, and G. Eisman, "PEM fuel cell membrane hydration measurement by neutron imaging," *J. Power Sources*, vol. 162, no. 1, pp. 271 – 278, 2006.

[53] A. Turhan, K. Heller, J. Brenizer, and M. Mench, "Quantification of liquid water accumulation and distribution in a polymer electrolyte fuel cell using neutron imaging," *J. Power Sources*, vol. 160, pp. 1195–1203, 2006.

[54] J. P. Owejan, T. A. Trabold, D. L. Jacobson, D. R. Baker, D. S. Hussey, and M. Arif, "In situ investigation of water transport in an operating PEM fuel cell using neutron radiography: Part 2 -Transient water accumulation in an interdigitated cathode flow field." *Int. J. Heat Mass Transfer*, vol. 49, pp. 4721–4731., 2006.

[55] H. Ju, G. Luo, and C.-Y. Wang, "Probing Liquid Water Saturation in Diffusion Media of Polymer Electrolyte Fuel Cells," *J. Electrochem. Soc.*, vol. 154, no. 2, pp. B218–B228, Feb. 2007.

[56] M. A. Hickner, N. P. Siegel, K. S. Chen, D. N. McBrayer, D. S. Hussey, D. L. Jacobson, and M. Arif, "Real-time imaging of liquid water in an operating proton exchange membrane fuel cell." *J. Electrochem. Soc.*, vol. 153, pp. A902–A908., 2006.

[57] M. A. Hickner, N. P. Siegel, K. S. Chen, D. S. Hussey, D. L. Jacobson, and M. Arif, "Understanding Liquid Water Distribution and Removal Phenomena in an Operating "PEMFC" via Neutron Radiography," *J. Electrochem. Soc.*, vol. 155, no. 3, pp. B294–B302, Mar. 2008.

[58] Y.-S. Chen, H. Peng, D. S. Hussey, D. L. Jacobson, D. T. Tran, T. Abdel-Baset, and M. Biernacki, "Water distribution measurement for a PEMFC through neutron radiography," *J. Power Sources*, vol. 170, no. 2, pp. 376–386, Jul. 2007.

[59] P. Boillat, D. Kramer, B. Seyfang, G. Frei, E. Lehmann, G. Scherer, A. Wokaun, Y. Ichikawa, Y. Tasaki, and K. Shinohara, "In situ observation of the water distribution across a PEFC using high resolution neutron radiography," *Electrochem. Commun.*, vol. 10, pp. 546–50, 2008.

[60] E. H. Lehmann, P. Vontobel, G. Frei, and C. Brnnimann, "Neutron imaging–detector options and practical results," *Nucl. Instrum. Methods Phys. Res., Sect. A*, vol. 531, no. 1-2, pp. 228 – 237, 2004, proceedings of the 5th International Workshop on Radiation Imaging Detectors.

[61] A. Weber and M. Hickner, "Modeling and high-resolution-imaging studies of water-content profiles in a polymer-electrolyte-fuel-cell membrane-electrode assembly," *Electrochim. Acta*, vol. 53, no. 26, pp. 7668 – 7674, 2008.

[62] S. Dutta, S. Shimpalee, and J. Van Zee, "Three-dimensional numerical simulation of straight channel pem fuel cells," *J. Appl. Electrochem.*, vol. 30, no. 2, pp. 135–146, Feb. 2000.

[63] K. Haraldsson and K. Wipke, "Evaluating pem fuel cell system models," *J. Power Sources*, vol. 126, no. 1-2, pp. 88 – 97, 2004.

[64] D. Cheddie and N. Munroe, "Review and comparison of approaches to proton exchange membrane fuel cell modeling," *J. Power Sources*, vol. 147, no. 1-2, pp. 72–84, Sep. 2005.

[65] D. A. McKay, J. B. Siegel, W. Ott, and A. G. Stefanopoulou, "Parameterization and prediction of temporal fuel cell voltage behavior during flooding and drying conditions," *J. Power Sources*, vol. 178, no. 1, pp. 207–222, Mar. 2008.

[66] P. Berg, K. Promislow, J. S. Pierre, J. Stumper, and B. Wetton, "Water Management in PEM Fuel Cells," *J. Electrochem. Soc.*, vol. 151, no. 3, pp. A341–A353, Mar. 2004.

[67] H. Dohle, A. A. Kornyshev, A. A. Kulikovsky, J. Mergel, and D. Stolten, "The current voltage plot of PEM fuel cell with long feed channels," *Electrochem. Commun.*, vol. 3, no. 2, pp. 73–80, Feb. 2001.

[68] A. Z. Weber and J. Newman, "Using a quasi-potential transformation for modeling diffusion media in polymer-electrolyte fuel cells," *SIAM Journal on Applied Mathematics*, vol. 70, no. 2, pp. 488–509, 2009.

[69] J. T. Gostick, M. W. Fowler, M. D. Pritzker, M. A. Ioannidis, and L. M. Behra, "In-plane and through-plane gas permeability of carbon fiber electrode backing layers," *J. Power Sources*, vol. 162, no. 1, pp. 228–238, Nov. 2006.

[70] R. Fluckiger, S. A. Freunberger, D. Kramer, A. Wokaun, G. G. Scherer, and F. N. Buchi, "Anisotropic, effective diffusivity of porous gas diffusion layer materials for PEFC," *Electrochim. Acta*, vol. 54, no. 2, pp. 551–559, Dec. 2008.

[71] J. Nam and M. Kaviany, "Effective diffusivity and water-saturation distribution in single and two-layer PEMFC diffusion medium," *Int. J. Heat Mass Transfer*, vol. 46, pp. 4595–4611, 2003.

[72] J. T. Gostick, M. W. Fowler, M. A. Ioannidis, M. D. Pritzker, Y. Volfkovich, and A. Sakars, "Capillary pressure and hydrophilic porosity in gas diffusion layers for polymer electrolyte fuel cells," *J. Power Sources*, vol. 156, no. 2, pp. 375–387, Jun. 2006.

[73] B. Markicevic, A. Bazylak, and N. Djilali, "Determination of transport parameters for multiphase flow in porous gas diffusion electrodes using a capillary network model," *J. Power Sources*, vol. 172, p. 706 717., 2007.

[74] E. Kumbur, K. Sharp, and M. Mench, "On the effectiveness of Leverett approach for describing the water transport in fuel cell diffusion media," *J. Power Sources*, vol. 168, no. 2, pp. 356–368, Jun. 2007.

[75] E. C. Kumbur, K. V. Sharp, and M. M. Mench, "Validated leverett approach for multiphase flow in PEFC diffusion media ii. compression effect," *J. Electrochem. Soc.*, vol. 154, p. B1305B1314, 2007.

[76] Q. Ye and T. V. Nguyen, "Three-Dimensional Simulation of Liquid Water Distribution in a PEMFC with Experimentally Measured Capillary Functions," *J. Electrochem. Soc.*, vol. 154, no. 12, pp. B1242–B1251, 2007.

[77] T. V. Nguyen, G. Lin, H. Ohn, and X. Wang, "Measurement of Capillary Pressure Property of Gas Diffusion Media Used in Proton Exchange Membrane Fuel Cells," *Electrochem. Solid-State Lett.*, vol. 11, no. 8, pp. B127–B131, 2008.

[78] H. Ju, "Analyzing the effects of immobile liquid saturation and spatial wettability variation on liquid water transport in diffusion media of polymer electrolyte fuel cells (PEFCs)," *J. Power Sources*, vol. 185, no. 1, pp. 55–62, Oct. 2008.

[79] J. Benziger, J. Nehlsen, D. Blackwell, T. Brennan, and J. Itescu, "Water Flow in the Gas Diffusion Layer of PEM Fuel Cells," *J. Membr. Sci.*, vol. 261, pp. 98–106, 2005.

[80] K. Promislow, P. Chang, H. Haas, and B. Wetton, "Two-Phase Unit Cell Model for Slow Transients in Polymer Electrolyte Membrane Fuel Cells," *J. Electrochem. Soc.*, vol. 155, no. 7, pp. A494–A504, 2008.

[81] A. Stefanopoulou, I. Kolmanovsky, and B. McCain, "A dynamic semi-analytic channel-to-channel model of two-phase water distribution for a unit fuel cell," *IEEE T. Contr. Syst. T.*, vol. 17, no. 5, pp. 1055–1068, Sept. 2009.

[82] J. E.-S. Chia, I. G. Kevrekidis, and J. B. Benziger, "The STR PEM Fuel Cell as a Reactor Building Block," *AIChE J.*, vol. 52, pp. 3902–3910, 2006.

[83] P. Chang, G.-S. Kim, K. Promislow, and B. Wetton, "Reduced dimensional computational models of polymer electrolyte membrane fuel cell stacks," *Journal of Computational Physics*, vol. 223, no. 2, pp. 797–821, May 2007.

[84] W. Huang, L. Zheng, and X. Zhan, "Adaptive moving mesh methods for simulating one-dimensional groundwater problems with sharp moving fronts," *International Journal for Numerical Methods in Engineering*, vol. 54, no. 11, pp. 1579–1603, 2002.

[85] G.-S. Kim, P. Sui, A. Shah, and N. Djilali, "Reduced-dimensional models for straight-channel proton exchange membrane fuel cells," *J. Power Sources*, vol. 195, no. 10, pp. 3240 – 3249, 2010.

[86] C. Siegel, "Review of computational heat and mass transfer modeling in polymer-electrolyte-membrane (pem) fuel cells," *Energy*, vol. 33, no. 9, pp. 1331 – 1352, 2008.

[87] T. Berning and N. Djilali, "A 3D, Multiphase, Multicomponent Model of the Cathode and Anode of a PEM Fuel Cell," *J. Electrochem. Soc.*, vol. 150, no. 12, pp. A1589–A1598, Dec. 2003.

[88] T. Berning and N. Djilal, "Three-dimensional computational analysis of transport phenomena in a PEM Fuel Cella parametric study," *J. Power Sources*, 2003.

[89] P. T. Nguyen, T. Berning, and N. Djilali, "Computational model of a PEM fuel cell with serpentine gas flow channels," *J. Power Sources*, vol. 130, no. 1-2, pp. 149–157, May 2004.

[90] K. Jiao, B. Zhou, and P. Quan, "Liquid water transport in straight micro-parallel-channels with manifolds for PEM fuel cell cathode," *J. Power Sources*, vol. 157, pp. 226–243, 2006.

[91] J. Benziger, E. Chia, E. Karnas, J. Moxley, C. Teuscher, and I. G. Kevrekidis, "The stirred tank reactor Polymer Electrolyte Membrane fuel cell," *AIChE J.*, vol. 50, pp. 1889–1900, 2004.

[92] A. J. d. Real, A. Arce, and C. Bordons, "Development and experimental validation of a PEM fuel cell dynamic model," *J. Power Sources*, vol. 173, no. 1, pp. 30–324, Nov. 2007.

[93] C. Ramos-Paja, C. Bordons, A. Romero, R. Giral, and L. Martinez-Salamero, "Minimum fuel consumption strategy for pem fuel cells," *Industrial Electronics, IEEE Transactions on*, vol. 56, no. 3, pp. 685 –696, March 2009.

[94] A. Arce, J. Del Real, C. Bordons, and R. Ramirez, "Real-time implementation of a constrained mpc for efficient airflow control in a pem fuel cell," *IEEE T. Ind. Electron.*, vol. PP, no. 99, pp. 1 –1, 2009.

[95] J. B. Siegel, S. V. Bohac, A. G. Stefanopoulou, and S. Yesilyurt, "Nitrogen front evolution in purged polymer electrolyte membrane fuel cell with dead-ended anode," *J. Electrochem. Soc.*, vol. 157, no. 7, pp. B1081–B1093, 2010.

[96] B. A. McCain, "Modeling and analysis for control of reactant and water distributions in fuel cells," Ph.D. dissertation, The University of Michigan Dept. of Mechanical Engineering, 2008.

[97] T. Zawodzinski, C. Derouin, S. Radzinski, R. Sherman, V. Smith, T. Springer, and S. Gottesfeld, "Water Uptake by and Transport Through Nafion 117 Membranes," *J. Electrochem. Soc.*, vol. 140, no. 4, 1993.

[98] T. Trabold, J. Owejan, D. Jacobsen, M. Arif, and P. Huffman, "In Situ Investigation of Water Transport in an Operating PEM Fuel Cell Using Neutron Radiography: Part I-Experimental Method and Serpentine Flow Field Results," *Int. J. Heat Mass Transfer*, vol. 49, pp. 4712–4720, 2006.

[99] P. A. Chuang, A. Turhan, A. K. Heller, J. S. Brenizer, T. A. Trabold, and M. M. Mench, "THE NATURE OF FLOODING AND DRYING IN POLYMER ELECTROLYTE FUEL CELLS," in *Third International Conference on Fuel Cell Science, Engineering and Technology*, 2005.

[100] J. S. Yi and T. V. Nguyen, "An along-the-channel model for proton exchange membrane fuel cells." *J. Electrochem. Soc.*, vol. 145, pp. 1149–1159, 1998.

[101] T. Fuller and J. Newman, "Water and thermal management in solid-polymer-electrolyte fuel cells," *J. Electrochem. Soc.*, vol. 140, no. 5, pp. 1218–1225, 1993.

[102] S. Dutta, S. Shimpalee, and J. Van Zee, "Numerical prediction of mass-exchange between cathode and anode channels in a PEM fuel cell," *Int. J. Heat Mass Transfer*, vol. 44, pp. 2029–2042, 2001.

[103] U. Pasaogullari and C.-Y. Wang, "Two-Phase Modeling and Flooding Prediction of Polymer Electrolyte Fuel Cells," *J. Electrochem. Soc.*, vol. 152, no. 2, pp. A380–A390, 2005.

[104] L. You and H. Liu, "A two-phase flow and transport model for the cathode of pem fuel cells," *International Hournal of Heat and Mass Transfer*, vol. 45, pp. 2277–2287, 2002.

[105] Q. Guo, V. Sethuraman, and R. White, "Parameter Estimates for a PEMFC Cathode," *J. Electrochem. Soc.*, vol. 151, no. 7, pp. A983–A993, 2004.

[106] B. Carnes and N. Djilali, "Systematic Parameter Estimation for PEM Fuel Cell Models," *J. Power Sources*, vol. 144, pp. 83–93, 2005.

[107] G. Suares and K. Kosanovich, "Parameter and State Estimation of a Proton-Exchange Membrane Fuel Cell Using Sequential Quadratic Programming," *Industrial and Engineering Chemical Research*, vol. 36, pp. 4264–4272, 1997.

[108] G. Suares and K. Hoo, "Parameter Estimation of a Proton-Exchange Membrane Fuel Cell Using Voltage-Current Data," *Chem. Eng. Sci.*, vol. 55, pp. 2237–2247, 2000.

[109] H. Ju and C. Wang, "Experimental Validation of a PEM Fuel Cell Model by Current Distribution Data," *J. Electrochem. Soc.*, vol. 151, no. 11, pp. A1954–A1960, 2004.

[110] D. Natarajan and T. V. Nguyen, "Current distribution in PEM fuel cells. Part 1: Oxygen and fuel flow rate effects," *AIChE J.*, vol. 51, no. 9, pp. 2587–2598, 2005.

[111] W. T. Ott, A. D. McKay, and A. Stefanopoulou, "Modeling, Parameter Identification, and Validation of Water Dynamics for a Fuel Cell Stack," in *Proceedings of 2005 ASME International Mechanical Engineering Congress & Exposition*, 2005.

[112] D. Natarajan and T. Van Nguyen, "A Two-Dimensional, Two-Phase, Multicomponent, Transient Model for the Cathode of a Proton Exchange Membrane Fuel Cell Using Conventional Gas Distributors," *J. Electrochem. Soc.*, vol. 148, no. 12, pp. A1324–A1335, Dec. 2001.

[113] Y. Wang and C. Wang, "Transient Analysis of Polymer Electrolyte Fuel Cells," *Electrochim. Acta*, vol. 50, pp. 1307–1315, 2005.

[114] ——, "Dynamics of Polymer Electrolyte Fuel Cells Undergoing Load Changes," *Electrochim. Acta*, vol. 51, pp. 3924–3933, 2006.

[115] Y. Shan, S.-Y. Choe, and S.-H. Choi, "Unsteady 2d pem fuel cell modeling for a stack emphasizing thermal effects," *J. Power Sources*, vol. 165, pp. 196–209, 2007.

[116] S. Shimpalee, D. Spuckler, and J. V. Zee, "Prediction of transient response for a 25-cm2 pem fuel cell," *J. Power Sources*, vol. 167, pp. 130–138, 2007.

[117] J. Pukrushpan, H. Peng, and A. Stefanopoulou, "Modeling and Analysis of Fuel Cell Reactant Flow for Automotive Applications," *J. Dyn. Syst. Meas. Contr.*, vol. 126, no. 1, pp. 14–25, 2004.

[118] P. H. Rodatz, "Dynamics of the Polymer Electrolyte Fuel Cell: Experiments and Model-Based Analysis," Ph.D. dissertation, Swiss Federal Institute of Technology, ETH, 2003.

[119] A. Hernandez, D. Hissel, and R. Outbib, "Nonlinear State Space Modeling of a PEMFC," *Fuel Cells*, no. 1, pp. 38–46, 2005.

[120] A. Schilter, D. McKay, and A. Stefanopoulou, "Parameterization of Fuel Cell Stack Voltage: Issues on Sensitivity, Cell-to-cell Variation, and Transient Response," *Proceedings of the ASME 4th International Conference on Fuel Cell Science, Engineering and Technology*, vol. FUELCELL2006-97177, 2006.

[121] T. Springer, T. Zawodzinski, and S. Gottesfeld, "Polymer Electrolyte Fuel Cell Model," *J. Electrochem. Soc.*, vol. 138, no. 8, pp. 2334–2341, 1991.

[122] T. F. Fuller, "Solid polymer-electrolyte Fuel Cells," Ph.D. dissertation, University of California, Berkeley, 1992.

[123] S. Motupally, A. Becker, and J. Weidner, "Diffusion of Water in Nafion 115 Membranes," *J. Electrochem. Soc.*, vol. 147, no. 9, 2000.

[124] H. Yamada and Y. Morimoto, "Practical approach to polymer electroyte fuel cell modeling," *Research and Development Review of Toyota CRDL*, vol. 39, no. 3, 2004.

[125] H. Ju, C. Wang, S. Cleghorn, and U. Beuscher, "Nonisothermal Modeling of Polymer Electrolyte Fuel Cells," *J. Electrochem. Soc.*, vol. 152, pp. A1645–A1653, 2005.

[126] G. Lin, W. He, and T. V. Nguyen, "Modeling Liquid Water Effects in the Gas Diffusion and Catalyst Layers of the Cathode of a PEM Fuel Cell," *J. Electrochem. Soc.*, vol. 151, no. 12, pp. A1999–A2006, 2004.

[127] J. Amphlett, R. Baumert, R. Mann, B. Peppley, and P. Roberge, "Performance Modeling of the Ballard Mark IV Solid Polymer Electrolyte Fuel Cell, I. Mechanistic Development," *J. Electrochem. Soc.*, vol. 142, 1995.

[128] B. McCain and A. Stefanopoulou, "Order reduction for a control-oriented model of the water dynamics in fuel cells," in *Proceedings of 4th International Conference on Fuel Cell Science, Engineering and Technology*, vol. FUELCELL2006-97075, 2006.

[129] N. Djilali and D. Lu, "Influence of heat transfer on gas and water transport in fuel cells," *International Journal of Thermal Science*, vol. 41, pp. 29–40, 2002.

[130] S. Ge, X. Li, B. Yi, and I.-M. Hsing, "Absorption, Desorption, and Transport of Water in Polymer Electrolyte Membranes for Fuel Cells," *J. Electrochem. Soc.*, vol. 152, no. 6, pp. A1149–A1157, 2005.

[131] M. Kaviany, *Principles of Heat Transfer in Porous Media, second ed.* New York: Springer, 1999.

[132] P. Costamagna, "Transport phenomena in polymeric membrane fuel cells," *Chem. Eng. Sci.*, vol. 56, pp. 323–332, 2001.

[133] J. Hinatsu, M. Mizuhata, and H. Takenaka, "Water uptake of perfluorosulfonic acid membranes from liquid water and water vapor," *J. Electrochem. Soc.*, vol. 141, pp. 1493–1498, 1994.

[134] K. Dannenberg, P. Ekdunge, and G. Lindbergh, "Mathematical Model of the PEMFC," *J. Appl. Electrochem.*, vol. 30, pp. 1377–1387, 2000.

[135] T. Zawodzinski, T. Springer, F. Uribe, and S. Gottesfeld, "Characterization of Polymer Electrolytes for Fuel Cell Applications," *Solid State Ionics*, vol. 60, 1993.

[136] Y. Wang and C. Wang, "Two-phase Transients of Polymer Electrolyte Fuel Cells," *J. Electrochem. Soc.*, vol. 154, no. 7, pp. B636–B643, 2007.

[137] S. Litster, D. Sinton, and N. Djilali, "Ex situ visualization of liquid water transport in PEM fuel cell gas diffusion layers," *J. Power Sources*, vol. 154, pp. 95–105, 2006.

[138] F. Barbir, *PEM Fuel Cells: Theory and Practice*. Burlington, Ma: Elsevier, 2005.

[139] J. T. Pukrushpan, A. G. Stefanopoulou, and H. Peng, "Control of fuel cell breathing," *IEEE Contr. Syst. Mag.*, vol. 24, no. 2, pp. 30–46, Apr 2004.

[140] J. B. Siegel, D. A. McKay, and A. G. Stefanopoulou, "Modeling and validation of fuel cell water dynamics using neutron imaging," in *Proc. American Control Conference*, 11–13 June 2008, pp. 2573–2578.

[141] J. St-Pierre, D. P. Wilkinson, S. Knights, and M. Bos, "Relationships between water management, contamination and lifetime degradation in PEFC," *Journal of New materials for Electrochemical Systems*, vol. 3, pp. 99–106, 2000.

[142] M. Arcak, H. Gorgun, L. Pedersen, and S. Varigonda, "A nonlinear observer design for fuel cell hydrogen estimation," *IEEE Trans. Control Syst. Technol.*, vol. 12, no. 1, pp. 101–110, 2004.

[143] J. Pukrushpan, A. Stefanopoulou, S. Varigonda, L. Pedersen, S. Ghosh, and H. Peng, "Control of natural gas catalytic partial oxidation for hydrogen generation in fuel cell applications," *IEEE Trans. Control Syst. Technol.*, vol. 13, no. 1, pp. 3–14, 2005.

[144] K. Yoshizawa, K. Ikezoe, Y. Tasaki, D. Kramer, E. H. Lehmann, and G. G. Scherer, "Analysis of Gas Diffusion Layer and Flow-Field Design in a PEMFC Using Neutron Radiography," *J. Electrochem. Soc.*, vol. 155, no. 3, pp. B223–B227, Mar. 2008.

[145] D. Hussey, D. Jacobson, and M. Arif, "In situ fuel cell water metrology at the NIST neutron imaging facility," *Proceedings of the ASME International Conference on Fuel Cell Science, Engineering and Technology*, 2007.

[146] D. A. McKay, W. T. Ott, and A. Stefanopoulou, "Modeling, Parameter Identification, and Validation of Water Dynamics for a Fuel Cell Stack," in *Proceedings of 2005 ASME International Mechanical Engineering Congress & Exposition*, vol. IMECE 2005-81484, Nov 2005.

[147] B. A. McCain, A. G. Stefanopoulou, and I. V. Kolmanovsky, "A multi-component spatially-distributed model of two-phase flow for estimation and control of fuel cell water dynamics," in *2007 46th IEEE Conference on Decision and Control*, 12-14 Dec. 2007, pp. 584–589.

[148] A. Y. Karnik, A. G. Stefanopoulou, and J. Sun, "Water equilibria and management using a two-volume model of a polymer electrolyte fuel cell," *J. Power Sources*, vol. 164, no. 2, pp. 590 – 605, feb 2007.

[149] Z. H. Wang, C. Y. Wang, and K. S. Chen, "Two-phase flow and transport in the air cathode of proton exchange membrane fuel cells," *J. Power Sources*, vol. 94, pp. 40–50., 2001.

[150] A. Turhan, K. Heller, J. Brenizer, and M. Mench, "Passive control of liquid water storage and distribution in a PEFC through flow-field design," *J. Power Sources*, vol. 180, pp. 773–783, 2008.

[151] L. Onishi, J. Prausnitz, and J. Newman, "Water-Nafion Equilibria. Absence of Schroeder's Paradox," *J. Phys. Chem. B*, vol. 111, no. 34, pp. 10 166–10 173, 2007.

[152] A. Weber and J. Newman, "Modeling Transport in Polymer-Electrolyte Fuel Cells," *Chemical Reviews*, vol. 104, no. 10, pp. 4679–4726, 2004.

[153] C. H. Woo and J. Benziger, "PEM fuel cell current regulation by fuel feed control," *Chem. Eng. Sci.*, vol. 62, no. 4, pp. 957–968, Feb. 2007.

[154] B. McCain, J. Siegel, and S. A. G., "Stack-Level Validation of a Semi-Analytic Channel-To-Channel Fuel Cell Model for Two-Phase Water Distribution Boundary Value Control," in *American Control Conference*, 2008.

[155] A. Z. Weber, R. M. Darling, and J. Newman, "Modeling Two-Phase Behavior in PEFCs," *J. Electrochem. Soc.*, vol. 151, no. 10, pp. A1715–A1727, Oct. 2004.

[156] R. Borup, J. Meyers, B. Pivovar, Y. S. Kim, R. Mukundan, N. Garland, D. Myers, M. Wilson, F. Garzon, D. Wood, P. Zelenay, K. More, K. Stroh, T. Zawodzinski, J. Boncella, J. E. McGrath, M. Inaba, K. Miyatake, M. Hori, K. Ota, Z. Ogumi, S. Miyata, A. Nishikata, Z. Siroma, Y. Uchimoto, K. Yasuda, K.-i. Kimijima, and N. Iwashita, "Scientific Aspects of Polymer Electrolyte Fuel Cell Durability and Degradation," *Chemical Reviews*, vol. 107, no. 10, pp. 3904–3951, 2007.

[157] J. Benziger, "Fan the flame with water: Current ignition, front propagation and multiple steady states in polymer electrolyte membrane fuel cells," *AIChE J.*, vol. 55, no. 12, pp. 3034–3040, 2009.

[158] S. Basu, C.-Y. Wang, and K. S. Chen, "Phase change in a polymer electrolyte fuel cell," *J. Electrochem. Soc.*, vol. 156, no. 6, pp. B748–B756, 2009.

[159] N. R. Amundson, T.-W. Pan, and V. I. Paulsen, "Diffusing with stefan and maxwell," *AIChE J.*, vol. 49, no. 4, pp. 813–830, 2003.

[160] M. Adachi, T. Navessin, Z. Xie, B. Frisken, and S. Holdcroft, "Correlation of in situ and ex situ measurements of water permeation through nafion nre211 proton exchange membranes," *J. Electrochem. Soc.*, vol. 156, no. 6, pp. B782–B790, 2009.

[161] P. W. Majsztrik, M. B. Satterfield, A. B. Bocarsly, and J. B. Benziger, "Water sorption, desorption and transport in Nafion membranes," *J. Membr. Sci.*, vol. 301, no. 1-2, pp. 93–106, Sep. 2007.

[162] M. M. Mench, *Fuel cell engines*. Hoboken, N.J.: John Wiley & Sons, 2008.

[163] J. S. Newman., *Electrochemical systems*, 2nd ed. Englewood Cliffs, N.J: Prentice Hall, 1991.

[164] D. M. Bernardi and M. W. Verbrugge, "A Mathematical Model of the Solid-Polymer-Electrolyte Fuel Cell," *J. Electrochem. Soc.*, vol. 139, no. 9, pp. 2477–2491, 1992.

[165] A. Katsaounis, S. Balomenou, D. Tsiplakides, M. Tsampas, and C. Vayenas, "The role of potential-dependent electrolyte resistance in the performance, steady-state multiplicities and oscillations of PEM fuel cells: Experimental investigation and macroscopic modelling," *Electrochim. Acta*, vol. 50, no. 25-26, pp. 5132–5143, Sep. 2005.

[166] J. B. Siegel, S. Yesilyurt, and A. G. Stefanopoulou, "Extracting Model parameters and Paradigms from Neutron Imaging of Dead-Ended Anode Operation," in *Proceedings of FuelCell2009 Seventh International Fuel Cell Science, Engineering and Technology Conference*, 2009, pp. 439–446.

[167] S. A. Freunberger, M. Reum, J. Evertz, A. Wokaun, and F. N. Buchi, "Measuring the Current Distribution in PEFCs with Sub-Millimeter Resolution," *J. Electrochem. Soc.*, vol. 153, no. 11, pp. A2158–A2165, 2006.

[168] R. Taylor and R. Krishna, *Multicomponent mass transfer*. New York: Wiley, 1993.

[169] S. Ge, B. Yi, and P. Ming, "Experimental Determination of Electro-Osmotic Drag Coefficient in Nafion Membrane for Fuel Cells," *J. Electrochem. Soc.*, vol. 153, no. 8, pp. A1443–A1450, 2006.

[170] W. Borutzky, B. Barnard, and J. Thoma, "An orifice flow model for laminar and turbulent conditions," *Simulation Modelling Practice and Theory*, vol. 10, no. 3-4, pp. 141–152, 2002.

[171] M. Grtsch and M. Mangold, "A two-phase PEMFC model for process control purposes," *Chem. Eng. Sci.*, vol. 63, pp. 434–447, 2008.

[172] J. Larminie and A. Dicks, *Fuel Cell Systems Explained*, 2nd ed. Hoboken, NJ: Wiley InterScience, 2003.

[173] E. Mueller, F. A. Kolb, A. G. Stefanopoulou, D. A. McKay, and L. Guzzella, "Correlating Nitrogen Accumulation with Temporal Fuel Cell Performance," in *Proc. of Dynamic Systems and Control Conference (DSCC08)*, ser. , Paper TuAT5.1, 2008.

[174] W. H. Hogarth and J. B. Benziger, "Operation of polymer electrolyte membrane fuel cells with dry feeds: Design and operating strategies," *J. Power Sources*, vol. 159, no. 2, pp. 968 – 978, 2006.

[175] J. Nam, P. Chippar, W. Kim, and H. Ju, "Numerical analysis of gas crossover effects in polymer electrolyte fuel cells (PEFCs)," *Applied Energy*, vol. 87, no. 12, pp. 3699 – 3709, 2010.

[176] H. Gorgun, F. Barbir, and M. Arcak, "A voltage-based observer design for membrane water content in pem fuel cells," in *Proceedings of the 2005 American Control Conference*, vol. 7, June 2005, pp. 4796 – 4801.

[177] M. A. Hickner, N. P. Siegel, K. S. Chen, D. S. Hussey, D. L. Jacobson, and M. Arif, "In Situ High-Resolution Neutron Radiography of Cross-Sectional Liquid Water Profiles in Proton Exchange Membrane Fuel Cells," *J. Electrochem. Soc.*, vol. 155, pp. B427–B434, 2008.

[178] J. B. Siegel, X. Lin, A. G. Stefanopoulou, and D. Gorsich, "Neutron imaging of lithium concentration in battery pouch cells," in *Sumbitted to The American Control Conference*, 2011.